Kingdom of Morocco
Sultan Moulay Slimane University
Polydisciplinary Faculty of Khouribga

Doctoral School: Science and Technology
Doctoral Training Center: Applied Physics
Laboratory: Laboratory of Nanosciences and Modeling

PhD. Thesis No.: 300 /2020

DOCTORAL DISSERTATION

By

MOHAMMED EDDYA

For the degree of

Doctor

In

Physics and Engineering Sciences

Option: Material Science and Biomaterials Engineering

Developement of Hydroxyapatite-Metal (Cu, Co, Ni, Mn), and Chitosan-Hydroxyapatite-Carbon (CNT, CNH, GNPs) Hybrids Nanoparticles: From synthesis to Biomedical, Energetic and Environmental Applications

23/12/2020

Jury members:

Ahmed FAHLI, ……. Professeur, Présidence de UHP, Settat …….. President
Abdelkader OUTZOURHIT, .Professeur, FS Semlalia, Marrakech…... Reporter
Ahmed LIBA, …….. Professeur, FST, Béni Mellal …….. Reporter
Sanaa HAYANI-MOUNIR, … Professeur Habilité, FPK, Khouribga ….. Reporter
Mohamed MOUSSETAD, …Professeur FS Ben M'Sik, Casablanca…… Examiner
Youness ZAHIDI, ……Professeur Assistant, FPK, Khouribga …... Invited
Khalil EL-HAMI, ……Professeur, FPK, Khouribga …. Director of thesis

Foreword

This thesis has been prepared in fulfilment of the requirements for a Ph.D. at the University of Sultan Moulay Slimane, Beni Mellal, Morocco, under the direction of Professor Dr. Khalil El-Hami.

ACKNOWLEDGEMENT

Firstly, and before everything, I would like to thank gratefully ALLAH glory be to Him, for giving me the enthusiasm, stamina and facilitate the way for me to carry out this work from conception to completion. I would not have been able to do this without Him. Praise to Allah, Lord of the Worlds.

I would like to express my highest thanks and time recognition to my Director thesis **Prof.Dr. Khalil El-Hami** for his brilliantly mentoring, scientific help, and material assistance during all this study. I feel very grateful to have an opportunity to intern at this research team and for having him as my supervisor. He was so patient with me and shears his excellent experience to all of us. Thank you so much Prof. Dr. Khalil El-Hami. I greatly appreciated that when training me you took the to break things down to a level that I could understand and then build upon. The valuable skills I've learned from Prof.Dr. Khalil El-Hami over the past years has given me the excellent scientific research.

Special thanks to Prof. Dr. M. Kaddami and Z. Bakher from University of Hassan 1st of Settat, Morocco for their help and fruitful discussion without forgetting Prof. Dr. M. Liba from University of Moulay Slimane of Beni Mellal, Morocco for Uv-visible apparatus. Special thanks to Prof. Dr. M. Lamire, Prof. Dr. S.Krimi, Pr Dr. A.El Makssoudi, Prof. Dr. R.Elouatib, and A.Akhrouf from University Hassan II of Casablanca, Morocco for FT-IR and DRX apparatus. M thanks to dear Abderahim HASRI from Hassan I University of Settat, Morocco for XRD and XRF apparatus.

My gratitude to Prof. Dr. Abdelkader Outzourhit and Mr. Rachid El-Moutamanni from Cadi Ayyad University, Marrakech Morocco for SEM-EDX tools analysis, without forgetting Prof Tlemçani Mouhaydine from the University of Evora, Portugal, for receiving me and their help during my scientific stay at Evora city without forgetting Prof. Patricia Moita from Hercules Laboratory, University of Evora, Portugal for TG-DTG apparatus.

Phrases cannot display how much I thank and I appreciate my parents Mr. Hadj Jilali EDDYA and Mrs. Hadja Fatna MOUMEN for all that I am now. Their beliefs of obdurate work, perseverance, patience, and excellence have permitted me to climb through challenges. They are my inspiration and motivation.

I am also grateful to my wonderful brothers, Abdellah, Nadia, Wafaa, Nawal, Aziza, and Aziz, who have hoped always the success for me. I am also thankful equally to my other side, my lovely wife Mrs. Naoil NADI who I hope also the success for Him in its field as Doctor Pharmacist. Special thanks and love for my lovely daughter Marwa and my lovely son Souhail that understood my pain when the workload got tremendous and stressful. I am sorry for them for any moment, which I was not available to them.

Finally, I would like to appreciate all my friends in our laboratory of nanosciences and modeling and all my friends in the University of Sultan Moulay Slimane of Beni Mellal and in the University of Hassan 1st of Settat for their help through hard moments of my Ph.D. life. I do not forget tp thank my friends and colleague's trough all my country at the Caddy Ayyad University of Marrakech, University of Hassan II Ain chock and at University Hassan II Ben M'sik. Thanks to my friends at Polytechnica University of Bucarest in Romania, Evora University Portugal, University of Patras in Greece for their help, collaboration, and positive criticism throughout the conferences, training period, and common positive moment during this research.

I dedicate this thesis to my loving and wonderful parents,

Mr. Hadj Jilali EDDYA and Mrs. Hadja Fatna Moumen.

Thank you

ABSTRACT

Naturally, the Human body has a remarkable capacity to update minor bones weakness and regenerate it in case of minor injury continuously in its life. However, major weakness and injuries such as degradation or lacking spine, hips, and knee, require orthopedic surgeries. In addition, the same for tooth, the human body cannot regenerate it after its damage requiring partial or total dental implants. These bone or dental implants made from biomaterials. Our aim from this study is to develop hybrid particle biomaterials based on Hydroxyapatite HAP, Chitosan, and Carbon nanomaterials such as Graphene nanoplatelets C90 (GNPs_C90), Graphene nanoplatelets C97 (GNPs_C97), Multiwall Carbon Nanotubes MWCNT and Single-wall Carbon Nanohorns SWCNH by chemical deposition with easiness in synthesis route. We report also the first synthesis of HAP by sol-gel using albumin (egg white) compared with the four classical elaboration methods such as co-precipitation, solid state, and solid-liquid samples of HAP in order to improve these biomaterials. We use a reference sample of HAP bought from Fluka Chemika Comp. As well, Chitosan and chitin are, mainly, extracted from shells of fish such as lobsters, crabs, or shrimps. Originally, the raw material and the two compounds are identical. We aim to show the acid concentration effect on chitosan extraction from shrimp shells between concentrated and diluted acid; on surface morphology, thermal resistance, structural, elemental composition, optical, and optoelectronic properties. It also aims to reduce production time and increase the quantity. We focused mainly on comparing between Physico-chemical properties of Chitosan extracted by diluted (1M) and concentrated (20%) Chloric acids, and sometimes we compare by other concentrated acids like nitric acid (70%) and sulphuric acid (98%). Also, to choose the adequate chitosan product in particle sizes and degree of deacetylation to be linked with HAP and carbon nanomaterials. On the other side, incorporating metal ions into a calcium HAP structure is a successful pathway to increase their physical, chemical, and biological properties. For this reason, four transition metal ions (Mn^{2+}, Co^{2+}, Ni^{2+}, Cu^{2+}) were incorporated into HAP cell by easy ceramic route method, by dint of grinding and heat treatment to remove all the impurity and require the homogeneity. Those doped HAP show a good matrix structure after metal ions incorporations. We exploited their thermal and electrical conductivities to use them as a bio-ceramic amalgam for dental prosthesis and try to solve tooth damage after partial removal or carries damage. They offer a good

opportunity to solve tooth degradation due to the increase of the mechanical, electrical, and thermal performances with reducing the risk of toxicity lower than the international reference level of cobalt and nickel toxicity for health. Those bio-ceramic amalgams present a similar sensation of a natural tooth. Furthermore, these transition metal ions gave HAP a good photocatalytic activity. This property leads to apply our doped HAP in the photocatalytic fields of production and storage of energy and also in the environmental remediation to degrade and absorb the microscopic dyes and heavy metal ions from aqueous media. We performed the product's characterization by various tools such as X-ray diffraction spectroscopy, X-ray fluorescence analysis, UV-Visible spectroscopy, Fourier Transformed Infra-Red, Raman Spectroscopy, Thermogravimetry and Derivative Thermogravimetry (TG/DTG), Scanning Electron Microscopy (SEM), Energy-dispersive X-ray spectroscopy (EDX) analysis. The XRD study showed the existence of a Hexagonal phase for all our samples prepared in our laboratory and an orthorombic phase for the reference sample. The study by Uv-visible spectroscopy was performed to determine and compare the optical gap and the disorder of each sample of HAP. The FT-IR spectroscopy demonstrated that all our HAP samples had a similar mode of vibration of the chemical bonds (OH^-) and $(PO_4)^{3-}$. The doped HAP powders with metal ions were characterized by X-ray diffraction, and Fourier transforms infrared spectroscopy analysis to evaluate their structural and compositional changes. The only phase that is presented in the pure HAP sample was the hexagonal system. A Rietveld refinement has shown that doping with these ions affects the volume unit cell of HAP-M and it will be changed. We found that the samples doped HAP-M (M = Mn^{2+}, Co^{2+}, Ni^{2+}, Cu^{2+}) stabilizes only in the monoclinic phase. The optoelectronic results show that the incorporation of the metal ions into the HAP influences the gap energy, which affects an increase in electrical conductivity up to 130% and thermal conductivity up to 140% in our elaborated samples. The result of this work concerned the orthopedic application since the HAP is also a major constituent in the mineral part of bones. For Chitosan products, the results showed that all samples which we gained are good, about 80% degree of deacetylation, and pure mostly composed by carbon between (15 % - 45%), nitrogen (4% - 12%) and oxygen (42% and 81%), with appearance of essential peaks for chitosan in Raman analysis: 470 cm^{-1} → ν(C-C(=O)-C), 1000 cm^{-1} → ν(C-H), 1800 cm^{-1} → δ(C=COOR), δ(C=O), 2630 cm^{-1} → δ(CH) rings, 3250 cm^{-1} → ν(NH_2). All our chitosan

particles are ultrafine nanoscale between 8 and 34 nm. For the synthesis of hydride nanocomposites of Chitosan-HAP-Carbon nanomaterials, The results show a good concordance in chemical composition between mother particles of HAP with 35.60% of Calcium (Ca) and 13.90% of Phosphorus (P) and produced hybrid particles CS-HAP-SWCNH, CS-HAP-GNPs_C97, CS-HAP-MWCNT, and CS-HAP-GNPs_C90 with crystallites size around 50 nm, and an apparition of new band linkage C=C stretch and stretching vibration of the C=O group around 1630 cm^{-1} and NO_2 stretch around 1320 cm^{-1} caused by linked C_H/N_H. Those two and other new bands and the homogeneity of each product sowed by SEM prove a good deposition and linkage between HAP, CS, MWCNT, SWCNH, GNPs_C90, and GNPs_C97. All our hybrid nanoparticles provide good osteoconductivity due to their HAP compound and antibacterial and anti-microbial activity relaying to CS, with high physical and chemical properties for each hybrid particle according to its deposited carbon materials. We report by this study to contribute to the development of biomaterials designed for health, energy, and environment protection, and help Humanity to overtake some problems in these fields. Thanks to Allah lord of the world.

Résumé de la thèse de doctorat

Naturellement, le corps humain a une capacité remarquable à compenser la faiblesse des os dégradés et à les régénérer en cas des petites blessures d'une façon permanente au cours de la vie. Cependant, et en cas d'une faiblesse majeure ou des graves blessures telles que grande dégradation ou une absence d'une partie des os, soit dans la colonne vertébrale, les hanches ou les genou… nécessitent des chirurgies orthopédiques. Et de même pour les dents, le corps humain ne peut pas les régénérer après ses dégradations qui nécessitent des implants dentaires partiels ou totaux. Ces implants osseux ou dentaires sont fabriqués à partir des biomatériaux.

Notre objectif dans cette étude, est de développer des biomatériaux de particules hybrides à base d'hydroxyapatite HAP, Chitosane (CS) et des nanomatériaux de carbone tels que les nanoplaquettes de graphène C90 (GNPs_C90), les nanoplaquettes de graphène C97 (GNPs_C97), les nanotubes de carbone multi-parois MWCNT et les nanocornes de carbone à seul paroi SWCNH par méthode de dépôt chimique avec simplification de cette voie de synthèse. Nous avons également developpé une nouvelle methode de synthèse d'HAP par voie sol-gel par utilisation de l'albumine (blanc d'œuf) et on a comparé notre produit obtenu avec ceux synthétisés par quatre méthodes d'élaboration classiques telles que la méthode de coprécipitation chimique, voie solide, solide-liquide pour améliorer l'HAP. Nous avions utilisé un échantillon de référence d'HAP acheté d'auprès Fluka Chemika Company. D'autre part, le CS et la chitine sont principalement extractés de carapaces de crustacés comme les homards, les crabes ou les crevettes. À l'origine, la matière première et les deux composés sont identiques. Nous avions montré les effets de la concentration d'acide sur : l'extraction du CS des coquilles de crevettes entre les acides concentrés et les acides dilués sur :

- La morphologie de surface, la résistance thermique, la structure cristalline, la composition chimique élémentaire, les propriétés optiques et optoélectroniques.

Nous avions pu réduire le temps de production et augmenter la quantité produite. Nous nous sommes concentrés principalement sur la comparaison entre les propriétés physico-chimiques du CS extracté par l'acides chloridrique dilués (1 M) et concentrés (20%), et nous l'avions comparé avec d'autres acides concentrés comme l'acide nitrique (70%) et l'acide sulfurique

(98%) pour choisir le produit de CS adéquat en tailles de particules et en degré de désacétylation à associer à l'HAP et aux nanomatériaux de carbone.

L'incorporation d'ions métalliques dans une structure d'HAP de calcium est une voie efficace pour augmenter leurs propriétés physiques, chimiques et biologiques. Pour cette raison, quatre ions de métaux de transition (Mn^{2+}, Co^{2+}, Ni^{2+}, Cu^{2+}) ont été incorporés dans la maille d'HAP par une méthode de voie solide, à force de broyage et de traitement thermique pour éliminer toute impureté et avoir l'homogénéité. Ces HAP dopés présentent une bonne structure matricielle après incorporation d'ions métalliques. Nous avons exploité leurs conductivités thermique et électrique pour les utiliser comme amalgame bio-céramique dans les prothèses dentaires. Suites à cela, nous avions essayé résoudre les dommages aux dents après une dégradation partielle ou totale. Ces produits offrent une bonne opportunité pour l'augmentation des performances des amalgames dentaires ; mécaniques, électriques et thermiques tout en réduisant le risque de toxicité des ces produits, en respectant la norme internationale de la toxicité du cobalt et du nickel pour la santé. Ces amalgames basés sur des composites d'HAP-Métal biocéramiques présentent une sensation similaire aux dents naturelles. De plus, ces ions offrent à l'HAP une bonne activité photocatalytique. Cette propriété permet d'appliquer notre HAP dopée dans les domaines photocatalytiques de production et de stockage d'énergie. De plus, on peut l'extrapoler à la remédiation environnementale, pour dégrader et absorber les colorants microscopiques et les ions de métaux lourds des milieux aqueux. Nous avons effectué la caractérisation du produit par divers outils tels que la spectroscopie de diffraction des rayons X (DRX), l'analyse de fluorescence des rayons X, la spectroscopie UV-visible, la transformée de Fourier infrarouge, la spectroscopie Raman, la thermogravimétrie et la thermogravimétrie dérivée (TG/DTG), la microscopie électronique à balayage (MEB), analyse par spectroscopie à rayons X à dispersion d'énergie (EDX). L'étude DRX a montré l'existence d'une phase hexagonale pour tous nos échantillons préparés dans notre laboratoire et d'une phase orthorhombique pour l'échantillon de référence. L'étude par spectroscopie Uv visible a été réalisée pour déterminer et comparer les Gap optiques et le désordre énergétique de chaque échantillon d'HAP. La spectroscopie FT-IR a démontré que tous nos échantillons HAP avaient un mode de vibration similaire des liaisons chimiques (OH^-) et $(PO_4)^{3-}$. Les poudres d'HAP dopées par des ions métalliques ont été caractérisées par diffraction des rayons X et analyse de

spectroscopie infrarouge par la transformée de Fourier pour évaluer leurs changements structurels et de composition. La seule phase présentée dans l'échantillon d'HAP pure était le système hexagonal. L'affinement Rietveld a montré que le dopage avec ces ions affecte le volume de la maille élémentaire d'HAP-M. Nous avons constaté que les échantillons dopés HAP-M (M = Mn^{2+}, Co^{2+}, Ni^{2+}, Cu^{2+}) se stabilisent uniquement dans la phase monoclinique. Les résultats optoélectroniques montrent que l'incorporation des ions métalliques dans l'HAP influence l'énergie de l'entrefer, ce qui affecte une augmentation de la conductivité électrique jusqu'à 130% et de la conductivité thermique jusqu'à 140% dans nos échantillons élaborés. Le résultat de ce travail concerne l'application orthopédique puisque l'HAP est également un constituant majeur de la partie minérale des os. Pour les produits Chitosan, les résultats ont montré que tous les échantillons que nous avons obtenus sont purs : environ 80% de degré de deacetylation, principalement composés de carbone entre (15% - 45%), l'azote (4% - 12%) et oxygène (42% et 81%), avec apparition de pics essentiels pour le CS dans l'analyse Raman: 470 cm^{-1} → ν(C-C(=O)-C), 1000 cm^{-1} → ν(C-H), 1800 cm^{-1} → δ(C=COOR), δ(C=O), 2630 cm^{-1} → δ(CH) anneaux, 3250 cm^{-1} → ν(NH_2). Toutes nos particules de CS sont à l'échelle nanométrique pour 8 et 34 nm. Pour la synthèse de nanocomposites d'hydrures de nanomatériaux Chitosan-HAP-Carbone, les résultats montrent une bonne concordance dans la composition chimique entre les particules mères de HAP avec 35,60% de Calcium (Ca) et 13,90% de Phosphore (P) et les particules hybrides produites CS-HAP-SWCNH, CS-HAP-GNPs_C97, CS-HAP-MWCNT et CS-HAP-GNPs_C90 avec des cristallites d'une taille d'environ 50 nm, et une apparition d'une nouvelle liaison de bande C = C étirement et étirement des vibrations du groupe C = O autour 1630 cm^{-1} et NO_2 s'étirent autour de 1320 cm^{-1} causés par C_H / N_H liés. Ces deux nouvelles bandes prouvent un bon dépôt et une bonne liaison entre HAP, CS, MWCNT, SWCNH, GNPs_C90 et GNPs_C97. Toutes nos nanoparticules hybrides présentent une bonne ostéoconductivité grâce à leur composé d'HAP et leur activité antibactérienne et antimicrobienne grâce au CS, avec des propriétés physiques et chimiques élevées selon le type de carbonés déposés. Nous espérons par cette étude à contribuer au développement des biomatériaux conçus pour la santé, l'énergie et la protection de l'environnement.

List of Tables

List of Figures

List of Abbreviations, Symbols and Units

HAP	Hydroxyapatite
HAP-Ni	Hydroxyapatite-Nickel
HAP-Co	Hydroxyapatite-Cobalt
HAP-Cu	Hydroxyapatite-Copper
HAP-Mn	Hydroxyapatite- Manganese
CS	Chitosan
MNS	Nanomaterials
CNT	Carbon Nanotubes
GNPs	Graphene Nanoplatelets
SWCNT	Single-Wall Carbon Nanotubes
MWCTS	Multi-Walled Carbon Nanotubes
SWCNH	Single-Wall Carbon Nanohorns
C-MNS	Carbon Nanomatterials
XRD	X-Ray Diffraction
XRF	X-Ray Fluorescence
EDX	Energy-dispersive X-ray spectroscopy
FTIR	Fourier-transform infrared spectroscopy
TG	Thermogravimetry
DTG	Derivative Thermogravimetry
TG-DTG	Thermogravimetry- Derivative Thermogravimetry

SEM	Scanning electron microscopy
Uv-Vis	Uv-visible spectroscopy
Ca	Calcium
P	Phosphorus
O	Oxygen
H	Hydrogen
Ni	Nitrogen
C	Carbon
Mn	Manganese
Co	Cobalt
Ni	Nickel
Cu	Copper
P_2O_5	Phosphorus Pentoxide
CaO	Calcium Oxide
$Ca(OH)_2$	Calcium Hydroxide
HCl	Hydrochloric acid
HNO_3	Nitric Acid
H_2SO_4	Sulphuric Acids
H_3PO_4	Phosphoric Acid
Chitosan NA	Chitosan Extracted by Concentrated Nitric Acid
Chitosan SA	Chitosan Extracted by Concentrated Sulphuric Acid
Chitosan CA	Chitosan Extracted by Concentrated Hydrochloric Acid
Chitosan DCA	Chitosan Extracted by Diluted Hydrochloricc Acid
Chitosan FC	Chitosan from Fluka Chemika Company
CS-HAP-SWCNH	Chitosan-Hydroxyapatite-Single Walled Carbon Nanohorns
CS-HAP-MWCNT	Chitosan-Hydroxyapatite-Multi Walled Carbon Nanotubes
CS-HAP-GNPs_C97	Chitosan-Hydroxyapatite-Graphene Nanoplatelets Grade C 97
CS-HAP-GNPs_C90	Chitosan-Hydroxyapatite-Graphene Nanoplatelets Grade C 90
σ	Electrical conductivity
λ	Thermal conductivity

Eg	Gap energy
Eu	Urbach Energy
T%	Optical Transmittance
A%	Optical Absorbance
R%	Optical Reflectance
s	Second
min	Minute
m	Meter
nm	Nanometer
l	Liter
ml	Milliliter
kg	Kilogram
g	Gram
mg	Milligram
N	Newtons
(N/m^2)	Newtons per square metre
A	Ampere
K	Kelvin
°C	Celsius degree
mol	Mole
eV	Electronvolt
W	Watts
S	Siemens
W/(m·K)	Watts per meter-kelvin
S/m	Siemens per meter
ppm	Parts Per Million

Table of contents

Chapter I :

INTRODUCTION

I.1 Background study

Since the last century, life expectancy increased from 46.8 years in 1950-1955 to 70.8 years in 2010-2015 [1], So increase by 24 years (World Bank Open Data). Some prospective studies seek to estimate life expectancy at birth in the future. These scientific studies predict an increase in life expectancy in most countries by 2025 (ONU /World Population Prospects 2019 revision). This can be attributed to the continuous improvement of human life, food availability, health care provided today, particularly with the development of devices such as pacemakers, heart valves, aortic implants, and stents, vaccinations and m others. However, for human bones, this overall increase in the average human lifespan has increased the likelihood of bone fractures. Indeed, with age, the bones, and especially the supporting bones such as the spine, hips, and knees, are susceptible to damage by diseases or by imprudence, recklessness, or accident. The same goes for teeth; the increase in life expectancy presents a challenge against tooth damaged by caries or by other incidents. As a result, there has been growing interest in the biomedical field; orthopedic and orthodontic to develop stents/scaffolds to restore damaged bone function [2,3,4] and dental implant and amalgams to resolve the teeth damage. These scaffolds, amalgams, and orthopedics implants are made from biomaterials such as polymers, ceramics, minerals, and their composites. Thus, highlighting the role of biomaterials in improving the quality of human life and extending life in general [5].

It is important to note that the selection of vital materials depends on the repair or restoration of the bones. For example, the bones, ligaments, and scaffolding that hold the cartilage in joints can withstand stress. Another factor that can determine the choice of biological material is the interaction between biological material and the human body. This means that the biomaterial must be biocompatible with the organism and be able to promote healing or bone growth [6].

To date, bio-preferred materials for dental and bone-bearing implants have been prepared from ceramic metal or mineral polymers due to the high strength of the minerals. In the early 1960s, Sir John Charlie developed the first successful hip replacement in stainless steel and high molecular weight polyethylene (UHMWPE) [7]. As a result, a complete knee replacement was developed between 1968 and 1972. However, these metal implants suffered

Early failure due to the formation of wear particles or the accumulation of wear products in the tissues surrounding the implantation [8, 9].

In other words, the inability of the mineral implants to adapt to the biological environment caused the scaffolding to collapse before the bone healed. Therefore, mineral-based implants must be changed/replaced to reach a revision rate of 10% in 10 years [10, 11]. The Table 1 and the figure .1, show the development of life expectancy in the world between 1950 and 2015s.

Table 1. Life expectancy in the World between 1950-2015s [12]

Life expectancy in the World							Differential
1950–1955	**1960–1965**	**1970–1975**	**1980–1985**	**1990–1995**	**2000–2005**	**2010–2015**	**1950–2015**
46,8	51,1	58,1	62	64,5	67	70.8	▲ **24**

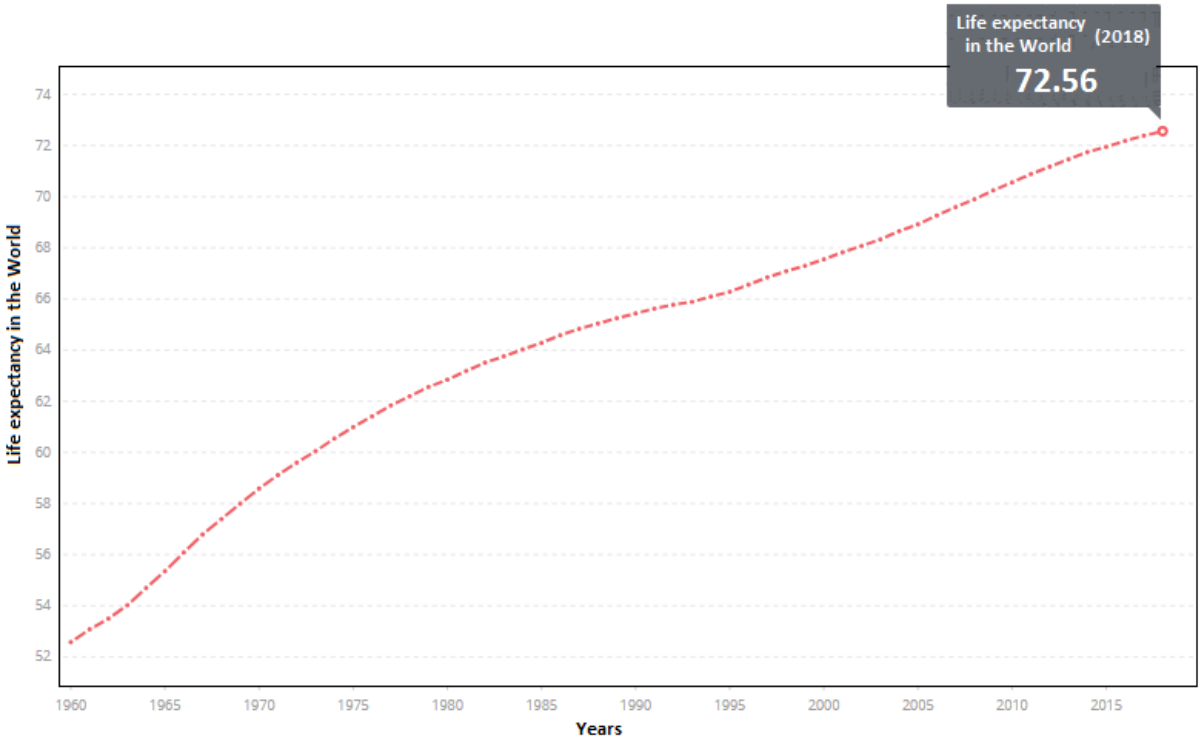

Figure 1. Life expectancy's growth in the World between 1950-2015s [12]

I.2 Problem statement and Motivation

The metallic polymers [13, 14] and ceramic-metal implantation [15, 16] presents a numerous disadvantage. We look for new and improved development of biomaterials composites to developed the mechanical properties of materials used actually for healthcare and give them new biological properties and increase its biocompatibilities. Different metal or polymers have been successfully used in various medical applications and they are satisfactory in the mechanical requests. But certain metal as Mercury, Cobalt, Nickel, and their alloys are

very dangerous for human health due to their high toxicities and low biocompatibility. Also, they have a short lifespan reason to the dislocation between metals and bones. The recent metallic implants based on Titanium are satisfactory in mechanical and biological properties [17, 18] but it is not accessible by everyone due to its high cost [19, 20]. On the Other side, even if ceramics are biologically active substances and provide good binding capacity with bone, they also display low tensile strength and toughness when breaking which limits their use in large quantities to load implants. For all previous reasons, we combined ceramics especially HAP and few quantities of metals for increasing its mechanical and electrical properties. Also, to coupled HAP Chitosan and carbon nanomaterials and small quantities of Carbon Nanotubes and Carbon Nanohorns and Graphene nanoplatelets to product hybrids nanomaterials powders synthesized by a safe and easy chemical process. These biomaterials provide very well mechanical strength and display very good electrical properties to ensure the osteoconductivity [21] and they are biocompatible [22] and biologically active [23] due to the presence of chitosan. We are synthesized and developed these biomaterials addressed to dental and orthopedic fields with low cost to be accessible by numerous people with low incomes.

I.3 Scope of study

I.3.1 Preparation of Hydroxyapatite –

HAP will be synthesized via different methods: Co precipitation, Solid-state method, Solid liquid method, Solid-liquid equilibrium of the quasi ternary system P_2O_5-CaO-H_2O, and our Novel method of preparation of HAP by Sol-gel method using albumin. All HAP powders will be characterized using XRD, FTIR, Uv-visible spectroscopy. We will compare the structural, optical, opto-electronical and vibrational properties of all produced HAP to Chose the optimal method that give a pure HAP with good physico-chemical properties

I.3.2 Development of Hydroxyapatite –

HAP will be developed via doping by few quantities of metallic chromophore ions of Co, Ni, Cu and Mn. This incorporation gave us four biomaterials for the use in dental amalgams, with more mechanical and electronic performance, and less risk of toxicity compared to metallic amalgams that cause problems of human health due toxicity and inflammation. These results can also be used in the orthopedic application to solve the problem of increasing concentration of cobalt after installation cobalt chromium alloy of hip and knee metallic implants that causes various problems after installation. Also, these powders reason to their high photovoltaic activity since their gap energies can be applied to fabricate a developed solar panels to be used in areas of production of sulphuric acid were the solar panels based on silicon can't be utilized due to their rapid corrosion due to existence of sulphuric acid in the atmospheric air of zone of production like Aljorf Lasfar in Morocco.

I.3.3 Extraction of Chitosan-

Chitosan will be extracted from Shrimp Shells by Diluted and Concentrated Acids aims to show the acid concentration effect on physic-chemical properties of Chitosan on Surface morphology, thermal stability, structure, elemental composition, optical and opto-electronic properties. It also aims to compare between time of production using the diluted (1M) and concentrated (20%) Chloric acids, and sometimes we compare by other concentrated acids like nitric acid (70%) and sulphuric acid (98%), in order to optimise our method of extraction for reducing the production time and increasing the quantity with high quality.

I.3.4 **Preparation of hybrids nanocomposite-**

Chitosan-HAP-Carbon (GNPs, MWCNT, and SWCNH) hybrid nanoparticles will be prepared via our developed method of chemical deposition by keeping HAP, Chitosan and Carbon soluble simultaneously by common solvents aims to produce homogenate hybrids nanoparticles in surfaces and in depth. These hybrids nano-powders displays high antibacterial and antimicrobial activities according to existence of chitosan, and high biocompatibility in fact that HAP is the major compound of mineral part of human bone, and high mechanical strength and electrical properties due to presence of few quantities of MWCNT, SWCNH or GNPs. These Biomaterials do not display risk of toxicity regarding their natural sources and respect the allowed quantities of carbon material nanosclae for health according to the international standards of health for biomedical applications.

I.3.5 **Characterization of the nanocomposites-**

All synthesized nanocomposites are characterized by X-ray fluorescence (XRF) analysis to investigate the variation on composition following the carbon kind used, X-ray diffraction (XRD) and Energy-dispersive X-ray spectroscopy (EDX) analysis for deduce the structural properties, Fourier Transformed Infra-Red (FTIR) spectral analysis for displaying the assignments and appeared bonds between Chitosan-HAP-Carbon, and the Scanning electron microscopy (SEM) analysis for morphological properties.

I.3.6 **Application of our materials:**

Dental amalgams-

It is well explained that all our produced materials provide high compatibility to be used in the fabrication of dental and orthopedic amalgams and implants. Besides, we optimized our doped HAP by low concentration of metallic ions to have similar electrical and thermal conductivities of tooth to ensure the sensitivity of hot and cold of patient after installation of amalgams or dental implants, reason that major materials used in the fields of dentals substitution give no sensation of cold, warm or hot for patients.

Energy production –

Optical properties of HAP doped by metallic ions will be investigated by Uv-visible spectroscopy to deduce their behavior with light, also to calculate their intrinsic and modified gap energies. These products are bio-degradable semiconductor able to be used for solar panels fabrication and environment protection.

Energy storage –

HAP will be coupled by Spinels Oxide which is used already as materials of storage of electrical energy. The synthesis of spinels oxide and doped spinel oxide by lead are well done and its structure is well defined, and its combinaison with HAP was considered as outlook.

Protection of environment –

Transition metal metal ions were fixed and immobilized by HAP, this metal ions are considered as chemical germs for increasing the HAP capacity of absorption and adsorption of pigments and microscopic dyes.

I.4 Aims and objectives

This study aims to develop the physico-chemical properties of HAP by doping by metallic ions and synthesis of hybrids nanoparticles of reinforced and active HAP with Chitosan and Carbon nanomaterials (MWCNT, SWCNH and GNPs).

Hence, the objective of this research was accomplished by studying the following targets:

i. Synthesis, optimisation and characterization of HAP.
ii. Development of HAP by doping by metallic ions.
iii. Extraction, optimisation and characterization of Chitosan.
iv. Develop the chemical deposition method for synthesis the nanohybrids and homogenate nanocomposites of Chitoan-HAP-Carbon.
v. Characterization of nanocomposites of Chitoan-HAP-Carbon.
vi. Investigation of the effect of use of MWCNT, SWCNH and GNPs in the elemental composition, morphological, and structural properties of HAP.
vii. Seek the outlook to use our produced powder in addition of our focused biomaterial field for health to other material fields as energy production and storage also for environment protection.

I.5 Thesis outline

This thesis includes nine chapters and an appendix about structural refinement of all our materials. The overviews of the chapters in this manuscript are as follows:

Chapter 1- involves the background of this research, the problem description, the aims and objectives, scope and cHAPters profile of this study.

Chapter 2- gives an in-depth review of the literature linked to the development of polymers and HAP with different metal and carbon nanomaterial and their impact on their physico-chemical properties and biocompatibility.

Chapter 3- describes the methods used in carrying out of the experiments and technical analysis applied for characterization of produced materials in this work: XRD, XRF, EDX, FTIR, RAMAN Spectroscopy, TG-DTG, SEM, Uv-visible spectroscopy. Also, we will give details about the raw materials used in the synthesis of HAP or extraction of Chitosan, as well the particularity of solvents used in the synthesis of our hybrid nanocomposites.

Chapter 4- addresses the synthesis of HAP by diverse methods and the characterization by various tools analysis. Furthermore, the vibrational assignments, structural, optical, and optoelectronic properties of the produced samples of HAP have been discussed.

Chapter 5- discuss the doping of HAP by low concentration of chromophore ions of Co^{2+}, Ni^{2+}, Cu^{2+}, and Mn^{2+} by ceramic route methods and characterization by XRD, FTIR and UV-visible for, structural, vibrational and opto-electronic properties exploration.

Chapter 6- treat the extraction of Chitosan from shrimp shells by diluted and concentrated acids for optimizing the extraction process. Additionally, Elemental composition, structural, thermal, vibrational assignment, optical and opto-electronical, morphological properties and degree of deacetylation were discussed.

Chapter 7- addresses the synthesis of hybrids nanoparticles of Chitosan-HAP-Carbon (MWCNT, SWCNT, and GNPs) by chemical method deposition. and investigation about the effect of MWCNT, SWCNT, and GNPs on the elemental composition, vibrational assignment, structural, and morphological properties of produced nanocomposites.

Chapter 8- describes the possibility of application of HAP doped by low concentration of chromophore ions of Co^{2+}, Ni^{2+}, Cu^{2+}, and Mn^{2+} on bio-ceramic amalgams for dental application. Their Optoelectronic properties, electrical and thermal conductivities were highlighted and their toxicities were discussed,

Chapter 9- concludes the principal findings regarding the aim and objectives of this study and presents the prospect for future works to generalize the use of our powders in energy fields in production and storage and environmental protection by absorption and immobilization of heavy metal ions.

Chapter II : LITERATURE REVIEW OF HYDROXYAPATITE, CHITOSAN AND CARBON-DERIVATIVES

II.1 Introduction

This chapter provides a literature review of HAP and their potential application in biomedical fields for bones and teeth that we illustrate mainly significant information and description. A review of the application of HAP for energy and protection of the environment are also exhibited. In the last section of first part, we regrouped the techniques of modification of HAP and its biocompatibility. In the second part, we provided lectures in the literature about Chitosan. Firstly, we presented their largest recourses as a crustacean (shrimp shells, crabs, and lobster) and mushrooms, and then we gave its goodness for human health and its friendship towards the environment. Finally, we presented its biocompatibility and biological activity, especially their antibacterial and antimicrobial activities. In the third part, we presented a review of carbon nanomaterial that we will use in this study as Graphene, Carbon nanotubes, and Carbon Nanohorns, also their methods of synthesis and their physical, mechanical, thermal, electrical, and morphological properties. We further presented their ability to be combined with chitosan and HAP. Finally, we illustrate the methods deposition and we terminated the chapter by summary.

II.2 Hydroxyapatite

II.2.1 Definition of Hydroxyapatite

HAP with the chemical formula $Ca_{10}(PO_4)_6(OH)_2$ is an inorganic material very important in biology and chemistry [24]. The biological HAP is the phosphates of most common crystalline calcium [25], it's the first mineral constituent of bones, enamel dental and dentine. It is very flexible in terms of composition and morphology. Synthetic HAP, often used as a biomaterial, also has a number of increasing applications as a heterogeneous catalyst for a number of important organic reactions. To better understand the functioning of these materials which often have an atypical basic but very interesting reactivity in term of conversion and selectivity, we must look at the different parameters (structure, substitution, stoichiometry ...) that make this material a singular system both for applications in heterogeneous catalysis than in various other fields.

II.2.2 **Synthesis methods of hydroxyapatite**

- Synthesis by co-precipitation

The general principle of this method is to add drop by drop or all at once a reagent in aqueous phase to the other reagent in aqueous phase before leaving the mixture, at the desired pH, with stirring at a temperature between 25 ° C and 100 ° C usually for a time varying from 5h to 24h. Commonly used reagents can be of two types:

a - In the case of a direct neutralization $Ca(OH)_2$ and H_3PO_4 will be the reagents and this choice has the advantage of not leaving residual counter-ions [26]. On the other hand, the resulting HAP is often quite carbonated, which can make complex evaluation of their basic reactivity.

b - In the case of a double decomposition by continuous precipitation we will use rather $Ca(NO_3)_2$ [27], and $(NH_4)_2HPO_4$ [28], or $(NH_4)H_2PO_4$ because although it is possible to find traces of nitrates and ammonium ions in the final HAP, these ions are easily eliminated by heating. The major drawback of this method lies in the risks of non-reproducibility especially in terms of stoichiometry. Indeed, the number of parameters to control with accuracy is more important for this method than for others (pH, rate of addition, synthesis temperature, starting reagents, stirring speed ...) [29]. But this versatility is also the main advantage of this technique since it is possible to vary one by one these parameters to study their impact on the final material in terms of morphology, stoichiometry or catalytic activity and thus to obtain great variety of samples With this method of synthesis the particles obtained are often thinner and higher specific surface areas than those obtained for a synthesis by dry method that requires high temperatures [30].

- Hydrothermal synthesis

The hydrothermal method is based on the direct mixing of the reagents under pressure in an autoclave at a given temperature. The variety of precursors used in this method is quite important: for calcium precursors found those conventionally used for the co-precipitation method $Ca(NO_3)_2$ [31], [32] and $Ca(OH)_2$ [30, 33] but also less common precursors such as $CaCO_3$ [34] or a mixture of phosphate and calcium precursors: $Ca(H_2PO_4)_2$ or $CaHPO_4$ which play the role source of calcium and phosphorus. There is also mention of Na_2HPO_4 [35] which has the disadvantage of having for counter ion a cation possibly insertable in the apatite

structure and which may have an intrinsic influence on acidobasic properties of the material. This method has the advantage of being simple to implement but requires time rather long synthesis times (several days) to obtain pure HAP [36]. Nevertheless, she allows relatively reproducible particles of relatively homogeneous [31]. Nevertheless, if some report to be able to control the ratio Ca / P via this method [30], most articles do not mention this parameter.

- Microwave irradiation synthesis

The microwave irradiation method is a variant of the methods more therefore uses mainly the same precursors (calcium nitrate and ammonium phosphate). Indeed, compared to a conventional autoclave synthesis, theSynthesis time and temperature required are greatly lowered. Nevertheless, properties, textures and morphology of the materials obtained are modified in relation to a typical hydrothermal synthesis [36]. In these syntheses, are sometimes added EDTA-like agents that will form Ca-EDTA complexes. From the stability of these complexes will depend on the crystal growth of HAP [37]. Likewise, with respect to co-precipitation, the synthesis time is much less we go from 19 to 45 minutes against 5 to 24 hours in classic cases. Moreover, this method heating system offers the advantage of better reproducibility, a distribution of narrower particles and since the heat is generated from the inside of the materials and not from an external source of heat, unlike other methods of heating, the temperature is homogeneous over the entire volume of solution [37].

- Synthesis by sol-gel

The sol gel method has the double advantage of using very high temperatures close to the ambient and therefore be energy efficient and allow a mix of precursors calcium and phosphorus at the molecular level causing an increase in the homogeneity of the final HAP [38]. It is mainly developed in the field of biological applications where it offers an alternative to thermal spraying for the manufacture of coatings consisting of thin layers which is a difficult process to control and requires extremely high temperatures. In addition, it allows a better control of the formation of certain phases and guarantees the purity of these phases [39]. On the other hand, the sol-gel process has the risk of hydrolysis of the precursors used [40] and claims a much larger quantity of precursors than in the other methods. The precursors used vary between conventional precursors such as $Ca(NO_3)_2$ and $(NH_4)_2HPO_4$ or H_3PO_4 and conventional month precursors such as $(CH_3O)_3P$ or KH_2PO_4.

- Solid-state synthesis

This method is different from others because it is not part of the methods of wet but dry synthesis. The principle is based on calcination, generally between 900 ° C and 1100 ° C of solid reactants in stoichiometric quantities [26]. The precursors used can be a mixture of calcium carbonates and TCP or TCP and $Ca(OH)_2$ [41]. For obtaining a pure HAP, this method is not necessarily ideal because it requires a lot of energy (very high temperature), but on the other hand, it makes it easy to obtain two-phase compounds TCP / HAP or HAP / CaO which makes it possible to obtain ratios Ca / P> 1.67.

II.2.3 **Properties of hydroxyapatite**

The chemical crystallinity and morphology of HAP is highly dependent on synthesis process. Because of its very stable structure, the HAP breaks down, in the absence of water, only at very high temperatures. After synthesis of the HAP from the $Ca(OH)_2$ system, H_3PO_4 at pH 10.6 and 95 ° C. Have got crystals whose size is on the order of 110-160 nm in length and 40-70 nm wide and noted that this size does not change significantly by increasing the duration of reflux heating [42]. In the same study, the authors performed heat treatment of HA at 900 ° C and 1100 ° C and resulted in the following remarks:

- No new phase was observed when heating the HAP for 2h at 900 ° C and 1100 ° C.
- After heat treatment, the cell parameters decrease slightly, which has been attributed to a partial loss of OH^- ions and formation of vacant sites.
- During the heat treatment the crystalline growth is pronounced and the crystals take a spherical shape with a diameter greater than 160 nm.

- During thermogravimetric analysis of 20 to 900 ° C, the mass loss was 3 to 4% a loss of 1 to 1.5% observed at a temperature below 200 ° C is attributed to the adsorbed water, whereas the loss of mass between 200 and 900 ° C would correspond (in the absence of HPO_4^{2-}) with strongly bound to water. The behavior of calcium phosphates at high temperatures depends in particular on the molar ratio Ca / P. Thus, the calcination at 900 ° C. for 12 hours of apatite including Ca / P is greater than 1.67 leads to the formation of a stoichiometric HAP and lime, then that a calcium deficient apatite would decompose into a mixture of β-TCP and HA stoichiometric if Ca / P is between 1.50 and 1.67 and, in a mixture of β-TCP and Calcium pyrophosphate if Ca / P is less than 1.50 [43]. The theoretical density of HAP is 3.156 g / cm^3

[42]. By studying the influence of sintering temperature on the microstructure and the mechanical properties of the enamel N. Oktar has shown that the density of HAP is greater for temperatures high sintering temperature (1200-1300 °C) [44]. Although some studies in the literature show a congruent dissolution of apatite (Ca / P thus having the same value both in the solid and in the solution), a lot of experimental data tend to prove that apatite does not dissolve congruent way [45]. Also, there are differences between the data in the literature as to to the value of the solubility product of HAP. However, at 25 ° C and pH 5 at pH 7 pKS values between 115 and 117 have been reported. Physical properties: Have been widely studied. Thus, the IR absorption of HAP is due to vibrations of PO4 3- and OH^- ions. The IR spectrum of HAP is characterized by two peaks for OH- at 3562 cm^{-1} and 631 cm^{-1} and a peak group for PO_4^{3-} to 474, 570, 601, 954, 1030 and 1081 cm^{-1} as shown in Figure. 2. The Figure. 3 below represent the X-ray diffraction pattern characteristic of HAP according to Fowler.

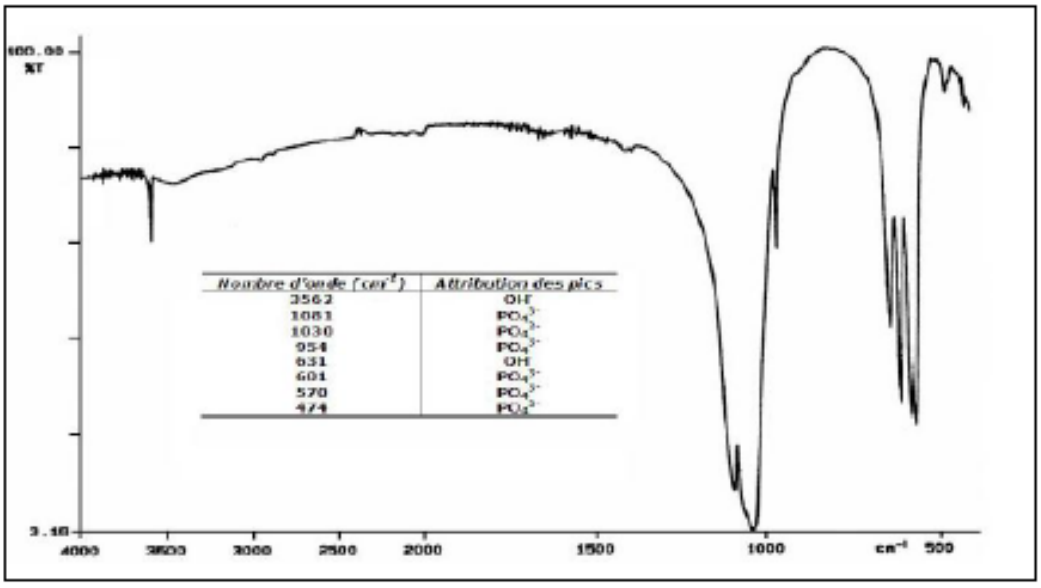

Figure 2. Infrared spectrum of HAP [46].

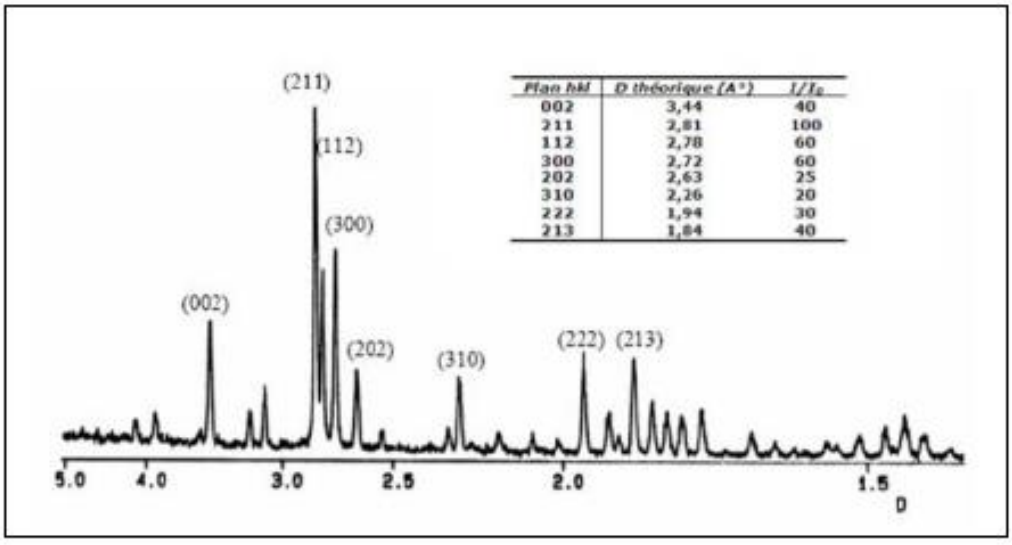

Plan hkl	D théorique (A°)	I/I0
002	3,44	40
211	2,81	100
112	2,78	60
300	2,72	60
202	2,63	25
310	2,26	20
222	1,94	30
213	1,84	40

Figure 3. X-ray diffraction pattern of HAP [46].

II.2.4 **Hydroxyapatite structure**

Phosphocalcic apatites that enter into the constitution of calcified tissues can be described from HAP. The stoichiometric HAP has the chemical formula: $Ca_{10}(PO_4)_6(OH)_2$ It crystallizes in the hexagonal system according to space group P63/m [47]. The dimension of the elemental cell of HAP is of the order of: a = b = 9.432 Å, c = 6.881 Å. The cell contains 10 Ca^{2+}, 6 PO_4^{3-} and 2 OH^-. The atomic ratio Ca / P of the stoichiometric phosphocalcic HAP is of the order of 1.67. The Ca^{2+} is defined by Ca (I) or Ca (II) depending on their environment. Four calcium ions occupy the Ca (I) position in two layers at levels 0 and 1/2 of the cell. The remaining six ions occupy the Ca (II) position in two layers: three located at levels 1/4 and three others at levels 3/4. The six PO4 tetrahedral ions 3- are found in two layers where they are located at the levels 1/4 and 3/4 of the cell. Also, OH^- ions exist approximately at the same height as the planes containing the Ca (II) atoms (1/4 and 3/4). If we consider the structure parallel to the c axis, PO_4^{3-} ions constitute columns, linked to each other. In fact, a phosphorus atom is linked to three oxygen atoms of a column and an oxygen atom of a neighboring column. The PO_4^{3-} ion assemblies are in the form of honeycomb which constitutes the frame of the network and provides great stability to the structure of apatite. This assembly is parallel to the c axis and contains open tunnels.

II.2.5 **Crystallographic properties of Hydroxyapatite**

The content of the asymmetric unit, taking into account the multiplicities of different positions of Wyckoff occupied by atoms, leads to cell content of ten calcium cations, six phosphorus anions, two hydrogen cations and twenty-six anions oxygen (oxides). This gives a stoichiometry in accordance with the formulation $Ca_{10}(PO_4)_6(OH)_2$. Phosphorus anions occupy four coordination sites, generated by the arrangement of four first-neighbor oxygen anions as it is shown in Figure. 4. The distance average <dP-0> = 1.467Å is less than the sum of the ionic radii of these two elements Σ RI (P-O) = 1.750Å. This is in accordance with the expected distances for the anion $(PO_4)^{3-}$.

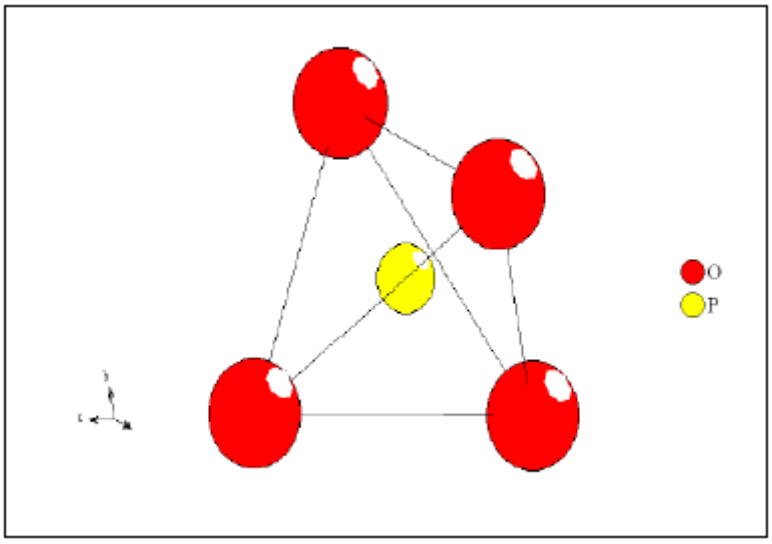

Figure 4. Tetrahedral site of phosphorus anions [48].

The elemental cell of HAP is shown in the figure. 5. The structure can then be described as an arrangement of anions $(PO_4)^{3-}$ stabilized by cations Ca^{2+}.

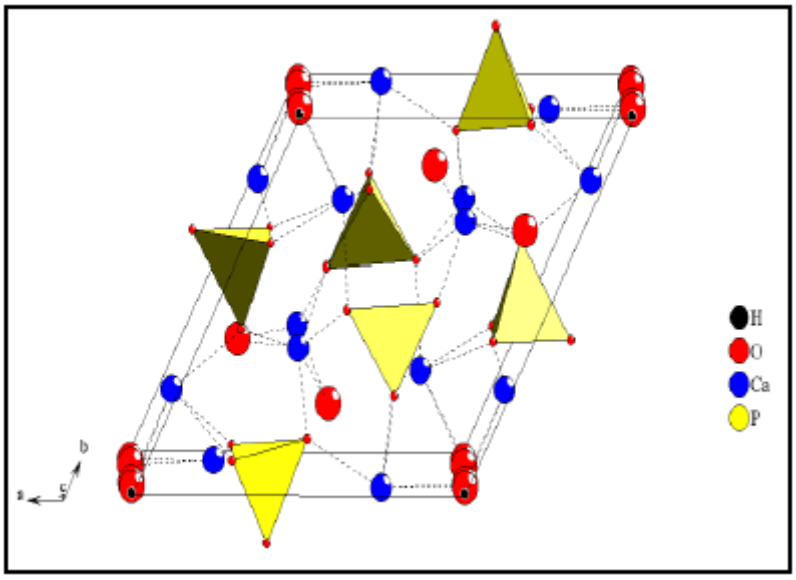

Figure 5. Elemental cell of $Ca_{10}(PO_4)_6(OH)_2$ [48].

We will notice the presence of the anions (OH^-) located on the crystallographic axis (Figure .6)

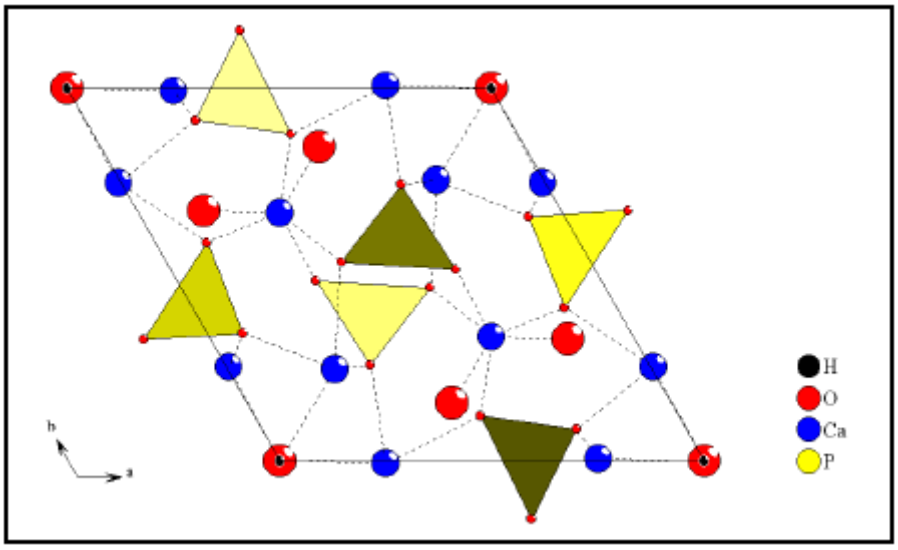

Figure 6. Elementary cell of $Ca_{10}(PO_4)_6(OH)_2$ projection on the plane (010) [48].

Tunnels play a very important role in the physico-chemical properties of apatite. Due to the existence of tunnels, apatites can behave either as ion exchangers, either as compounds in which different ions can be substitute.

These substitutions induce a slight variation in the mean diameter of the tunnels and thus modify the properties of the apatites. The different apatites derive from HAP by total or partial substitution of cations and anions by other cations or anions or gaps. However, according to the general formula of apatites, anions XO_4^{3-} can not be replaced by gaps. The different possibilities of substitutions are listed In Table. 2:

Table 2. Possible substitution in the HAP Cell.

Ca^{2+}		PO_4^{3-}		OH^-		
Sr^{2+}	Na^{2+}	AsO_4^{3-}	SO_4^{2-}	F^-	CO_3^{2-}	
Pb^{2+}	K^+	VO_4^{3-}	HPO_4^{2-}	Cl^-	S_2^{3-}	O_2
Cd^{2+}	La^{3+}	SiO_4^{3-}	CO_3^{2-}	Br^-	O^{2-}	H_2O
Mn^{2+}	Mg^{2+}			I^-	Hole	
Ba^{2+}	Hole					

- Ca^{2+} substitution

Mg^{2+} and Na^+ are very abundant ions in biological tissues. Incorporation of Mg^{2+} into the apatite structure is limited but may decrease the parameter a in the cell as well as the degree of crystallinity. Because of the similarities of atomic size between Ca^{2+} and Na^+, the incorporation of the latter does not change the crystalline parameters. On the other hand, substitution with carbonates decreases the parameter a, and slightly increases the c parameter of apatite.

- Substitution of PO_4^{3-}

CO_3^{2-} leads to a mineral defined as apatite type B which is the most important in the biological apatites. It occurs during the preparation of apatites either by direct precipitation, either by hydrolysis of the other calcium phosphates in the presence of carbonate. The incorporation rate of carbonate is directly dependent on the presence of other cations. For example, the presence of Na^+ increases the substitution rate, while Sr^{2+} decreases it. This substitution decreases the size and crystallinity of the crystal and increases therefore its solubility.

- Substitution of OH^-

Generally, the anions that replace the OH^- ions are arranged in the tunnels of apatite. CO_3^{2-} can enter the tunnels synthetic apatites prepared high temperature (1000 ° C) or in some biological

apatites. There is then an increase in parameter a, and decrease of parameter c. Substitution of OH^- with F^- increases the structural stability and crystallinity and thus decreases the solubility of apatite crystals. She can also decrease the parameter a without changing the parameter c. When a Cl^- between in tunnels, the parameter a increases and the parameter c decreases sharply.

II.2.6 **Stoichiometry**

HAP is also very adaptable in terms of stoichiometric deviation. The stoichiometry of these solids is defined by the Ca / P ratio and can range from 1.50 to 1.67, this last value corresponding to the so-called stoichiometric formulation material $Ca_{10}(PO_4)_6(OH)_2$. Previously it has been shown that substitution by charge ions different could lead to a change in the ratio between species which can also result in a variation of the Ca / P ratio but there are other causes for this stoichiometry gap that can result in systems generally under stoichiometric, Ca / P <1.67, but also stoichiometric with Ca / P> 1.67 [49].

Hydroxyapatite for biomedical application: Bones and teeth

II.2.7 **Generalities about bone tissue**

Bone tissue is a particular conjunctive whose matrix, like that of teeth, has a mineral phase. It is also a tissue that can regenerate itself partially. It has three main functions, mechanical, metabolic and hematopoietic. The primary role of bone tissue is a function of supporting the body and protecting the organs. The set of bones form the skeleton that constitutes the body's frame and serves anchoring to soft tissues (tendon, muscle, ligament). Bone tissue is a very tissue resistant capable of withstanding significant mechanical stress. However, far to be a static tissue, it undergoes a permanent remodeling under the joint action of osteoclasts, which degrade the old bone, and osteoblasts that synthesize the new mineralized matrix. This remodeling allows the adaptation of the fabric to the mechanical stresses of its environment. There is a decrease in bone mass in astronauts, which can be limited by the daily application of mechanical stimuli during flight [50]. The remodeling of bone tissue is also a way of regulating the release or storage of minerals and thus ensure, together with the intestine and the kidneys, the control of phosphocalcic metabolism. Indeed, the bone contains 98% of the calcium of the body of which about 1% is exchangeable with extracellular liquids. The density of the bones of rats undergoing a calcium deficient diet thus decreases compared to a normal diet. This deficiency results in an increase in the number of differentiated bone cells within the tissue [51]. Finally,

bone tissue, and in particular bone marrow cells, provide a structural and functional support to hematopoietic cells. The bones contain indeed cavities, medullary spaces, containing the hematopoietic marrow, whose cells strains, at the origin of the 3 lines of blood globules, are in the vicinity of cells bone. Some of them are pluripotent stem cells, likely to to differentiate into multiple lineages (fibroblasts, chondrocytes, osteoblasts, adipocytes).

II.2.8 **Structure of bone tissue**

- Compact bone and cancellous bone

Bone tissue consists of two types of bone, trabecular bone or cancellous bone, and the cortical bone, or compact bone (Figure.7). Compact bone represents about 80% of the mass bone. It is organized in osteomes or cylinders of Havers. These structural units are formed of concentric lamellae around conjunctivo-vascular channels, the Havers, connected by perpendicular channels, the Volkmann canals. These channels allow the irrigation of bone tissue. The second type of bone is trabecular bone or spongy. This bone, much less dense than the previous one, is organized into a network three-dimensional spans of anastomosis. Minority in the adult skeleton, it is yet at the base of all bone tissue. The bone undergoes a permanent reworking. During development, the first bone formed is spongy. It is then degraded and replaced by compact or trabecular bone depending on its location and function.

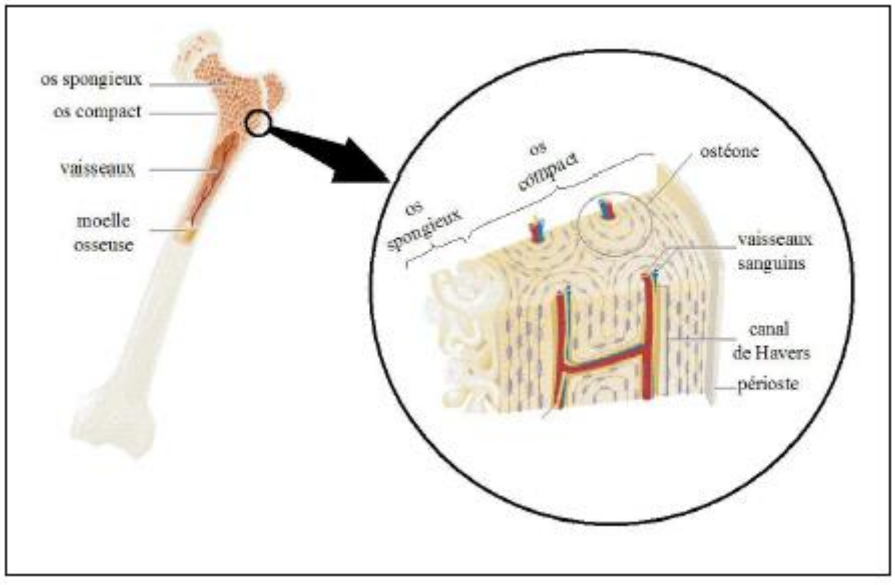

Figure 7. General structure of bone tissue shown on a long bone [Bahlali, 2014].

Cortical bone essentially fulfills the mechanical function of bone tissue and bone spongy metabolic function. The bone grows by apposition of cells and matrix on the free surfaces of the rigid fabric. This growth takes place in two ways. Ossification membrane of the flat bones (skull, scapula) results directly from a differentiation of mesenchymal cells into bone cells, osteoblasts or osteoclasts, while in endochondral ossification of long bones a cartilaginous matrix is first formed and replaced by bone.

- Mineral matrix: Natural Hydroxyapatite

Bone tissue, like teeth, is a mineralized tissue. The mineral phase of bone represents about 65% of its total weight. The crystalline phase is similar to HAP $Ca_{10}(PO_4)_6(OH)_2$ (Figure .8), deposited as small needles hexagonals associated with the organic matrix.

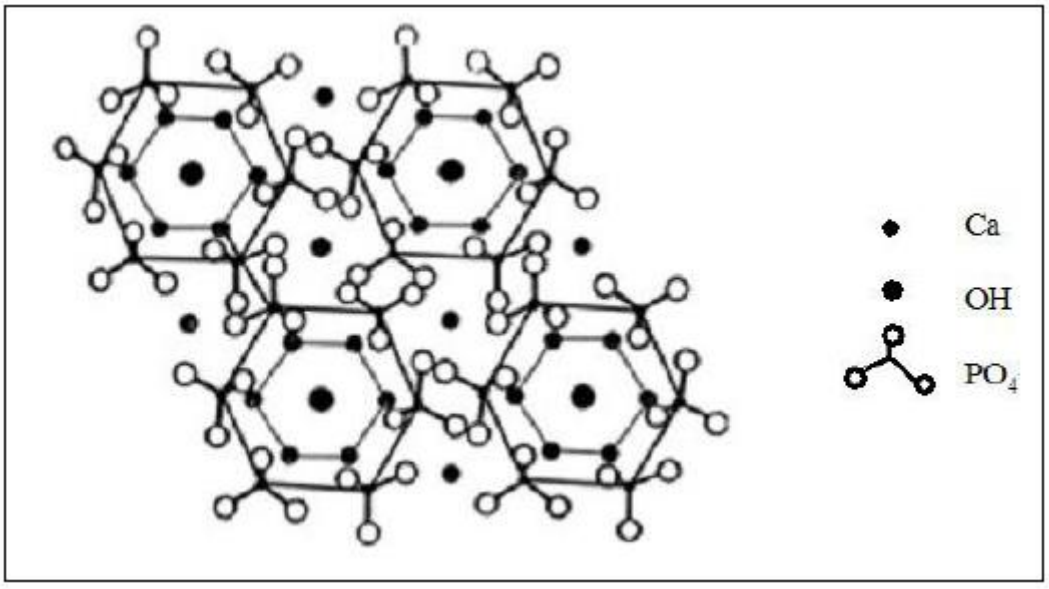

Figure 8. Arrangement of atoms of HAP in the hexagonal crystal structure [Bahlali, 2014].

In bone, other elements are incorporated in the structure of apatite and in particular carbonates, CO_3^{2-} substituted for phosphates or hydroxides; fluoride ions, F^-, substituted for the hydroxide; or cations, magnesium or sodium, which can be substitute for the calcium ion. Stoichiometric HAP has an ideal ratio of calcium and phosphate of the order of: Ca / P = 5/3 = 1.67. The young tissues of the body, in rapid renewal, contain poorly crystallized HAP, relatively soluble, and rich in carbonates. His report Ca / P is low and tends to 1.33. Older or less renewed tissues,

such as the flat bones of the skull, contain apatites more crystallized, and their Ca / P ratio tends to that of HAP [52].

- Organic matrix: Collagen

Collagen is a protein that is the most abundant of the human body and component majority of extracellular matrices, constitutes 90% of the organic matrix of the bone. Several types of collagen have been identified in vertebrates but the bone is predominantly composed of type I collagen. These are the bone cells synthesize the bone matrix and then control its mineralization. The mineral is located in and around the collagen fiber [53]. This entanglement confers on the bone outstanding mechanical properties and adapted to its structural function. Properties of collagen or HAP suggest that collagen fiber rather gives the bone tissue a tensile strength while the mineral brings the compressive strength. The combination of the two gives the bone tissue mechanical properties whose However, precise mechanisms remain to be elucidated [54], [55] Collagen is organized in parallel fibers within superimposed layers with alternating the orientation of the fibers, which gives a lamellar appearance to the bone tissue. Collagen is composed of polypeptide chains wound in triple helices, crosslinked and themselves wound in super-helices of not right within mature collagen fibers in the matrix. In a fiber, the collagen fibrils are ordered in parallel, each end being shifted 67 nm from the end of the neighboring molecules. The HAP crystals are interposed between these fibrils within the matrix (figure .9).

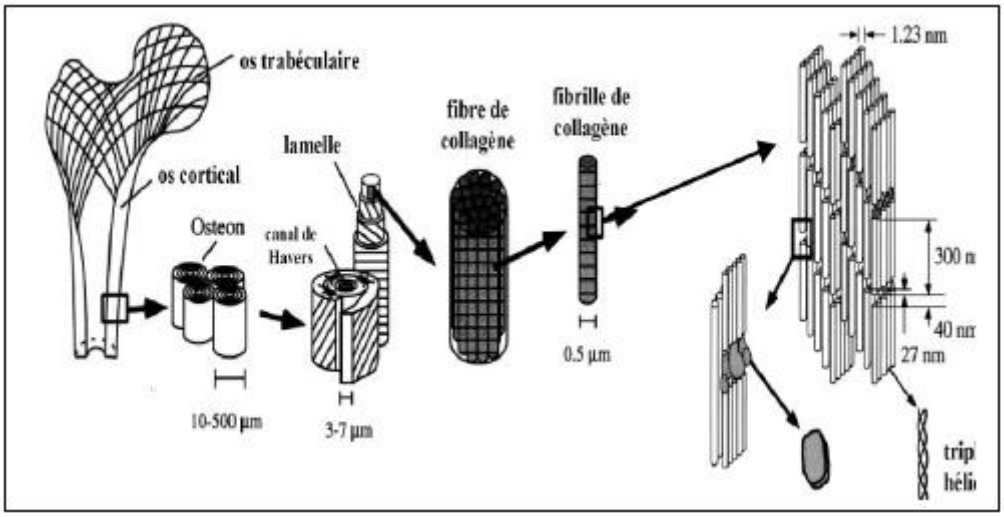

Figure 9. Structural organization of bone [55]

II.2.9 **Synthetic materials for dental and orthopedic prosthesis**

Among the powers possessed by the living beings is the cure of diseases, whether psychological or physical. This strength to recover is exploited in m areas of medication, surgery, and organ replacement and treatment like a dental and orthopedic prosthesis. Hence, each domain presents countless research opportunities. Among all these areas, we have chosen, in this work, to prepare and treat the materials used usually in the replacement of worn or damaged bones or teeth. There are two types of materials frequently used in this field namely synthetic and natural. Synthetic materials are more used in the past because it requires moderate working conditions on tools and on energy. But from a natural therapy and healthcare point of view, the natural materials are more interesting and safer for the human body. It remains relative from one country to another following the economy, social security, and purchasing power of patients. HAP is a natural material that constituted the major compound of the mineral part of the bone and tooth. It presents around 70% of the bone composition, 70% of dentine, and 97% of dental enamel [56]. Consequently, HAP is an adequate material to remedy the bones and teeth due to its naturality [57], non-toxicity [58], and biocompatibility [59]. Synthetic HAP is similar to natural HAP in the human bone and teeth tissues in morphology and composition [60]. It has a hexagonal structure, and a stoichiometric Ca/P ratio of 1.67, which is identical to bone apatite. An important characteristic of HAP is its stability when compared to other calcium phosphates. Thermodynamically, HAP is the most stable calcium phosphate compound under physiological conditions as temperature, pH, and composition of the body fluids [61, 62]. With the progress of nanotechnology, a major impact has been remarked in materials science. The production of nanomaterials has gained considerable attention toward biomaterials, especially for HAP. The nano-HAP powder is formed by nanoparticles of HAP with a size less than 100 nm in diameter. It is more practical than bulk HAP powder [63] and attracting interest as a biomaterial in prosthetic applications due to its outstanding properties:

- Biocompatibility [64]
- Bioactivity [65]
- Osteoconductivity [66]
- Non toxicity and non inflammatory nature [67]
- Ability to be combined with other biomaterials [68]
- Ability to be deposited on irregular surfaces [69,70, 71]

The nano-HAP bioceramic has been entered into a variety of biomedical applications as:

- Bone tissue engineering [72]
- Endothelial filling for orthopedic, traumatology, spine, maxillofacial and dental surgery. [73]
- Orthopedic and dental implant coating [74]
- Restoration of periodontal defects [75]
- Edentulous ridge augmentation [76]
- Endodontic treatment like pulp capping [77]
- Repair of mechanical furcation perforations and apical barrier formation [78]
- Desensitizing agent in post teeth bleaching [79]
- Remineralizing agent in toothpaste [80]
- Early carious lesions treatment [81]
- Drug and gene delivery [82, 83]

Titanium and stainless-steel implants are often covered with HAP coatings to trick the human body to admit an external thing and reduce the implant rejection rate. HAP can also be used in cases where there are bone voids or defects. This process is carried out through powders, blocks, or beads toward the material being placed in the affected areas of bone. Thanks to its biocompatibility, it stimulates the bone to grow and rebuilds the defect. It leads generally to shorter recovery times than cases observed if HAP is not employed.

The dental enamel consists of 97 wt.% of nano-HAP and 3 wt% [84, 85] of organic material and water. Besides, the nano-HAP represents 70 wt.% of dentin composition. Consequently, the nano-HAP is the main component of enamel, and it gives an appearance of glossy white by light scattering phenomenon. and it dismisses the penetration of liquids and micronutrient inside the tooth by closing the small pores of the enamel surface. Synthetic nano-HAP simulates the size of natural dentinal or enamel HAP [86]. Experimental results demonstrate the advantages of nano-HAP in enamel restoration by making it in toothpaste and mouth-rinsing solutions to ensure the restoration of demineralized dentinal and enamel surfaces by inserting HAP nanoparticles in these defects.

Hydroxyapatite for energy

II.2.10 **Lithium-sulfur batteries development**

Lithium-sulfur batteries are considered among important hopeful candidates for the advancement of materials of energy storage system. However, the effect of polysulfide shuttle holds the most important limitation for its useful application in 2016 Liu et al [87] as it is shown in figure. 10, were they added the nano-HAP in the sulfur cathode and carbon-coated separator to limit this unwanted effect and consequently to maintain the batteries performance. The cathode of sulfur with nano-HAP showed a remarkable reversible capacity and a durable performance than that of the initial sulfur cathode. Also, its reversible areal capacity was more powerful than that of commercialized lithium-ion batteries Hence the approach utilizing nano-HAP as a polysulfide absorbent gives an excellent potential for resolving the polysulfide shuttle matter and improving a high performance of Lithium Sulphur batteries for energy storage.

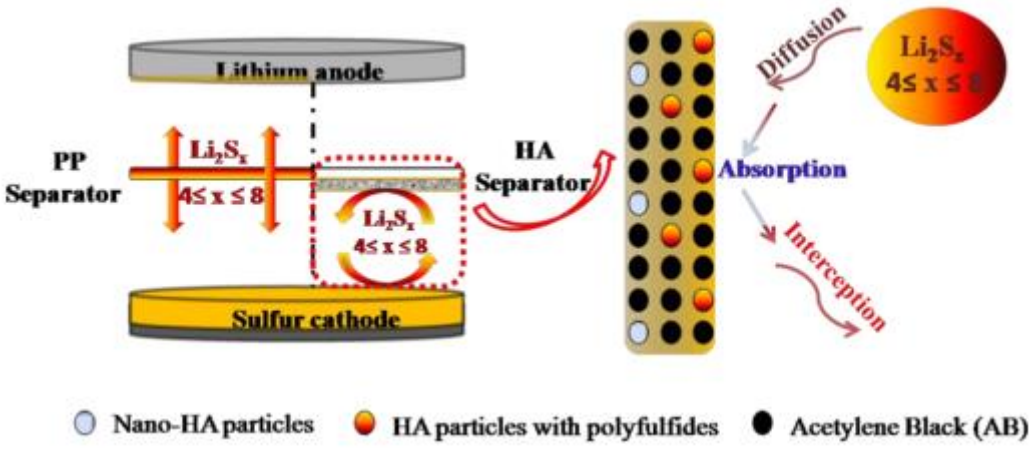

Figure 10. Schematic diagram of the HA separator: the HA separator serves as a functional barrier by Liu et al [87].

II.2.11 **Lithium- ion batteries development**

Separators represent a crucial function in the electrochemical safety and performance of batteries based on lithium-ion. The commercial microporous polyolefin-based separators frequently bear of lower electrolyte wettability, insufficient thermic stability, and critical security concerns. Within, a new type of very soft and permeable separator based on HAP nano-wires with remarkable fire resistivity, thermic resistance, and higher electrolyte wettability is listed by Li et al in 2017 [88] as it is shown in figure 11. The high thermic stability of HAP

materials allows the separator to maintain its structural integrity at 700 °C temperature. The fire resistance of HAP assures great protection for advanced lithium batteries ions with enhanced performance and high safety.

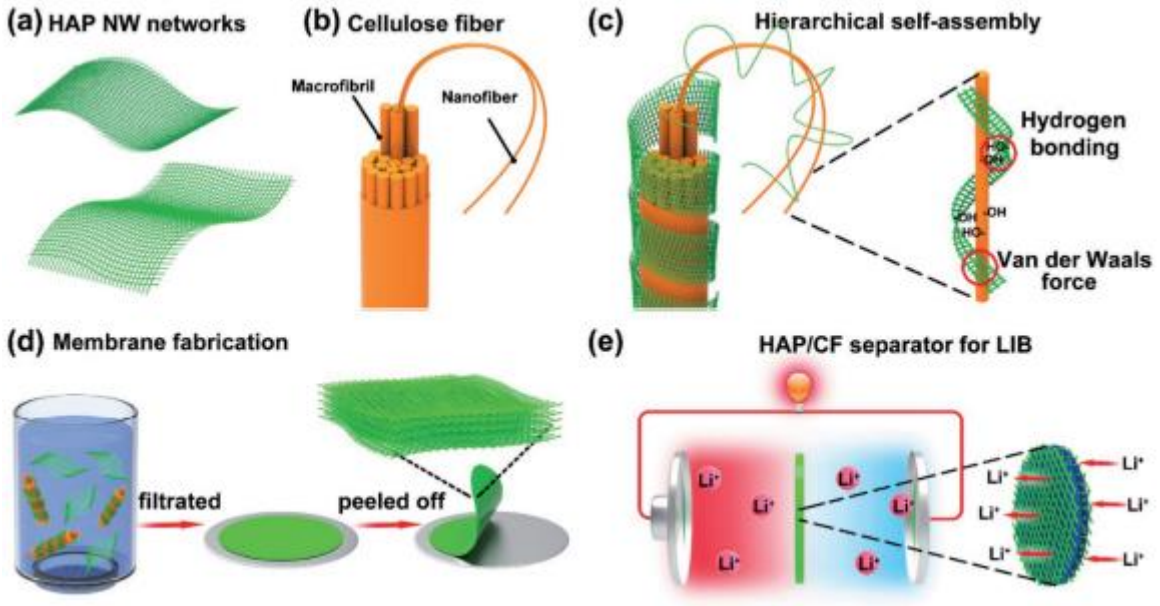

Figure 11. Schematic illustration of the new kind of highly flexible and porous separator based on HAP NW networks with excellent thermal stability, fire resistance, and superior electrolyte wettability. a) HAP NW networks. b) CFs. c) Hierarchical assembly of HAP NW networks and CFs. d) Suction filtration process for fabricating the layered and highly porous HAP/CF separator. e) The application of the HAP/CF separator in the LIB [88].

II.2.12 **Fuel Cell batteries development**

Increasing energy costs, limited energy equipment, and increasing pollution are the principal issues that must be counted in the cost analysis of energy sources. These problems for a variety of fuel sources can be reduced because a fuel cell can operate with a variety of fuel sources by adjusting its membrane. Fuel cells offer an improvement over existing technology such as the internal combustion engine by transforming the fuel directly to energy. Rather than combusting the fuel and using the heat to produce energy, fuel cells use an electrochemical process that obtains energy directly from the fuel. These electrochemical reactions are greatly more useful and are capable of converting more of the fuel to usable energy. The reactions are also cleaner and have very few undesirable reactions.

A standard fuel cell diagram is shown in figure 12, here. The diagram displays hydrogen and oxygen of the air as the fuel. Instead of hydrogen, other fuel sources may be methanol, ethanol, or biomass. As exhibited, the hydrogen penetrates on the anode side of the fuel cell and is converted into protons and electrons. This reaction HAPpens because of the catalyst at the surface of the electrolyte, also named the membrane. The protons move through the membrane, whereas the electrons are forced almost to an obvious circuit since the membrane is an insulator. The electrons produce energy in the external circuit and then meet the proton and oxygen at the cathode to produce the product. In this case, only the product is water. The cathode also uses a catalyst of either pure platinum or a platinum alloy.

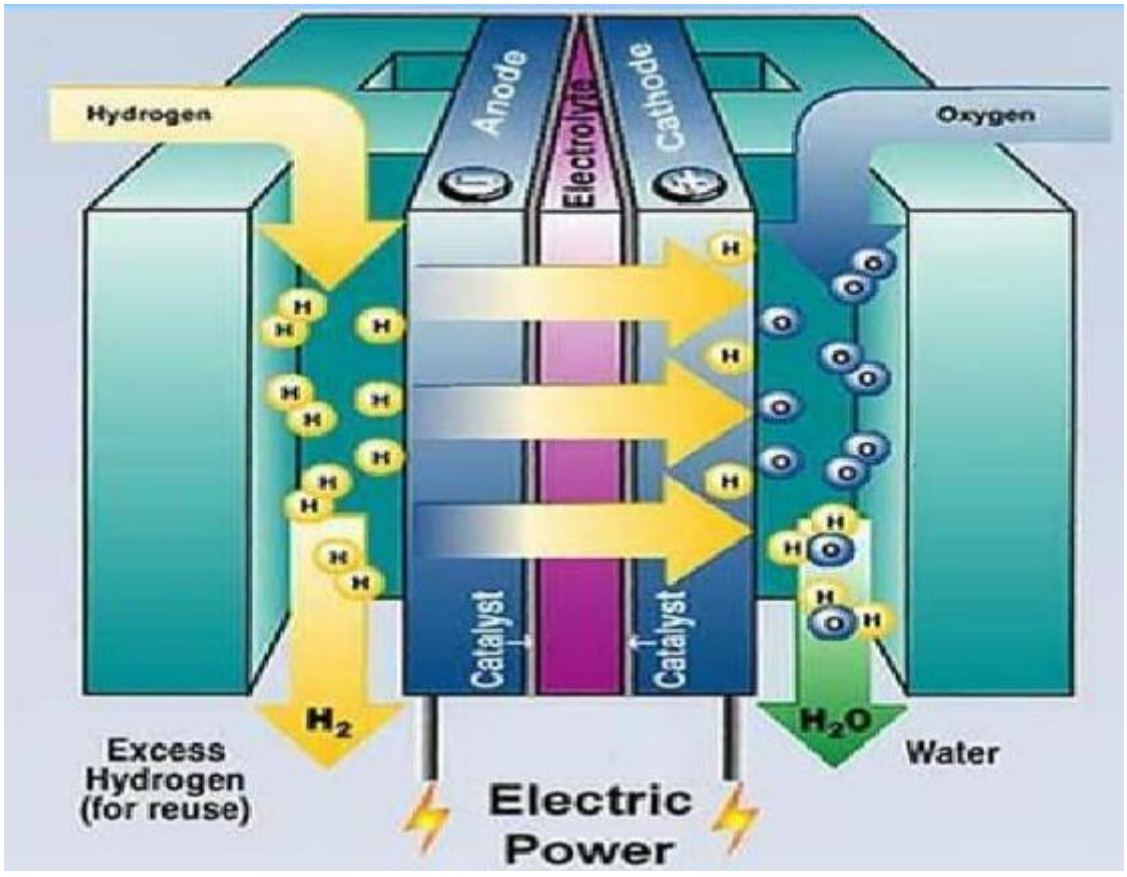

Figure 12. Standard fuel cell diagram [source US D.O.E., office of energy efficiency and renewable energy]

HAP is a material conductor of protons for temperature under 200C. This property could be employed for producing an intermediate fuel cell. Operating amidst 200C to 300C would give

the benefits of the high and low temperature fuel cell. In this temperature range, a nonprecious catalyst could nevertheless be used, but the temperature would not require expensive heat resistant ceramics. A membrane of HAP or some hybrid material stands a potential means for produce an intermediate fuel cell [89].

II.2.13 **Hydroxyapatites for solar energy conversion as photocatalysis**

HAP is a material presenting great performance as photocatalyst; this quality, coupled with its capacity to remove heavy metal from aqueous media, offers it a multi-functional thing for the protection of the environment. Further studies, founded basically on the findings obtained by many scientists, were performed, to increase the performance of the materials and/or shift the bandgap into the visible light. The use of diverse dopants and combining with other photocatalysts are done for HAP for increasing its photocatalytic properties and facilitate also the degradation of the pollutants since HAP acts two roles in one time, production of energy and remediation of the environment. A standard description of the photocatalysis reaction for an inorganic semiconductor is schematized in figure .13. Figure .14 represent some technic of modification of HAP for getting the photocatalytic activities.

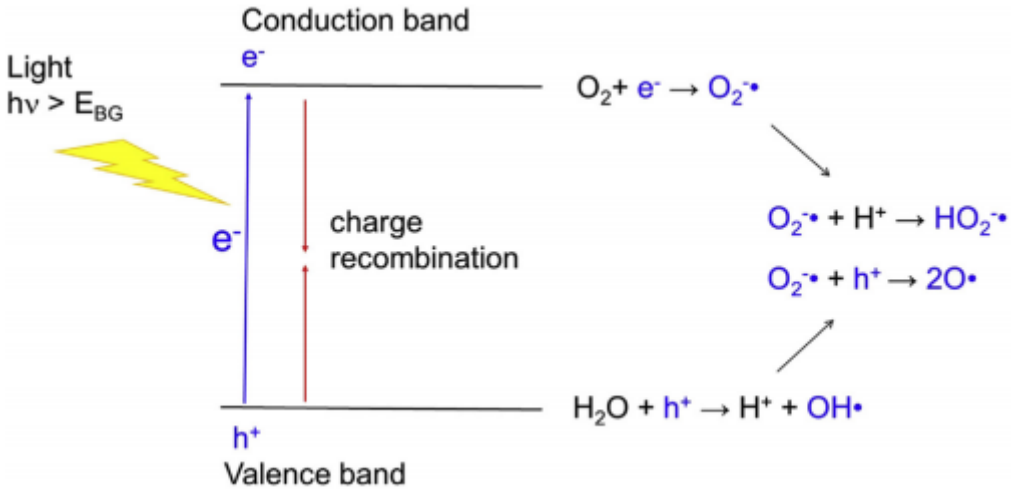

Figure 13. Representation of the photocatalysis reaction scheme for an inorganic semiconductor (SC) [90].

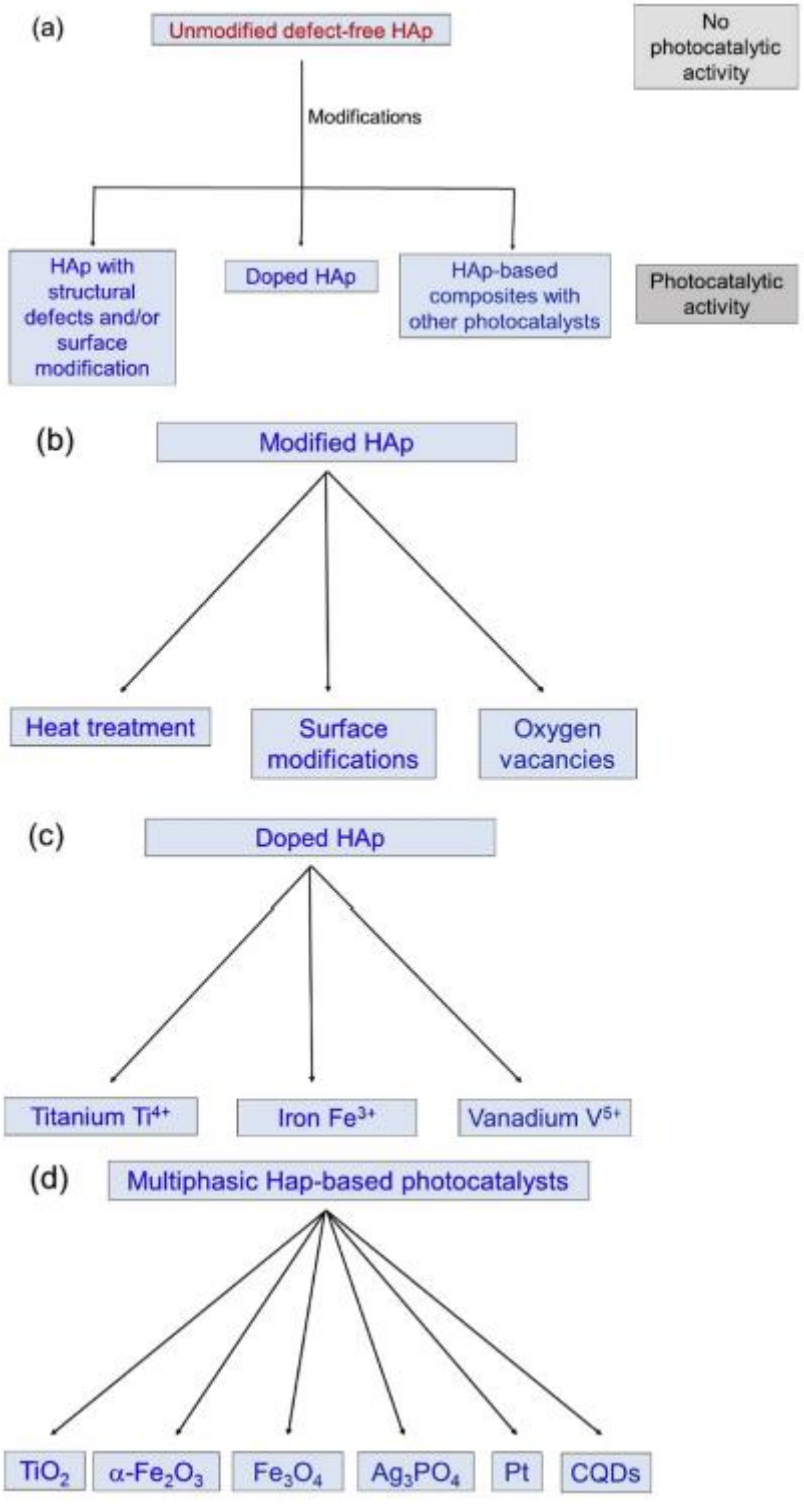

Figure 14. Scheme of HAP-based photocatalytic materials [90].

- Photocatalytic single phase Hydroxyapatite

A few kinds of HAP with stoichiometric defect-free displays no photocatalytic activity, since to its insulating nature. nevertheless, were reported to present photocatalytic properties; although the reasons for this behavior are not entirely clear, the most likely explanation for the presence of defects in the HAP structure, as well as some specific surface modifications. Table 3. summarizes the most important statements on this point.

Table 3. Single-phase photocatalytic HAP materials [90].

Preparation method	Characteristics of the material	Testing conditions (irradiation, pollutant, catalyst load)	Degradation efficiency/ photocatalyst performance	Reference
Gas phase				
Chemical precipitation followed by heating at 200C	Surface area: 66.5 m2/g	λ = 254 nm, 8.8 μW/cm2 Methyl mercaptane	96% in 4 h	Nishikawa and Omamiudab (2002)
Hydrothermal synthesis followed by heating at 200 °C	Rod-shaped particles (80 * 14 nm) Surface area: 101 m2 /g Ca/P = 1.64	Dimethyl sulphide	30% in 1 h	Tanaka et al. (2012)
Liquid phase				
Chemical precipitation followed by heating at 400°C	Surface area: 56 m2 /g	UV mercury lamp, 250 W Calmagite 3.0 g/L	92% in 12 h	Reddy et al. (2007)
Chemical precipitation from mussel shell, followed by heating at 800 °C	Ca/P = 1.66	λ = 340 nm, 0.81 mW/cm2 Methylene blue 2.0 g/L	62% in 24 h	Shariffidin et al. (2013)

Thermal extraction from cod fish bones (treatment in calcium acetate)	Needle-like crystals (1 - 2 μm) Surface area: 19.29 m2 /g Ca/P = 1.60	λ= 365 nm, 8 W Methylene blue λ = 365 nm, 1.84 mW/cm2 Fluoxetine 4.0 g/L	80% in 8 h 75% in 24 h	Piccirillo et al. (2013) Marquez-Brazon et al. (2016)
Chemical precipitation in presence of yeast	Nanofibres (300*6 nm)	λ = 365 nm, 300 W Methylene blue 0.1 g/L	75% in 5 h	Tripathi et al. (2015)

- Doped photocatalytic Hydroxyapatite

The important common dopant to get photocatalytic HAP is the titanium. The initial report on Ti-doped HAP was published by Wakamura et al. (2003); they synthesized the powder material by co-precipitation method, adding a titanium salt (Ti(SO4)2) to the reaction between calcium and phosphorus. Outcomes showed that titanium-doped powders can absorb light with a wavelength shorter than 380 nm, i.e. in the UV range. The photocatalytic activity of these first materials was examined both in liquid and gas phases, monitoring the degradation of albumin and acetaldehyde under UV light radiation (see Table 4), with both chemicals being effectively degraded.

Table 4. Ti-doped photocatalytic HAP materials [90]. Note: X_{Ti} = Ti/(Ti + Ca) (mol/mol).

Preparation method	**Characteristics of the material**	**Testing conditions (irradiation, pollutant, catalyst load)**	**Degradation efficiency/ photocatalyst performance**	**Reference**
Gas phase				
Hydrothermal	XTi ≤ 0.8 Nanoparticles with irregular shape (~50 nm) Surface area: 85 m^2 /g	X_{Ti} = 0.1 UV, 1 mW/cm^2 Acetaldehyde	100% after 100 h	Wakamura et al. (2003)
Co-precipitation followed by thermal treatment (650 °C)	X_{Ti} = 0.1 Particle smaller than 100 nm Surface area: 85 m^2 /g	X_{Ti} = 0.1 Xe lamp (UV + Vis), 1.25 mW/cm^2 Acetaldehyde	CO_2 formed from the degradation about half than that formed with TiO_2	Tsukada et al. (2011)

Commercial material (Tahiei Chemical Industrial Co), subsequent Cr^{3+} impregnation of the powder	X_{Ti} = 0.1 Cr^{3+} grafting up to 102 mol/L Rod-shaped particles (60*20 nm) Surface area 46- 50 m^2 /g	X_{Ti} = 0.1 Cr^{3+} grafting 104 mol/L Visible (Xe lamp) Acetaldehyde	Complete degradation after 3 h	Wakamura et al. (2011)
Hydrothermal, subsequent Cu^{2+} impregnation of the powder	X_{Ti} = 0.1 Cu^{2+} grafting up to 0.1 % wt Surface area: 47.8 m^2 /g	X_{Ti} = 0.1 Cu^{2+} = 0.05 % wt λ = 365 nm, 1 mW/cm^2 Acetaldehyde	CO_2 formed from the degradation about double for Cu^{2+} impregnated material than for unmodified Ti-HAP	Nishikawa et al. (2013)
Commercial material	(Hautoform TA) Surface area: 39 m^2 /g	UV, 1 mW/cm^2 2-propanol (IPA)	CO_2 formed from the degradation about a quarter than that formed with TiO_2	Tsuruoka et al. (2015)
Liquid phase				
Hydrothermal	X_{Ti} = 0.8 Nanoparticles with irregular shape (~50 nm) Surface area: 85 m^2 /g	X_{Ti} = 0.1 UV, 1 mW/cm^2 Albumine	100% after 12 h (comparable to TiO_2)	Wakamura et al. (2003)
Hydrothermal synthesis followed by thermal treatment (190 °C)	X_{Ti} = 0.5 Rod-shaped crystals (70 *10 nm) Surface area: 150-177 m^2 / g	UV (λ = 365 nm) and Vis (λ > 400 nm) Methylene blue 0.4 g/L	UV: 70% after 1 h (comparable to TiO_2) Vis: 55% after 1 h (higher than TiO_2)	Anmin et al. (2007)
Co-precipitation followed by thermal treatment (650 °C)	X_{Ti}= 0.2 Rod-shaped particles Surface area: 34-53 m^2 /g	λ = 365 nm, 1 mW/cm^2 Bovine serum albumin, myoglobin, lysozyme 12.5 g/L	Complete selective lysozyme degradation	Kandori et al. (2013)

Hydroxyapatite for environment

Experimental nanostructured composite air filters including HAP were seen to be useful in absorbing and decomposing the carbon dioxide, which could ultimately lead to its use in decreasing car exhaust pollutants [91]. An alginate/nano-HAP composite was produced and field-tested as fluoride adsorbent [92]. This biocomposite eliminated fluoride through the

mechanism of ion-exchange with biocompatibility and biodegradability in both. Recently, applications in catalysis and protein detachment were improved and successfully examined using calcium phosphates in nanostructure form [93], which suggests much innovative employment for these materials.

Dye elimination from wastewater is significant due to its unfriendly effects on the environment and human health [94]. The difficulty of dye removal is due to its complex structure. Nanocomposite dye adsorption is found to be a hopeful technique to eliminate dye wastes due to its high removal capacity at low concentration. Among different adsorbents used, HAP is a biocompatible adsorbent that is moderately effective in both anionic and cationic dye removal. Lately, modification of HAP by doping with other materials to increase its removal performance has gained significant attention [95]. In the fact of the high solubility of water, it is challenging to remove dyes from wastewater by traditional methods [96]. Degradation of certain dye provides few products which are out of control more than the dye itself. Dye molecule coheres to the surface of the fiber by hydrogen bonding, van der Waals forces, or electrostatic interactions [97]. Due to the improper coloring process, the surplus dyestuffs mix with water and are discharged as effluent. When these dyes enter the environment, they can cause serious pollution as shown in Figure 15. And the largest synthetics and natural way of the output of dyes are schematized in the figure 16.

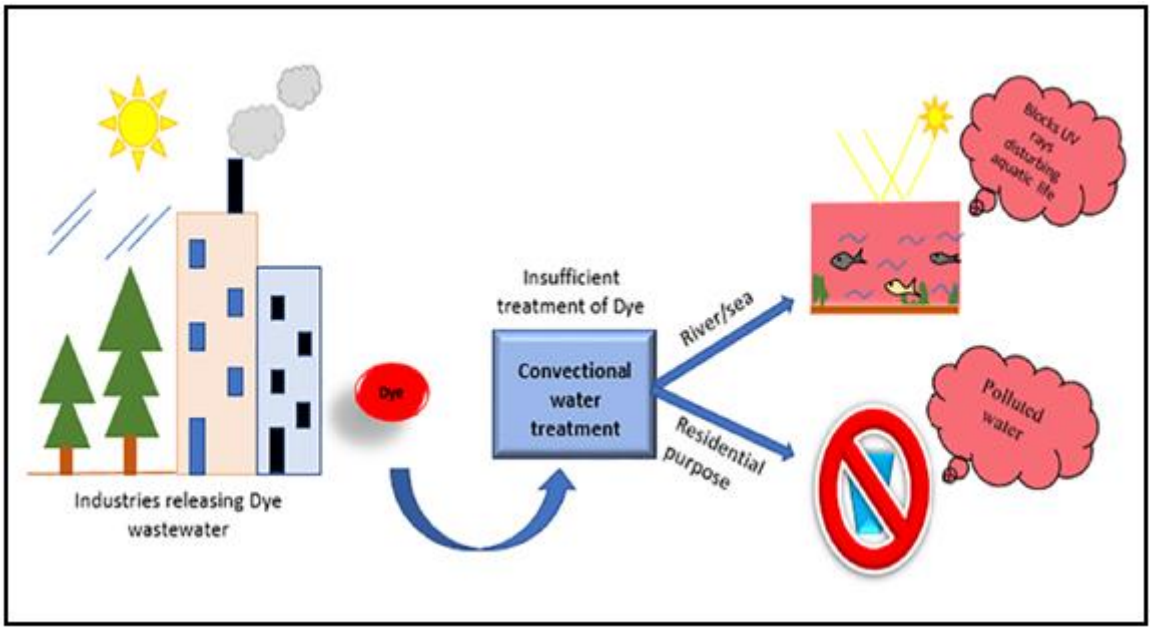

Figure 15. Scheme of some fate of dye in the environement [190]

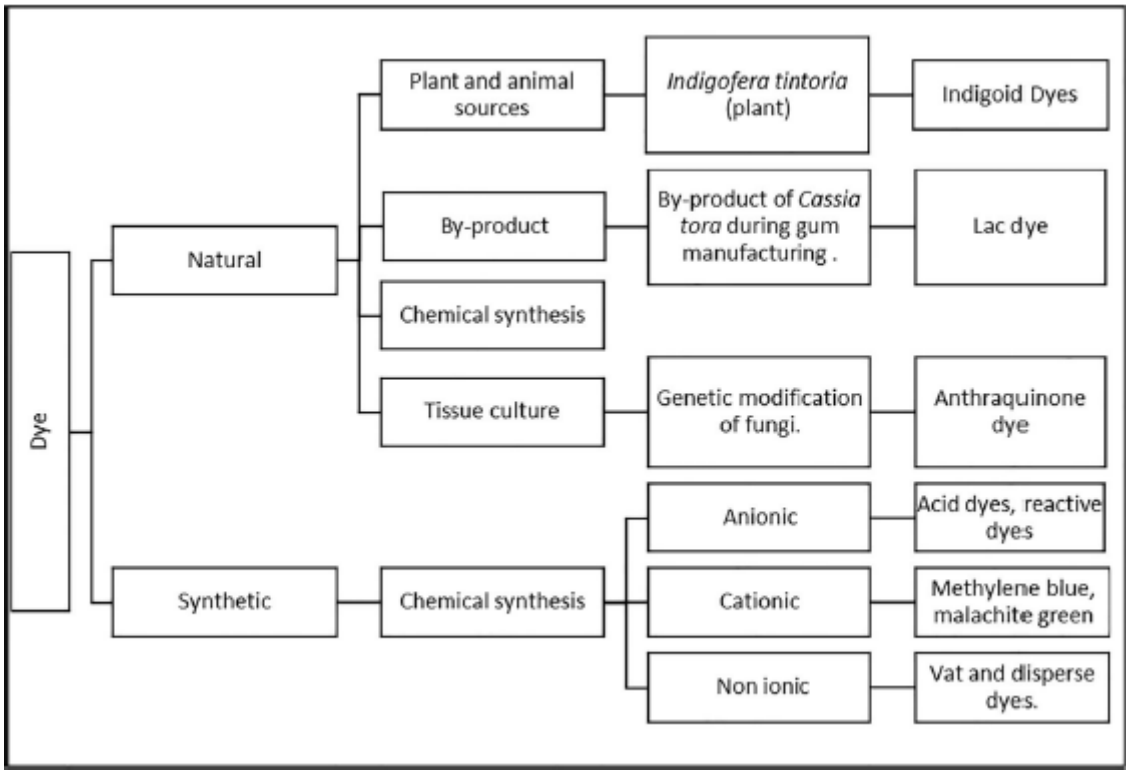

Figure 16. Most Synthetics and natural way of production of dye [190]

II.2.14 **Elimination of Congo red dye from aqueous media**

The increase of toxic and carcinogenic artificial dyes relieved with industrial effluents has become an increasing environmental concern, as they endanger the biodiversity of aquatic ecosystems and the goodness of water sources. However, the elimination of non-biodegradable dyes from wastewater still requires techniques with great costs and environmental impacts. Among various removal strategies such as coagulation, photocatalytic degradation, membrane separation, biological treatment, adsorption is a hopeful method that may utilize mass-produced low-cost materials. HAP is a well-known member of the calcium phosphate family with high biocompatibility, can be used as an adsorbent for the removal of toxic dyes from aqueous solutions. Adsorption rate is one of the key indicators to judge the adsorption performance of a nanomaterial. Here, HAP nanoparticles show a rough surface and a high BET surface area (82.94 $m^2.g^{-1}$), and present an excellent adsorption rate for the elimination of congo red dye for example in aqueous solution with the highest adsorption capacity of 337.330 $mg.g^{-1}$

following study of GUAN et al in 2018 [98] about the capacity of HAP to exclude congo red dye from aqueous media.

Their results show that HAP nanoparticles can become effective quickly, low-cost, and environmentally friendly alternatives to the existing industrial wastewater treatment to remove anionic and organic dyes. Figure .17 illustrates the schematic representation of the interaction of anionic Congo red dye molecules onto HAP nanoparticles.

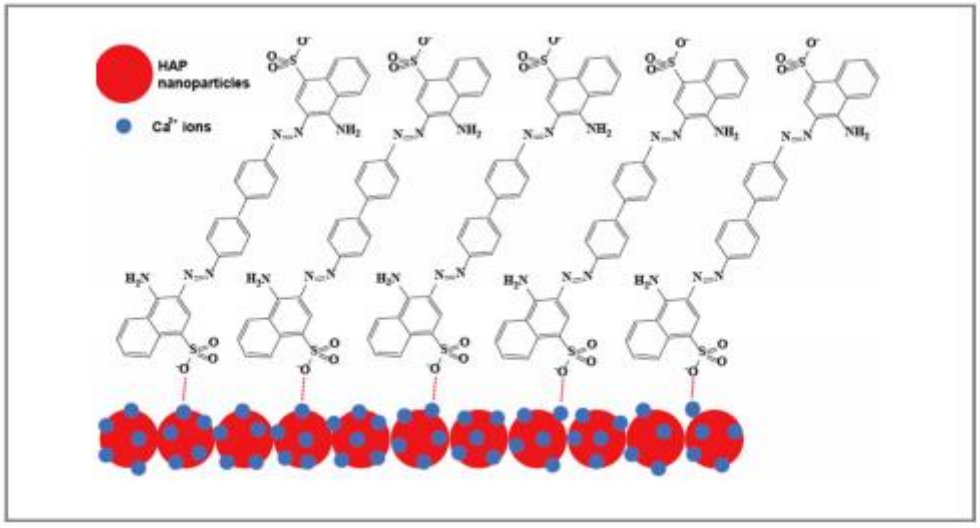

Figure 17. Schematic representation of interaction of anionic congo red dye molecules onto HAP nanoparticles [98].

II.2.15 **Elimination of Acid Black 172 dye from aqueous media**

A large number of natural and artificial dyes are used for textile dyeing methods and also in other activities such as pharmaceutical, paper, and pulp manufacturers. M dyes and their reaction products are very dangerous due to the existence of toxic or even carcinogenic groups. One of the major problems requiring a solution by the textile industries is removing dyes from effluent. To solve this problem some physical (adsorption, ion exchange, liquid-liquid extraction), chemical (oxidation, flocculation, and sedimentation) methods have been tried and biological (bacterial and fungal bio-absorption, biodegradation in aerobic or anaerobic conditions). Among these, adsorption appears to be a good alternative to treating effluents, being a simple, non-toxic, and low-cost method. HAP has been identified as a good absorbent for environmental processes due to its specific structure conferring ion-exchange property and adsorption affinity towards pollutants. This biomaterial has already been used to remove heavy

metal ions and organic compounds (phenols, dyes, etc.) from water. This complex group of mineral pigments is widely used in textile dyeing and is known for its high solubility, purity, and fastness properties. Unfortunately, most of these dyes are toxic, carcinogenic, and harmful to human health due to their aromatic composition and heavy metal ions in them. Acid Black 172, a water-soluble complex Cr (VI) dye, used for rapid black dyeing on wool, nylon, and leather substrates, as well as for coloring paper. White, its waste poses a real risk to human health and the environment, and therefore it must be properly handled. The uncalcined nanoHAP has been used successfully by Ciobanu et al in 2014 [99] as an adsorbent for eliminating this Acid Black 172 dye from aqueous solution. Because the uncalcined HAP has a crystal size smaller than 70 nm and a high specific surface area around 325 m^2 /g. The Ciobanu et al study's results indicate that the uncalcined nanoHAP possessed excellent adsorption ability towards Acid Black 172 dye and can be applied as a low-cost adsorbent for eliminating the dye from wastewater. Figure .18 shows the SEM image and adsorption and desorption isotherm with a pore size dispersion of the uncalcined HAP. Table .5 summarize the Kinetic parameters for AB172 dye adsorption on uncalcined HAP.

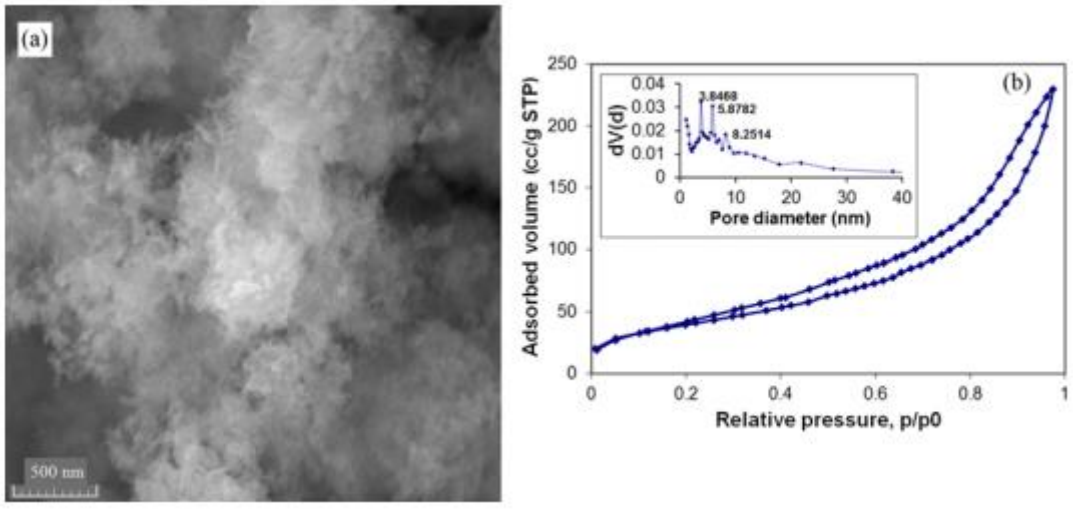

Figure 18. a. SEM image and b. adsorption and desorption isotherm with pore size distribution of the uncalcined HAP [99]

Table 5. Kinetic parameters for AB172 dye adsorption on uncalcined HAP [99].

Kinetic model	Parameter	Initial dye concentration (mg/L)			
		50	100	200	400

	q_e, exp (mg/g)		**24.33**	**48.44**	**95.57**	**193.55**
Pseudo-first order	**q_e, calc (mg/g)**		**29.47**	**50.25**	**102.18**	**174.66**
	k_1 (min^{-1})		**0.0691**	**0.0640**	**0.0689**	**0.0792**
	R^2		**0.9343**	**0.9738**	**0.9793**	**0.9812**
Pseudo-second order	**q_e, calc (mg/g)**		**22.22**	**52.08**	**103.09**	**217.39**
	k_2 (g/mg·min)		**0.0090361**	**0.0018770**	**0.0013716**	**0.0006551**
	R^2		**0.9972**	**0.9929**	**0.9920**	**0.9971**
Intraparticle diffusion	**I**	**$k_{id(I)}$ (mg/g·$min^{1/2}$)**	**3.6645**	**6.4465**	**16.7400**	**31.2710**
		$c_{(I)}$ (mg/g)	**1.1970**	**1.1963**	**7.5693**	**18.6160**
		R^2 (I)	**0.9682**	**0.9676**	**0.9896**	**0.9969**
	II	**$k_{id(II)}$ (mg/g·$min^{1/2}$)**	**2.4297**	**4.1784**	**6.8332**	**8.1647**
		$c_{(II)}$ (mg/g)	**6.1191**	**17.0280**	**44.1880**	**132.3300**
		R^2 (II)	**0.9500**	**0.9361**	**0.9121**	**0.9390**

II.2.16 **Elimination of Malachite green dye from aqueous media**

Malachite green is a synthetic pigment that is widely used in various industrial fields and has a structure. Green malachite is used in the textile coloring industry, paper making, food industry, and other biological fields. As a synthetic dye, malachite green has an unfortunate effect on the environment and the water system. The presence of green malachite in the aquatic system damages biological and reproductive systems and also has carcinogenic and mutagenic effects. These dangerous effects were caused by the high accumulation of malachite green, so a zero level of malachite green should be checked. Various authorities around the world have implemented restrictions on the use of green malachite in the food industry. Discharges of malachite green waste containing aquatic ecosystems colorize the water and prevent sunlight from penetrating the water. Therefore, removing green malachite from wastewater before discharging it into the environment is an environmental requirement. Various procedures have been developed to remove organic dyes from wastewater. These procedures include

electrocoagulation, buoyancy, chemical oxidation, filtration, ion exchange, ozone, membrane separation, and microbial decomposition. It is also possible to use adsorption techniques to remove organic dyes with high efficiency and a high removal rate. Adsorption is an easy and simple procedure to remove uncontrollable species of water currents. The adsorption process has an economic impact when applied in wastewater treatment technology. In 2016, Zahar and colleagues [100] modified HAP to produce modified organic HAP that absorbed malachite green from an aqueous medium and the result was satisfactory. Whereas, organically modified compound HAP can be applied to remove malachite green pigment from aqueous solutions. It has a great equilibrium absorption capacity of 188.18 mg / g. Isotherm studies showed that the absorption of malachite green over organic apatite is well proportioned to Langmuir isotherms with a high correlation coefficient and high absorption capacity.

II.2.17 **Adsorption of different dyes from aqueous media by hydroxyapatite nanocomposites**

Dye elimination by HAP nanocomposite has been recently practiced Adsorption occurs when it penetrates adsorbent through diffusion due to the affinity betwixt them Adsorbate goes deep into the absorbent material over time filling all available vacancies Trivedi and Mandavgane 2018 The removal of dyes by different HAP nanocomposites is shown in Table 6.

Table 6. Absorption of different dyes by HAP nanocomposites [190].

Adsorbent	Dye	Specific surface area (m2/g)	Adsorption capacity (mg/g)	Adsorption parameters					Isotherm	Kinetics	Tends and conclusions	Reference
				Contact time (min)	Dose (mg/ L)	pH	Initial concentration	Temp (°C)				
HAP/hydroxy ethyl cellulose/poly ethylene glycol	Methyl orange	–	135.1	–	32.35	–	32. 7	50	Langmuir	Pseudo second order	Multi coordination, H - bonding sites in surface resulted in high efficiency with spontaneous adsorption of MO.	Azzaoui et al. (2019)

HAP/cerium oxide	Eriochrome Black T	–	143.1	60	50	5	50	–	Freundlich	Pseudo first order	HAP doping enhances the biocompatibility.	Chaudhary et al. (2016)
HAP/chitosan composite	Congo red	–	769	480	50	5	400	–	Langmuir	Pseudo second order	Composite containing 50% of chitosan resulted in high adsorption efficiency.	Hou et al. (2012)
Zein/nHAP	Congo red	73.73	416.7	20	5.5	5.8	400	35	Langmuir	Pseudo second order	Surface area and number of reactive sites increased by doping zein with HAP increasing adsorption capacity.	Nasab et al. (2018)
HAP/chitosan	Acid yellow 220	119.022	303	45	10	–	500	–	Freundlich	–	Enhancement in properties of HAP due to chitosan resulted in rapid adsorption was observed within 30 s	Manatunga et al. (2016)
HAP/titanium	Reactive red 141	87.42	28.41	300	–	8.3	20	–	Langmuir	Pseudo second order	Doping enhance the surface area.	Asjadi, Salahi, and Mobasher pour (2016)
Hide substance/chitosan/HAP	Methylene blue	5.5*10–5	3.8	210	50	12	–	27	Langmuir	Pseudo second order	A low-cost composite was produced by using a waste origin material.	Chatterjee et al. (2018)
Magnetic HAP-supported nickel oxide nanocomposite	Methylene blue	63.7	7.2	180	1000	8	7.5	25	Langmuir	Pseudo second order	Enhanced adsorption capacity.	Phasuk et al. (2018)
HAP-alginate composite spheres	Methylene blue	–	87.89	180	1000	9	50	25	Langmuir	–	HAP composite was found to have higher efficiency than bare HAP	Aslanov, Uzunoğlu, and Özer (2017)

HAP/hydrolyzed polyacrylamide 75	Methylene blue	–	435.6	180	20	5.76	400	25	Temkin	Pseudo second order	Spontaneous adsorption was observed with good regeneration ability of adsorbent.	Mansri, Mahroug, and Dergal (2019)

II.2.18 **Applications in archeology and climato-paleontology**

HAP are substances that have also been investigated in archeology and paleontology The HAP analysis from animal or human residue teeth and bones allow for the reconstruction of feeding patterns in the respective time thus even reconstituting plants and thus returning to the climate [101] Indeed it has been shown that the ratio of strontium to calcium Sr / Ca makes it possible to determine the type of animal nutrition and even makes it possible to differentiate among herbivores and carnivores [102] In the same way it has been seen that the quantity and distribution location A or B of the carbonates within these fossil apatites should be determined by studying the proportion of these carbonates the nature of the plants that the animals ingest and again to infer climatic data for the time in place In which they were living [103].

II.2.19 **Other chemical applications**

Properties other than the biocompatibility of HAP such as its substitution ability can also be exploited, allowing it to clean water contaminated with mineral cations by acting as an inorganic cation exchanger [104]. It is also used frequently in chromatography to separate proteins and other biomolecules. HAP is considered effective due to the combined effects of the calcium and phosphate groups exposed on the crystal surface which give the material a sharp selectivity that allows for the separation of complex mixtures. [105, 106]. Since a relatively recent period, HAP has been a popular material in the heterogeneous catalysis field. For example, they are used in the selective oxidation of alcohols [107] or methane [108], but in combination with ruthenium or nickel type. In this type of reaction, the active species is the metallic type $Ru(OH)_2$ or nickel in metallic form and partially oxidized, and HAP simply acts as a relatively stable medium, and the duration of the reaction between these metals and the apatite structure, even under catalysis conditions. Likewise, in a water gas shift reaction, HAP is used as a support for gold particles (HAP has no activity per se in this reaction even at temperatures above 400 ° C), and this Au / HAP combination allows good activity in this reaction to degrees Heat as low as 110 ° C. [109] In acid catalysis, HAP can be used to replace

$AlCl_3$ in Friedel-Crafts reactions [110] to make the process less polluting. Although better efficacy was achieved for $ZnCl_2$ supported on HAP (conversion of 97% of toluene in 2 min), HAP alone was also active (conversion of 95% of toluene to 120 min). Here the acidic properties intrinsic of HAP in addition to its simple support function are used. In primary catalysis, the basic acidic properties of HAP are the gain. In some cases, these properties can be psychedelic, as in the case of the Knoevenagel reaction [111], where the addition of potassium fluoride increases the base that is exhaled before the doping is taken. The authors attribute this rise in the activity to the change in conformation induced by KF doping, which is not surprising because fluorine is readily replaced by hydroxyl groups and the substitutes have already been reported using different charge ions (such as K^+) and often result in a reorganization of substances to counterbalance for the charge.

II.3 Chitosan

II.3.1 **Definition of Chitosan**

Chitosan is a polysaccharide constituted by the irregular distribution of D-glucosamine combined in ß- (1-4) (deacetylated unit) and N-acetyl-D-glucosamine (acetylated unit). It is getting by chemical deacetylation (in an alkaline medium), also by enzymatic of chitin, the composition of the exoskeleton of crustaceans or the endoskeleton of cephalopods ... or the wall of mushrooms. This natural material is demineralized by treating it with hydrochloric acid, then deproteinized by a solution of soda or potash, and eventually whitened it thanks to an oxidizing means. The degree of acetylation (DA) is the rate of acetylated units in comparison with the number of total units, it can be calculated from the exploitation of FTIR spectrums or by a strong base titration. The limit between chitosan and chitin corresponds to a DA of 50%: under this, the composite is called chitosan, beyond, chitin. Chitosan is soluble in an acid medium, unlike insoluble chitin. It is important to distinguish between the degree of acetylation (DA) and the degree of deacetylation (DD). One is the reverse of the other, that is to say, that chitosan having a DD of 85%, has 15% of acetyl groups and 85% of amine groups on its chains.

II.3.2 **Brief History of Chitosan**

Research on extraction and characterization of chitin began in 1811 with the studies of the French chemist Henri Braconaut in which some fungal species were subjected to aqueous

alkaline treatment which allowed the extraction of the fungus for which it was named In 1843 Lassen conducted research on the exoskeletons of Bombyx mori silkworm showing the existence of nitrogen in the composition of chitin Chitosan was found in 1859 by treating chitin with superheated potassium hydroxide In 1878 Lederhose indicated that chitin contained compounds such as glycosamine and acetic acid However only in 1894 did Gilson confirm the presence of glycosamine units However in 1894 the German Felix Hoppe Seiler named the compound chitosan [112] The chemical composition of chitosan was determined in the year 1950 [113] The first reports of chitosan production appeared in 1970 in Japan and the United States By 1986 Japan already had 15 commercially producing industries of chitin and chitosan Japan and the United States are the world leaders in the production of chitosan and are prominent in researching this polysaccharide in its many applications chitosan is economically attractive and profitable [114] In 1983 the first studies were conducted with fungal chitosan in Brazil and confirmed the presence of chitosan in the cell walls of fungi belonging to the class Zygomycetes and Mucorales [115].

II.3.3 **Occurrence of sources in the nature**

Chitin is a natural polymer with a highly organized crystalline structure consisting of nitrogen, white and solid, and has a low chemical reactivity. It is the second most abundant polysaccharide in nature, after the cellulose. It is insoluble in water and organic solvents, displaying, after purification, as a yellowish powder. It has a high molecular weight and is chemically composed of N-acetyl-2-amino-2-deoxy-D-glucose units linked together by glycosidic bonds β (1 → 4) as it is shown in Figure 19, forming a linear chain with some of the deacetylated monomer units [116].

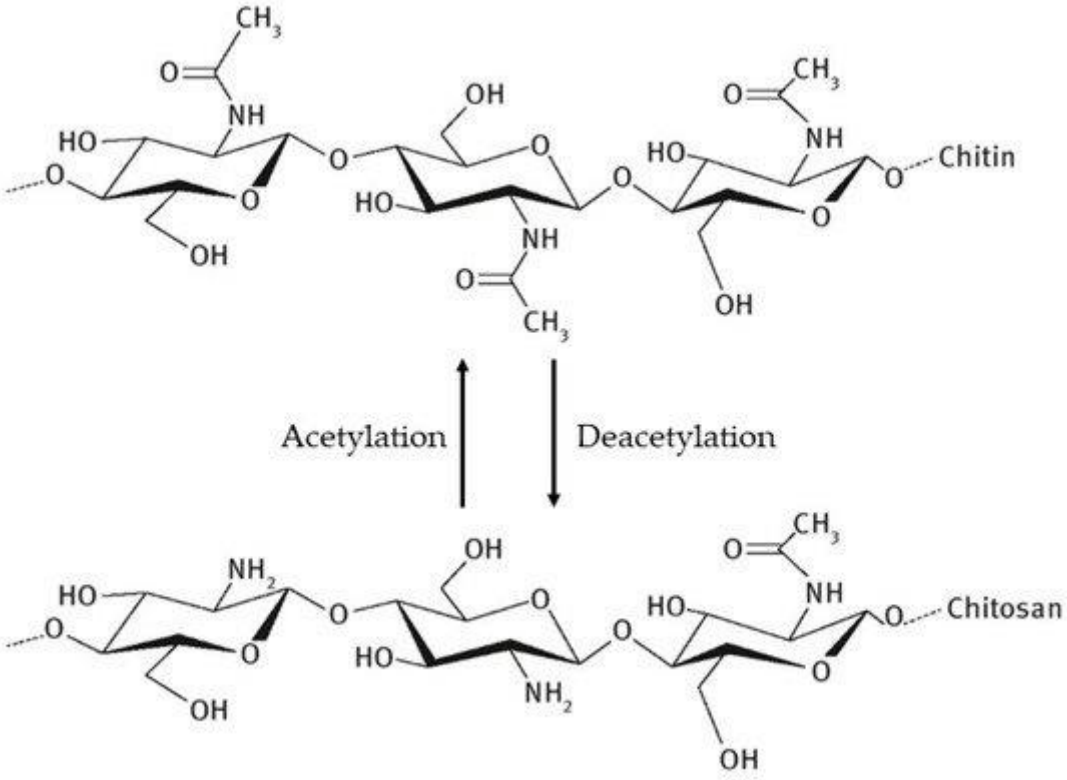

Figure 19. Chemical structures of chitin and chitosan.

Chitin is commonly remained in nature and is the main component of the exoskeleton of marine shellfish and can be gained in the structure of insects, arthropods, and mollusks [117]. Figure 20 illustrates the main sources for chitin production and extraction.

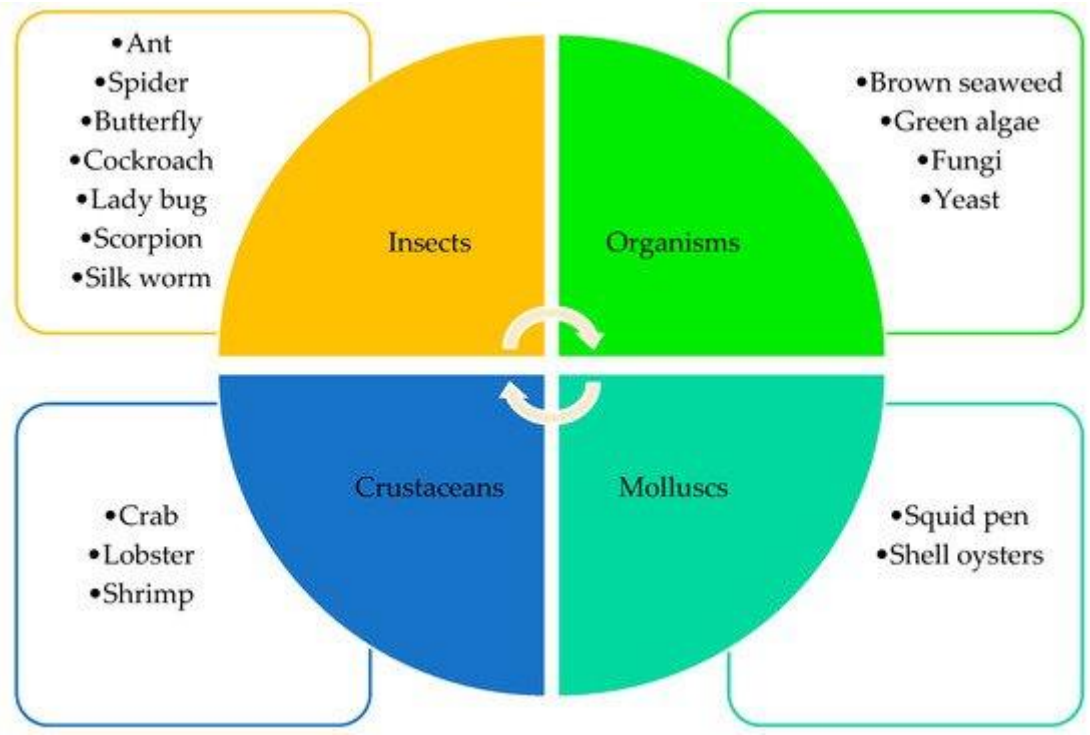

Figure 20. Sources of chitin production [114, 117].

The polymorphism of chitin could be comprehended using X-ray diffraction, in which three crystallin structures are remarked, α, β and γ, which differ according to the number of chains in each cell, the degree of hydration, and the unit size. α-chitin is the current abundant form, as it is observed in the exoskeletons of arthropods, where the polymeric chain combinations are opposite, favoring the presence of many hydrogen bonds within the chain which results in a densely arranged material as it is shown in figure 21. In-chitin, the distribution is parallel and is found in animals that show flexibility and resistance, such as squid. The γ-chitin exhibits a combination of both positions [118].

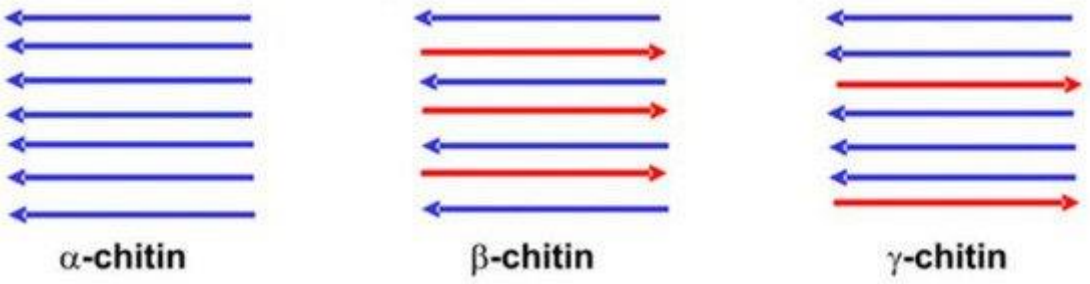

Figure 21. Polymorphic structures of chitin [114].

Chitin derivatives have high economic value due to their biological activities and applications, being biodegradable and biocompatible polymers as well as produced by renewable natural sources. Harnessing the by-products of crustacean processing is a profitable activity because of their richness in high value-added compounds [119].

II.3.4 **Chitosan isolation from natural resources**

The liquid waste from the fishing industry, if it is released untreated into the environment beforehand, causes physical and chemical changes in water being, which may cause the death of aquatic animals and affect the local micro-fauna and microflora, since these residues are characterized by high concentrations of nitrogen And phosphorous, organic carbon, suspended solids, and oxygen [120].

Seafood is a better source of animal protein in countries, along with the good portion, these natural materials produce some inedible residue [121]. An important part of environmental pollution is caused by the losses from fishing industrial activities, which triggers an environmental emergency due to their disagreeable odor, attracting and exciting the reproduction of insects. They can also be dangerous to human health when deployed without prior treatment [114]. Seafood loss is a great possible source of raw substance for chitin extraction [122]. Despite, due to their origin from natural resources and their chemical and physical variability, the properties of chitin and chitosan can have a direct impact on their applications [123]. Characteristics that may be related to the extraction process are molecular weight, degree of deacetylation, degree of purity, viscosity, and crystallinity [124].

II.3.5 **Chemical Extraction**

This sort of extraction is based on the use of a powerful alkaline solution, like sodium hydroxide hydrolysis at high concentrations and temperatures, prompting the failure of polymeric chains and producing chitosan with a high degree of deacetylation. The chemical extraction process included three fundamental steps as it is shown in Figure 22, an alkaline solution for deproteinization, an acid solution for demineralization, and a discoloration. Remarkably, all these steps directly affect the physicochemical properties of the chitin gained. The source for chitin production will be washed, dried, and grind for giving powder particles.

This process of classical extraction can cause difficulties in the disposal of waste produced, which is needed for the neutralization and detoxification of wastewater.

II.3.6 **Chemical Deproteinization**

The deproteinization requires the separation of chemical bonds connecting proteins and chitin, needing chemicals to depolymerize the biopolymer, whose elimination of the linked proteins is a necessary step in the polysaccharide purification.

Conventional extraction of chitin from marine litter through protein denaturation requires the choice of strong bases and acids at adequate temperatures, which needs high energy loss and generates effluents at high chemical concentrations, obliging suitable treatment to neutralize them. The use of strong acids and bases during the chitin extraction drives to a raise in the charge of materials required in the process, also yield a low purity product.

II.3.7 **Chemical Demineralization**

Demineralization is a means for the elimination of minerals, mainly calcium carbonate, utilizing strong acids [125]. The large commonly applied acids in this treatment process are hydrochloric acid, sulfuric acid, acetic acid, formic acid, and nitric acid. The demineralization HAPpens by the breakdown of calcium carbonate in calcium chloride, with the liberation of carbon dioxide, as shown in the reaction:

$$2HCl+CaCO_3 \rightarrow CaCl_2+H_2O+CO_2\uparrow$$

II.3.8 **Discoloration**

This is a supplementary step during the extraction process and is done if you want to obtain a noncolored product as it tries to remove astaxanthin and β-carotene dyes when they are existing already in the extraction source. It employs organic or inorganic solvents essentially hydrogen peroxide, acetone or, sodium hypochlorite [126].

II.3.9 **Biological Extraction**

The biological extraction technique necessitates the use of microorganisms that deliver enzymes and organic acids at a moderately low cost, with a disinfectant and greener process, approving the production of chitin with high quality [127, 128].

The biological extraction process has been made more handsome by getting high-quality outcomes, with the charge of production remaining affordable and not producing high concentration chemical Liquid waste, as stated in the chemical process. Biological techniques commonly used for chitin extraction are protein deproteinization and enzymatic fermentation using microorganisms.

II.3.10 **Enzymatic Deproteinization**

Enzymatic deproteinization of the fish waste industry to get hydrolyzed protein is a process based on the add of enzymes for fragmentation of protein, owning the interest of not providing environmental degradation products [129]. Proteases are of the highest regard for protein elimination through chitin extraction from fishing manufacturing waste. The proteases required in the protein removal method from seafood deposits are papain, trypsin, pepsin, alkalase, and pancreatin [130].

II.3.11 **Fermentation**

Hydrolyzed proteins can be taken by proteolytic enzymes generated by the lactic acid bacteria stimulated due to a base pH in the solution media. The benefit of this manner is that it enables the recovery of value-added by-products like proteins, enzymes, and dyes that can be used, in food manufacturing [131].

The effectiveness of fermentation within microorganisms depends accurately on the quantity of glucose concentration or inoculum in the medium, the pH during the production, and fermentation time. This type of removal using microorganisms is a trend in bioremediation and biotechnology researches [132].

Fermentation could be produced using protease-producing bacteria like Pseudomonas aeruginosa, Bacillus subtilis, Pseudomonas maltophilia, and Serratia marcescens [133, 134, 135, 136].

II.3.12 **Chitin to Chitosan Conversion**

Chitosan is a polysaccharide gained from chitin by reaction of deacetylation throughout alkaline hydrolysis and following by treatment with acidic solutions, consisting of 2-amino-2-deoxy-D-glucopyranose units combined by glycosidic bonds β (1 → 4) as show the Figure 19. Nevertheless, the polymers change in the relative proportion and solubility of certain units. They can function as an ionic exchange resin for remaining solvable in organic acids and diluted minerals; although, their deposition occurs with a pH value upper 6.0 [137].

Chitosan is all chitin derivatives that have a degree of deacetylation of 50% or higher. The relative proportions of these units make distinct fundamental characteristics, like the degree of deacetylation and molecular weight, whose basic properties are related to the physicochemical and biological characteristics of the polymer [138,139].

Chitosan has the character of solubility in an acidic medium because of the free amino groups comprising protonated (NH_3^+), where the precipitation trend grows from the moment the pH nears 6.0, concerning the increase of -NH_2 groups in the molecular organization. Thus, amino groups make it viable for them to link to negatively charged materials, like other polysaccharides, enzymes, and cells, meaning unsolvable in water, alcohol, concentrated acids, and acetone [140].

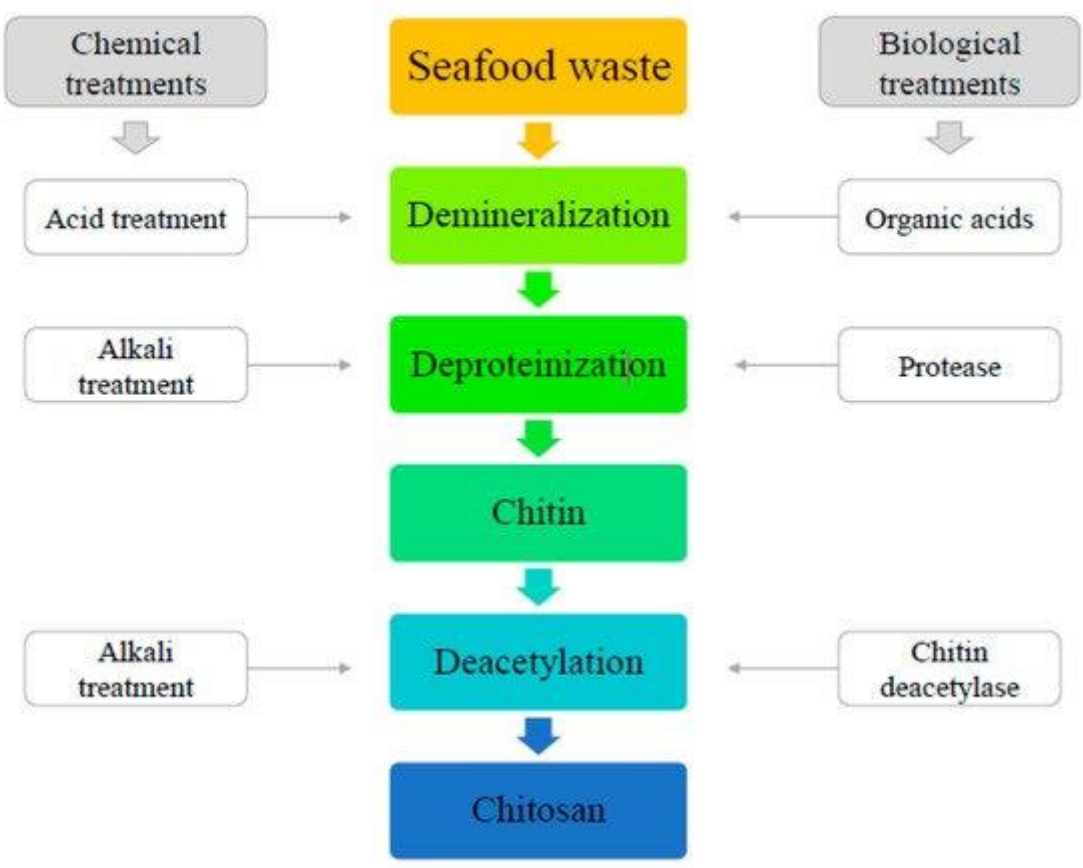

Figure 22. Chitin and chitosan production by chemical and biological treatments [114].

In recent years, studies have been done on chitosan to show a close relationship correlation between the morphological and structural characteristics of chitin, chitosan and their derivatives, their characteristics, and their possible applications [141].

This polymer can be observed in nature in few quantities in the cell walls of some mushrooms as Zygomycetes, or it can be gained from chitin by alkaline hydrolysis of exoskeletons and crustacean of arthropods. Crustacean shells include 15% to 20% of chitin, 25% to 40% of protein, and 40% to 55% of calcium carbonate wish is responsible to the rigidity of crustacean.

II.3.13 **Chitosan Applications**

New technological approaches are required to develop the environment and human lives. What performs chitosan a material of manufacturing powers are its large potential application and properties, like cationic biopolymer behavior, water insolubility, positive global charge in biological pH, and readily capable of producing gels. These properties give it interest for medicine, agricultural applications, environment, and food, as indicated in Figure 23 [114].

Active Ingredient

Nanotechnology has applications in fields such as engineering, medicine, medicine, and agriculture, which have revolutionized various processes and products [142]. Chitosan is a polymer of great industrial and biotech importance due to its abundant extractive source, being biocompatible and positively charged, and defining it as a potential material for an active ingredient delivery system.

Chitin-based nanomaterials and chitosan can be used as carriers of cosmetic ingredients, such as nano chitin face masks that can release active ingredients in different doses and can be used as anti-bacterial, anti-inflammatory, sunscreen, and anti-inflammatory. Aging cosmetics according to the selected active ingredient [143]. Nanotechnology can also be applied in agriculture, with the agricultural industry being preferred to be greener. Nanoparticles can increase the effectiveness of agrochemicals, leading to lower doses and fewer applications, as well as reducing environmental pollution risks and promoting effective pest control in agriculture [144,145].

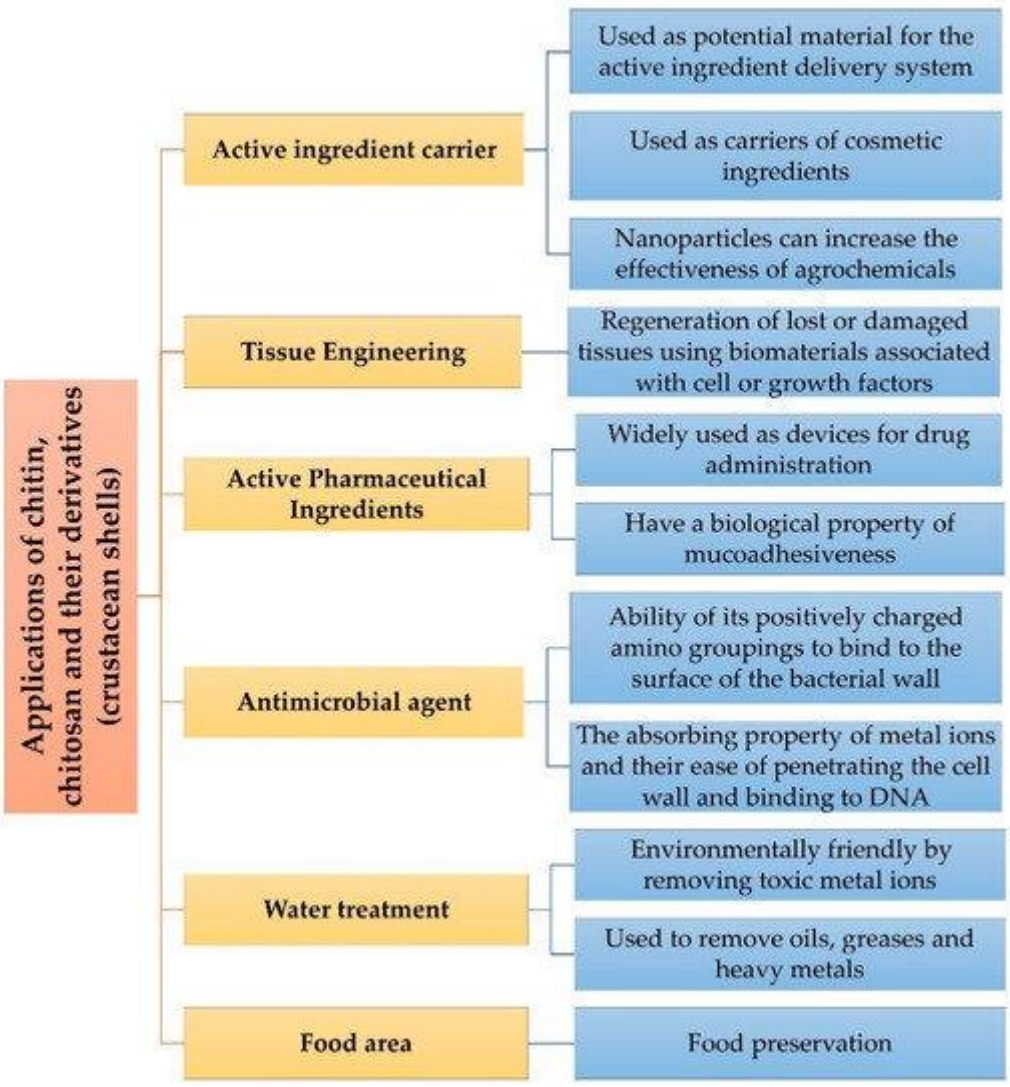

Figure 23. Flowchart of the summary of the main applications of chitin/chitosan [114].

Tissue Engineering

Artificial tissue engineering represents a major advance in the field of biomedicine because it aids in reconstructive processes, and favors an improvement in the quality of human life [146]. It involves regenerating lost or damaged tissues with the use of cell-related biomaterials or growth factors [147].

An important requirement for scaffolds is that they have a homogeneous structure with high porosity to ensure penetration and diffusion of nutrients into cells [148].

Characteristics of biomaterial selection for tissue engineering are: the presence of interconnected pores, controlled biodegradability, adjustable chemical surface, mechanical

properties similar to the implant site, unimportant toxicity, ease of obtaining desired shapes and sizes [149].

Active Pharmaceutical Applications

Several polymers have been used in the production of mucous adhesive delivery systems; However, chitosan and its derivatives are the most widely used due to their toxicity, biocompatibility, antimicrobial activity, and adequate penetration [150].

Chitosan based nanoparticles are widely used as drug administration devices because they have features that are useful as a means of loading drugs. It has a biological property of mucosal torsion, which means a transient opening of the epithelial connections for drug entry [151].

Chitosan is a natural polysaccharide with non-toxic, hypoallergenic, biocompatible, and biodegradable property, and chitosan derivatives have been reported as anticoagulants. The literature describes that chitosan has a close structure similar to heparin, and based on this feature, molecules of chitosan derivatives were synthesized [152,153,154,155,156].

Anticoagulants are used clinically for various medical conditions such as blood clots and have the highest annual growth rate among the top ten therapeutic areas. The developed compounds showed faster efficacy and effectiveness than Nicoumalone 1 hour after taking the drug. The n-alkyl sulfur derivatives of chitosan have been proposed as stronger anticoagulants than the tetrachitosan sulfur / sulfur derivatives [157].

In this sense, the most notable commercial application for chitosan is its use as a functional system for hemostasis. Therefore, chitosan-based wound dressings are available in the market for clinical use as HemCon® Bandage and ChitoFlex products (HemCon Medical Technologies, UK), as well as CELOX ™ (Medtrade Products, England); All products are FDA approved (http://www.hemcon.com and http://www.celoxmedical.com, respectively) [158].

Antimicrobial Agent

Investigations have reported chitosan's antimicrobial activity, but the mechanism has not yet been fully elucidated and studies are fundamental in the search for the elucidation of chitosan's potential. One of the most studied properties of chitosan is its antimicrobial activity, which is related to the ability of its positively charged amino groups to bind to the surface of a bacterial wall or plasma membrane because it has a negative charge. Thus, there is a change in cell permeability, the flow of ions, and proteins from the cytoplasm into the extracellular space aids

and causes cell death [159]. The high degree of acetylcysteine, the high molecular weight of chitosan, and antibacterial activity induce changes in cell permeability and inhibition of bacterial transport [160,161,162]. Decreased degree of acetylation of chitosan and a decrease in pH of antibacterial activity; However, the reduced molecular weight and activity towards Gram-negative bacteria, as well as the molecular weight and degree of acetylcysteine, affected the antifungal activity with different fungi [163].

Other factors related to chitosan's antimicrobial activity are the absorption property of metal ions, ease of penetration into the cell wall and their binding to DNA, inhibition of RNA synthesis, and low molecular weight of chitosan induced by inhibition of DNA transcription and mRNA synthesis in Escherichia coli [164,165,166].

Therefore, the antimicrobial activity of chitosan and its derivatives is widely explored to produce self-preserving materials through food preservation and packaging. Chitosan films have great uses in food packaging materials, forming a protective antimicrobial barrier and maintaining the nutritional quality of foods [167, 168].

Water treatment

Water and the range of services generated by this depleted natural resource contribute to poverty reduction, economic growth, as well as social and environmental sustainability, thus contributing to improved social welfare [169]. Wastewater from food, textile, vegetable oil processing, oil production, and local sanitation companies is a major source of pollution, as it contains various organic compounds and is not properly treated before being discharged into liquid waste [170]. Adsorption is the adhesion or fixation of particles or electrostatic bonding of a liquid to a solid surface, which enables the disposal of compounds, metal ions, or other materials using an inactive absorbent of biological origin or natural products, employing attraction forces between materials. Biological absorbent and sorbent [171]. The literature cites some adsorbents that are effective in removing toxic metal ions and are environmentally friendly, such as chitin, chitosan, cellulose, and guarana [172]. Chitosan is used to remove oils, grease, and heavy metals [173, 174]. An increase in the degree of deacetylation of chitosan is associated with a greater number of amino groups, which are the main absorption centers, where the degree of acetylation and pH are the main factors affecting the absorption capacity of chitosan [175, 176].

Food technology

Chitosan biopolymer is a biocompatible, non-productive, non-toxic, biofunctional molecule that has attracted remarkable attention as a potential food preservative of natural origin [177,178,179]. Chitosan produced from shrimp isolate was previously prepared as GRAS (generally recognized as safe) based on scientific procedures for multiple technical effects in several food classes [180]. Applications of chitosan were investigated to extend bread life by inhibiting delayed starch and/or by inhibiting microbial growth. The authors assessed the chitosan molecule with a 493 kDa layer over the life span of a baguette surface using 0.5%, 1.0%, or 1.5% chitosan diluted in 1.0% acetic acid. The results indicated chitosan barrier properties with baguette-coated chitosan at 1%, less weight loss, stiffness, and slope compared to control during storage for 36 h at 25 ° C [181].

Chitosan is obtained by extracting it from biological waste using energy-saving methods. Chitosan is much cheaper compared to other biopolymers. However, the exceptional properties of chitosan make it a relatively stronger candidate for food packaging applications. The most common and economical method for producing chitosan is from chitins. However, it is also possible to obtain chitosan directly from some fungal cell walls [182,183] and other resources [184]. Chitosan film has been used extensively to extend the shelf life of food, with the addition of Ca^{2+} ions to alter the penetration rate of CO_2 and O_2 across chitosan membranes and to increase the useful life of the fruit [185]. The raw materials were shown to prepare a series of films from the formulation of chitosan and glycerine preserved strawberries [186]. Coating with a chitosan film by immersion in a 1% polysaccharide solution containing 0.1% Ca^{2+} prevents changes in the organoleptic properties of vegetables [187]. Besides, chitosan is also useful in the production of food wrapping paper, which acts as an inhibitor of microbial growth [188]. Membranes consisting of chitosan and polyvinyl alcohol combined with lignin nanoparticles increased strength compared to the single component films, the antibacterial effect against gram-negative microorganisms, and the synergistic antioxidant effect of chitosan and lignin [189].

Heavy metal ions fixation

Different absorbents have been used to remove different types of dyes and heavy metal ions from wastewater especially those harmful to mankind. Activated carbon, plant or cellulosic

waste, clays, and biopolymers are among the common sorbents used. Chitosan, a kind of biopolymer, is a good absorbent for removing various types of anionic and cationic dyes as well as heavy metal ions. Chemical modifications leading to the formation of chitosan derivatives, chitosan grafting, and chitosan compounds have received significant attention, extensive study and extensively reported in the literature. A review by NGAH et al in 2011 is summarized for most applications and the heavy metal ion absorption mechanism by Chitosan [191]. The NGAH et al review provides relevant literature over the past ten years on the use of chitosan compounds to remove dyes and heavy metal ions. A list of chitosan compounds with their absorption capacity and experimental conditions was compiled. The use of biopolymers such as chitin and chitosan are an emerging adsorption method for removing dyes and heavy metal ions, even at low concentrations (Crini, 2006). Chitosan is a type of naturally occurring polyamino polysaccharide, synthesized from diacetylchitin, which is a polysaccharide that mostly consists of unbranched chains of _- (1 → 4) -2-acetoamido-2-deoxy-d-glucose. Chitin is the second most abundant polymer in nature after cellulose. It can be extracted from crustaceans such as prawns, crabs, fungi, insects and other crustaceans (Wan Ngah & Isa, 1998). Chitosan is known as the ideal natural support for enzyme fixation due to its special properties such as hydrophilicity, bio-compatibility, biodegradability, non-toxicity, absorption properties, etc. (Kumar, 2000). Chitosan can be used as a sorbent to remove heavy metals and dyes due to the presence of amino and hydroxyl groups, which can act as active sites (Wu, Tseng, & Juang, 2001). The amino groups can cations from chitosan, and then the anionic dyes are strongly absorbed by electrostatic attraction in an acidic medium (Kumar, 2000). However, chitosan is very sensitive to pH because it can form a gel or dissolve depending on the pH values (Chiou, Ho, & Li, 2004). To improve the performance of chitosan as an adsorbent, cross-reactants such as glyoxal, formaldehyde, glutaraldehyde, epichlorohydrin, ethylene glycon-diglycidyl ether and isocyanates were used (Crini & Badot, 2008). Cross-linking agents not only stabilize chitosan in acidic solutions so that it becomes insoluble but also enhance its mechanical properties (Chiou et al., 2004). Chitosan derivatives have been extensively examined as absorbents (Amit and Mica, 2009). Among them are derivatives of chitosan that contain nitrogen, phosphorous and sulfur such as heterocyclic atoms, and other derivatives such as chitosan crown ethers and chitosan ethylene diaminitra acetic acid (EDTA) / DTPA complexes

(Pharma, Deshpande, 2004), &. More recently, chitosan compounds have been developed to absorb heavy metals and dyes from wastewater. Various types of materials have been used to form a compound with chitosan such as montmorillonite (Wang and Wang, 2007), polyurethane (Wen, Li, Jeong, Min, and Li, 2009), activated clay (Zhang and Guangxan, 2004), bentonite (Wan Ngah, Ariff). , & Hanafiah, 2010), polyvinyl alcohol, polyvinyl chloride, kaolinite (Chu, Jiang, and Xiao, 2010), oil palm ash (Hamid, Hasan, and Ahmed, 2008) and Perlite (Kalyani, Agithha, Srinivasa, and Krishnaya, 2005) . Chitosan has been shown to have better absorption capacity and resistance to acid environment (Veera, Krishnaiah, Jonathan, Edgar, & Richard, 2008). This review paper will highlight the use of chitosan as absorbents, which includes the method of preparation and the mechanisms and factors that can affect its absorption capacity. Table 7 regroups some examples of absorption of various heavy metal ions by chitosan.

Table 7. Absorption of differents heavy metal ions by Chitosan [191].

Adsorbent	Adsorbate	Adsorption capacity (mg/g)	pH	T (◦C)	Kinetic model	Isotherm	Reference
Chitosan/cotton fibers (via Schiff base bond)	Hg(II)	104.31	5.0	35	Pseudo first order	Langmuir, Freundlich	Qu, Sun, Fang, et al. (2009)
Chitosan/cotton fibers (via C–N single bond)	Hg(II)	96.28	5.0	25	Pseudo second order	Langmuir, Freundlich	Qu, Sun, Fang, et al. (2009)
Chitosan/cotton fibers (via Schiff base bond)	Cu(II)	24.78	6.5	25	–	Langmuir, Freundlich	Zhang et al. (2008)
Chitosan/cotton fibers (via Schiff base bond)	Ni(II)	7.63	6.5	25	–	Langmuir, Freundlich	Zhang et al. (2008)
Chitosan/cotton fibers (via Schiff base bond)	Pb(II)	101.53	6.5	25	–	Freundlich	Zhang et al. (2008)
Chitosan/cotton fibers (via Schiff base bond)		15.74	6.5	25	–	Langmuir, Freundlich	Zhang et al. (2008)
Chitosan/cotton fibers (via Schiff base bond)	Au(III)	76.82	3.0	25	Pseudo second order	Langmuir, non linear Langmuir, Redlich–Peterson	Qu, Sun, Wang, et al. (2009)

Chitosan/cotton fibers (via C–N single bond)	Au(III)	88.64	3.0	25	Pseudo second order	Langmuir, non linear Langmuir, Redlich–Peterson	Qu, Sun, Wang, et al. (2009)
Magnetic chitosan	Cr(VI)	69.40	4.0	–	–	Langmuir	Huang et al. (2009)
Chitosan/magnetite	Pb(II)	63.33	6.0	–	–	Langmuir	Tran et al. (2010)
Chitosan/magnetite	Ni(II)	52.55	6.0	–	–	Langmuir	Tran et al. (2010)
Chitosan/cellulose	Cu(II)	26.50	–	25	–	Langmuir	Sun et al. (2009)
Chitosan/cellulose	Zn(II)	19.81	–	25	–	Langmuir	Sun et al. (2009)
Chitosan/cellulose	Cr(VI)	13.05	–	25	–	Langmuir	Sun et al. (2009)
Chitosan/cellulose	Ni(II)	13.21	–	25	–	Langmuir	Sun et al. (2009)
Chitosan/cellulose	Pb(II)	26.31	–	25	–	Langmuir	Sun et al. (2009)
Chitosan/perlite	Cu(II)	196.07	5.0	–	–	Langmuir	Kalyani et al. (2005)
Chitosan/perlite	Ni(II)	114.94	5.0	–	–	Langmuir	Kalyani et al. (2005)
Chitosan/perlite	Cd(II)	178.6	6.0	25	–	–	Shameem et al. (2006)
Chitosan/perlite	Cr(VI)	153.8	4.0	25	–	Langmuir	Shameem et al. (2003)
Chitosan/perlite	Cu(II)	104.0	4.5	25	–	Langmuir	Shameem et al. (2008)
Chitosan/ceramic alumina	As(III)	56.50	4.0	25	–	Langmuir, Freundlich, Redlich–Peterson	Veera, Krishnaiah, Jonathan, et al. (2008)
Chitosan/ceramic alumina	As(V)	96.46	4.0	25	–	Langmuir, Freundlich, Redlich–Peterson	Veera, Krishnaiah, Jonathan, et al. (2008)
Chitosan/ceramic alumina	Cu(II)	86.20	4.0	25	–	Langmuir, Freundlich, Redlich–Peterson	Veera, Krishnaiah, Ann, et al. (2008)

Chitosan/ceramic alumina	Ni(II)	78.10	4.0	25	–	Langmuir, Freundlich, Redlich–Peterson	Veera, Krishnaiah, Ann, et al. (2008)
Chitosan/ceramic alumina	Cr(VI)	153.8	4.0	25	–	Freundlich	Veera et al. (2003)
Chitosan/montmorillonite	Cr(VI)	41.67	4.0	25	Pseudo second order	–	Fan et al. (2006)
Chitosan/alginate	Cu(II)	67.66	4.5	–	Pseudo second order	Langmuir	Wan Ngah and Fatinathan (2008)
Chitosan/calcium alginate	Ni(II)	222.2	5.0	–	Pseudo second order	Langmuir	Vijaya et al. (2008)
Chitosan/silica	Ni(II)	254.3	5.0	–	Pseudo second order	Langmuir	Vijaya et al. (2008)
Chitosan/PVC	Cu(II)	87.9	4.0	–	Second order	Langmuir	Srinivasa et al. (2009)
Chitosan/PVC	Ni(II)	120.5	5.0	–	Second order	Langmuir	Srinivasa et al. (2009)
Chitosan/PVA	Cd(II)	142.9	6.0	50	Pseudo second order	Langmuir	Kumar et al. (2009)
Chitosan/PVA	Cu(II)	47.85	6.0	–	Second order	Langmuir	Wan Ngah et al. (2004)
Chitosan/sand	Cu(II)	10.87	4.2	–	–	Langmuir	Wan et al. (2007
Chitosan/sand	Cu(II)	8.18	–	–	Pseudo second order	Langmuir	Wan, Kan, Buenda, and Maria (2010)
Chitosan/sand	Pb(II)	12.32	–	–	Pseudo second order	Langmuir	Wan et al. (2010)
Chitosan/clinoptilolite	Cu(II)	574.49	5.0	–	Pseudo second order	Langmuir	Dragan, Dinu, and Timpu (2010)

Chitosan/clinoptilolite	Cu(II)	719.39	5.0	25	Pseudo second order	Langmuir	Dinu and Dragan (2010)
Chitosan/clinoptilolite	Co(II)	467.90	5.0	25	Pseudo second order	Langmuir	Dinu and Dragan (2010)
Chitosan/clinoptilolite	Ni(II)	247.03	5.0	25	Pseudo second order	Langmuir	Dinu and Dragan (2010)
Chitosan/nano-HAP	Fe(III)	6.75	–	–	–	–	Kousalya, Muniyappan, and Sairam (2010)
Poly(methacrylic acid) grafted-chitosan/bentonite	Th(IV)	110.5	5.0	30	Pseudo second order	Langmuir	Thayyath et al. (2010

II.3.14 **Antimicrobial properties of Chitosan**

Chitosan has good antimicrobial properties. These depend on several factors: its nature, degree of polymerization, its origin, substrate composition, and environmental conditions such as substrate moisture for example. Its anti-microbial effect has anti-fungal, anti-bacterial, and algae effects. It works in different ways. First, it has an inhibitory effect on certain enzymes. Moreover, its chelating nature causes it to block mineral cations which limit the production of toxins and the growth of microorganisms. Finally, the ammonium groups in chitosan have both bactericidal and bactericidal effects, especially if they are tetrahydro-fluor. Its bactericidal effect is optimal to a pH of 6.0 instead of 7.5. These conditions allow greater access to the amine groups, with chitosan pKa ranging from 6.2 to 7.32. Moreover, chitosan films offer a wide range of applications in food packaging materials which can be attributed to their antimicrobial properties [192]. Chitosan-based coatings for fruits and vegetables with antimicrobial agents, such as essential oils, acid, and nanoparticles were recently revised by [193, 194]. For example, it has been reported that bacterial damage to young carrots is delayed after the application of chitosan based coating that maintains the overall quality of the product [195]. Chitosan films containing propolis inhibit Staphylococcus aureus, Enteric Salmonella, Escherichia coli, and Pseudomonas aeruginosa [196]. Poly films (phenyl alcohol) and chitosan mixtures containing dual-function cellulose/zinc oxide nanocrystals showed antibacterial activity towards the bacterial species Salmonella choleraesuis and Staphylococcus aureus

[197,198]. Similar properties were also observed for poly (phenyl alcohol) / chitosan-enhanced nanocrystals / multifunctional ZnO-Ag nanofiling mixture [199].

II.4 Carbon nanomaterials

Carbon nanomaterials are important parts of the family of nanomaterials with different forme, each with unique properties. Carbon nanomaterials can be classified into 0D like a diamond particle as an example or fullerene, and carbon dots, 1D for example, CNTs, CNFs, and nanorods, 2D like graphene, graphite sheets, and diamond nanostructures, and 3D as nanoscale diamond-like carbon (DLC) films, nanocrystalline diamond (NCD) films, and fullerite). Carbon nanomaterials composed entirely of sp^2-bound graphitic carbon were found in all reduced dimensions including fullerene (0D-NMs), CNTs (1D-NMs), and graphene (3D-NMs). Figure 24 shows the broad family of carbon nanometers.

II.4.1 Graphene, Carbon nanotubes, Carbon Nanohorns

Graphene

Since the initial experimental evidence of the electronic properties of graphene in 2004, recent years have seen great advances in research. Graphene, which is the building block of all forms of graphite (including carbon nanotubes (CNTs), graphite, and fullerene), has a single layer of carbon atoms in a closely packed two-dimensional honeycomb network. Graphene has a specific large surface area (theoretical value 2630 $m^2.g^{-1}$) [201], and both sides of its flat sheets are available for the absorption of particles. Moreover, the large, indeterminate electron system of graphene can form a strong interaction with the benzene ring, which may make graphene a good choice for extracting benzene form compounds.

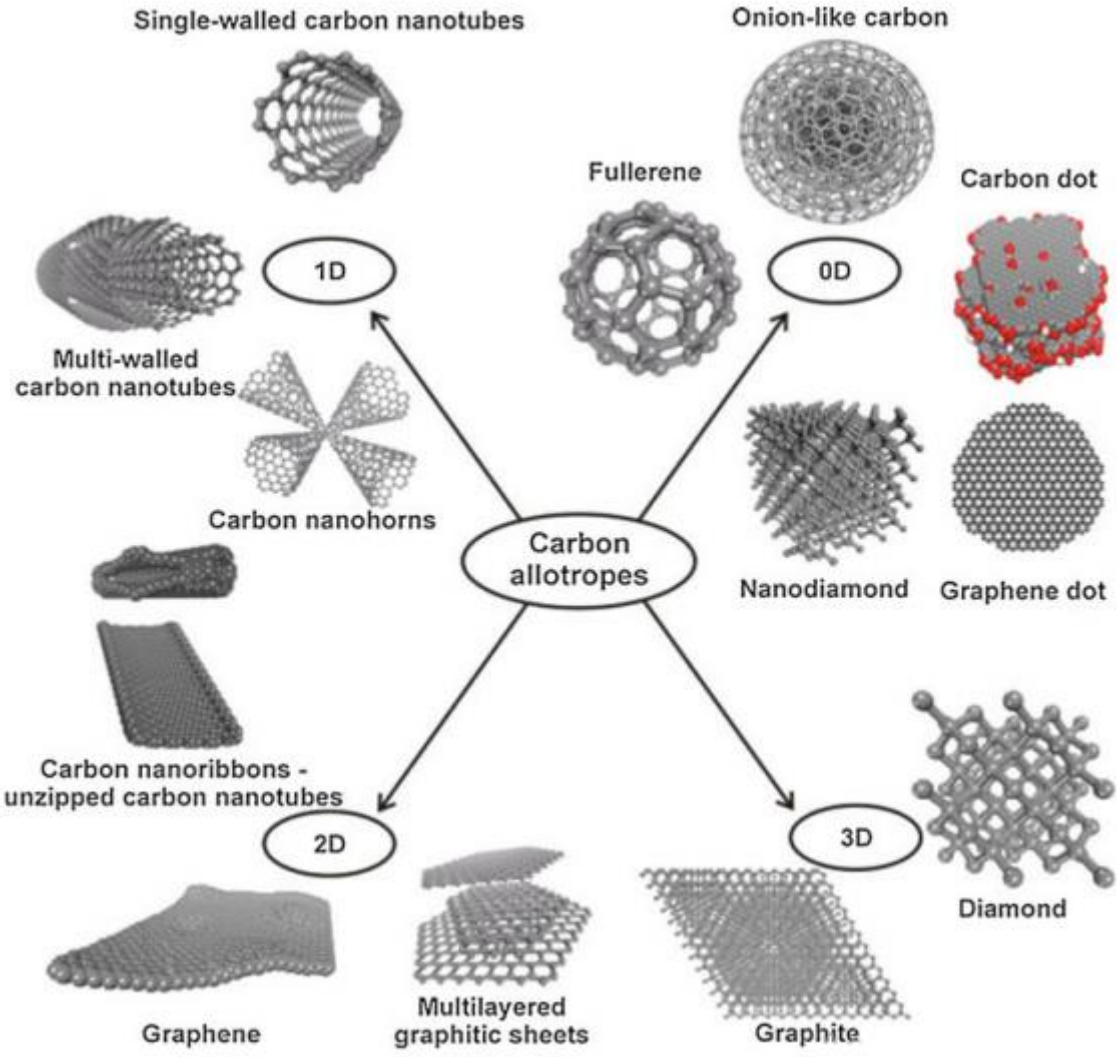

Figure 24. Different structures carbon nanoallotropes: Carbon dots, nanodiamond, fullerenes, carbon nanotubes, carbon nanohorns, graphene, carbon nanoribbons, and combined superstructures [200].

Finally, graphene can be easily modified with functional groups, particularly via graphene oxide. Graphene's exceptional properties make it an excellent candidate as a good adsorbent in various sample preparation methods.

Single-Wall Carbon Nanotubes (SWCNT)

Most of the single-walled carbon nanotubes (SWCNT) are approximately 1 nanometer in diameter, and the tube can be millions of times in length. The structure of SWCNT can be visualized by wrapping a one-atom-thick layer of graphite called graphene into a seamless cylinder. The way a graphene sheet is wound is represented by a pair of indicators (n, m) called

a spiral vector. The two integers n and m denote the number of unit vectors along with two directions in the honeycomb crystal lattice of graphene. If m = 0, the nanotubes are called "zigzag," which is called the hex pattern as we move around the perimeter of the tube. If n = m, then the nanotubes are called an "armchair", which describes one of the two confirmations of cyclohexane which is a hexagon of carbon atoms. Otherwise, they are called "helix", where the value of m lies between herringbone frames and an armchair. The word "helix" means a coil, and it indicates that the tubes may be bent in any direction [202]. Figure 25, shows a diagram of the single-wall carbon nanotube.

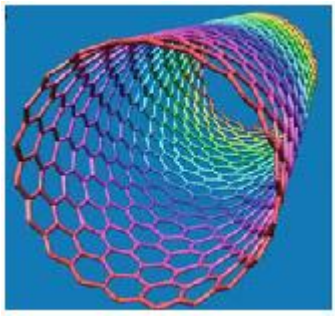

Figure 25. Single walled Carbon Nanotube [203]

Multi-Walled Carbon Nanotubes (MWNTS)

There are two models that can be used to describe multi-walled nanotube structures. In the Russian dummy model, the graphite plates are arranged in concentric cylinders, for example, a single wall nanotube (SWNT) inside a single wall nanotube. In the parchment model, a single sheet of graphite is wrapped around itself, in the form of a scroll of parchment or newspaper that is wrapped. The interlayer distance in the multi-walled nanotubes is close to the distance between the two layers of graphite in graphite, about 3.3 (330 m). The special place of double-walled carbon nanotubes (DWNT) should be emphasized here because their shape and properties are similar to SWNT but their resistance to chemicals has been greatly improved. This is particularly important when the function is required (that is, grafting chemical functions onto the surface of the nanotubes) to add new properties to the CNT. In the case of SWNT, the covalent function will break some of the C = C double bonds, leaving "holes" in the structure on the nanotube and thus modulating its mechanical and electrical properties. In the case of DWNT, only the exterior wall is modified. The synthesis of DWNT on the Gram scale was first

proposed in 2003 by the CVD technique, from the selective reduction of oxide solutions in methane and hydrogen [204]. Figure 26 shows the representation of double-walled nanotubes (DWNT) and multi-walled nanotubes. And Table 8 shows a comparison between SWCNT and MWCNT.

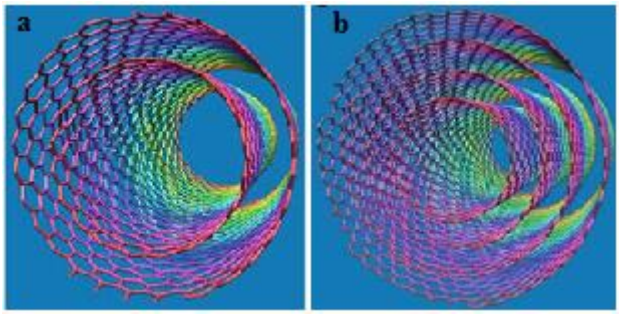

Figure 26. Representation of a- Double-wall Nanotubes (DWNT) and b - Multiwalled Nanotubes [203]

Table 8. Comparison between SWCNT and MWCNT

SWCNT	MWCNT
Single layer of grapheme	Multiple layer of graphene
Catalyst is required for synthesis	Can be produced without catalyst
Bulk synthesis is difficult as it requires Bulk synthesis is difficult as it requires atmospheric condition	Bulk synthesis is easy
Purity is poor	Purity is high
A chance of defect is more during Functionalization	A chance of defect is less but once occurred it‘s difficult to improve
Less accumulation in body	More accumulation in body
It can be easily twisted and are more pliable	It cannot be easily twisted

Single-Wall Carbon Nanohorns (SWCNH)

It was first reported by Harris et al and Iijima et.al. [205] Single-walled carbon horns (SWCNHs) are single-walled horn-shaped tubes with a conical tip. [206] The primary advantage of net dissolved solid waste is that no synthesis catalyst is required, so high purity materials can be produced. Its high surface area and excellent electronic properties led to

promising results for its use as an electrode material for storing energy. [207]. Currently, SWCNH has been widely studied for various applications, such as gas storage, absorption, catalyst support, drug delivery system, magnetic resonance analysis, electrochemistry, application of biosensing, photoelectric cells and photoelectrochemical cells, phototherapy, fuel cells, etc [208, 209, 210]. Figure 27 shows the representation of carbon nanohorns.

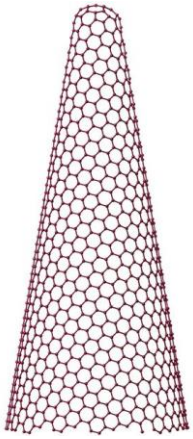

Figure 27. Representation of Carbon Nanohorns [Source wikipedia]

II.4.2 **Methods of Productions of Carbon Nanomatterials**

Recently, the emerging need for high-speed electronics and renewable energy has spurred scientists to discover, develop, and assemble new classes of NMs in unconventional device structures. Among these materials, CNMs have received special attention due to their exceptional structure and physical properties. Carbon nanotubes are perHAPs the most widely researched nanomaterial due to their thermal, electrical, and mechanical properties. They discovered in 1991, and their promise to be a super material with endless applications is still under investigation. While the potential of NMs, such as CNTs, is still being investigated, there is a lack of technologies to exploit their unique properties. In particular, there is a necessity to connect NMs with small scale and machine platforms. Combination methods such as arc vacuum [211, 212], laser ablation [213, 214], pyrolysis [215, 216], and many types of chemical vapor deposition (CVD) (217, 218, 219, 220) provide different methods for producing CNMs. CVD is a versatile method for producing high-quality carbon nanotubes by pyrolysis in the steam phase of carbon-containing gas (C2H2, CO, hexane, CH4) with metallic nanoparticles or volatile metal compounds such as iron phthalocyanine, nickel phthalocyanine, or ferritin. These

organometallic compounds serve as the basis for both the catalyst and the carbon. Usually, the pyrolysis of metal NPs or organometallic compounds is performed in an Ar / H2 environment at a high temperature in a quartz tube. It is believed that upon thermal decomposition of organometallic compounds, it is the metallic particles that first begin to form on the surface of the substrate. As more metal particles collect, the size of the catalytic center increases. Once the catalytic center reaches the optimum CNT core size, the dissolved carbon precipitates in the form of CNTs. The hydrogen present in the CVD process increases the production of CNTs [221]. It was also found that, in the presence of sulfur (from thiophene), the yield of SWNTs could be greatly increased and the filament of SWCNT could grow [222, 223]. The advantages of CVD were the possibility of continuous production at a large scale, low temperature, and controllability. The CVD method is commonly used to produce both SWCNTs and MWCNTs [224, 225, 226, 227]. The fitting of carbon nanotubes by the universal CVD method is of great interest due to its ability to be easily modified and expanded in terms of quantities produced. The challenge for the CVD method lies in the many variables involved, which can have dramatic effects on the material produced [228, 229]. The use of metal NPs as a catalyst for the CVD process is of great interest due to a large amount of commercially available particles and the low concentrations of particles in the solution required facilitating the growth of carbon nanotubes. The use of thin films and nanoparticles as catalyst sources is a well-documented method for providing a catalyst for the synthesis reaction [230, 231]. The success of CVD as a foolproof method for producing high-quality commercial carbon nanotubes requires a complete and effective study of all growth parameters related to a given synthesis setup [232, 233]. Classically manufacturing CVDs for CNTs needs high temperatures (up to 900 ° C) and processing windows over 100 minutes, most of which is attributed to the manufacturing process and cooling of the manufacturing room. This high-temperature technology provides direct, non-conductive installation of carbon nanotubes for most electronics and such microelectromechanical systems (MEMS). Attempts to reduce synthesis temperatures using plasma-enhanced chemical vapor deposition have resulted in nanostructure growth temperatures as low as 120 ° C [234, 235]. However, to produce high-quality tubes, relatively high temperatures are required. Local tuning can avoid these pitfalls, making it easier to integrate CNMs into only preferred regions leaving the rest of the device platform unaffected.

Research studies on graphene have grown enormously in the past few years. The great interest in graphene arose from the unique linear dispersion of the bond at the Fermi level, giving the growth to new physical properties. GO is widely recognized as a promising material in a diverse field, although its composition and structure have not been fully controlled. General approaches have been developed to control the degree of oxidation of graphene materials in two ways: graphite oxidation via KMnO4 in sulfuric acid to GO and reduction of GO by 80% (v / v) hydrazine (rGO) hydrate.

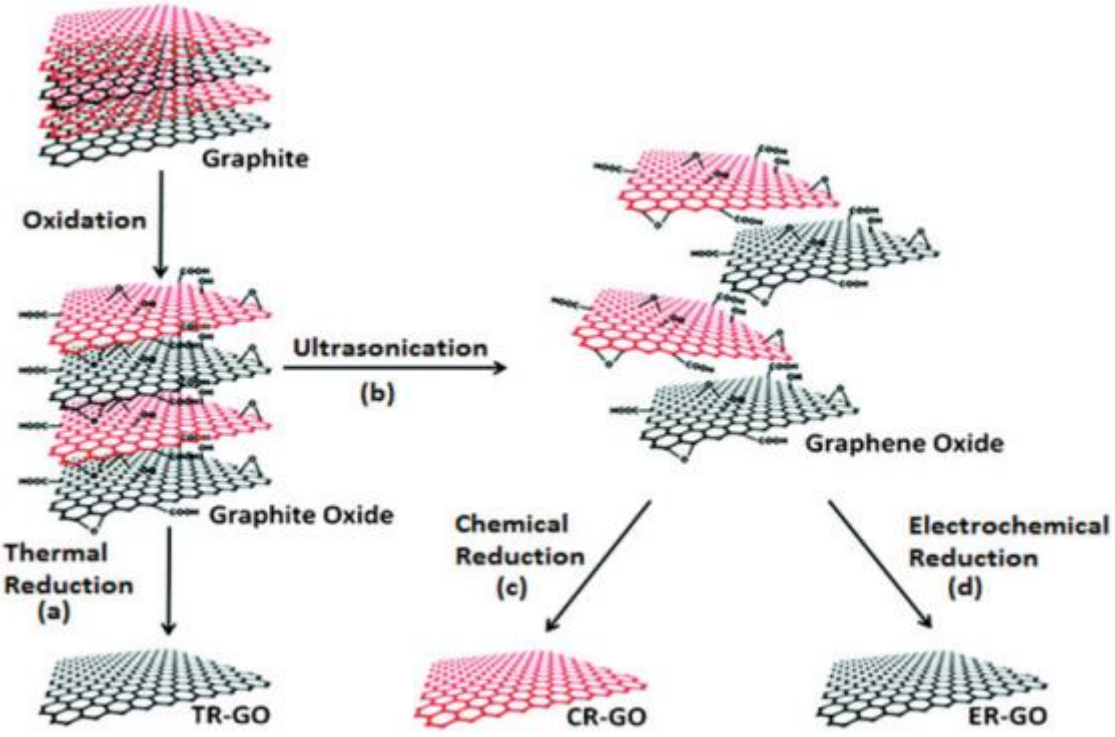

Figure 28. Schematic representation of chemically modified graphene synthesis [107].

Although the oxygen content in rGO may be the same as in GO, both have different properties such as electronic conductivity, oxidative capacity, and adsorption capacity. These differences arise from the difference in the type of defect in the graphene sheets and the graphite core structure. It was announced that rGO with 23.1 wt% oxygen showed the best behavior as an electrode for a double-layer electrode capacitor. Thus, the isolation of a single layer of free-standing graphene from thermally oriented graphite, this achievement astonished the scientific

community to study free-standing graphene for the first time by Novoselov and C. [236] Figure 28 shows a schematic diagram of the composition of chemically modified graphene. Nano-graphene (GNRs) is one of the recent discoveries in the field of CNMs. A typical GNR is a thin, stretchy strip of monolayer carbon. Recently, attempts have been made to form nanotubes by controlling the lateral dimensions of graphene, as its electronic properties depend on the width and edge type [237, 238].

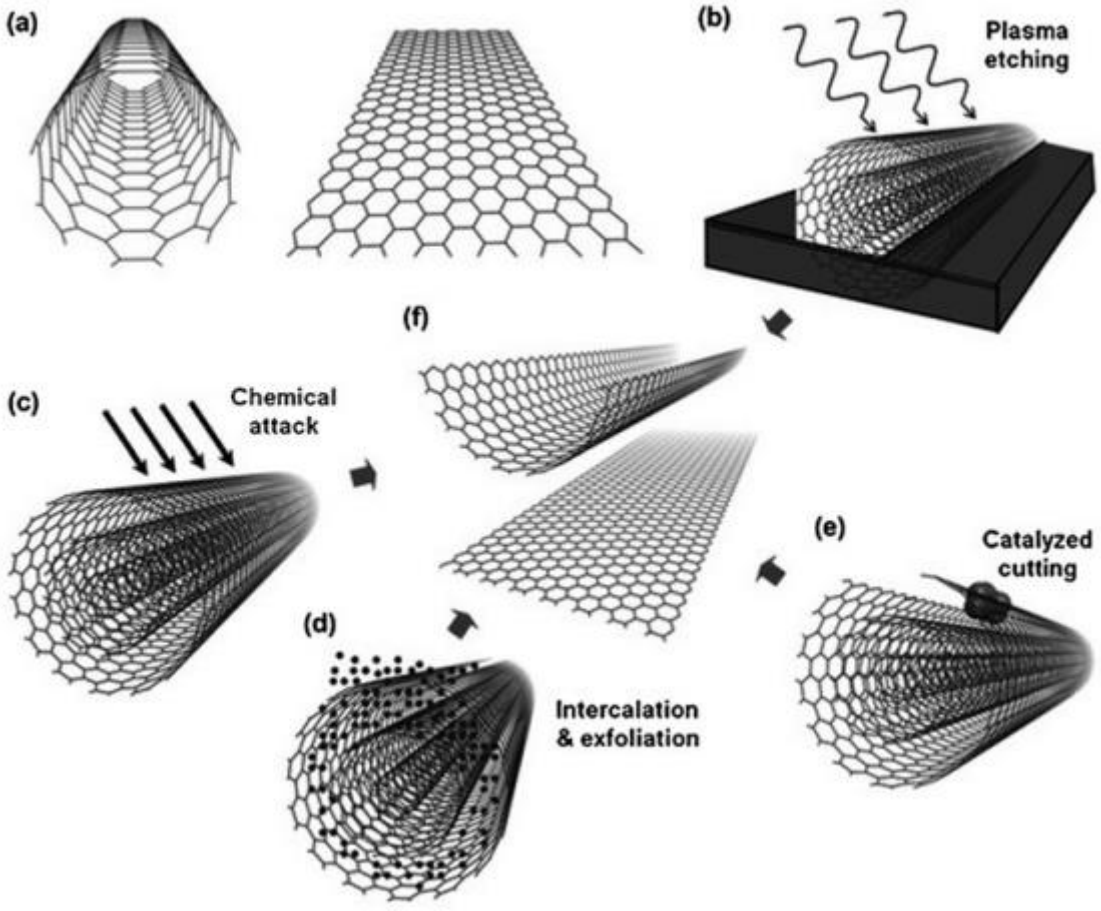

Figure 29. Schematic presentation of various methods to fabricate GNRs by unzipping CNTs [243].

Carbon nanotubes (CNTs) are GNR wrapped with slight perturbations. Over the past twenty years, studies have been concerned with the synthesis, separation, and control of reproductive symmetry and the metallic/semiconducting nature of carbon nanotubes [239, 240]. Moreover, over the past few years, several methods have been successfully developed for decompression of carbon nanotubes longitudinally and subsequently synthesizing a large amount of well-

symmetric GNRs [241, 242] (Figures 29 and 30), including cutting metallic nanoparticles, Oxidation and reduction, plasma etching and sonication [112, 115]. When considering the methods available to synthesize GNRs, factors governing growth and formation can be interrelated and are common among the various synthetic methods [110, 116, 117].

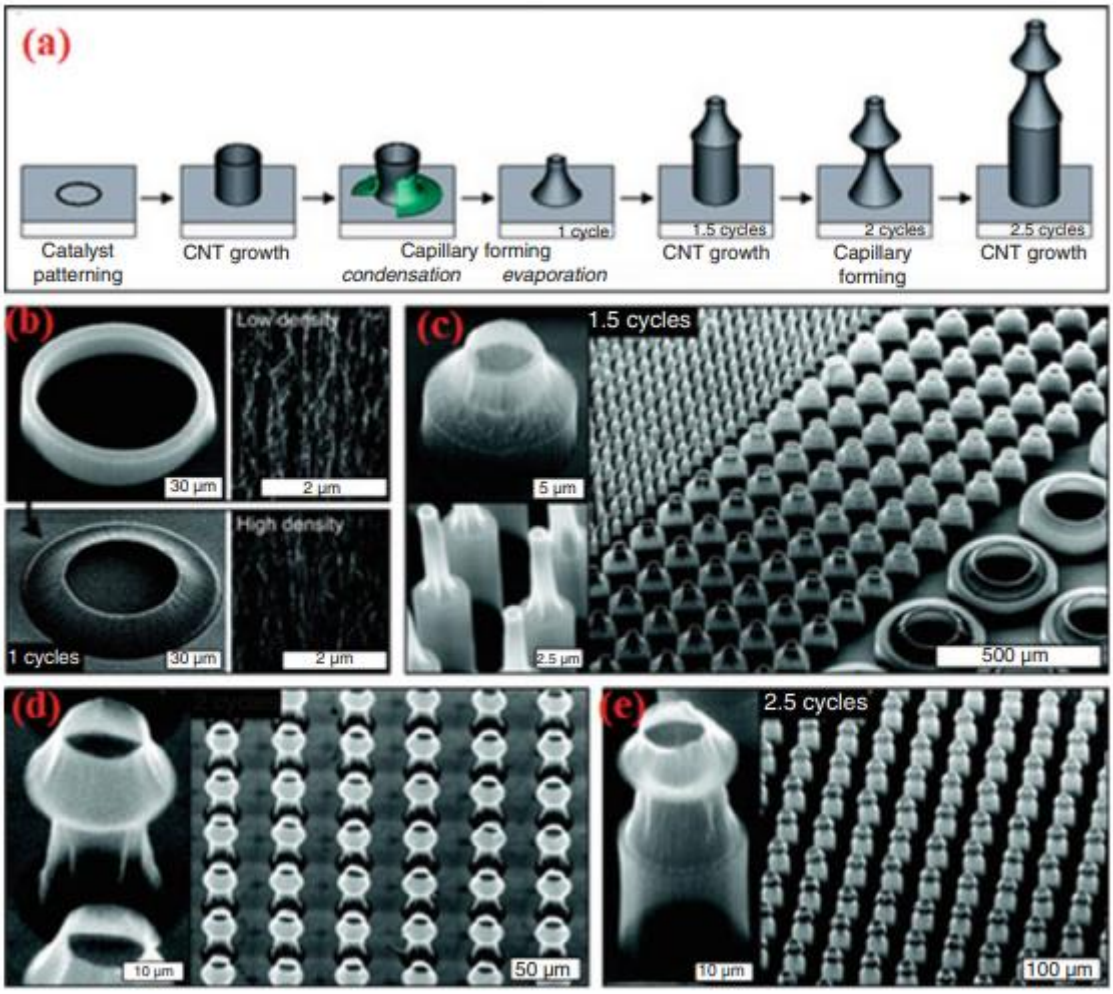

Figure 30. Fabrication of cylindrical CNT microbellows by iteration of growth and capillary forming [243].

II.4.3 **Functionalization of Carbon-Based Nanomaterials**

Thanks to their properties, the potential applications of carbon nanotubes cover areas such as vehicles, electronics, field emissions, energy, and nanomedicine. For many of these fields, nanotubes need chemical modification by bringing new functions to their surfaces. Thus, for the manufacture of composites based on carbon nanomaterials, the function, in particular the

covalent function helps disperse the nanotubes in a polymer matrix for example. Nanotubes, thanks to their nanometric dimensions, can act as carriers of molecules to guide drugs.

The job description also makes it possible to group donor-recipient groups, to separate or even sort the nanotubes according to their metallic or semiconducting nature. These chemical modifications make it possible to visualize the manufacture of organic or hybrid solar cells, from transistors. However, the properties of the nanotubes must be preserved, which is not often the case with the covalent activation techniques developed thus far.

Carbon atoms in nanotubes are great at forming covalent bonds with other types of atoms for a number of reasons: Carbon atoms have a natural ability to form covalent bonds with other elements due to a property called electronegativity. Electronegativity is a measure of how strong an atom holds the electrons that are spinning around it. The electronegativity of carbon (2.5) lies in the middle of the electronegativity range of substances ranging from potassium (0.8) to fluorine. Since carbon has electronegativity in the middle of the band, it can form stable covalent bonds with a large number of elements.

- All the carbon atoms in the nanotubes are present on the surface of the nanotube and thus can be accessed by other atoms.
- The carbon atoms in the nanotubes are only bound to three other atoms, so they have the ability to bind to a fourth atom.

These factors make it relatively easy to bind to a variety of atoms or molecules with the nanotubes, which alters the chemical properties of the nanotube. (This method is called a Functionalization) If we take this bonding further, if the molecules attached to the carbon nanotubes are also bound to the carbon fibers, then the functional carbon nanotubes can bind to the fibers in the composite, resulting in a stronger material [244]. Covalent activation in CNMs is dependent on interactions with skeletal-binding CNMs that contain oxygen. The covalent function of CNMs can also be used to synthesize graphene-based sheets by improving the heat distribution performance [245]. The non-covalent function uses different functional molecules or active species as aggregating media to activate surface CNMs via non-covalent interactions [246, 247, 248]. The most complex method for the chemical use of jet waste is to introduce carboxylic acid groups (-COOH) to the surface by an oxidation process that uses concentrated acids such as H_2SO_4, HNO_3, HCl, or with H_2O_2, or an acidic mixture [249, 250].

II.4.4 **Applications of carbon nanomaterials**

CNM, in particular, 1D and 2D, is known for its remarkable mechanical strength: its measured toughness and flexibility is greater capital than financially manageable high-strength materials (for example, high tensile steel and carbon fibers). However, the option to incorporate 1D and 2D CNM into polymer compounds as super-strong carriers has not been filled with acceptable results, largely due to their insufficient interaction with the surrounding matrices. Modern M research endeavors have been directed towards integrating 1D and 2D CNMs within different materials in order to take advantage of their multi-process nature (i.e., electrical and thermal conductivity, and optical properties) rather than focusing solely on composite mechanical strength. For example, the salient electrical properties of 2D and 2D CNMs combined with their nanoscale dimensions are of surprising importance in electronics for building nanocircuits [250, 251]. Besides, 1D and 2D CNMs are known to take on low threshold electric fields for field emission, compared to other common field emitters. Thus, 1D and 2D CNMs exhibit strong field-emitting brilliance, which can be used in lighting elements. CNMs have revealed a huge interest in a myriad of apps. CNMs are chemically altered to introduce specific moieties (for example, actuation groups, atoms, and polymers) to impart properties suitable for biological applications such as. These clefts can bring about some improvements such as improved material compatibility, cellular sensitivity, increased solubility, biocompatibility, and cellular sensitivity [252]. Its applications include cell and tissue labeling agents, injectable drug delivery systems, and biomaterial auxiliaries.

Electrochemical Biosensors

CNMs are favorable for electrochemical sensors because they increase the electrically active surface area, enhance the absorption of particles, and enhance electron transport. CNMs 1D and 2D were incorporated into electrochemical sensors for biomolecules, and the methods included traditional dip-and-drop coating methods. New research has also been concerned about the use of several new types of CNMs in sensor applications. Various forms of graphene are used for sensor applications; These include rGO microbilts [253], graphene nanofoam, graphene nanoscale disks, and graphene nanoscale flowers [254, 255, 256]. Electrochemical sensors were used because they seemed to be a simple, cheap tool for sensing a variety of biological

compounds. Graphene-based electrochemical sensors have been reviewed by researchers covering a wide range of biological analyzes and approaches [257].

Drug Delivery System

It has greatly benefited from advances in nanotechnology using a variety of NMs (i.e., liposomes, polymers, nanospheres, and polymer bonds) as vectors for transferring therapeutic agents as shown in Figure 31.

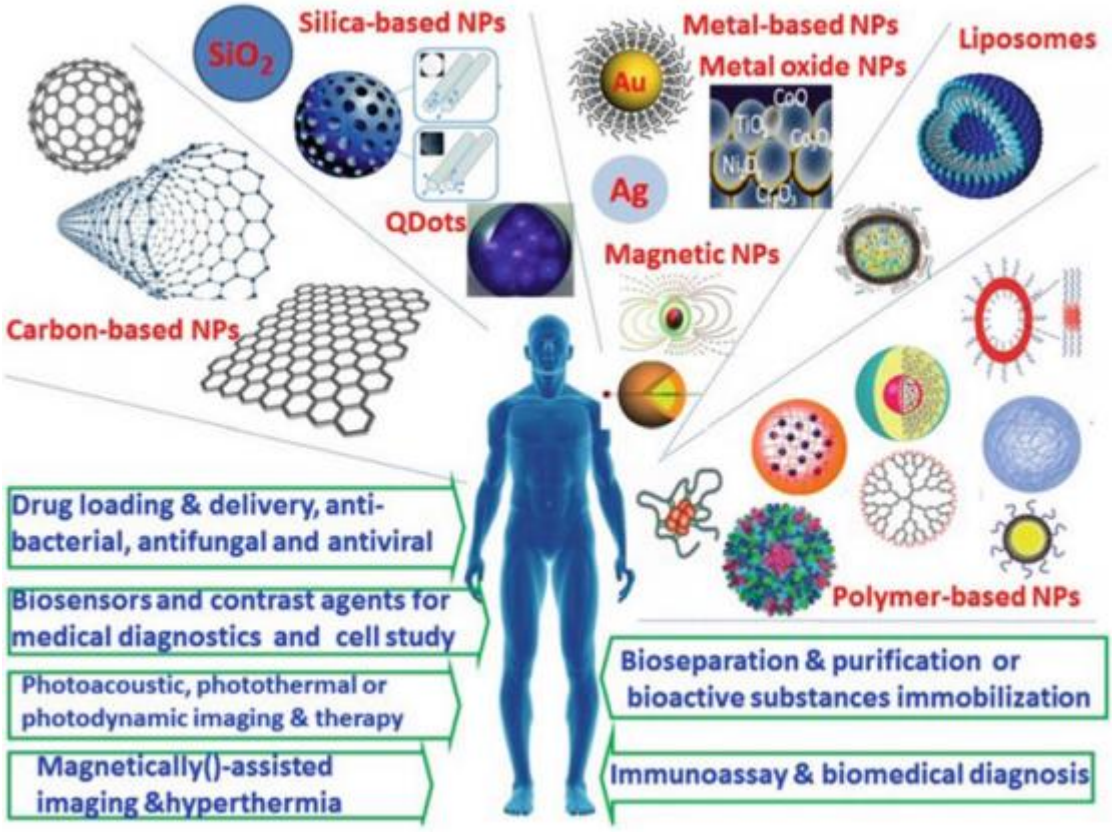

Figure 31. Some examples for biomedical applications of carbon nanomaterials [259].

. Also, the CNM products have been subjected to extensive research as drug delivery systems, as they have been shown to interact with many biomolecules (ie proteins and DNA) through physical absorption. In addition, therapeutic molecules or covalently targeting molecules have been linked with CNMs via several chemical modifications [258]. In an interesting study, Zheng et al provided great insight into the interactions between DNA molecules and CNTs.

Spectroscopic and microscopic analyzes gave evidence for steady, stable interactions between DNA molecules and CNTs, resulting in individual scattering.

The molecular dynamics modeling showed that there is a helical wrapping of ssDNA chains around the CNT due to the binding of a single-stranded DNA base (ssDNA) to the CNT surface via π–π stacking (Figure. 32).

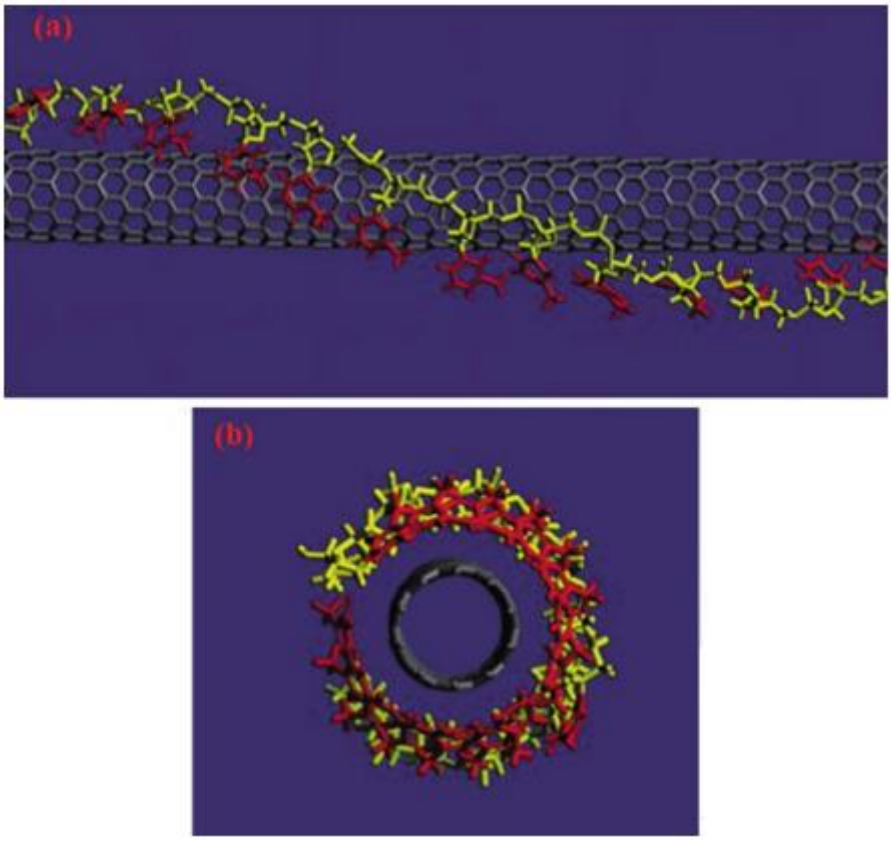

Figure 32. Binding model of CNT with DNA sequence [262].

As with CNTs and CNFs, several biomedical applications have been studied including injectable cellular labeling agents, drug delivery systems, and scaffold reinforcements using graphene and GO [260]. Drug-loaded FA-GO showed an increase in cancer-targeting ability and anti-cancer activity compared to drugs carried with unmodified GO. Sun et al, demonstrated too that conjugated GO (polyethylene glycol) can be used with targeting molecules as a cellular sensor using GO's intrinsic luminescence feature in the near-infrared field. In different paper, Zhang et al, combined GO with (polyvinyl alcohol) hydrogels to improve its mechanical strength [261].

Electronic Devices

The component materials used in electronic devices have been developed from classic hard chips to soft electronics over the past 30 years (Fig.33). At present, many challenges are trying to overcome before the practical use of materials available to manufacturers of electronic devices such as amorphous silicon (a-Si), low-temperature polycrystalline silicon (p-Si), semiconducting metal oxides, nanowires, and organic semiconductors. For example, a-Si is cheaper and can be applied to large displays but suffers from poor mobility and flexibility. The low temperature of p-Si has the advantage of relatively high mobility but low uniformity and low processability [263]. Metal oxides are of high cost due to their deficiency of rare earth elements and their poor environmental stability. Polymers have great bending ability but are deprived of movement and chemical stability. CNMs such as 1D CNTs and 2D graphene layers have been extensively explored to present a new technology based on flexible electronics requiring bendability, high mobility, and high transmittance [264, 265, 266]. High-quality SWCNTs are of interest to transistors due to their low electron dispersion and their beamwidth dependent on the screw diameter and angle. Moreover, SWCNTs are compatible with a high-grade field-effect transistor (FET) and CNT architectures PEN (125 μm) Ti / Au (10/150 nm) Ti / Au (10/100 nm) Al2 / O3 (40 nm) line bit NRAM cell 10mm Au-coated high power amplifier CNT line electrode source (a) (b) Flexible TFT memory (c) (d) Electronic linking of CNT film CNT forest CNTs thermal interface CNTs Word line DSSGD Figure. 34, CNT applications in microelectronics. (A) Flexible TFTs utilizing CNT networks deposited by CVD aerosol. (B) A CNT-based non-volatile random-access memory (NRAM) cell fabricated with spin coating and CMOS-compliant CNT solution etching. (C) The 150nm CMOS-compatible vertical interfaces developed by Imec and Tokyo Electron Limited. (D) CNT bumps used to improve heat dissipation in high power amplifiers [266]. (Copyright 2013, Science) A broad family of carbon nanomaterials: classification, properties ... 23 dielectric materials [267, 268]. In 2012, SWCNT-FETs with channel lengths less than 10 nm exhibited a normal current density (2.41 mA mm 1 at 0.5 V), which is significantly greater than that obtained for silicon devices [269, 270]. CNT thin-film transistors (TFT) are particularly interesting to lead in organic light-emitting diode (OLED) displays because they have higher mobility than amorphous silicon (about 1 cm^2 V1 sec) [271]. Flexible CNT-TFTs with a mobility of 35 cm 2 V1 s and an on / off ratio of 6 are illustrated in Figure. 34a [272, 273]. The International Semiconductor

Technology Roadmap proposes that carbon nanotubes could replace copper in microelectronic junctions, due to their low dispersion, high ability to withstand current, and resistance to electrical migration. In the end, the concept of non-volatile memory relying on the electromechanical transposition of individual CNTs for marketing (Figure. 34b) was changed by the modeling of interlocking thin-film CNTs as functional bases. Complementary metal oxide (CMOS) semiconductors were generated - compatible with a diameter of 150 nm (Figure. 34c) with a single CNT contact hole resistance of 2.8 kOhm on chips with a full 200 mm diameter. Also, CNT bumps used to improve heat dissipation in high-power amplifiers, carbon nanotubes can act as an electrical connection and heat dissipators for use in high-power amplifiers (Figure. 34d).

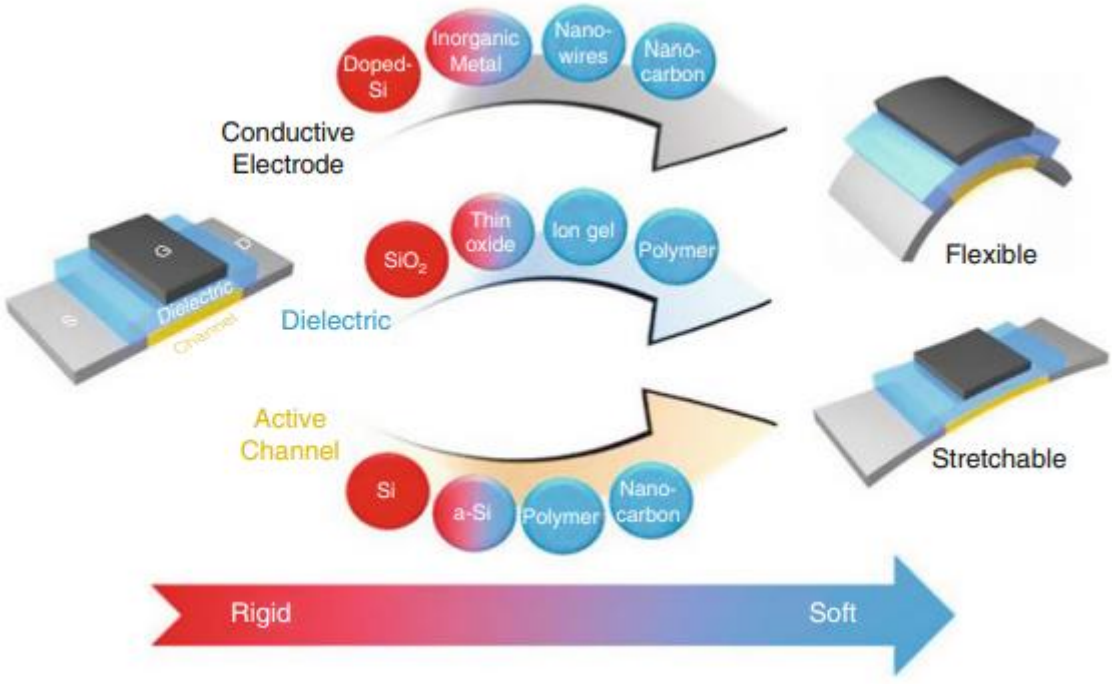

Figure 33. Classification of materials from rigid to soft [274].

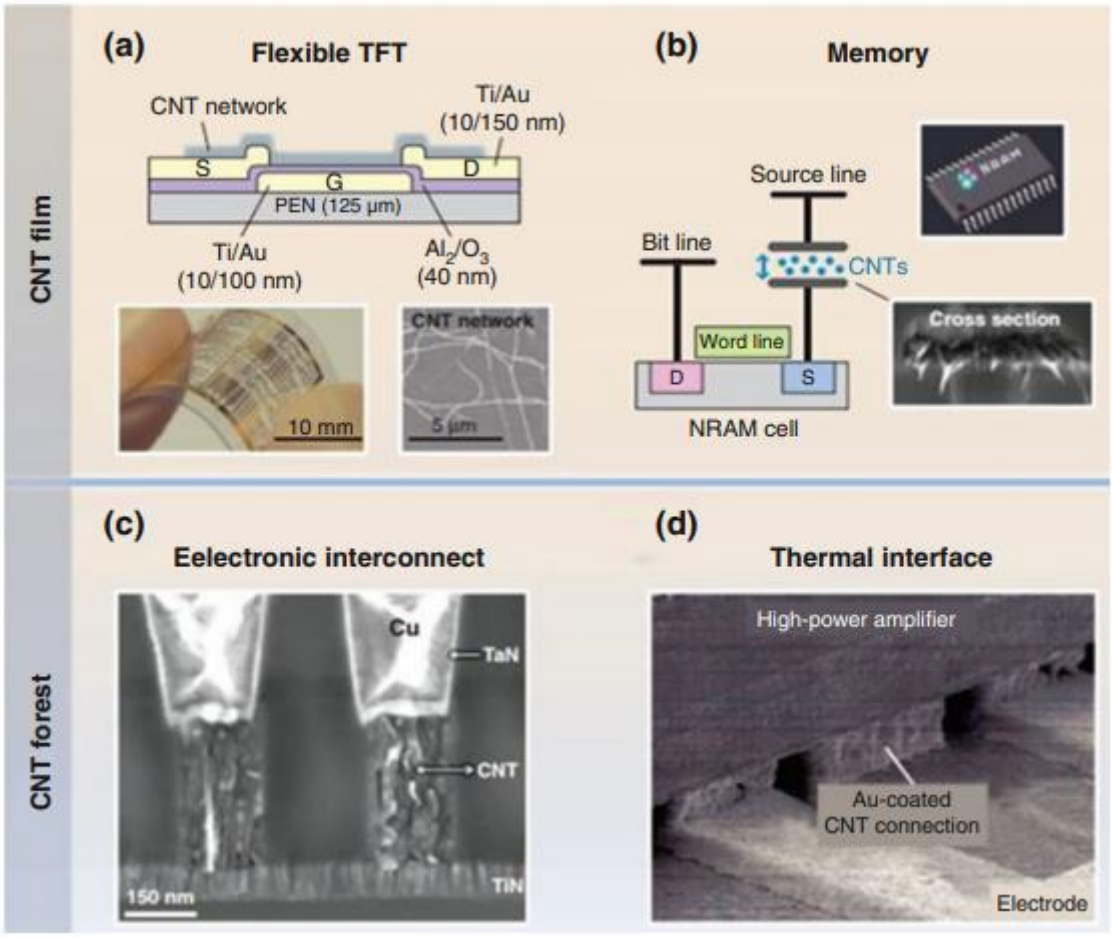

Figure 34. CNT applications in microelectronics. (a) Flexible TFTs using CNT networks deposited by aerosol CVD (b) CNT-based nonvolatile random-access memory (NRAM) cell fabricated by using spin-coating and patterning of a CMOS-compatible CNT solution. (c) CMOS-compatible 150-nm vertical interconnects developed by Imec and Tokyo Electron Limited. (d) CNT bumps used for enhanced thermal dissipation in high power amplifiers [275].

Environmental Protection and Improvement

CNMs can be used as liquid nanoscale absorbents along with gas-phase adsorption of environmental pollutants due to their special nanoscale adsorbent properties (such as high surface area and low particle size resulting in large numbers of active adsorption centers). CNMs have been widely used as effective adsorbents for removing contaminants (dyes and metal ions). For example, MWCNTs were run on the surface with Fe_3O_4 nanoparticles and showed a boundary absorption performance towards Hg (II) (as a heavy metal ion model) with a high adsorption capacity of 238.78 mg / g1 [276]. In addition, when ZnO nanoparticles were loaded on the surface of MWCNTs, they showed a high ability to remove dyes from aqueous

solutions (Congo red dye with an absorbance capacity of 249.51 mg / g and a removal rate of 99.8%) [277]. Among the CNMs, CNFs, CNFs, and graphene it receives the most attention due to its unique properties, which include thermal conductivity, electrical conductivity, chemical stability, and tensile strength. The concept of using CNTs, CNFs, and graphene for water filtration has been proposed by research focusing on their use as nanofilm filters for selective water transport. Recent research on the use of carbon nanotubes and graphene-based membranes as improved adsorbents to isolate contaminants from water has shown encouraging results [278] (Figures 35 and 36). SWCNTs and MWCNTs are the two primary forms of carbon nanotubes. Each one is effective absorbents for specific chemicals.

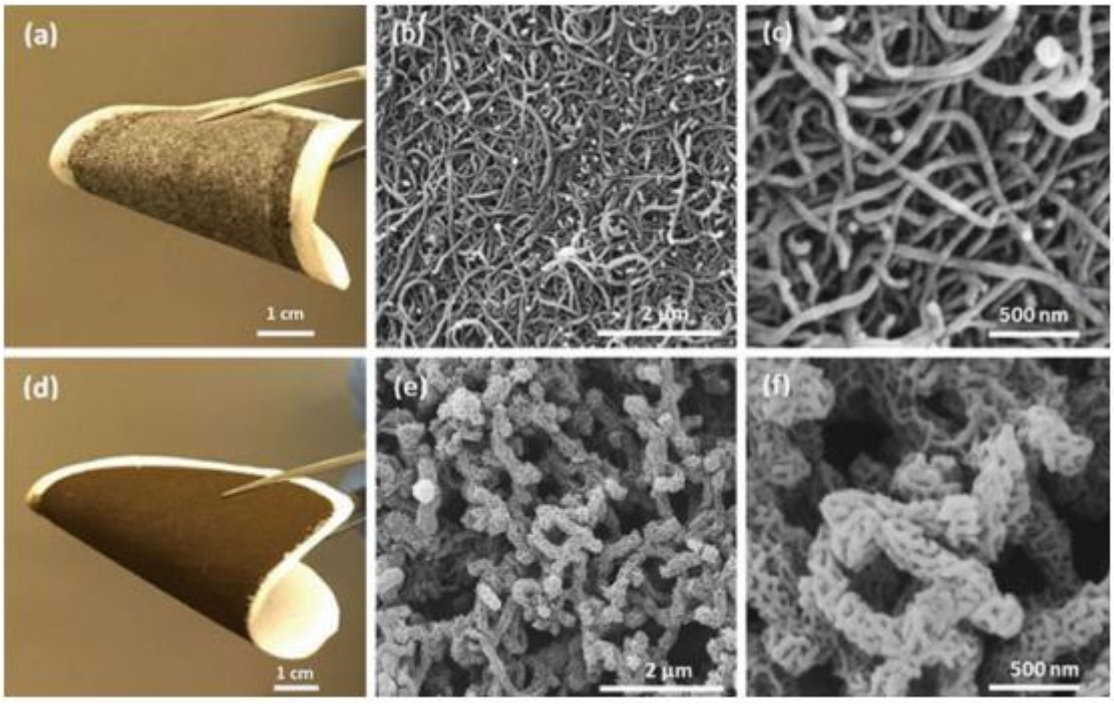

Figure 35. A novel architecture for CNTs-membranes towards fast and efficient oil/water separation: (a) Photo of membrane based on MWCNT/cellulose microfibers. (b) and (c) SEM images of MWCNT coated membrane. (d) Photo of membrane based on MWCNT-MnO_2/cellulose microfibers. (e) and (f) SEM images of MWCNT-MnO_2 coated [279].

While advances in self-supporting ceramic nanofibre mats remain a challenging problem due to the intrinsic fragility of the material, CNF sheets of a large area with amazing mechanical properties can simply be made. At the entrance, its high chemical resistance, compared to polymeric filters, makes it suitable for filtration [281, 282].

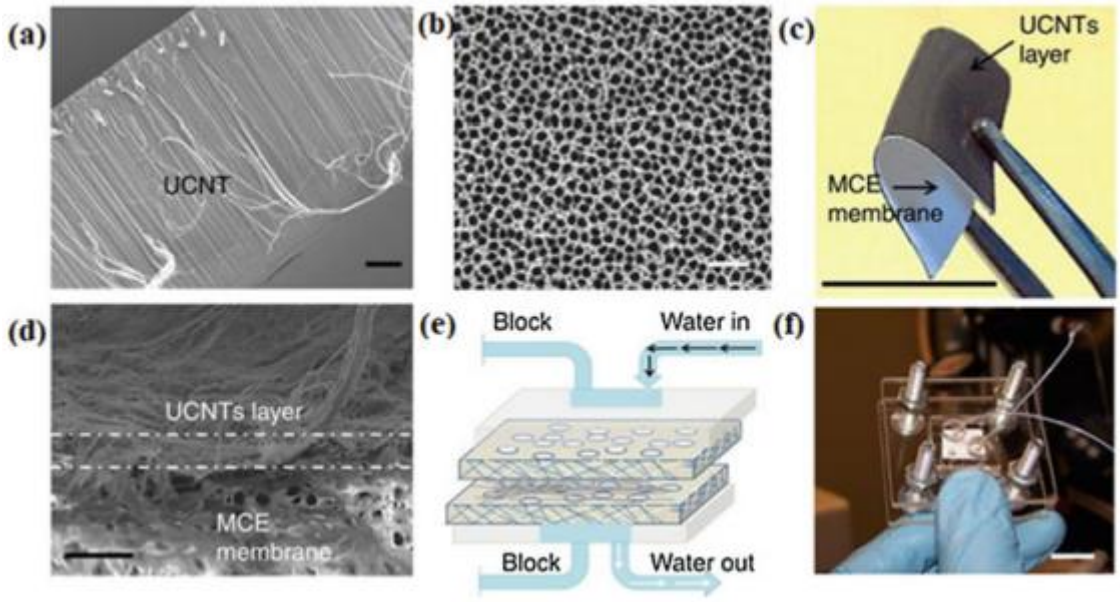

Figure 36. Carbon nanotube membranes with ultrahigh specific adsorption capacity for water desalination and purification [280].

Various studies on graphene for water purification have focused on nanofiltration of graphene sheets as filter membranes. To be used for water purification, graphene is generally changed to GO via acid treatment. The oxidation of graphene leads to the introduction of a large number of hydrophilic oxygen-containing groups crosswise on the graphene sheet, including the hydroxyls and epoxides. The deeper effect of chemical modification is to increase the flow of water through the GO materials due to the increased water resistance, which enables the formation of membranes with more water flow and permeability.

Energy Production and Storage

CNMs (CNTs, CNFs, and graphene) have been studied for a wide range of applications in energy conversion systems, such as solar cells and fuel cells (Fig.37). Each type of carbon material has its advantages and disadvantages. For example, CNT and CNF tubes are a good choice for increasing the energy density of electrochemical capacitors (ECs) due to their excellent electrical properties and exceptional tube-like porous structure facilitating ion diffusion. However, high manufacturing costs greatly limit more comprehensive applications. Graphene has the virtues of high surface area and high conductivity, but it can be easily restored

during preparation. Three-dimensional carbon materials are emphasized due to the high surface area and rich pore structures.

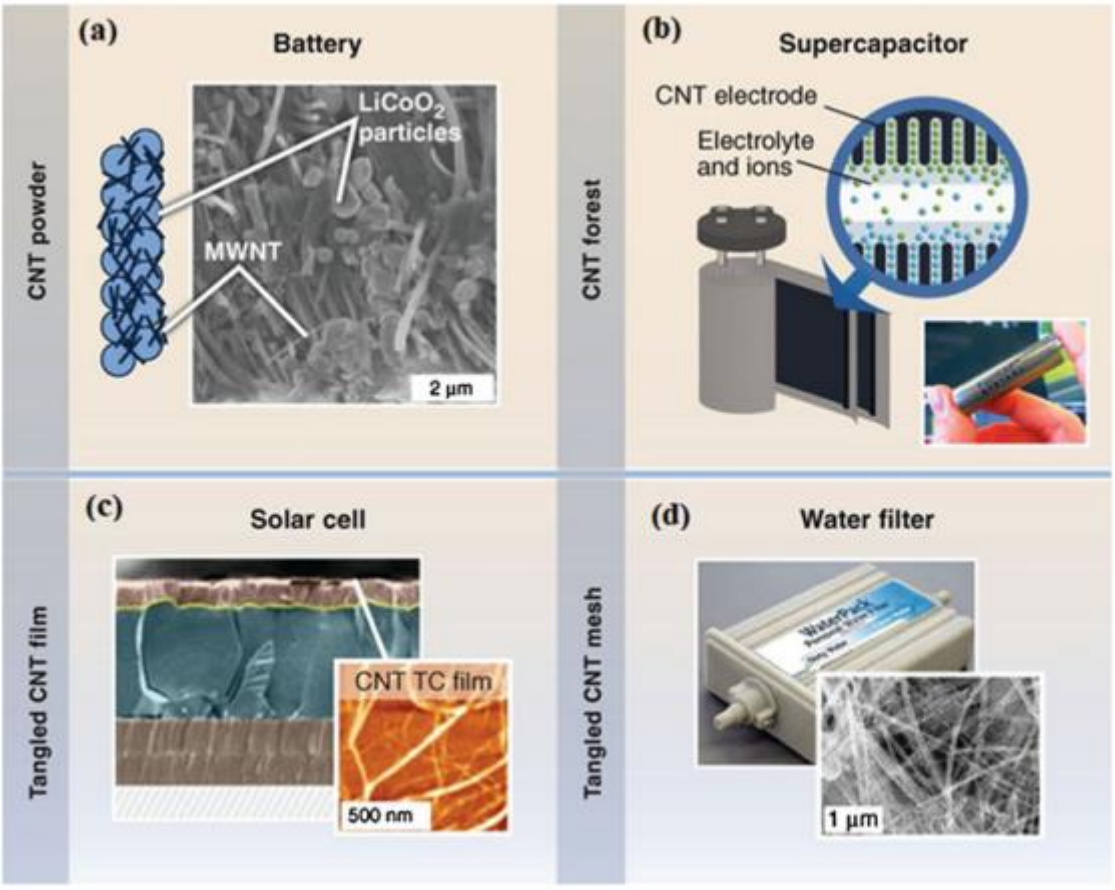

Figure 37. Some applications of CNTs in energy production, energy storage, and water treatment [283].

However, the specific capacitance is largely determined at a high current density due to its fine pores and relatively low conductivity. Onion-like carbon can be completely available to ions, resulting in exceptional performance, but limited capacity (~ 30 F / 1) [284]. Due to recent advances in CNM synthesis and management, functionalism, and self-assembly technologies, energy storage performance has increased significantly [285, 286]. CNMs have been applied to produce electrical capacitors. An energy storage mechanism (electric double layer) using this material allows for a fast charge or discharge rate and excellent cycle stability. The porous carbon nanoparticles and nanostructures were recycled from agriculture waste using a simple, catalytic-free pyrolysis process. The material obtained shows excellent ultra-high capacity performance due to its porous nature. However, its energy density is lower than that of

pseudocapacitors (metal oxide and conductive polymers) where the charges are stored or released through redox reactions that occur at or near the surface of the electrode material. Therefore, the combination (hybridization) between CNMs and pseudo-capacitance materials (metallic oxides or conductive polymers) provides an efficient solution to achieve high capacitance and extremely stable supercapacitor. For example, the in situ rGO nanostructures were prepared as a nanocomposite with MnO_2 nanoscale flowers using a one-step electrochemical approach. The hybrid nanocomposite exhibits a high specific capacity of 473 ° F and high stability of 95% which is significantly higher than that reported for pure rGO and MnO2. This is because the 2D conductive pathway for rGO enables a fast and reversible redox reaction for MnO2. For example, important studies have confirmed the full utilization of graphene's surface area. These materials have been viewed as a new generation of electrode materials for photovoltaic connections due to their high surface area (theoretically estimated at 2,630 m2 g1), adequate porosity, high electrical conductivity, wide potential windows, and rich surface chemistry [287]. Oxidation followed by reduction of GO has proven to be the most efficient method for mass production of graphene for industrial applications. After commercializing the Li-ion (LIB) battery from Sony Labs, carbon-based rechargeable batteries have received widespread attention. Here, the metallic lithium is replaced by a carbon host structure, which can reverse the lithium ions with low electrochemical potentials [288, 289]. However, there are drawbacks associated with carbon-based anode materials such as the low theoretical specific capacitance (372 mAh for graphite [290] and the capacity for low rate. Chemical doping techniques have been used to improve their performance through surface modifications [291].) Creation of phosphorous, boron, and nitrogen to develop Li-ion storage capacity arising from enhanced reaction and electrical conductivity. Fuel cells are promising candidates for clean energy conversion in the search for alternatives to conventional fossil fuel technology Noble materials, over-voltage required for oxygen reduction reaction (ORR), and degradation of electrical stimuli It is the main practical application of CNMs. Doped atoms in CNTs and graphene frameworks through theoretical and experimental studies are able to modify the electron domain structure of carbon nanostructures and thus adjust the mechanical properties and electrical stimulation activity. For example, an easy and stimulant-free method for graphene assembly has been reported. A Saturation of boron (BG) by GO thermal annealing

in the presence of B_2O_3 was performed by Sheng et al. [292]. Phase the electrophoresis in a three-electrode system using a BG or graphene-modified glass carbon electrode (denoted as BG / GCE and graphene / GCE, respectively) in an aqueous solution saturated with O_2 0.1 M KOH. Researchers recently discovered that graphene doped with elements having the same electronegativity as carbon, such as S and Se, could also exhibit enhanced catalytic activity in contrast to the commercial Pt / C catalyst in alkaline solutions [293]. However, these psychedelic carbonates usually exhibit ORR activity in alkalis but are poor in acids. To arrive at this problem, oligo-walled CNT-graphene complexes exhibiting ORR activities in both acid and alkaline solutions were synthesized [294].

II.5 Conclusion

In this chapter, we have presented a review study about HAP and its properties and different method of its production, also its technique of modification by substitution of this composition without forgetting its potential application in various fields in biomedical, energies and environmental application. As the same for Chitosan, we have presented its natural resources, method of extraction, and its properties also its important application in the biomedical field and environmental remediation. Finally, we introduced very large information about different types of carbon nanomaterials and especially Graphene, Carbon nanotubes and carbon nanohorns. We have displayed their properties, method of production, functionalization, and severals application in biomedical, energy production and storage and environmental protection. We are perceived that all presented materials provide some common properties like biocompatibility and the ability to be linked at other materials and also they have several common applications.

Chapter III:

METHODOLOGY AND TECHNICAL ANALYSIS

III.1 Introduction

This chapter is subdivided in two parts. The first part regards initially the raw materials used in this study for synthesis of the HAP nanoparticles, extraction chitosan, and finally for synthesizing Chitosan-HAP-Carbon hybrids nanoparticles.

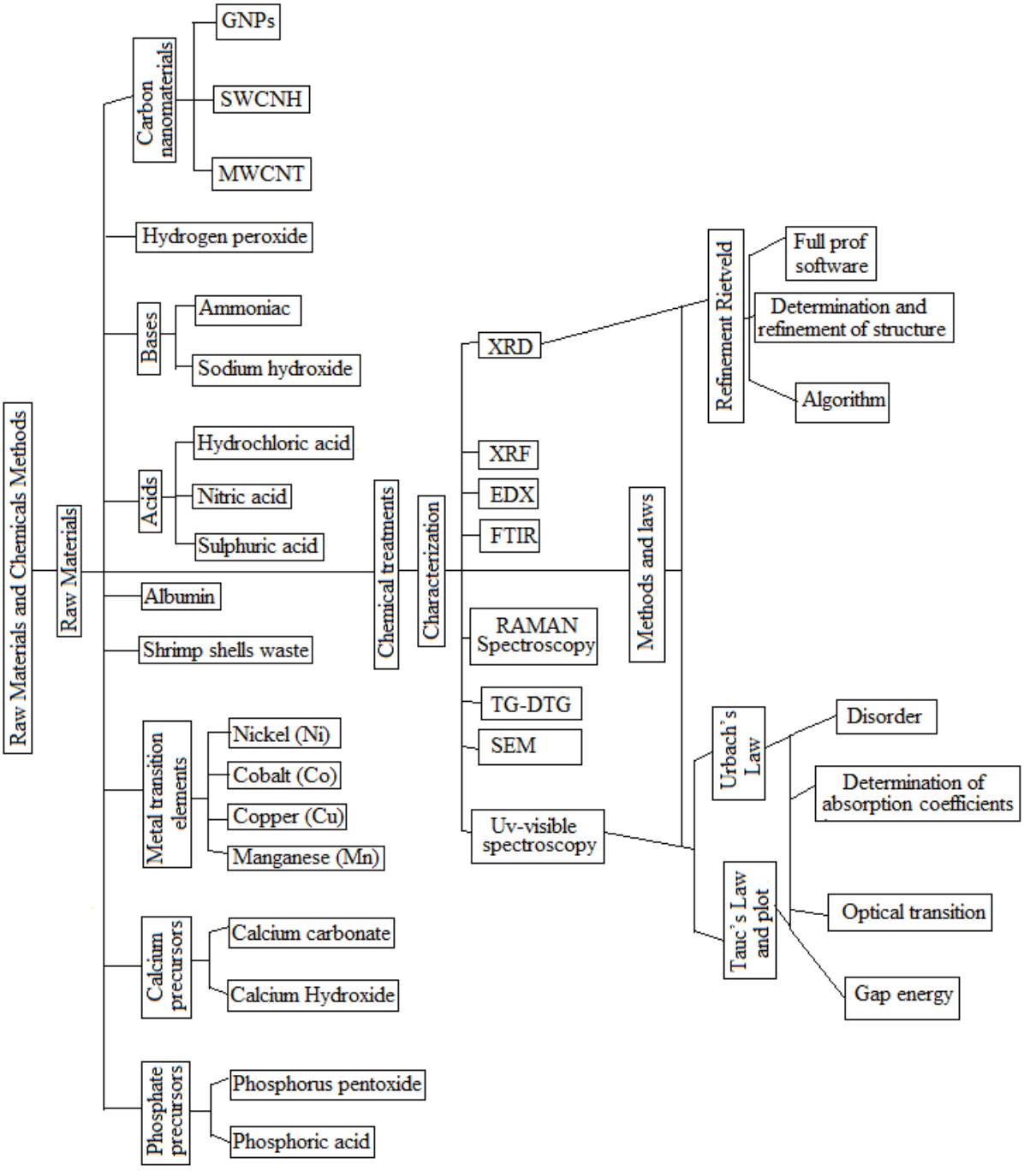

Figure 38. Schematic representation of the methodology of the study

On the next, this part exhibits the experimental methods applying for preparing samples used in this study. As for the second part, it identified the techniques of analysis and characterization used in this study, namely: X-ray Diffraction, XRF, EDX, FTIR, RAMAN Spectroscopy, TG-DTG, SEM, Uv-visible spectroscopy. The figure 38 shows a general schematic representation of the sample preparation and characterization.

Part A: METHODOLOGY

III.2 Raw Materials and Chemicals Methods

III.2.1 **Raw Materials**

- Phosphate precursors:

- Phosphorus pentoxide

Phosphorus pentoxide, or formerly phosphoric anhydride, is the phosphorus oxide long known by the formula P_2O_5 (which explains its name), but whose correct crude formula is P_4O_{10} (dimer). It is a highly hygroscopic compound which transforms into phosphoric acid by hydrating [295], because it is its anhydride. Phosphorus pentoxide is used as a very powerful desiccant, for example for the synthesis of acid anhydride from carboxylic acids according to the reaction R – COOH + R'– COOH → R – CO – O – CO – R ' + H_2O. However, it can only be used if the carbon chains R and R 'are simple enough. Indeed, during this synthesis, phosphoric acid is obtained as a by-product. In the laboratory, phosphorus pentoxide is also used as a desiccant in desiccators and for the drying of solvents extracted by heating under reflux [296]. The Figure .39, represente the structure and layrs of P_2O_5, and the Table 9 displays the chemical properties of P_2O_5.

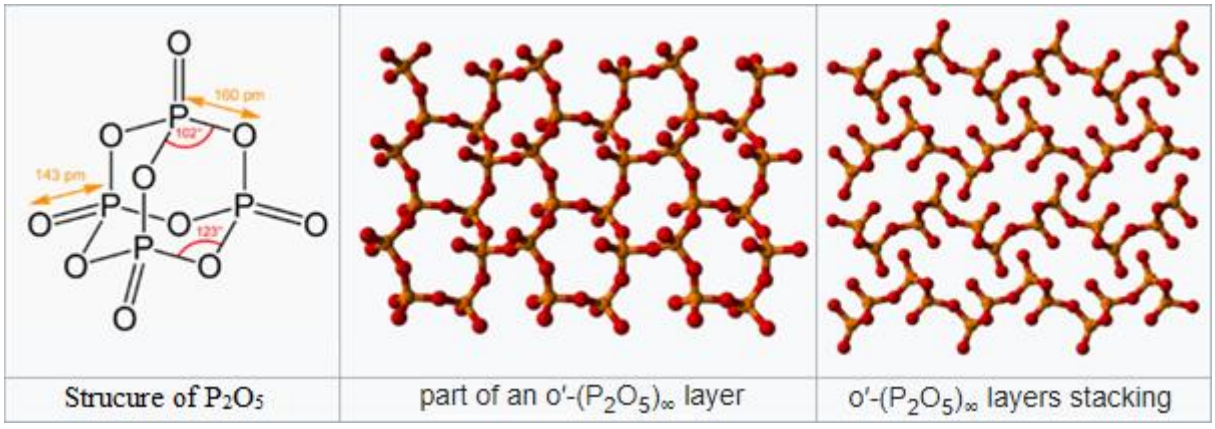

Figure 39. Representation of structure and layrs of P_2O_5 [Source wikipedia]

Table 9. Chemical properties of P_2O_5.

Chemical formula	P_4O_{10}
Molar mass	283.9 g mol^{-1}
Appearance	White powder very deliquescent odorless
Density	2.39 g/cm^3
Melting point	340 °C (644 °F; 613 K)
Boiling point	360 °C (sublimes)
Solubility in water	Exothermic hydrolysis
Vapor pressure	1 mmHg @ 385 °C (stable form)

- Phosphoric acid

Phosphoric acid is a chemical compound with the formula H_3PO_4. It is a trifunctional oxoacid (triacid) important in inorganic chemistry and fundamental in biochemistry [297]. It is a mineral acid obtained by treatment of phosphate rocks or by combustion of phosphorus.

At room temperature, phosphoric acid is a crystalline solid of density 1.83 which melts at 42.35 °C [298, 299]. It constitutes the basic raw material for the production of phosphates (or phosphate salts), via phosphogypsum slag [300, 301, 302]. The production of phosphoric acid is a source of a large accumulation of weakly radioactive waste and "Technologically enhanced natural radioactivity" [303]. In biology, the dimers and trimers of phosphoric acid are involved in m fields in biology such as energy carriers ADP / ATP, DNA and in bones [304]. Phosphoric acid is generally obtained by attack in an apatite reactor with sulfuric acid H_2SO_4 [305, 306, 307]. Apatite is often a mixture of; chlorapatite $Ca_5(PO_4)_3Cl$, fluorapatite $Ca_5(PO_4)_3F$, HAP $Ca_5(PO_4)_3(OH)$ and also carbonate-apatites where a CO_3OH or CO_3F group replace a PO_4 tetrahedron.

The reactions are therefore:

$Ca_5(PO_4)_3Cl + 5\ H_2SO_4 + 10\ H_2O \rightarrow 3\ H_3PO_4 + 5\ (CaSO_4,2H_2O) + HCl.$

$Ca_5(PO_4)_3F + 5\ H_2SO_4 + 10\ H_2O \rightarrow 3\ H_3PO_4 + 5\ (CaSO_4,2H_2O) + HF.$

$Ca_5(PO_4)_3OH + 5\ H_2SO_4 + 9\ H_2O \rightarrow 3\ H_3PO_4 + 5\ (CaSO_4{,}2H_2O)$.

The Figure .40 shows the structural representation of phosphoric acid, and the Table 10, show the chemical properties of phosphoric acid.

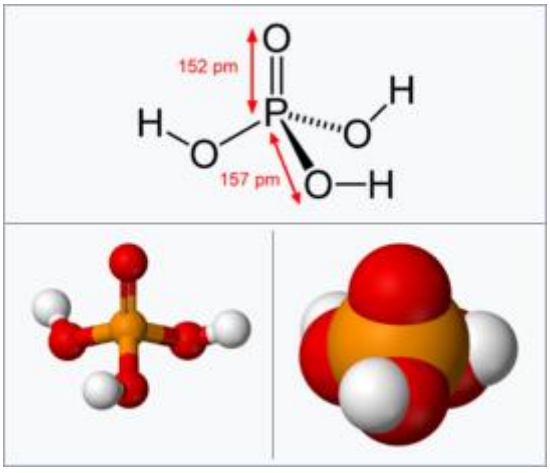

Figure 40. Representation of structure of phosphoric acid [Source wikipedia]

Table 10. Chemical properties of phosphoric acid.

Chemical formula	H_3PO_4
Molar mass	97.994 g·mol^{-1}
Appearance	Colorless syrup
Odor	Odorless
Density	1.6845 g·cm^{-3} (25 °C, 85%), 1.834 g·cm^{-3} (solid)
Melting point	40–42.4 °C (104.0–108.3 °F; 313.1–315.5 K)
Boiling point	212 °C (414 °F; 485 K)
Solubility in water	• 392.2 g/100 g (−16.3 °C) • 369.4 g/100 mL (0.5 °C) • 446 g/100 mL (15 °C) • 548 g/100 mL (20 °C)
Solubility	Soluble in ethanol

log *P*	−2.15
Vapor pressure	0.03 mmHg (20 °C)
Conjugate base	Dihydrogen phosphate
Magnetic susceptibility (χ)	$-43.8 \cdot 10^{-6}$ cm^3/mol
Refractive index (n_D)	• 1.3420 (8.8% w/w aq. soln.) • 1.4320 (85% aq. soln) 25 °C
Viscosity	2.4–9.4 cP (85% aq. soln.) 147 cP (100%)
Structure	
Crystal structure	Monoclinic
Molecular shape	Tetrahedral
Thermochemistry	
Heat capacity (*C*)	145.0 J/mol·K
Std molar entropy (S^o_{298})	150.8 J/mol·K
Std enthalpy of formation ($\Delta_f H^\ominus_{298}$)	−1271.7 kJ/mol
Gibbs free energy ($\Delta_f G^\circ$)	-1123.6 kJ/mol

The carbonates give carbon dioxide and water instead of part of the phosphoric acid after a certain time in the reactor (variable depending on the type of reactor used and the ore treated), a filtration operation is carried out on the resulting slurry in order to separate the phosphoric acid [308], thus made of calcium sulphate crystals dihydrate ($CaSO_4,2H_2O$) or semi-hydrate ($CaSO_4,1/2H_2O$) called phosphogypsum [309]. It can also be prepared by high-temperature calcination of the apatite with silica and carbon. The phosphorus vapor produced is oxidized to phosphorus pentoxide which reacts with water vapor [310].

Calcium precursors

Calcium carbonate CaO

Calcium oxide, with the chemical formula CaO, is the only known calcium oxide. it is obtained by calcining limestone at 825 ° C [311]. But it also exists in its natural state, in the form of a rare mineral which it is possible to observe in small white masses in the ejectas transformed at

high temperature among the common lavas on the flanks of volcanic formations [312]. CaO is said to be quicklime because it reacts violently with water, producing heat, depending on the reaction [313]:

$CaO + H_2O \rightarrow Ca(OH)_2$

We obtain the so-called "slaked" lime, it no longer reacts with water. Lime is a coating of choice because, by carbonation in the open air thanks to atmospheric CO_2 [314, 315]:

$Ca(OH)_2 + CO_2 \rightarrow CaCO_3 + H_2O$

It becomes calcium carbonate $CaCO_3$, or limestone, regaining its initial solidity [315]. Thus, the slaked lime plastered on the walls creates a layer of limestone generally colored red, orange or even yellow [316].

Calcium oxide is irritating to the skin because it reacts with the water present on the skin and produces slaked lime, which is very basic with pKa = 12.6 for the couple Ca^{2+} 2 H_2O / $Ca(OH)_2$ [317, 318]. The Figure .41 shows the structural representation of calcium oxide, and the Table 11 shows the chemical properties of calcium oxide.

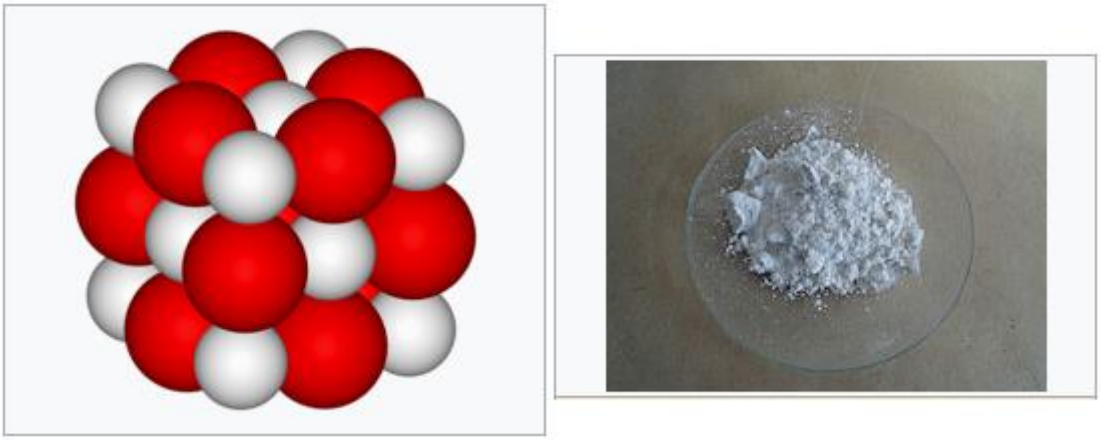

Figure 41. Representation of Structure of Calcium Oxide [Source wikipedia]

Table 11. Chemical properties of Calcium oxide.

Chemical formula	CaO
Molar mass	56.0774 g/mol
Appearance	White to pale yellow/brown powder
Odor	Odorless
Density	3.34 g/cm^3
Melting point	2,613 °C (4,735 °F; 2,886 K)

Boiling point	2,850 °C (5,160 °F; 3,120 K) (100 hPa)
Solubility in water	Reacts to form calcium hydroxide
Solubility in Methanol	Insoluble (also in diethyl ether, octanol)
Acidity (pK_a)	12.8
Magnetic susceptibility (χ)	-15.0×10^{-6} cm^3/mol
Structure	
Crystal structure	Cubic, cF8
Thermochemistry	
Std molar entropy (S^o_{298})	40 J·mol^{-1}·K^{-1}
Std enthalpy of formation ($\Delta_f H^\ominus_{298}$)	−635 kJ·mol^{-1}

- Calcium Hydroxide $Ca(OH)_2$

Calcium hydroxide is a mineral chemical body, an ionic compound of the calcium cation and the hydroxide anion, with the crude formula $Ca(OH)_2$. This ancient alkali was formerly called and is still called "slaked lime", "fatty lime" and "aerial lime", because this corrosive and hygroscopic powder was prepared from quicklime or calcium oxide produced formerly by the lime kiln of the chaufournier [319]. It is also a rare natural mineral [320], density 2.23, called portlandite by mineralogists because it is a simple product of hydrolysis of Portland cement [321, 322].

It is the main constituent dissolved in lime water or suspended in milk of lime [323]. Indeed, this alkaline earth mineral hydroxide is very little soluble in water [324]: depending on the composition of industrial slaked lime, often a little magnesian, between 1.1 g.L^{-1} and 1.6 g.L^{-1} to 20 ° C, approximately between 0.6 g.L^{-1} and 0.7 g.L^{-1} at 80 ° C. The pure compound in the laboratory is barely slightly more soluble. It's already very low solubility in water decreases slightly with temperature. Its solubility product constant is of the order of 5.02×10^{-6} at 25 ° C [325]. The Figure .42, shows the structural representation of Calcium Hydroxide, and Table 12 show the chemical properties of calcium hydroxide.

Figure 42. Structural representation of Calcium Hydroxide [Source wikipedia]

Table 12. Chemical properties of Calcium Hydroxide.

Chemical formula	$Ca(OH)_2$
Molar mass	74.093 g/mol
Appearance	White powder
Odor	Odorless
Density	2.211 g/cm^3, solid
Melting point	580 °C (1,076 °F; 853 K) (loses water, decomposes)
Solubility in water	• 1.89 g/L (0 °C) • 1.73 g/L (20 °C) • 0.66 g/L (100 °C)
Solubility product (K_{sp})	5.5×10^{-6}
Solubility	• Soluble in glycerol and acids. • Insoluble in alcohol.
Basicity (pK_b)	1.37 (first OH^-), 2.43 (second OH^-)
Magnetic susceptibility (χ)	$-22.0\cdot10^{-6}$ cm^3/mol
Refractive index (n_D)	1.574
Structure	

Crystal structure	Hexagonal, hP3
Space group	P3m1 No. 164
Lattice constant	a = 0.35853 nm, c = 0.4895 nm
Thermochemistry	
Std molar entropy (S^o_{298})	83 J·mol^{-1}·K^{-1}
Std enthalpy of formation ($\Delta_f H^\ominus_{298}$)	−987 kJ·mol^{-1}

- Albumin

Egg white is a part of the egg, composed mainly of albumin, ovalbumin, which protects the zygote (egg yolk) as it is shown in Figure .43 [326]. The egg white is 88% water [327]. Among the other constituents, there is 10.6% of globular proteins, the main one being called ovalbumin (more than 50% of all proteins) [328, 329]. This protein is structurally a serpin (a class of proteins), although it has no known function of inhibiting other proteins. It is interesting for its coagulant and surfactant properties; it is what helps stabilize the foam of snow whites. The other two main proteins in white are lysosyme and ovotransferrin. It also contains various other proteins such as ovomucoids, avidin, glycoproteins (such as ovomucin), glucoses (0.9%) and mineral salts (0.5%) [330]. The chicken egg white consists of four distinct zones, the proportion of which varies according to the weight of the egg, and therefore the age of the chicken: the fluid external white 23% of the total white, i.e. 8 g, thick intermediate 57% of total white, i.e. 20 g, internal fluid 17% of total white, i.e. 6 g, and chalazes 3% of total white, i.e. 1 g [331].

Figure 43. Illustration of egg's white after separation from egg's yolk.

- Shrimp shells waste

In this section, we are referred to the MAO et al.2017 review on shrimp waste [332]. Thus, shrimp waste is a potential source of animal protein along with important biomaterials such as chitin, fats (glycerides, phospholipids, and carotenoids), and calcium carbonate (Shahidi and Synowiecki, 1991). A previous report indicated that the dry weight of shrimp consisted of 18% chitin, 43% protein, 29% ash, and 10% fat (Snowy and Al-Khatib, 2000). Additionally, shrimp waste contains a wide range of bioactive ingredients such as unsaturated fatty acids, carotene pigments, free amino acids, and trace elements. Therefore, the effective recovery of these bioactive components from shrimp tailings has broad industrial and scientific applications.

It is reported that approximately 6-8 million tons of waste crustaceans are produced worldwide each year (FAO, 2014). With the development of aquaculture in recent years, shrimp culture has spread. In particular, shrimp production in Asia has increased rapidly these years, and accounted for more than 80% of global production (FAO, 2014). Moreover, about 45% of processed seafood consists of shrimp. Thus, the manufacturing industries contributed to the accumulation of a lot of waste shrimp (Chen et al., 2015; Holanda and Netto, 2006). In industries, shrimp are processed as meat, head, shell and tail as by-products (Knorr, 1991). Frozen peeled shrimp is the main export product for the shrimp processing industry. In general, approximately 45% to 60% of whole shrimp is transformed into by-products (head and hard shield) after processing, which varies with different species and processing methods (Sachindra and Mahendrakar, 2005; Sila et al., 2012). Increased shrimp residue is inevitable due to increased consumption. Shrimp waste disposal, especially with fishery waste, poses a serious environmental and economic problem due to the waste of valuable biological materials (Kandasamy et al., 2012; Morgan and Chuenpagdee, 2003). Biowaste is recognized as an abundant resource of biological compounds, including chitin, protein, fats, dyes, flavor compounds, and calcium carbonate (Bueno-Solano et al., 2009; Shahidi and Brown, 1998; Yan and Chen, 2015). Solar drying was previously used to treat waste and convert it into feedstock for veterinary and aquaculture practices. However, the processing conditions were unsanitary for the animal feed. Besides, shrimp residues were dried on the beaches, causing an unpleasant odor, surface pollution and other environmental pollution (Nwanna et al., 2004). Figure 44 shows some photos of shrimp shell waste.

Figure 44. Some pictures of shrimp shells waste [333]

- Acids

- Hydrochloric acid

Hydrochloric acid is a solution of hydrogen chloride in water. Hydrogen chloride, a strong acid, is a diatomic gas with the chemical formula HCl that ionizes completely in aqueous solution to give a variety of chemical species [334], including chloride anions Cl^- and hydronium H_3O^+ cations, the latter being on average solvated by five molecules of water; various varieties of oxonium ions are also present among the solutes. It is in the form of a colorless liquid with an aqueous appearance and a very recognizable pungent odor. Concentrated acid is very corrosive, with toxic fumes. It must be handled with care and it can have a negative pH [335, 336]. The Table 13 shows the chemical properties of hydrochloric acids.

Table 13. Chemical properties of Hydrochloric acids.

Chemical formula	$HCl_{(aq)}$
Appearance	Colorless, transparent liquid, fumes in air if concentrated
Odor	Pungent characteristic

Melting point	Concentration-dependent
Boiling point	Concentration-dependent
log *P*	0.00
Acidity (pK_a)	−5.9 (HCl gas)

- Nitric acid

Nitric acid is a chemical compound with the formula HNO_3. Colorless liquid when pure, this strong mineral acid of pKa = –1.37 is in practice used in concentrated aqueous solution. It was formerly called azotic acid by 19th century chemists, but also formerly the spirit of nitre by alchemists, or "etching" or aquae fortis by copper engravers. At a concentration higher than 86%, it is called fuming nitric acid, qualified as white or red depending on whether it is poor or rich in nitrogen dioxide NO_2 [337, 338]. Cut with a fifth or a quarter of nitrogen peroxide N_2O_4 [339] and less than one percent of hydrogen fluoride, it gives inhibited red fuming nitric acid, better known by the acronym IRFNA [340]. At concentration greater than 95%, it quickly develops at room temperature a yellowish coloration due to its decomposition releasing nitrogen dioxide NO_2 [341]. The Structural representation of Nitric acids is presented in the Figure .45 and its chemical properties are shown in Table 14.

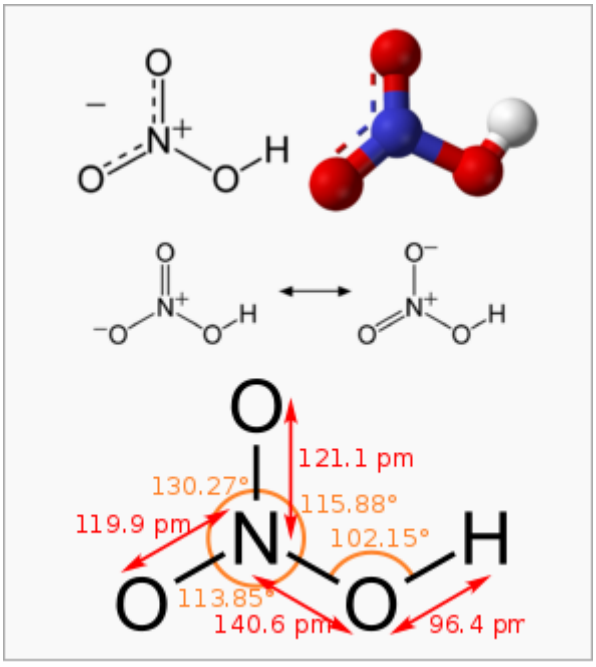

Figure 45. Structural representation of Nitric acids [Source wikipedia].

Table 14. Chemical properties of Nitric acids.

Chemical formula	HNO_3
Molar mass	63.012 g·mol^{-1}
Appearance	Colorless, yellow or red fuming liquid
Odor	acrid, suffocating
Density	1.51 g cm^{-3}, 1.41 g cm^{-3} [68% w/w]
Melting point	−42 °C (−44 °F; 231 K)
Boiling point	83 °C (181 °F; 356 K) 68% solution boils at 121 °C (250 °F; 394 K)
Solubility in water	Completely miscible
log *P*	−0.13
Vapor pressure	48 mmHg (20 °C)
Acidity (pK_a)	−1.4
Conjugate base	Nitrate
Magnetic susceptibility (χ)	-1.99×10^{-5} cm^3/mol
Refractive index (n_D)	1.397 (16.5 °C)
Dipole moment	2.17 ± 0.02 D
Thermochemistry	
Std molar entropy (S^o_{298})	146 J·mol^{-1}·K^{-1}
Std enthalpy of formation ($\Delta_f H^\ominus_{298}$)	−207 kJ·mol^{-1}

- Sulphuric acid

Sulfuric acid is a chemical compound with the formula H_2SO_4. It is a mineral acid whose strength with pKa = –3.0, is only exceeded by a few superacids. It is miscible with water in all proportions, where it dissociates by releasing hydronium cations:

$2\ H_2O + H_2SO_4 \rightarrow 2\ H_3O^+ (aq) + SO_4^{2-} (aq)$.

Sulfuric acid is a major industrial product, which has m applications, especially in lead-acid batteries [342] for cars and other vehicles, mineral processing [343], phosphate fertilizer manufacturing facilities [344], petroleum refining [345], mineral processing wastewater and chemical syntheses [346]. Resulting from the hydration of sulfur trioxide SO_3, itself resulting from the natural oxidation of sulfur dioxide SO_2 in the Earth's atmosphere where it is a notorious

pollutant [347]. Its high corrosiveness and the dangers represent are not so much due to its strong acid nature as to its greed for water which makes it an agent used in desiccation, capable of severely burning organic tissues [348]. This is the reason why, like caustic soda, it is much more dangerous than hydrochloric acid which is however also a strong acid. The Figure 46 shows the structural representation of sulphuric acid, and the Table 15 its chemical properties.

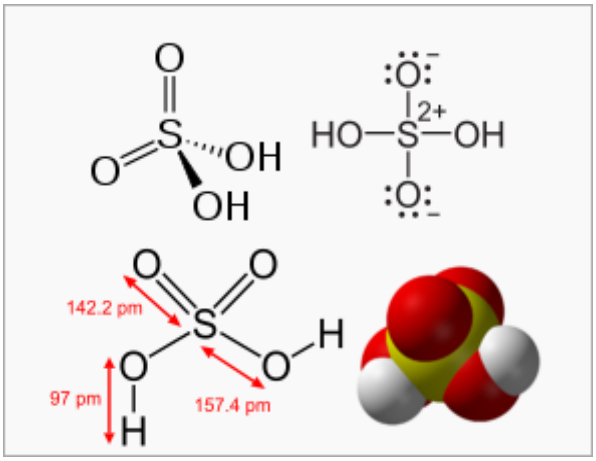

Figure 46. Structural representation of Sulphuric acid [Source wikipedia].

Table 15. Chemical properties of Sulphuric.

Chemical formula	H_2SO_4
Molar mass	98.079 g/mol
Appearance	Clear, colorless liquid
Odor	Odorless
Density	1.8302 g/cm^3, liquid
Melting point	10.31 °C (50.56 °F; 283.46 K)
Boiling point	337 °C (639 °F; 610 K) When sulfuric acid is above 300 °C (572 °F; 573 K), it gradually decomposes to SO_3 + H_2O
Solubility in water	Miscible, exothermic
Vapor pressure	0.001 mmHg (20 °C)
Acidity (pK_a)	−3, 1.99
Conjugate base	Hydrogen sulfate
Viscosity	26.7 cP (20 °C)
Thermochemistry	
Std molar entropy (S^o_{298})	157 J·mol^{-1}·K^{-1}

Std enthalpy of formation ($\Delta_f H^{\ominus}_{298}$)	$-814\ kJ{\cdot}mol^{-1}$

- Bases

- Ammonia

Ammonia is the basic aqueous solution of ammonia. It can be noted $NH_3 \bullet H_2O$, NH_4OH or better aqueous NH_3. It is therefore the product of the dissolution of ammonia NH_3 in the gaseous state in water. It is an ordinary industrial product, sometimes also very often a commercial solution at 35% by mass. Aqueous NH_3 is a common alkali in dyeing, used in the manufacture of textile fibers and their finishes, papers and their coatings [349,350], and also used in the chemical and pharmaceutical industry [351]. Water reacting with ammonia, weak base, to produce ammonium cations NH^{4+} and hydroxide anions HO^- in equal quantities, this solution was also called "ammonium hydroxide solution" and the statistical formula (NH^{4+} aq + HO^-aq) has been assigned to it. However, the NH_4OH compound (ammonium hydroxide) has never been isolated, and only a small proportion (around 1%) of the NH_3 molecules is actually hydrolyzed to NH^{4+} and HO^-. The ammonia gives off an odor a gas which mainly composes it and escapes fairly spontaneously; the aqueous solution releases hot even more easily the irritating ammonia gas [352]. The Figire .47, show the structural representation of ammonia and ammonium ion, and the Table 16 shows the chemical properties of Ammonia.

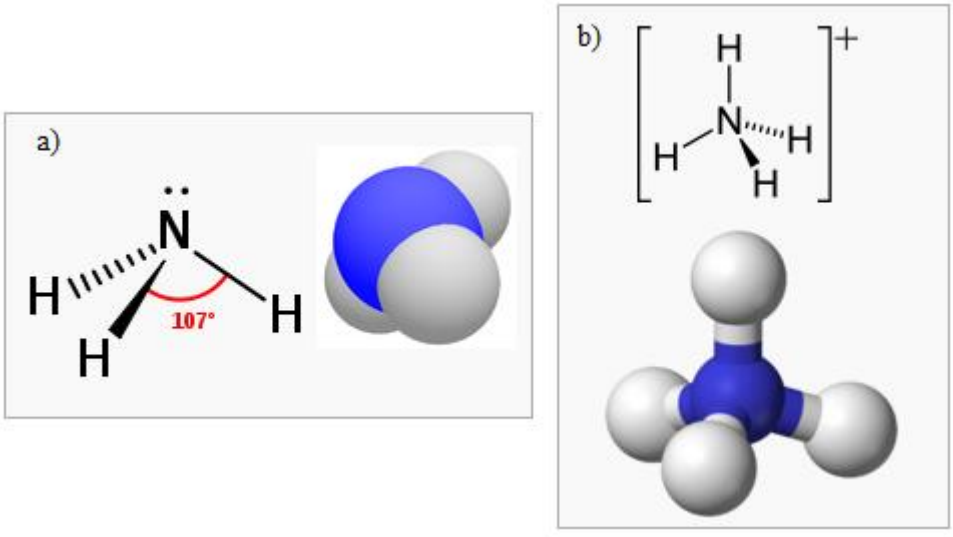

Figure 47. Structural representation of a). Ammonia and b). Ammonium ion [Source wikipedia].

Table 16. Chemical properties of Ammonia

Chemical formula	NH_3
Molar mass	17.031 g/mol
Appearance	Colourless gas
Odor	Strong pungent odour
Density	0.86 kg/m^3 (1.013 bar at boiling point) 0.769 kg/m^3 (STP) 0.73 kg/m^3 (1.013 bar at 15 °C) 681.9 kg/m^3 at −33.3 °C (liquid) 817 kg/m^3 at −80 °C (transparent solid)
Melting point	−77.73 °C (−107.91 °F; 195.42 K) (Triple point at 6.060 kPa, 195.4 K)
Boiling point	−33.34 °C (−28.01 °F; 239.81 K)
Critical point (*T*, *P*)	132.4 °C (405.5 K), 111.3 atm (11,280 kPa)
Solubility in water	47% w/w (0 °C) 31% w/w (25 °C) 18% w/w (50 °C)
Solubility	soluble in chloroform, ether, ethanol, methanol
Vapor pressure	857.3 kPa
Acidity (pK_a)	32.5 (−33 °C), 10.5 (DMSO)
Basicity (pK_b)	4.75
Conjugate acid	Ammonium
Conjugate base	Azanide
Magnetic susceptibility (χ)	$-18.0 \cdot 10^{-6}$ cm^3/mol
Refractive index (n_D)	1.3327
Viscosity	• 10.07 μPa·s (25 °C) • 0.276 mPa·s (−40 °C)
Structure	
Point group	C_{3v}
Molecular shape	Trigonal pyramid
Dipole moment	1.42 D
Thermochemistry	

Std molar entropy (S^o_{298})	193 $J \cdot mol^{-1} \cdot K^{-1}$
Std enthalpy of formation ($\Delta_f H^\ominus_{298}$)	−46 $kJ \cdot mol^{-1}$

- Sodium hydroxide NaOH

Pure sodium hydroxide is called caustic soda. Under normal conditions, it is in crystalline solid form. It is a mineral chemical body composed of the chemical formula NaOH, which is an ionic solid at room temperature. It is meltable around 318 ° C [353], it is generally in the form of pellets, flakes or white beads or translucent, corrosive. It is very hygroscopic; it is also often sold in the form dissolved in water. It is indeed very soluble in water. It is also very soluble in ethanol. Its acceptable daily dose has not been specified since 1966. It is sodium hydroxide, often called shorthand soda, or lye soda. It is a transparent viscous solution, which is even more corrosive than in its pure state. Its aggressiveness is amplified by its wetting appearance, which increases the action and contact with the skin [354]. The Table 17 shows the chemical properties of sodium hydroxide.

Table 17. Chemical properties of Sodium Hydroxide.

Chemical formula	NaOH
Molar mass	39.9971 g mol^{-1}
Appearance	White, waxy, opaque crystals
Odor	Odorless
Density	2.13 g/cm^3
Melting point	323 °C (613 °F; 596 K)
Boiling point	1,388 °C (2,530 °F; 1,661 K)
Solubility in water	418 g/L (0 °C) 1000 g/L (25 °C) 3370 g/L (100 °C)
Solubility	soluble in glycerol negligible in ammonia insoluble in ether slowly soluble in propylene glycol
Solubility in methanol	238 g/L

Solubility in ethanol	<<139 g/L
Vapor pressure	<2.4 kPa (at 20 °C)
Basicity (pK_b)	-0.56 ($NaOH(aq) = Na^+ + OH^-$)
Magnetic susceptibility (χ)	$-15.8 \cdot 10^{-6}$ cm^3/mol (aq.)
Refractive index (n_D)	1.3576
Structure	
Crystal structure	Orthorhombic, oS8
Space group	Cmcm, No. 63
Lattice constant	a = 0.34013 nm, b = 1.1378 nm, c = 0.33984 nm
Formula units (Z)	4
Thermochemistry	
Heat capacity (C)	59.5 J/mol K
Std molar entropy (S^o_{298})	64.4 $J \cdot mol^{-1} \cdot K^{-1}$
Std enthalpy of formation ($\Delta_f H^\ominus_{298}$)	-425.8 $kJ \cdot mol^{-1}$
Gibbs free energy ($\Delta_f G^\circ$)	-379.7 kJ/mol

- Hydrogen peroxide H_2O_2

Hydrogen peroxide is a chemical compound with the formula H_2O_2. Its aqueous solution is called hydrogen peroxide. It is colorless and slightly more viscous than water. Hydrogen peroxide has both oxidizing properties, for example with respect to iodide ions, and reducing properties, for example, with respect to permanganate ions. It is an effective bleaching agent [355]. It is used as an antiseptic [356]. Hydrogen peroxide exists naturally in living beings as a by-product of cellular respiration [357]. All aerobic organisms have enzymes, called peroxidases, which catalyze the disproportionation of H_2O_2 into H_2O and O_2 [358]:

$$2\ H_2O_2 \rightarrow 2\ H_2O + O_2\ (\Delta rH = -195.2\ kJ / mol).$$

The concentration of hydrogen peroxide solutions is generally indicated in "volumes" or in mol / l. By definition, 1 L of oxygenated water at x volumes is likely to release x liters of O_2 gas, measured under normal conditions of temperature and pressure, by disproportionation of H_2O_2.

The Figure .48 shows the representation of structure of hydrogen pyroxide, and the Table 18 displays its chemical properties.

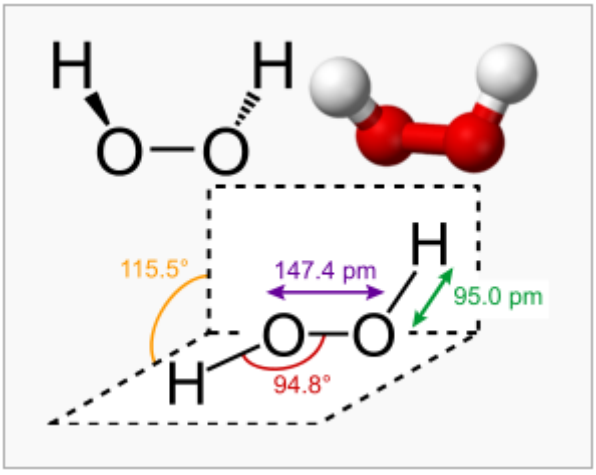

Figure 48. Structurale representation of Hydrogen pyroxide [Source wikipedia].

Table 18. Chemical properties of Hydrogen pyroxide.

Chemical formula	H_2O_2
Molar mass	34.0147 g/mol
Appearance	Very light blue color; colorless in solution
Odor	Slightly sharp
Density	1.11 g/cm^3 (20 °C, 30% (w/w) solution) 1.450 g/cm^3 (20 °C, pure)
Melting point	−0.43 °C (31.23 °F; 272.72 K)
Boiling point	150.2 °C (302.4 °F; 423.3 K) (decomposes)
Solubility in water	Miscible
Solubility	soluble in ether, alcohol insoluble in petroleum ether
log *P*	-0.43
Vapor pressure	5 mmHg (30 °C)
Acidity (pK_a)	11.75
Magnetic susceptibility (χ)	$-17.7\cdot10^{-6}$ cm^3/mol
Refractive index (n_D)	1.4061

Viscosity	1.245 cP (20 °C)
Dipole moment	2.26 D
Thermochemistry	
Heat capacity (*C*)	1.267 J/(g·K) (gas) 2.619 J/(g·K) (liquid)
Std enthalpy of formation ($\Delta_f H^\ominus_{298}$)	−187.80 kJ/mol

- Metal transition elements

A transition metal, or transition element, is, according to the definition of IUPAC [359, 360], a chemical element whose atoms have an incomplete electronic sublayer d, or which can form cations whose electronic sublayer d is incomplete [361]. This definition corresponds to elements sharing a set of common properties. Like all metals, they are good conductors of electricity. They are solid under normal conditions of temperature and pressure, with a high density and high melting temperature. They most often have remarkable catalytic properties, both in their atomic form and in their ionic form. They can form a large variety of ionic species in a wide range of oxidation states, thanks to the small energy between these different oxidation states [362], which gives rise to variously colored complexes due to the different electronic transitions within the incomplete d sublayer. They are also likely to form m paramagnetic compounds under the effect of unpaired electrons in the sublayer d [363]. Among all metal transition we choose just four Ni, Co, Cu and Mn.

- Nickel (Ni) [364].

Nickel is the chemical element with atomic number 28, symbol Ni. It is a transition metal element from block d, the lightest in group 10. The nickel atom has two electronic configurations, [Ar] $3d^8 4s^2$ and [Ar] $3d^9 4s^1$, which are very close in energy - the symbol [Ar] indicates the electrons of the heart which have the configuration of the argon atom. There is disagreement about the configuration to be considered to be of lower energy. Chemistry textbooks indicate the electronic configuration of nickel as [Ar] $4s^2 3d^8$, or equivalently as [Ar] $3d^8 4s^2$. This choice is in accordance with the Klechkowski rule, which provides that the 4s sub-layer will be filled before 3d. It is also supported by the experimental fact that the lower energy state of the nickel atom is a level of the $3d^8 4s^2$ configuration, namely the level $3d^8$ (3F) $4s^2$ 3F,

J = 415. However, each of these two configurations corresponds to a set of quantum states of different energies. The two sets of energies overlap, and the average energy of the states of the configuration [Ar] $3d^9 4s^1$ is actually lower than the average energy of the states of the configuration [Ar] $3d^8 4s^2$. For this reason, research publications on calculations of atomic structure consider that the fundamental electronic configuration of nickel is [Ar] $3d^9 4s^1$. The nickel atom is paramagnetic.

- Cobalt (Co) [365].

Cobalt is the chemical element with atomic number 27, symbol Co. The cobalt of electronic structure [Ar] $4s^2 3d^7$ is the second element of the eighth secondary group; this transition metal is part of the iron group. The simple cobalt body has physical properties quite similar to those of iron and nickel. From a chemical point of view, it is less reactive than iron. Cobalt is also an element of group 9, of which the first three Co, Rh and Ir constitute the group of cobalt. Cobalt 60 has m uses as a source of gamma γ rays, due to its relatively short half-life (5.27 years), therefore easier to eliminate in comparison with other isotopes emitting such particles. We thus find the "cobalt 60 bombs", sources of γ rays of 1.17 and 1.33 MeV.

- Copper (Cu) [366].

Copper is the chemical element with atomic number 29, symbol Cu. Copper is an element of group 11, of period 4, an element of the chalcophil transition metal block. In the periodic table of the elements, copper is of the same family as silver and gold, because each one has an orbital s occupied by a single electron on fully filled p and d sublayers, which allows the formation of metallic bonds (electronic configuration Ar $3d^{10} 4s^1$). The three metals of this "copper group" have a character of nobility and increased rarity, from semi-noble copper to genuinely noble gold, the first character being explained by their weak atomic radii and their atomic stacking compactities, their higher ionization potentials due to the d sublayers, their relatively high melting points and their low reactivities or relative chemical inertias.

- Manganese (Mn) [367].

Manganese is the chemical element with atomic number 25, symbol Mn. Manganese is an element of group VII and of period IV, and therefore of the middle of the first series of so-called transition metals. The manganese group includes for chemist manganese, technetium, rhenium and, incidentally, the synthetic radioactive bohrium transactinide. The electronic

structure of the manganese atom, ie [Ar] $4s^2 3d^5$ justifies a maximum oxidation state equal to 7 or VII7. In nature, states II and III (the latter stabilized in the form of complexes) are the most common. Manganese, taking 1.55 as the Pauling electronegativity value, is the most electropositive and also the most abundant element of this seventh secondary group.

III.2.2 **Methods and laws**

-Tauc's plot

The Tauc diagram is used to determine the optical band gap, or Tauc gap, in a semiconductor. Tauc gap is often used to describe the practical optic properties of amorphous materials. Jan Tauc showed that the optical absorption spectrum of amorphous germanium is similar to the spectrum of indirect transitions in crystalline germanium (plus the tail due to localized states at low energies), and proposed an extrapolation to find the optical gap for these crystal-like states. Typically, the Tauc diagram shows the amount of energy h of the light on the coordinate and the quantity (αhν) 1 / r on the coordinate, where α is the absorption coefficient of the substance [368]. The value of r denotes the nature of the transition: r = 1/2 for permissible direct transfers, r = 3/2 for prohibited direct transitions, r = 2 for permissible indirect transitions, r = 3 for prohibited indirect transitions [369]. The resulting plot has a distinct linear system that indicates the onset of absorption. Thus, extrapolating this linear region to the coordinate yields the optical band gap energy of the material.

- Urbach's Law

- Optical transition in amorphous materials

OJL Band Transfer Model for Amorphous Materials - A brief tutorial of optical transitions in amorphous materials. The following electron state density diagram illustrates the types of light transitions as shown in Fig. 49, which will be discussed below:

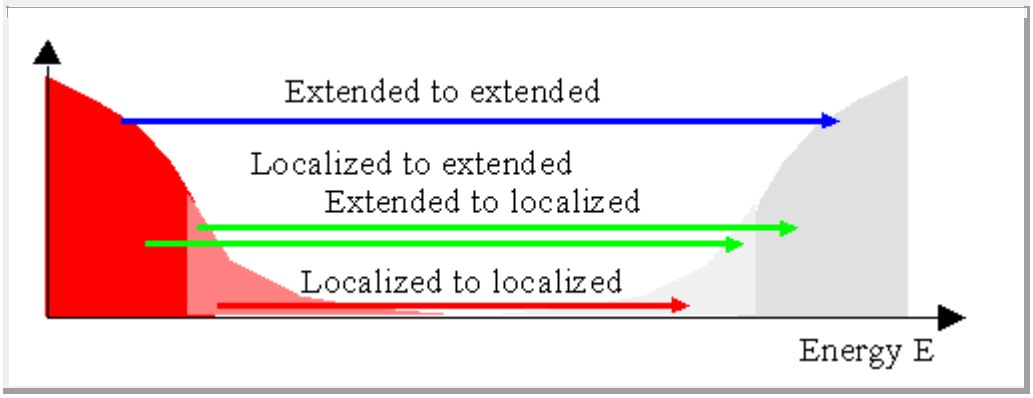

Figure 49. Possible electronical states extention in amorphous materials [370].

- Extended states

The transitions from elongated to elongated states are very similar to those known from crystalline materials. As can be seen from the diagram, they define the absorption of light at high energies (above the gap energy) or short wavelength. In the case of parabolic bands as it is shown in Figure. 50 (without the tail states) the density profile of the states is as follows:

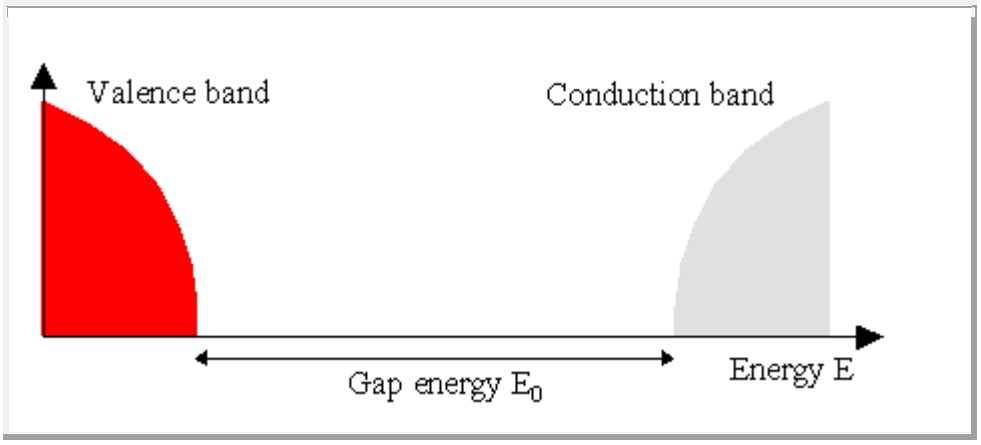

Figure 50. Shematization of state distribution for Valence and Conduction bands [370].

This leads to an absorption coefficient of the form [371]

$$\alpha(\omega) \sim \frac{1}{\omega}(\hbar\omega - E_0)^2$$

Hence a plot of

$$\sqrt{\omega\alpha(\omega)} \sim \hbar\omega - E_0$$

versus energy, it should lead to a straight line that gives its intersection with the y-axis the energy gap E_0, the so-called "Tauc gap". Tauc gap is often used to describe the optical properties of amorphous materials. From the above considerations, it is evident that the Tauc gap gives information on the energy separation of states spanning the valence and conduction bands [372].

- Extended to localized and localized to extended state transitions

Below the gap where no absorption is observed in ideal crystalline materials in the transitions of amorphous materials from the occupied extended states of the valence band to the blank tail states of the conduction strip. Likewise, transitions from the occupied par-band states to the extended null states of the conduction band are possible. Both types of transitions must contain similar matrix elements.

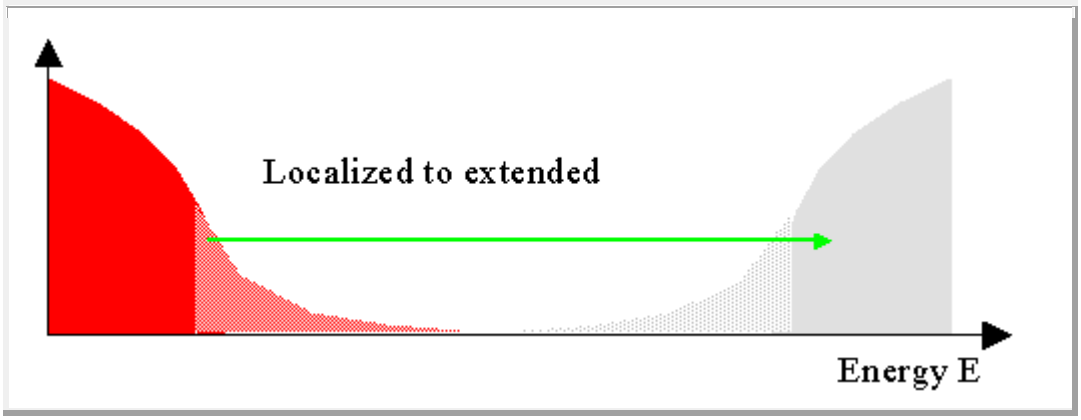

Figure 51. Schematization of states transitions from localized to extended states [370].

For the transitions from the localized states to the extended states as shown in Figure 51 (and for the extended to localized states) with the exponential decay of the local case density in the gap, one finds an exponential relationship between the absorption coefficient and the frequency (1):

$$\alpha(\omega) \sim \exp\left(\frac{\hbar\,\omega}{E_U}\right) \qquad (1)$$

where E_U is called 'Urbach energy' (2,3) [373, 374].

$$\ln \alpha(\omega) = C + \frac{\hbar \omega}{E_U} \quad (2)$$

$$E_U = \frac{\hbar}{d/d\omega \ln \alpha(\omega)} \quad (3)$$

The Urbach energy can be determined by drawing the logarithm of the absorption coefficient as relationships (2,3) and taking the inverse of the slope of the linear portion of the graph [375].

- Localized to localized states transitions

Typically, these transformations are not very important since the number of states involved is low and the elements of the transition matrix are much smaller compared to those of the transitions mentioned above. This is due to the fact that the elements of a matrix are integrals over all of the space over the product of two functions (the initial and the derivative of the final state) separated in space and thus show almost no overlap. Transitions from positional to localized states may lead to absorption in lower energy regions of the spectrum which in most cases are the near to medium infrared region.

- Determination of absorption coefficients

The leading graphic constructions are based on the Tauc gap and Urbach energy on the assumption that the absorption coefficient is determined in optical experiments [376]. This is not the case: what is being measured is the reflection and transmittance of a sample. Conversion from measured reflectance and transmittance data to absorption coefficients is not as easy as is commonly believed. Indeed, in the case of thin films with multiple reflections and multiple interference effects, the absorption coefficient cannot be extracted from the measured spectra directly. Hence, it is not a good idea to serve as an "interface" between experiments and theory. In almost all cases, the modeling approach is the best option. A dielectric function model with the density parameters of the combined states would be ideal. The OJL approach discussed below provides only what is needed: the gap energy characterizing the extended states and the foundations of the tail state distributions are shown as direct parameters in the OJL isolation function model [377].

- Refinement Rietveld

- Description of the method

** Position and surface of the peaks*

The Rietveld method is a method for X-ray diffraction and neutron powder analysis. It was developed in 1969 by the Dutch crystallographer Hugo Rietveld [378]. This method consists of simulating the diffraction of a crystal model of the sample and then modifying the parameters of that model so that the simulated diffraction pattern is as close as possible to the measured diffraction pattern [379]. Depending on the characteristics we are interested in and the number of parameters to be fine-tuned, the program can be more or less complex. The basis of this method is the crystal diffraction theory. If we know: the structure of the crystal; The nature and location of the atoms within the lattice; Atomic scattering factors (Rayleigh scattering coefficient of X-rays over atoms); Absorption coefficients Then we can determine the position of the diffraction peaks, as well as their surface, to a nearby factor (this factor depends on the strength of the radiation source, the efficiency of the detector, etc.). It is also possible to take into account the preferential orientation (texture) of the sample.

** Peak shape*

To simulate the shape of each vertex, we can use a rudimentary mathematical function, without specific meaning, for example, Gaussian or Lorentzian function, Pseudo Voigt function, or Pearson VII function, and optimize its width to half the height of H (FWHM, full width at half maximum) [380]. So, we have width m to refine like vertices. However, we know that the width is a function dependent on the 2θ position of the peak and thus we can relate the widths of the peaks belonging to the same phase by this function and improve the function parameters. The typical function of an X-ray diffraction measurement is (4):

$$\mathrm{H}(2\theta) = \mathrm{H}_0 + \frac{\mathrm{H}_1}{\cos\theta} + \mathrm{H}_2 \cdot \tan\theta, \qquad (4)$$

for neutron diffraction, we generally use Cagliotti's law (5) (1958) [381, 382]:

$$\mathrm{H}(2\theta) = \sqrt{\mathrm{U} \cdot \tan^2\theta + \mathrm{V} \cdot \tan\theta + \mathrm{W}}. \qquad (5)$$

Therefore, there are only three width parameters to be refined for each stage, whatever the number of peaks. We can also determine the shape of the vertices from the laws of geometric optics applied to the diffraction scale configuration.

** Algorithm*

The algorithm used to modify the parameters of the model or regression, which is called fitting, is an algorithm that aims to reduce the quadratic difference between the simulated curve and the experimental curve; One talks about the least-squares error minimization algorithm. We generally use the weighted reliability factor Rwp in relationship (6) [383, 384]:

$$R_{wp} = \sqrt{\frac{\sum_i w_i \cdot (I_i^{exp} - I_i^{cal})^2}{\sum_i w_i \cdot I_i^{exp\,2}}} \qquad (6)$$

Where w_i is the weight assigned to point i, which is 1 / Ii^{exp}. I_f the simulation is perfect, then the reliability factor will have a value depending on the signal to noise ratio. I_f the source of radiation is an x-ray generator, then we know that the noise follows Poisson's law: its standard deviation is equal to the square root of the number of strokes accumulated at each point. Thus, we can define the lowest reliability factor R_0. The R_{wp}/R_0 function should usually tilt toward1.

** Quantification without standard*

Using this method, we can simulate a mixture of several stages. The ratio of each phase is one of the parameters to be refined, and thus the Rietveld method allows quantification.

This method is called "non-standard" because, unlike traditional quantitative methods, it is not feasible to calibrate the device bypassing samples of known composition. This method is particularly interesting when the phases have close peaks with m overlap. On the other hand, unlike the classical quantitative method (based on the surface or the height of a few peaks for each stage), the Rietveld method requires a measurement over a large angular range (usually 20 to 90 °) and with a good noise signal ratio, and thus a relatively long acquisition time, several tens of minutes To several hours depending on the signal-to-noise ratio.

** Determination and refinement of structure*

The Rietveld method can be used to determine the crystal structure; It is an alternative method for images of Lau on single crystals. The first step is to determine the symmetry of the crystal from the position of the vertices: the Bravais space and then the space group [385, 386, 387].

There are specific programs that generally operate by trial and error: the program reviews the various possible space combinations and identifies the space group that matches the best. One also defines the network parameters. This step is called indexing, as each peak in the diffraction, the diagram is linked to a crystal plane of Miller indices (hkl). Then the Rietveld method is used to determine the position of each atom within the network. To help the program converge, we can indicate the limitations: imposing the location of specific atoms, with tolerances; To force the atoms to remain grouped like types of molecules, one speaks of "solid bodies. In what is called the simulated annealing method, we randomly place the atoms and then let the algorithm converge; this process is repeated many times, and the solution that gives the least reliable factor is chosen.

- Full prof software [388].

FullProf Suite (for Windows, Linux and macOS) consists of a set of crystallography programs (FullProf, WinPLOTR, EdPCR, GFourier, etc ...) mainly developed for Rietveld (Structure Profile Optimization) analysis of the neutron (Wavelength) Constant, time of flight, nuclear and magnetic scattering) or X-ray powder diffraction data collected in a fixed or variable scattering angle step 2theta. The various programs can be run either in the standalone form (from the console window or directly clicking in a shortcut) or from the WinPLOTR and / or EdPCR interfaces. The software is distributed within FullProf Suite with the hope that it will be useful, but without a guarantee that it is free from internal errors. Under no circumstances will the authors (or their institutions) be liable to you for damages, including general, special, incidental or consequential damages arising from the use or inability to use the software (including but not limited to loss of data or data provided) Inaccurate or losses incurred by you or third parties, or the program's failure to work with other programs). The authors are not responsible for faulty results obtained with the software.

III.3 Technical Analysis

III.3.1 **XRD**

X-ray diffraction is a powerful nondestructive technique for characterizing crystalline materials using X-ray Diffractometer like XRD D8 Advance by Bruker Company for example as it is shouwn in Figure 52. It provides information on structures, phases, preferred crystal orientations (texture), and other structural parameters, such as average grain size, crystallinity,

strain, and crystal defects. XRD peaks are produced by constructive interference of a monochromatic beam of X-rays scattered at specific angles from each set of lattice planes in a sample. The peak intensities are determined by the atomic positions within the lattice planes. Consequently, the XRD pattern is the fingerprint of periodic atomic arrangements in a given material. An online search of a standard database for X-ray powder diffraction patterns enables quick phase identification for a large variety of crystalline samples. A simple search in the ICDD standard database of X-ray diffraction patterns allows a rapid phase identification in a large area of crystalline samples. The main applications of XRD analysis are:

• Identification / quantification of the crystalline phase

• Measurement of average crystal size, voltage or microtension effects in global density samples and in thin film samples

• Quantification of the preferred orientation (texture) in thin layers, in multilayer stacks and in manufactured parts

• Determination of the ratio of crystalline materials to amorphous materials in global density materials and in thin film samples

• Phase identification of a large quantity of samples of overall density and thin layer

• Detection of crystalline minority phases (at concentrations greater than> ~ 1%)

• Determination of the size of the crystallites for polycrystalline layers and polycrystalline materials

• Determination of the percentage of materials in crystalline form compared to the percentages of amorphous materials

• Measure less than a milligram of loose powder or dry solution samples for phase identification

• 50 angstrom thin layer analysis to observe the texture and phase behaviors

• Determination of the tension and composition of thin epitaxial layers

• Determination of the surface cut in monocrystalline materials

• Measurement of residual stress in metals and ceramics in the form of global densities

• Without destructive effects

• Quantitative measurement of the content of the phases and orientation of the texture

• Minimal or no requirements for sample preparation

• Ambient conditions for all the analysis

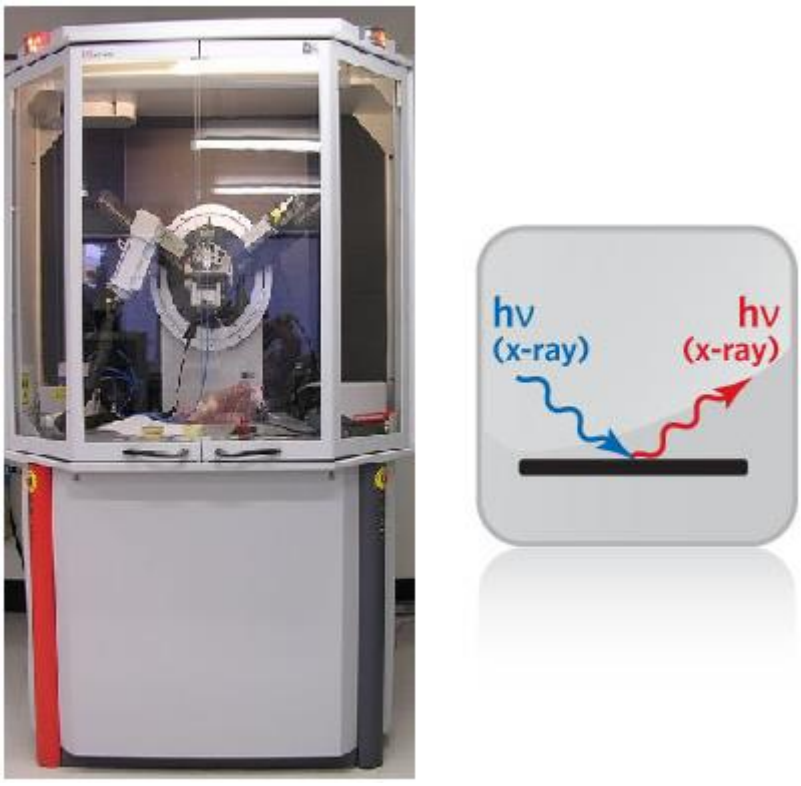

Figure 52. X-ray Diffractometer (XRD) D8 Advance by Bruker Company,

III.3.2 **XRF**

X-ray fluorescence (XRF) is a non-destructive technique used to quantify the elemental composition of solid and liquid samples. On use X-rays to excite the atoms which are in the sample, which makes them emit X-rays with energy characteristic of each element present. The intensity and energy of these X-rays are then measured. XRF is capable of detecting elements in Be-U concentrations ranging from ppm (parts per million) to 100% [389]. As X-rays are used to excite the sample, it is possible to analyze depths up to 10 µm in size. By using an appropriate reference standard, XRF analysis can accurately quantify the elemental composition of both solid and liquid samples. The Figure 53 show an example of XRF Spectrometer apparatus (XRF Spectrometer Zetium) which is used essentially for the pharmaceutical application due to its high accuracy. There are two XRF systems, a wavelength dispersing system (WDXRF) and an energy dispersing system (EDXRF). The difference is the way X-rays are detected. The instruments have very good energy resolution, resulting in less spectrum overlap and improved

background intensities. EDXRF instruments have a higher signal efficiency, which can shorten the analysis times. Having higher signal performance makes EDXRF systems suitable for small location analysis or mapping analysis.

• Elementary identification of unknown solids, unknown liquids and unknown powders

• Identification of metal alloys.

Figure 53. XRF Spectrometer XRF Zetium from Malvern Panalytical Company

III.3.3 **EDX**

Energy dispersive X-ray spectroscopy (or EDS, abbreviation for "Energy Dispersive X-ray Spectroscopy") is an analytical faculty that can be coupled with several applications, including scanning electron microscopy (SEM), transmission electron microscopy (TEM) and scanning transmission electron microscopy (STEM). Combined with these imaging tools, EDS can provide basic analysis on areas as small as the size of the nanometer in diameter. The impact of the electron beam on the sample produces X-rays which are characteristic of the elements present on the sample. The analysis can be used to determine the elementary composition of individual points or to bring out by cartography the lateral distribution of elements from the

digitized area in the form of an image. The Figure 54, show a Tescan VEGA3 apparatus With EDX System as example of Scanning Electron Microscope.

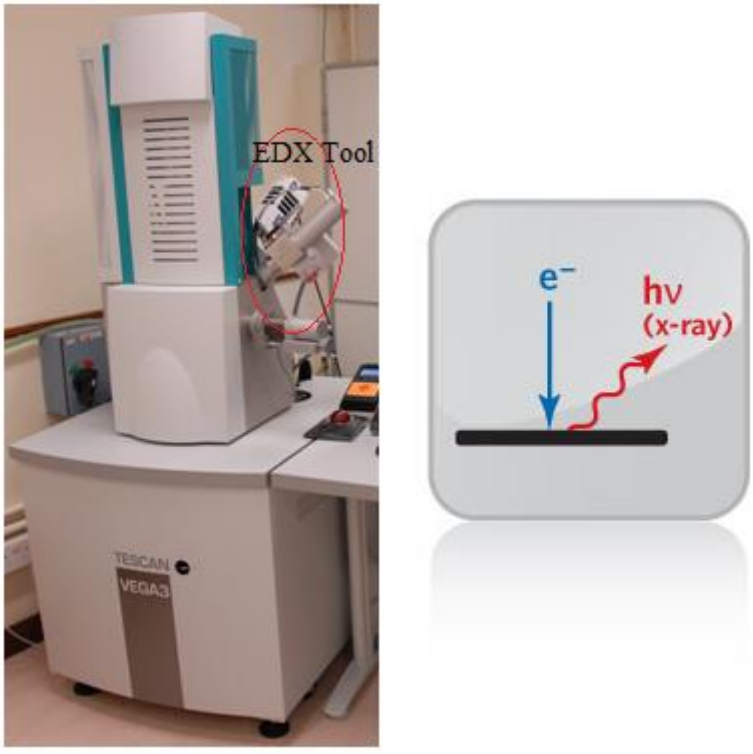

Figure 54. Scanning Electron Microscope (Tescan VEGA3) With EDX System

III.3.4 **FTIR**

Fourier-transform infrared spectroscopy (FTIR) [390, 391] is a technique used to obtain an infrared spectrum of absorption or emission of a solid, liquid or gas. An FTIR spectrometer simultaneously collects high-spectral-resolution data over a wide spectral range. This confers a significant advantage over a dispersive spectrometer, which measures intensity over a narrow range of wavelengths at a time. The term Fourier-transform infrared spectroscopy originates from the fact that a Fourier transform (a mathematical process) is required to convert the raw data into the actual spectrum. The goal of FTIR absorption spectroscopy is to measure the amount of light absorbed by a sample, as a function of the wavelength. The simplest technique for doing this is "dispersive spectroscopy", which is to illuminate the sample with a beam of monochromatic light of given wavelength, measure how much light is absorbed, and then repeat the operation for different wavelengths. The principle of Fourier transform spectroscopy is a

less intuitive way of obtaining the same information. Rather than illuminating the sample with a monochromatic beam of light, this technique uses a beam containing a combination of multiple frequencies of light, and the absorption by the sample is measured. The beam is then modified to contain a combination of different frequencies, the absorption by the sample is again measured, and the operation is repeated again, multiple times. Once all the data has been acquired, a computer takes all this data and calculates backwards to deduce the absorption at each wavelength. The Figure 55, show an example of FTIR apparatus IRAffinity -1S from SHIMADZU Company.

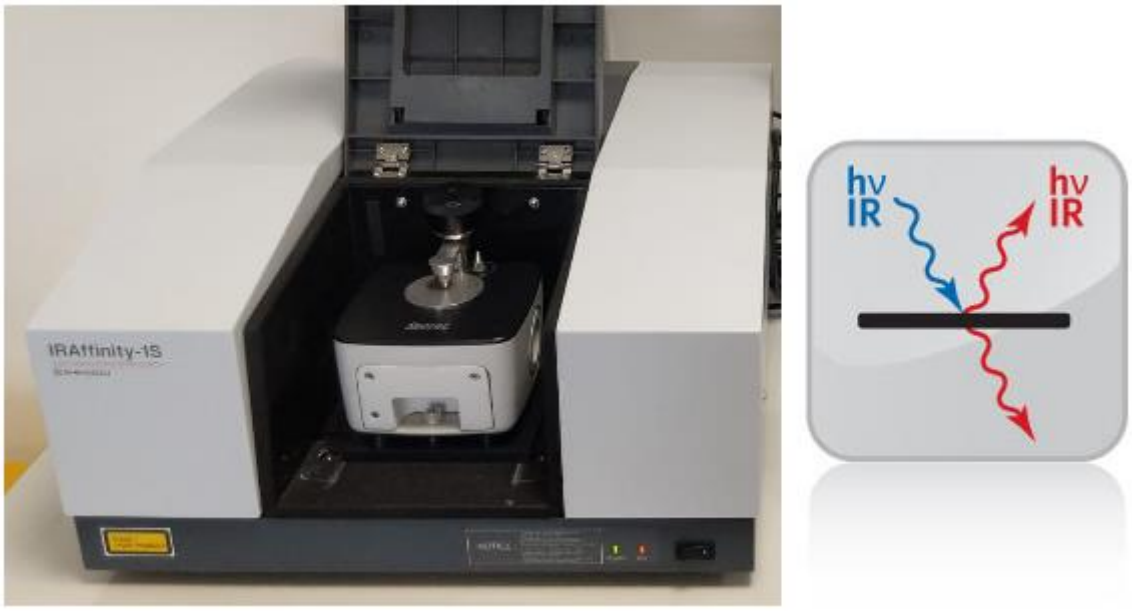

Figure 55. FTIR apparatus IRAffinity -1S from SHIMADZU Company

III.3.5 **RAMAN Spectroscopy**

Raman spectroscopy allows you to determine the chemical structure of a sample and to identify the compounds present by measuring nuclear vibrations, in a similar way to analysis by Fourier transform infrared spectroscopy (FTIR). However, the method used by the Raman analysis produces better spatial resolution and allows smaller samples to be analyzed [392, 393]. Raman is a good technique for quantitative analysis of mixed organic and / inorganic materials and can also be used to do semi-quantitative and quantitative analyzes. The figure .56 shows an example of Raman spectrometer Horiba Jobin-Yvon LabRam HR800. It is often used for:

• Identifying organic molecules, polymers, biomolecules and inorganic compounds both in global densities (in bulk) and in individual particles

• Raman analysis imagery and in-depth profiling is used to map the distribution of components in mixtures, such as drugs in excipients, tablets and coatings for delayed drug absorption

• Determine the presence of different types of carbon (diamond, graphite, amorphous carbon, adamantine carbon, nanotubes) and their parent proportions, chosen to which it is particularly suitable

• Determine inorganic oxides and their valence state

• Measure the stress and the crystal structure of semiconductors and other materials

• Identifying the strict molecular of organic and inorganic compounds to carry out contamination analyzes, classification of materials and measurement of stresses

• Characterization of carbon layers (graphite versus diamond)

• Non-covalent bonds (complex bonds, metallic bonds) Orientation (random structure versus organized structure)

Figure 56. Raman spectrometer Horiba Jobin-Yvon LabRam HR800 from Horiba Company

III.3.6 **TG-DTG**

Thermogravimetric analysis (TGA) [394], is a thermal analysis technique which consists in measuring the mass variation of a sample as a function of time, for a given temperature or temperature profile. Such an analysis presupposes good precision for the three measurements: mass, time and temperature. As the mass variation curves are often similar, it is often necessary to perform processing of these curves in order to be able to interpret them. The derivative of these curves shows at which points these variations are the most important.

ATG is often used in research and testing to determine the characteristics of materials such as polymers, to estimate the kinetics of oxidation in corrosion at high temperature, to determine the degradation temperatures, the moisture absorbed by the material, the amount of organic and inorganic compounds in a material, the decomposition point of an explosive and solvent residues.

III.3.7 **SEM**

A scanning electron microscope (SEM) [395] is a type of electron microscope that produces images of a sample by scanning the surface with a focused beam of electrons. The electrons interact with atoms in the sample, producing various signals that contain information about the surface topography and composition of the sample. The electron beam is scanned in a raster scan pattern, and the position of the beam is combined with the intensity of the detected signal to produce an image. In the most common SEM mode, secondary electrons emitted by atoms excited by the electron beam are detected using a secondary electron detector. The number of secondary electrons that can be detected, and thus the signal intensity, depends, among other things, on specimen topography. The Figure 57, show Tescan VEGA3 apparatus as example of Scanning Electron Microscope. SEM analysis is one of the most commonly used analytical tools due to the extremely detailed images it can provide quickly. Combined with an auxiliary detector EDS (Energy Dispersive X-ray Spectroscopy), SEM-EDS analysis can offer elementary identification of almost the entire periodic table of the elements. It gives quickly;

- High resolution images
- Elementary microanalysis and characterization of particles
- High resolution fast imaging
- Quick identification of the elements present
- Good depth of field
- Versatile platform that accepts m other tools

Figure 57. Scanning Electron Microscope (Tescan VEGA3)

III.3.8 **Uv-visible spectroscopy**

Uv-visible spectroscopy [396] or spectrometry is a spectroscopy technique involving photons whose wavelengths are in the ultraviolet (100 nm - 400 nm), visible (400 nm - 750 nm) range.) or near infrared (750 nm - 1,400 nm). Subject to radiation in this wavelength range, molecules, ions or complexes are likely to undergo one or more electronic transition (s). This spectroscopy is one of the methods of electronic spectroscopy. The substrates analyzed are most often in solution, but can also be in the gas phase and more rarely in the solid state. The electronic spectrum is the function which links the light intensity absorbed by the analyzed sample as a function of the wavelength. The spectrum is most often presented as a function of absorbance as a function of wavelength. It can also be presented as the molar extinction coefficient as a function of the wavelength. This technique is complementary to fluorescence spectroscopy which measures the light intensity emitted by a sample when it is illuminated at a wavelength where it absorbs. Fluorescence involves transitions from the excited state to the ground state

while absorption spectroscopy deals with transitions between the ground state and the excited state.

III.4 Conclusion

In this chapter, we gave a presentation of all raw materials and precursors that we used in this research, for the synthesis of HAP by different methods. As well, we illustrated four transition metals Ni, Co, Cu and Mn that we utilized for doping HAP. We are presented too the shrimp shells waste and different acids and bases that we used in the extraction of Chitosan. We also presented the methods and law that we applied for the determination of the optoelectronic and structural properties of our produced materials. Furthermore, we bestowed all technical analysis that we used for the characterization of our materials. We have defined all materials and described all methods, and technics of characterization used in this study, in order to help reader of this research to perceive the global vision of our followed way to reached to our target. Also, to build an impeccable mental mapping, to read, understand and remember perfectly this research.

Chapter IV:

SYNTHESIS, OPTIMISATION AND CHARACTERISATION OF HYDROXYAPATITE

IV.1 Introduction

Our aim is to prepare HAP with high symmetry and small grain's size. For elaboration of the bio powder of HAP (HAP) we use the calcium hydroxide and phosphoric acid mixing with albumin and make a comparative study with the classic method with solid state, co-precipitation and solid liquid spreading water H_2O. The HAP with general formula $Ca_{10}(PO_4)_6(OH)_2$ is a phosphorus apatite which crystallizes natural state in the hexagonal system [397]. It is the main constituent of bones and teeth; it has excellent affinity with bone tissue. So, its advantage is to create strong chemical bond with the bone. The HAP can be used also for the purification of aqueous media and the immobilization of uranium in nuclear waste [397]. Across the world, the HAP was produced by different chemical methods, in this work a HAP was synthesized by the sol-gel method, using albumin of egg white that is rich with water, Proteins and minerals. The eggs white contains 88% water. 10.6% proteins 0.9% glucose and 0.5% mineral salt [398]. Albumin has good homogeneity and helps to form the prepared phase [399]. Albumin was used to create a natural environment for growth of HAP, Similar to the one where the small chick bone is formed inside the eggshell. We use the heat for purification of HAP, because after thermic treatment, all impurities coming from egg white are removed. The hydroxapatite (HAP) has prepared by four different classical methods, Solid-liquid, Co-precipitation, Solide state (solid-solid), Solid-liquid of the quasi ternary system P_2O_5-CaO-H_2O at 25°C. We use a sample of HAP purchased from Fluka Chemica (Lot and Filling Cod 385330/1 14599) as reference. All methods will be detailed in this manuscript and each sample of HAP will be named by its method of preparation.

IV.2 Experimental method for hydroxyapatite synthesis

IV.2.1 Sol-gel method using albumin

To prepare 2g of HAP by sol-gel method using albumin, we mix a 1.3370 g of phosphoric acid H_3PO_4 85% (Sigma Aldrich P5811 Cas 7664-38-2) and 1.4750 g of calcium Hydroxid $Ca(OH)_2$ (Scharlau CA0215) with 30 ml of egg's white in beaker 100 ml. Then we agitate it by a magnetic agitator at home temperature during 8 hours, then we dry the solution in 80°C during 8 hours .Then we grind the product manually with mortar and pestle, and put it in the oven at 200°C and we raise the temperature by 200°C and achieve the inter grinding after each 24h. Until we reach 1000°c.

IV.2.2 **Solid liquid method**

Same thing for the classic method of the Solid liquid method, we replace the albumin by 30 ml of distilled water, we mix a 1.3370 g of phosphoric acid H_3PO_4 85% (Sigma Aldrich P5811 Cas 7664-38-2) and 1.4750 g of calcium Hydroxid $Ca(OH)_2$ (Scharlau CA0215) with 30 ml of distilled water in beaker 100 ml and we do the same previous manipulation and thermic treatment over.

IV.2.3 **Solid-state method**

For solid state method, all reagents are in the solid state. We grind directly and manually with mortar and pestle a 1.5774 g of ammonium phosphate $(NH4)_2HPO_4$ and 1.9927 g calcium carbonate $CaCO_3$, then we follow same thermic treatment than the sol-gel in the oven from 200°C to 1000°C and we raise the temperature by 200°C realizing an inter grinding every 24 hours duration.

IV.2.4 **Solid-liquid equilibrium of the quasi ternary system P_2O_5-CaO-H_2O**

For Solid-liquid equilibria of the quasi ternary system P_2O_5-CaO-H_2O we use a ternary diagram produt in work of PW Brown [400]. We mix manually with a spatula in beaker of 100 ml 5.5030 g of calcium oxide CaO 96% (Sigma Aldrich Cas 1305-78-8 Lot SZBG0140 V) and 4.0066 g of phosphorus pentoxide P_2O_5 99.99% (Sigma Aldrich 431419 Cas 1314-56-3) in 90.4904 ml of distilled water so that the total mass of the reagents be 100 g. The reaction temperature is maintained at 25 ° C by thermostat of liquid. This reaction lasted 138 hours. After reaction, the HAP product is surrounded by filter paper so that it is completely dry. No thermic treatment for this method. But the final product of HAP was well ground manually with mortar and pestle.

IV.2.5 **Co-precipitation method**

For Co-precipitation method, we solve 5.8148g of Calcium nitrate tetrahydrate $CaN_2O_6.4H_2O$ in 50ml of distilled water and we add 1.5774g of ammonium phosphate $(NH4)_2HPO_4$ and 0.5 ml of phosphoric acid 85% for the dissolution of the reagents to be completed . Then we agitate it by a magnetic agitator at 50°C during 2 hours, and then we add a few drops of the ammonia until the pH of the solution is seven values. Then we dry the solution in 100°C during 4 hours, then we grind the product manually with mortar and pestle and put it in the oven at 200°C to 1000°C and we raise the temperature by 200°C and realizing an inter grinding after every 24h

duration. The schema of synthesis process for HAP by different method has showns in the "**Fig. 58,**".

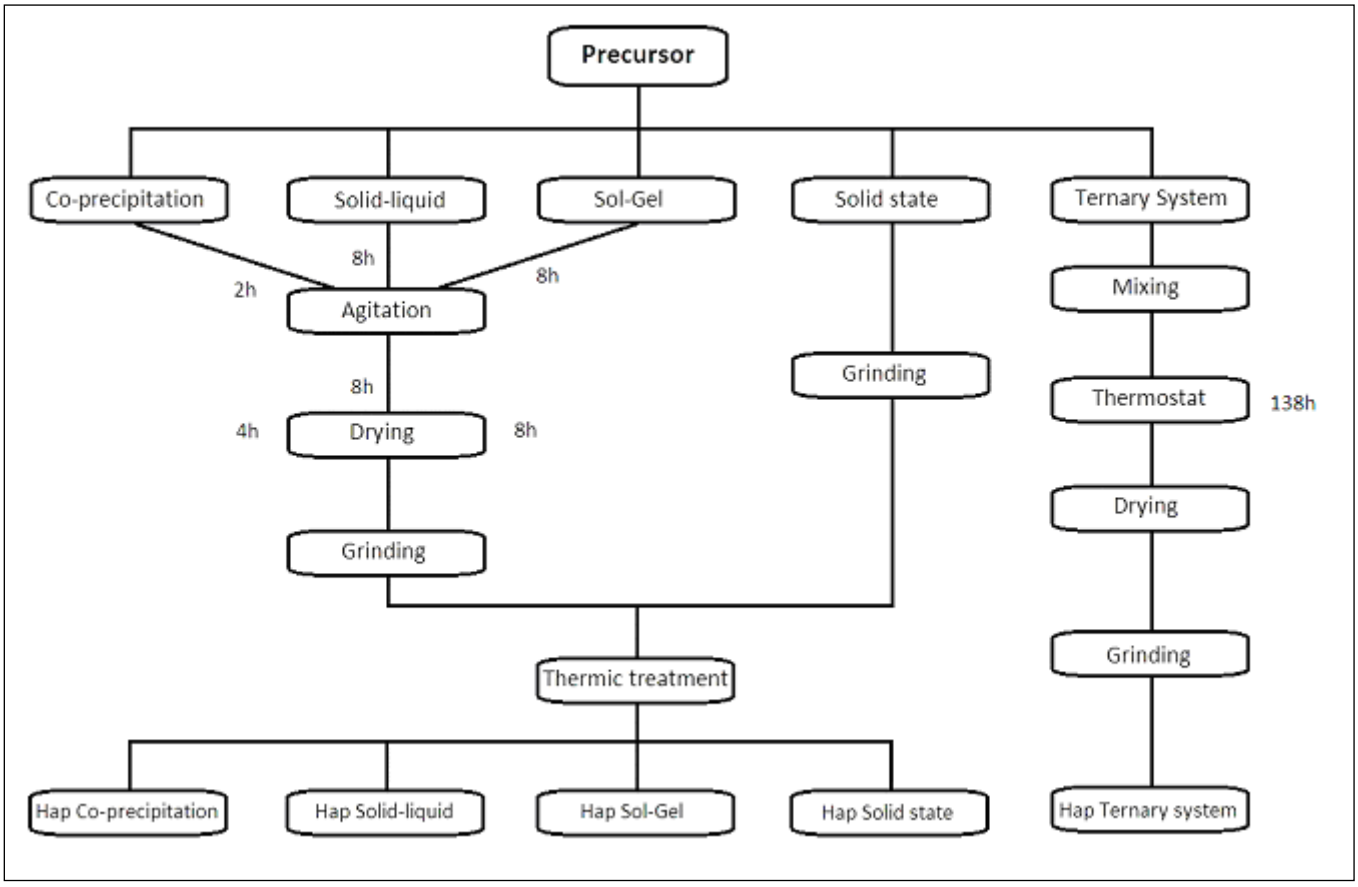

Figure 58. The synthesis process for HAP by different methods

IV.3 Characterization

IV.3.1 **XRD**

-Rietveld refinement

The powders obtained of HAP by different methods were characterized by X-ray diffraction (XRD) named Brucker D8 ADVANCE and refined in according to the Rietveld method. The Comparison of X-ray powder diffractograms of the HAP phase which has been prepared by different methods shown in "**Fig. 59,**".

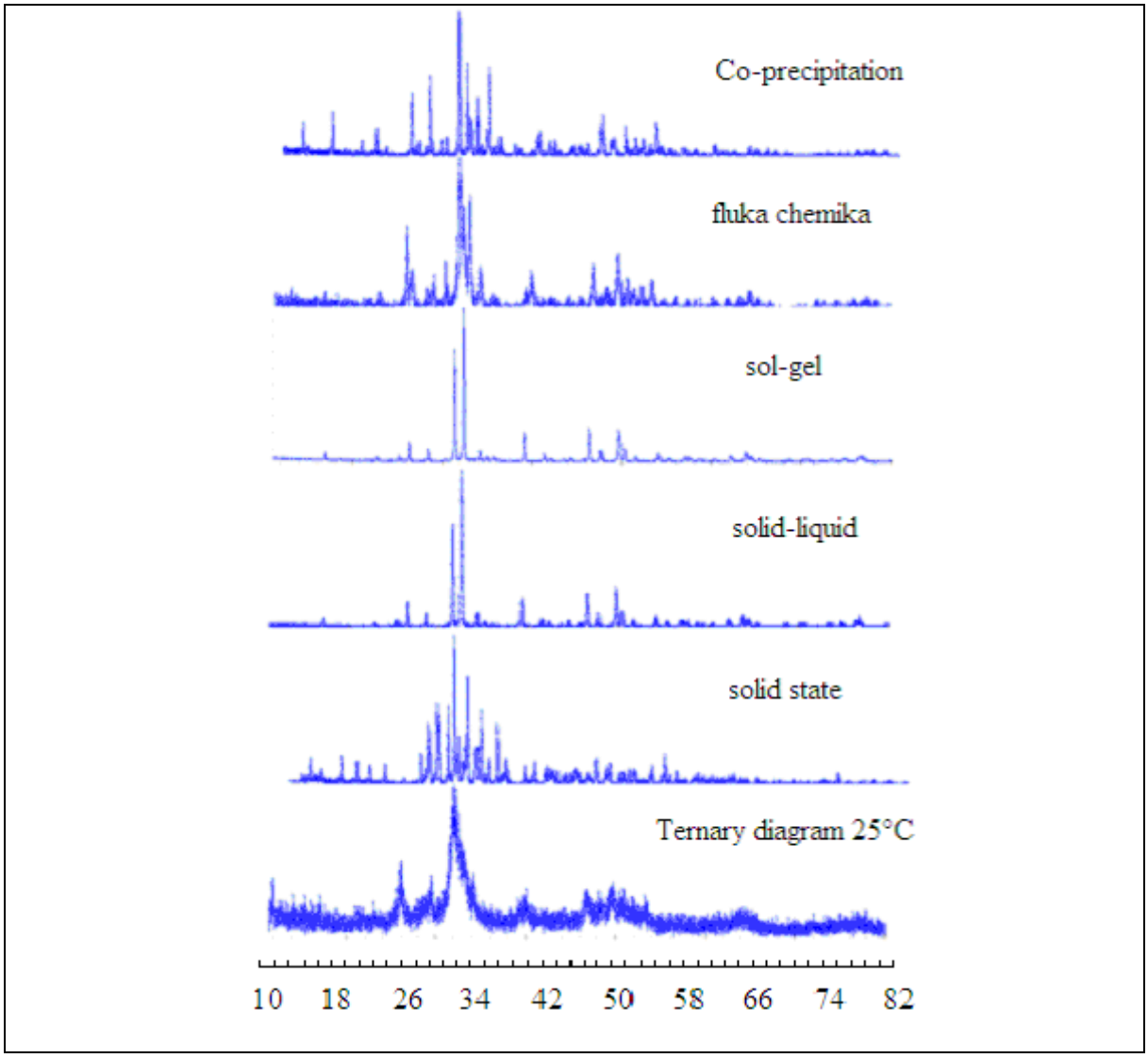

Figure 59. The Comparison of X-ray powder diffractograms of the HAP phase which has been prepared by different methods

The comparison of the spectra of the samples were characterized by X-ray diffraction show that the most intense peaks of the powders prepared in our laboratory and the reference of Fluka chemika corresponding to the diffraction nail in the vicinity of 32°. This is proof that we have succeeded in synthesizing the HAP phase by the methods cited in this work, yet the samples of HAP sol gel and liquid solid have calcined phases of high purity because their spectra are very thin and reduced except the peak more intense.

The refinement was performed using the program Fullprof. A list of the H K L data of HAP of the present work is shown in "**TABLE 19,**".

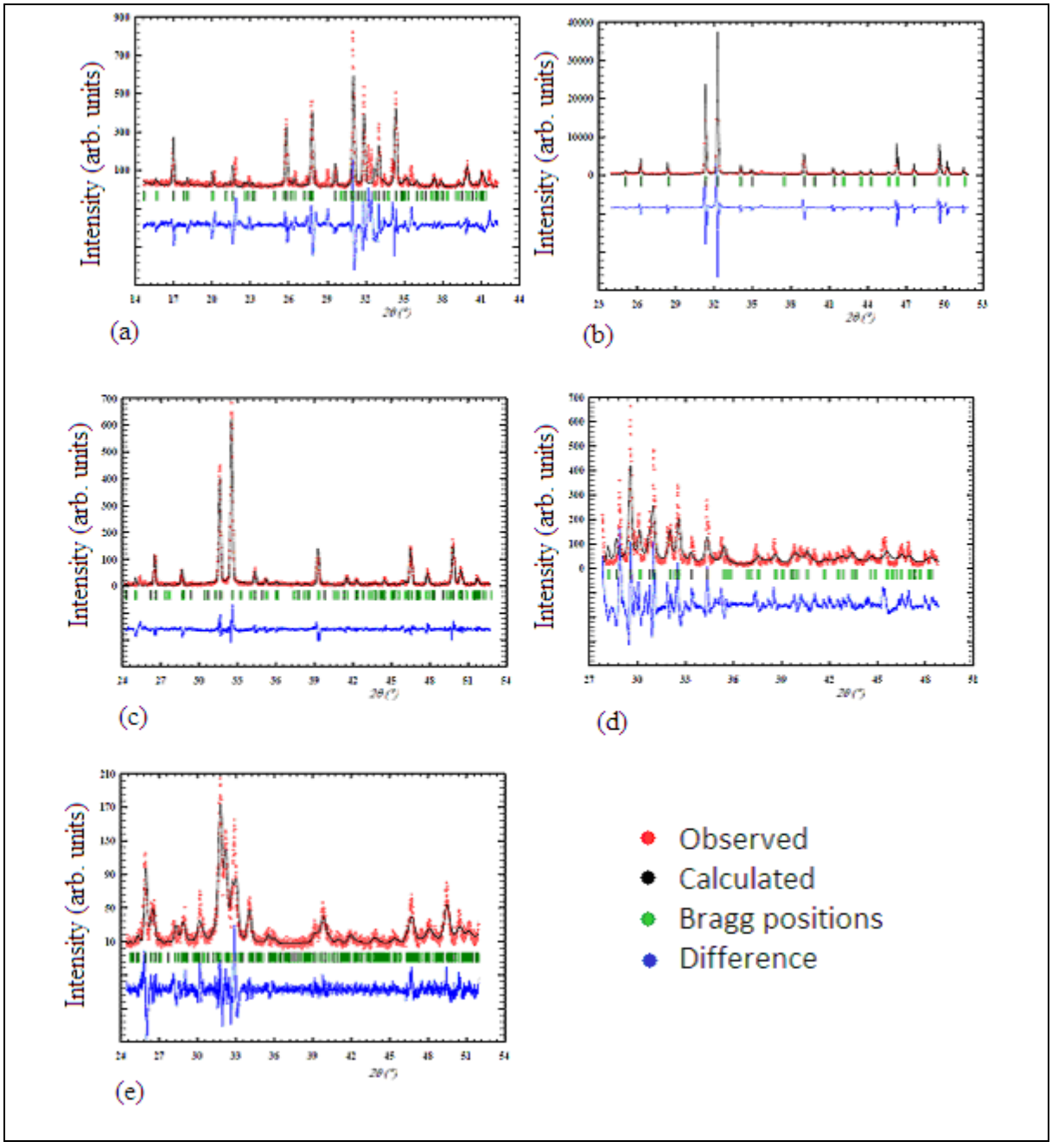

Figure 60. The Rietveld graphics. a) Co-precipitation), b) sol-gel, c) sol-liquid and d) solid state and e) fluka chemika.

Table 19. The most intense peaks, their positions and the miller indices H K L

	HAP per Co precipitation	HAP per solid-state	HAP per sol-gel	HAP per solid liquid	HAP per Fluka chemika
Intense peak %	89.05	43.8	2198.9	81.3	36.1
H K L	2 1 4	1 1 2	3 0 0	5 1 1	5 2 2
***2θ* [°]**	31.03	32.56	32.26	32.50	32.77

The refinement was performed using the program Fullprof of HAP for the present work is shown in "**Fig. 60,**" and its results are summarized in table 20. The surface of the diffraction peaks in the diagram (2θ, I) will give us information on the quantity of the present phase and the profusion of spots is related to the great variety of the orientations of the planes of reflection defined by a crystal lattice. It can be concluded that the results are consistent with the presence of some differences. These differences can be attributed to the presence of agglomerates or originated from the synthesis method; HAP particles produced by solid-state synthesis show relatively low agglomerates.

Table 20. The refinement factor for the HAP by different methods

Formula and method		HAP per Coprecipitation	HAP per solid-state	HAP per sol-gel	HAP per solid liquid	HAP from Fluka chemika
Profile Settings	U	0.32	1.18	0.01	-0.13	0.91
	V	0.002	-0.02	-0.01	0.10	0.03
	W	0.005	0.001	0.005	0.005	0.012
Profile agreement Factors	Rp	63.90	67.20	76.30	31.60	39.5
	Rwp	81.70	83.10	84.5	45.00	50.8
	Rexp	21.10	20.00	5.35	27.70	31.30
	Goff	3.90	4.20	16.00	1.60	1.60

- Structural properties

The cell volume of the HAP coprecipitantion, HAP solid liquid and HAP from fluka chemika samples is about 2000A°, while the cell volume of HAP by solid state is 1099.5A° and the cell volume of the HAP by sol gel is 541.9 A° , This has influenced in the size of grains of same hexagonal crystal system. More cell size is smal; more the size of grain is smal. We could not compare with the size's grains of sample from fluka chemika because its crystal system is hexagonal. The structural parameters of Hydroxyaatite by different methods are regrouped in table 21.

Table 21. The structural parameters of the Hydroxyaatite

Formula and method	HAP per Coprecipitation	HAP per solid-state	HAP per sol-gel	HAP per solid liquid	HAP from Fluka chemika
Crystal system	Hexagonal	Hexagonal	Hexagonal	Hexagonal	Hexagonal
Space group	P 6/m m m	P 6/mm m	P 6/mm m	P 6/mm m	P m m m
a [A]	12.05	14.63	9.60	23.52	21.40
b [A]	12.05	14.63	9.60	23.52	12.50
c [A]	16.84	5.92	6.78	4.17	9.31
V [A]	2120.92	1099.53	541.88	2002.47	2492.35
Alpha [°]	90.00	90.00	90.00	90.00	90.00
Beta [°]	90.00	90.00	90.00	90.00	90.00
Gama [°]	120.00	120.00	120.00	120.00	90.00

- Particle Size and Microstructure

The average crystallite size has easily been determined by Debby–Scherrer formula (7):

$$\mathbf{D}=\frac{\mathbf{k}*\boldsymbol{\lambda}}{\mathbf{B}*\cos(\boldsymbol{\theta})} \qquad (7)$$

Where B is the broadening of the diffraction line measured at half-maximum intensity, k is the wavelength (Cu Ka), h is the Bragg angle for a given diffraction and k is a constant, in general equal to 0.9 for powders.

The width of a diffraction line is derived from instrumental factors and physical characteristics of the powder. This can be traced back to the average size of the crystallites and their micro-stresses. The particles sizes of the HAP by different methods are summarized in table 22.

Table 22. The particles sizes of the HAP by different methods

Formula and method	HAP by Coprecipitation	HAP by solid-state	HAP by sol-gel	HAP by solid liquid	HAP from Fluka chemika
D (nm)	13.08	5.78	6.56	12.14	3.20

IV.3.2 **Uv-Visible spectroscopy**

- Optical properties: Transmission and absorption of hydroxyapatite

The measurement was taken using T92^{+} UV- visible spectrophotometer. The T92^{+} is a high-performance double beam spectrophotometer with a variable spectral bandwidth from 0.1-5nm, selected by a continuous variable slit.

For the HAP prepared by co-precipitation, a good transmittance is obtained, which at 45% of 35% prepared by ternary diagram also 27% prepared by liquid solid of more than 25% prepared by Solid stat and 17% by sol gel notament a weak transmission of HAP of fluka chemika [404]. This variation is due to the size of the grains of the powder produced by different methods since the smaller crystallite transmission is low. It can be seen that the transmittance in the region 400 to 800 nm is 18% with a small variation, whereas for wavelengths of less than 400 nm, the transmittance evokes the drop in the fundamental absorption. For all samples of HAP high energy bands were found in the ultraviolet range, these bands are attributed to charge transfer transitions between the Ca2 + and O2- ions, then a band in the visible (λ) = 550nm is attributed to an interatomic electronic transition.

- The dependence of $(\alpha hv)^2$ of hydroxyapatite on energy (eV)

Studies constitute a simple way for obtaining band gap energy and explaining the band structure of semiconductors and non-metallic materials [401]. Our optical investigation and discussions of HAP rely on measurements of transmittance, T (λ). These optical studies are used to determine absorption, optical energy gap (E_g), Urbach energy (E_U).

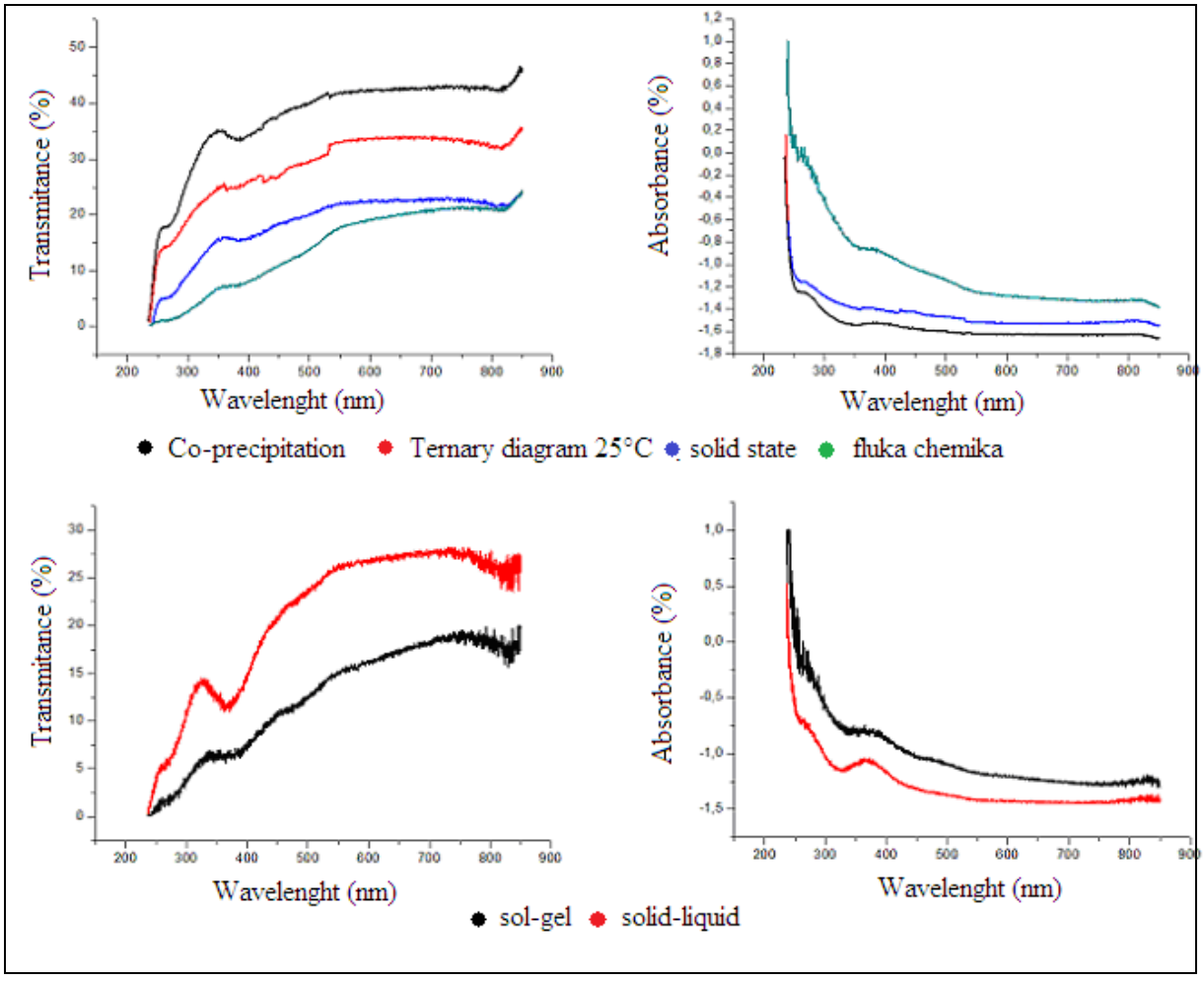

Figure 61. The transmission and absorption spectra of HAP

Generally, the absorption coefficient (α) is related to photon energy (h***v***) by the known equation (8) [402]:

$$\alpha h\nu = \alpha_0 (h\nu - E_g)^n \qquad (8)$$

E_g is the energy of the optical band gap and n is the energy factor of the transition mode, which is dependent upon the nature of the material, whether it is crystalline or amorphous.

For non-crystalline materials, indirect transitions are valid according to Tauc's relation [403,404]. The "**Fig. 61 and figure 62,**" shows the transmission spectra of HAP.

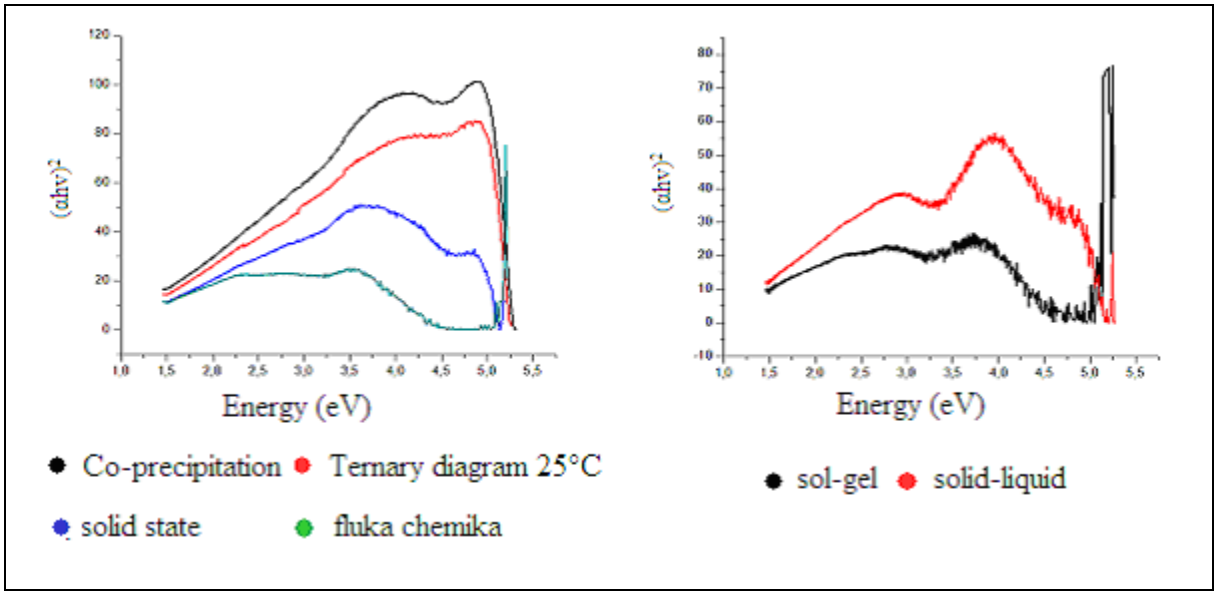

Figure 62. The dependence of $(\alpha hv)^2$ of HAP on energy (eV)

- Determination of the optical gap energy E_g

It has been shown in an earlier publication [405], that it is possible to derive the absorption coefficient from measurements of the diffuse reflectance of the samples.

The band gap of HAP has been determined from the transmission spectra by means of a graphical method by the use of a given relationship in this manuscript. The "**Fig. 63,**" and "**TABLE 23,**" gives an indication of the determination of Eg of all our samples HAPs by different methods. A small variation of Eg can be related to the crystallite size.

- Determination of the Urbach energy Eu of HAP

Absorption coefficient (α) depends on the photon energy. Near the optical band edge, the relationship between (α) and (hν) is known as Urbach empirical rule, which is given by these exponential equations (9) and (10) [406]:

$$\alpha=\alpha_0 e(hv/E_u) \quad (9)$$

$$Ln(\alpha)= Ln(\alpha_0) +hv/E_u \quad (10)$$

where **α** is a constant, (hυ) is the incident photon energy and E_U is the band tail width (Urbach energy) of the localized states in the optical energy gap, the behavior of Ln(α) against (hν) near the absorption edge is shown in "**Fig .64 and fig. 65,**".

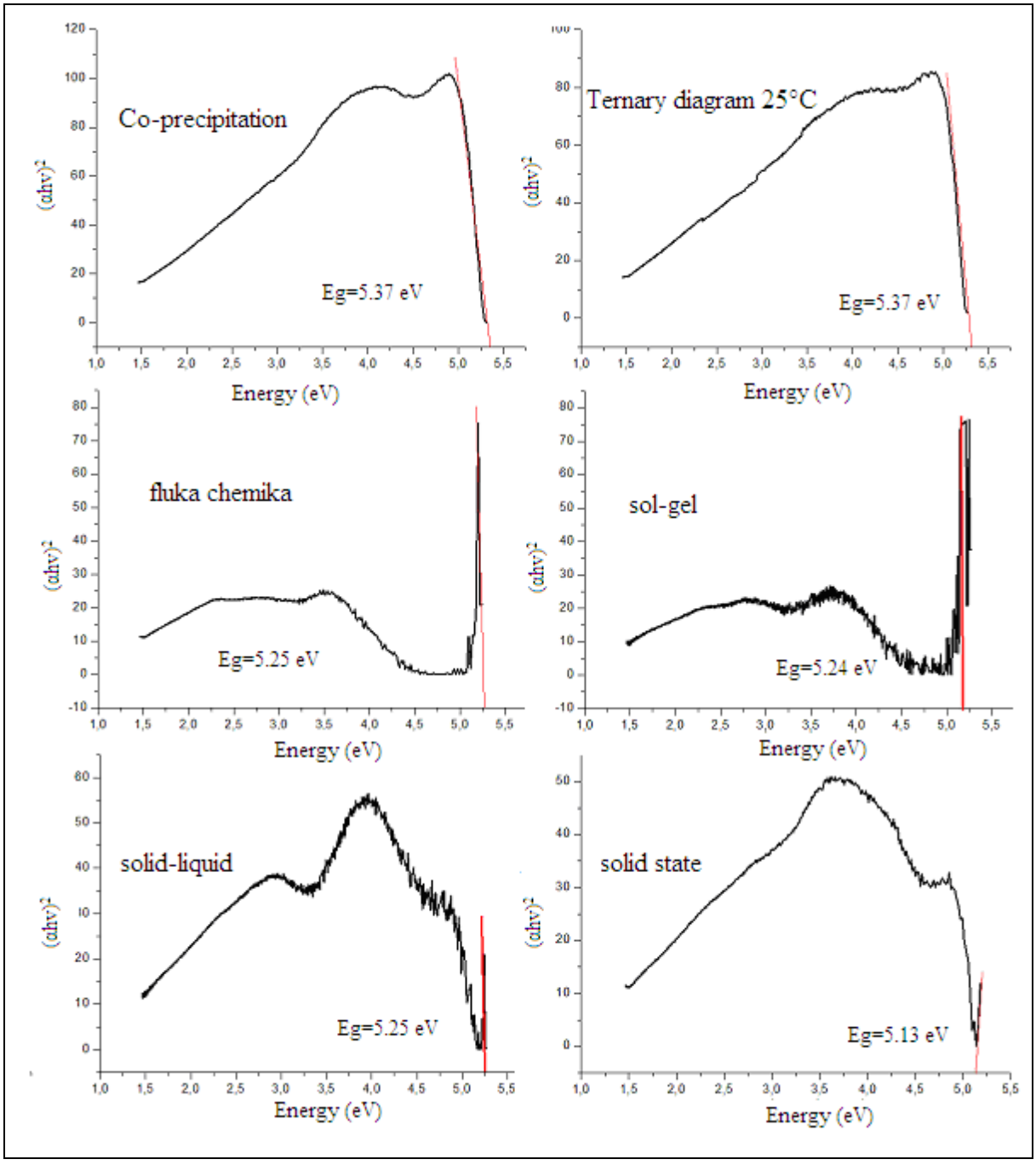

Figure 63. The determination of gap energy for HAP using the relationship $(\alpha h\nu)^2=\alpha_0(h\nu-E_g)$

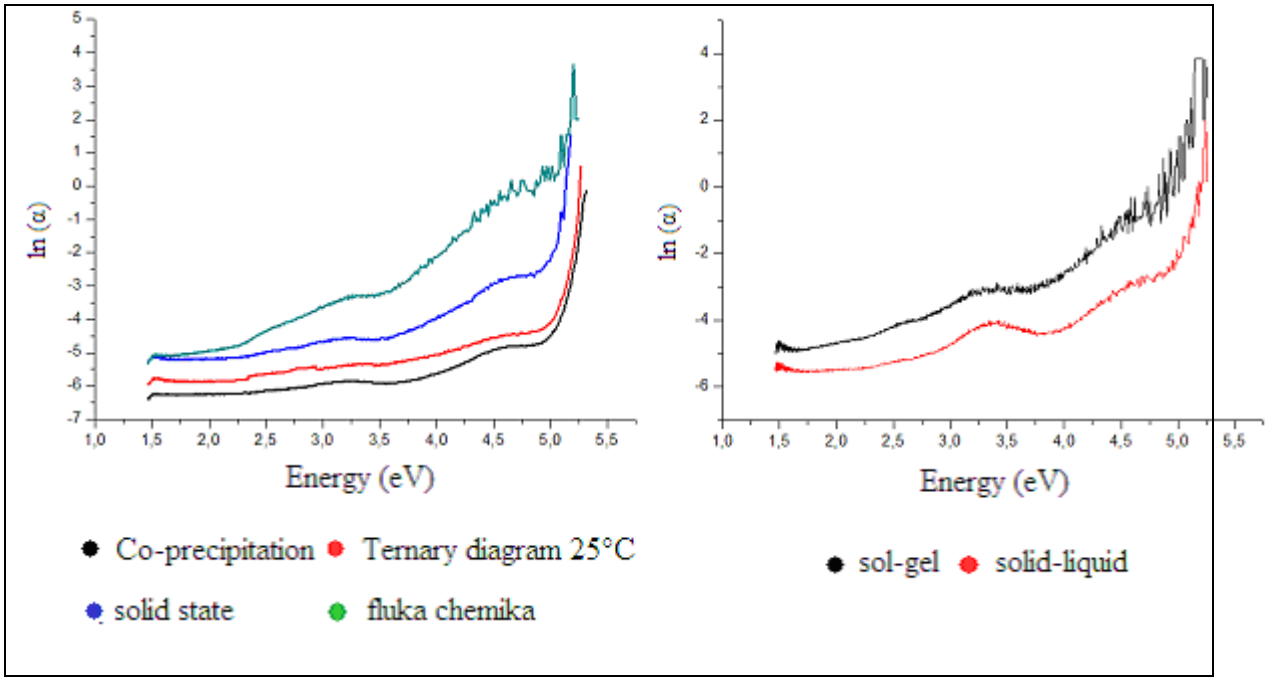

Figure 64. The change of ln (α) in Function of Energy (eV) for the HAP

It is possible to deduct the disorder from the variation of the absorption coefficients. The absorption coefficient is related to the disorder. According to the relation (4) determines the Urbach energy of HAP being the width of the band tail that characterizes the disorder, the study shown that there is a variation of Eu.

This disosder can be justificatied by pourful adsorption of all samples HAP. It can be said that the arrangement of atoms in the HAP samples is well organized; the methods of preparation of HAP have no effect on the arrangement of atoms.

Table 23. The values of the gap energy and Urbach energy for HAP by different methods

HAP and methode	HAP by Coprecipitation	HAP by ternary diagram 25°C	HAP BY Solid state	HAP (ref : Fluka chemika)	HAP by sol gel	HAP by Solid liquid
Eg^{opt} (ev)	5.37	5.37	5.13	5.25	5.24	5.25
Eu (ev)	0.20	0.20	0.20	0.20	0.22	0.21

The reciprocal of the slope of the obtained straight lines leads to determine the Urbach energy Eu. The obtained values of the band tail width were showns in "**TABLE 23,**".

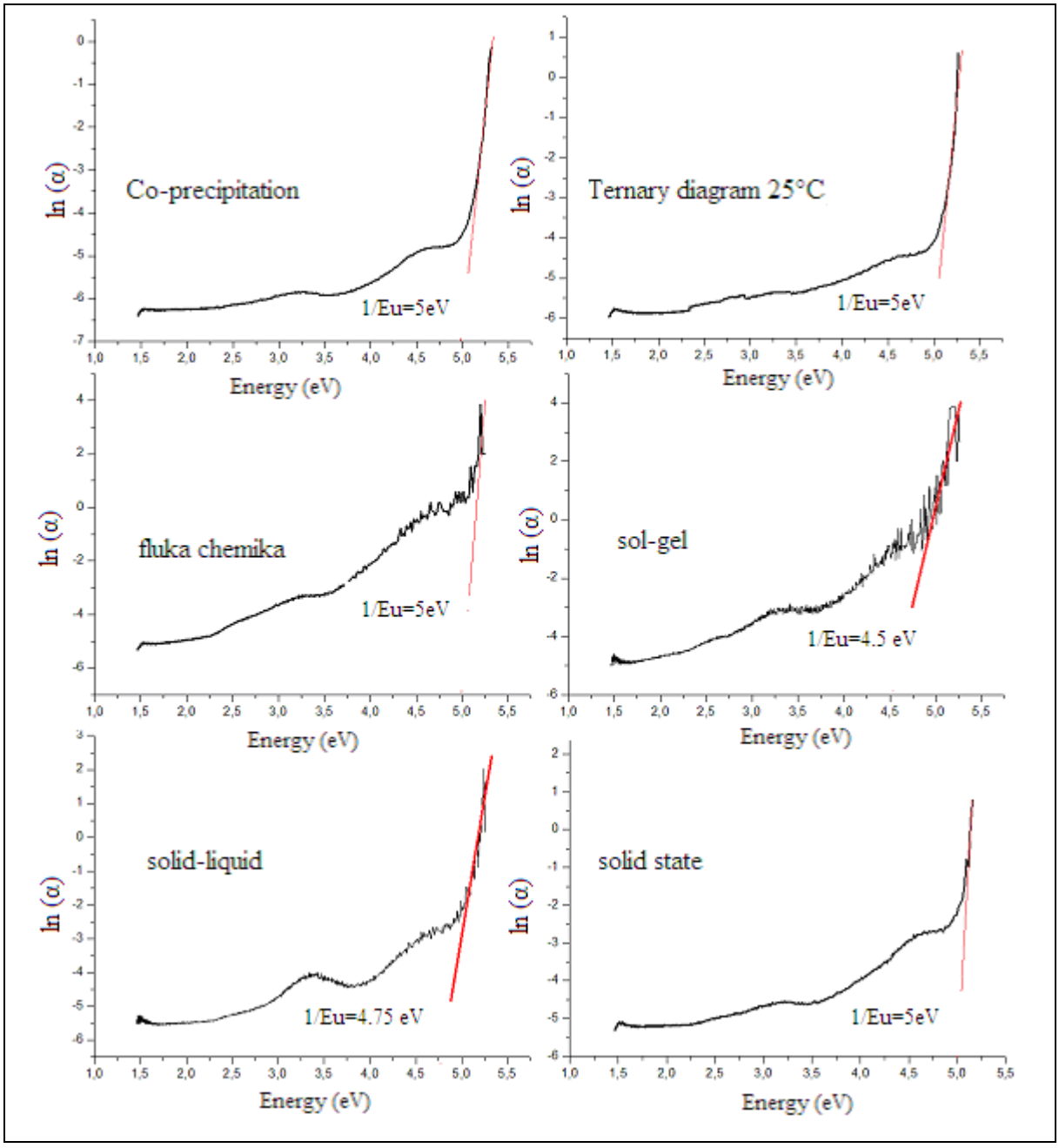

Figure 65. The determination of the disorder by extrapolation from the variation of ln (α) in Function of hν for HAP

IV.3.3 **FTIR**

FT-IR spectroscopy was performed in order to investigate the functional groups present in HAP, $Ca_{10}(PO_4)_6(OH)_2$ synthesized at 1000°C by coprecipitation, solide state, sol gel and solid liquid state methods, can be provider by IRAFFINITY-1S apparatus. The absorption peak in the region of 1600–1700 cm^{-1}, ascribed to O–H bending mode, is evidence of the presence of absorbed water in the synthesis products. These data clearly revealed the presence of various vibration modes corresponding to phosphate and hydroxyl groups. The FT-IR spectra of all samples has showns in the "**Fig. 66,**".

For all the samples the presence of strong OH vibration peak could be noticed. The peak observed at 625 cm^{-1} is attributed to the characteristic stretching and vibration modes of structural OH groups [407, 408]. The band at 1630 cm^{-1} corresponds to the adsorbed H_2O [409]. Bands characteristics of PO_4^{3-} tetrahedral apatite's structure are clearly observed at 473 cm^{-1}, 563 cm^{-1}, 960 cm-1, and 1033-1625 cm^{-1} [410, 411]. The peak at 473 cm^{-1} is attributed to $PO_4\nu_2$. The peak at 563 cm−1 is attributed to $PO_4\nu_4$. The peak at 960 cm^{-1} is attributed to $PO_4\nu_1$ and the peaks at 1033 -1625 cm^{-1} are attributed to $PO_4\nu_3$. The peak at 3250 and 3500 cm^{-1} are attributed to OH^-.

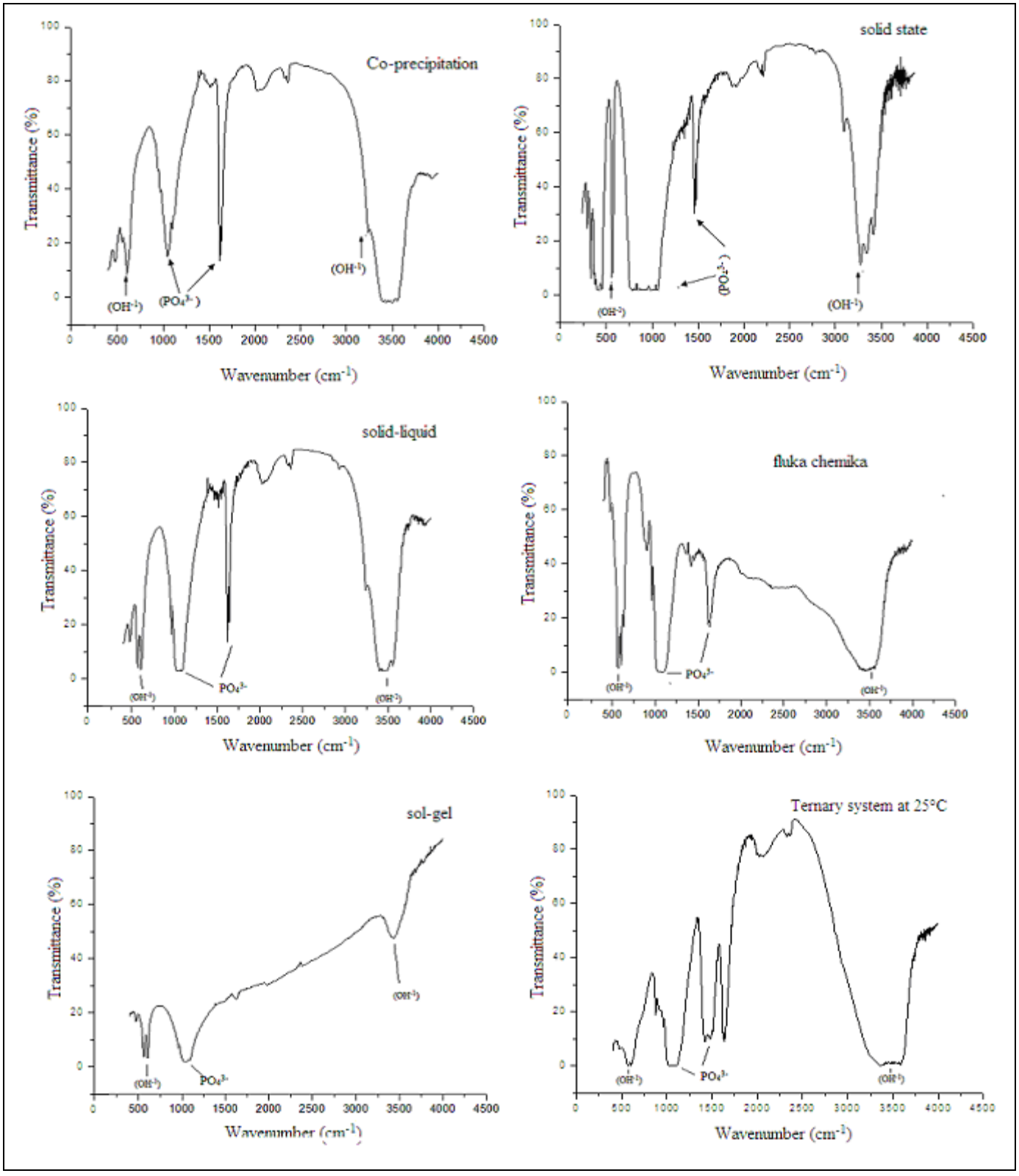

Figure 66. The transmittance infrared spectra of HAP samples synthesized by different methods

IV.4 Conclusion

In the above studies, HAP ceramic was synthesized by different methods for the purpose of choosing the best method for preparing HAP. The sample of HAP synthesized by sol gel with albumin has a hexagonal symmetry with small grain size. It is an ultra-fine powder without impurity, it is the best. The products have similar optical properties. The FT-IR analysis of the HAP samples showed vibratory modes corresponding to the phosphorus and hydroxyl groups for all HAP samples. Egg white contains 88% of the water and 12% of the various biological elements have given the opportunity to create a natural environment for the growth of HAP. These results show the success of the sol gel method by the egg's white for the synthesis of HAPs with suitable quality for potential applications in dental and orthopedic prosthesis due to its extreme homogeneity without impurity.

Chapter V:

HYDROXYAPATITE WITH CHROMOPHORE IONS, (Co^{2+}, Ni^{2+}, Cu^{2+}, Mn^{2+}), STRUCTURAL, VIBRATIONAL AND OPTO-ELECTRONICAL STUDY

V.1 Introduction

The crystalline structure arranges the atoms in crystal. These atoms are repeated periodically in space under the action of symmetry operations of the space group and thusly form the crystalline structure. This structure is a fundamental concept for m areas of science and technology. It is completely described by the crystal lattice parameters, its Bravais lattice, its space group and the position of the atoms in the asymmetric unit.

The HAP with general formula $Ca_{10}(PO_4)_6(OH)_2$ is a phosphorus apatite which crystallizes natural state in the hexagonal system [412, 413]. It is the main constituent of bones and teeth; it has excellent affinity with bone tissue. So, its advantage is to create strong chemical bond with the bone [414]. The HAP can be used also for the purification of aqueous media [415,416] and the immobilization of uranium in nuclear waste [417].

Around the world, m studies and substitution experiments have been carried out on HAPs to increase its physical, chemical and biological properties [418, 419, 420, 421]. The synthetic HAP used for orthopedic and dental application may be satisfactory in terms of mechanical properties [422, 423], but the problem of quick dislocation of crystalline structure is also present and causes damage of materials. By this study, we want to see the effect of weak Ca substitution of HAP by a metal ion (Mn^{2+}, Co^{2+}, Ni^{2+}, Cu^{2+}) on grain size and structural properties for increasing the mechanical properties of HAP.

When the atoms come together to form a solid, their valence electrons interact because of Coulomb forces, and they also sense the electric field produced by their own nucleus and that of the other atoms. In addition, two specific quantum mechanical effects occur. First, by Heisenberg's principle of uncertainty, constraining electrons to a small volume increases their energy.

V.2 Elaboration of Hydroxyapatite-Metal (HAP-M, M=Mn, Co, Ni, Cu)

Crystalline powders of HAP with general chemical formula $Ca_{10}(PO_4)_6(OH)_2$ were prepared by a solid-state method, all reagents are in the solid state. We mix and grind directly and manually with mortar and pestle a 1.5773 g of ammonium phosphate $(NH_4)_2HPO_4$ and 1.9927 g of calcium carbonate $CaCO_3$, then we put it in the oven at 200°C and we raise the temperature by 200°C and achieve the inter grinding after each 24 hours duration. Until we reach 1000°C.

Hydroxyapatite- metal-doped HAP-M, with chemical formula $Ca_{9.5}M_{0.5}(PO_4)_6(OH)_2$ where (M = Mn^{2+}, Co^{2+}, Ni^{2+}, Cu^{2+}) were also prepared by a solid-state method, and all reagents

precursors are in the solid state with well determined masses for each sample. See Table 24. We mix and grind directly and manually with mortar and pestle an ammonium phosphate $(NH_4)_2HPO_4$ and calcium carbonate $CaCO_3$ and precursor that contains metal for each sample as the following:

- Nickelapyrroline C_4H_6Ni for HAP- Nickel (HAP-Ni): $Ca_{9.5}Ni_{0.5}(PO_4)_6(OH)_2$.
- Copper (II) Chloride Dihydrate $CuCl_2.2H_2O$ for HAP-Copper (HAP-Cu): $Ca_{9.5}Cu_{0.5}(PO_4)_6(OH)_2$.
- Cobalt (II) nitrate hexahydrate $CoN_2O_6.6H_2O$ for HAP- Cobalt (HAP-Co): $Ca_{9.5}Co_{0.5}(PO_4)_6(OH)_2$.
- Manganese (II) carbonate CMnO3 for HAP- Manganese (HAP-Mn): $Ca_{9.5}Mn_{0.5}(PO_4)_6(OH)_2$.

Each sample was prepared independently of the others. And we follow the same thermic treatment than the HAP in the oven from 200°C to 1000°C and we raise the temperature by 200°C realizing an inter grinding every 24 hours duration.

The synthesis process as resumed in graphical representation as shown in (Fig. 67).

Table 24. Mass of reagents for synthesis of HAP HAP, HAP-M (M=Ni, Cu, Co, Mn).

Precursor Sample	$(NH_4)_2HPO_4$ (g)	$CaCO_3$ (g)	Precursor of metal (g)
HAP	1.5773 g	1.9927g	0 g
HAP-Ni	1.5627 g	1.8755g	m(C_4H_6Ni) = 0.2454 g
HAP-Cu	1.5627 g	1.8710g	m($CuCl_2.2H_2O$) = 0.1677 g
HAP-Co	1.5627 g	1.8753g	m($CoN_2O_6.6H_2O$) = 0.1853 g
HAP-Mn	1.5627 g	1.8790g	m($CMnO_3$) = 0.1136 g

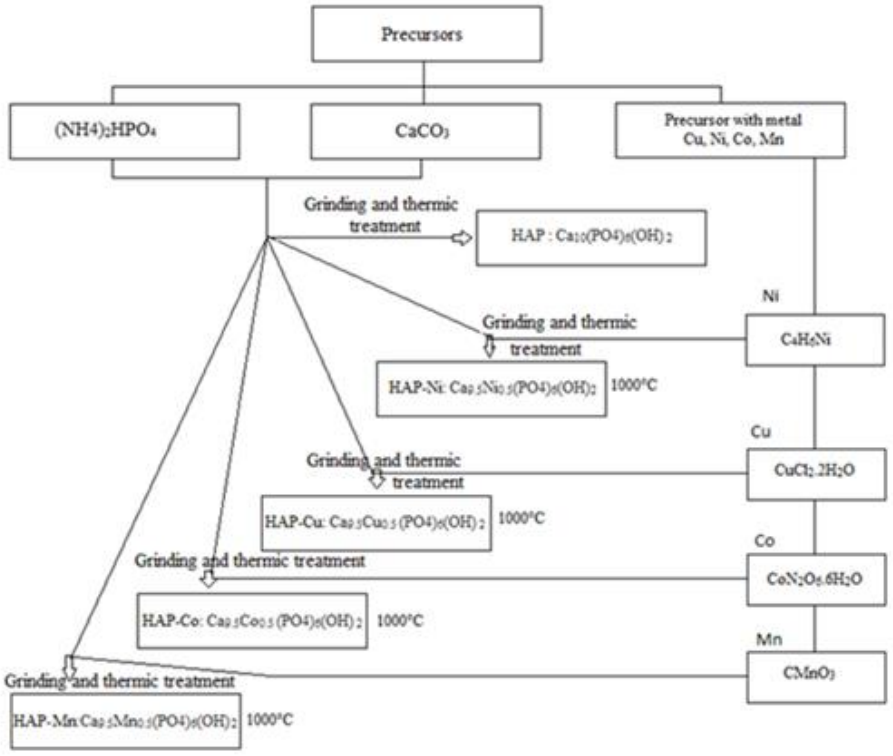

Figure 67. The synthesis process for HAP, HAP-M (M=Ni, Cu, Co, Mn) by solid state method.

V.3 Characterization

V.3.1 **XRD treatment by Rietveld refinement**

The structure of HAP has examined using XRD Bruker D8 ADVANCE. X-rays are electromagnetic radiation with photon energies in the range of 100 eV - 100 keV. For diffraction applications, only short wavelength x-rays (hard x-rays) in the range of a few angstroms (Å) to 0.1 angstrom (1 keV - 120 keV) are used. X-rays are ideally suited for probing the atomic structure of solids because their wavelengths (0.1-2Å) are of comparable length to the radii of atoms and they are sufficiently energetic to penetrate most solid materials to provide information about the bulk structure [424].

XRD pattern of the sample HAP showed the structure of the prepared sample was similar to the HAP as shown in Figure 68. There is a high consistency between the data of HAP and that from of the standard database, with lattice dimensions of a = b = 0.120632 nm, c = 0.168488 nm. None of the other impurity was observed in the XRD pattern, indicating that the chief inorganic phase of the sample is HAP crystal. The result obtain was similar to [425] as reported. When

the initial phase is replaced by the transition elements, it has been found that the cell changes the hexagonal structure to the monoclinic. Also, the size of the crystallites in nanometers of the samples which are synthesized by the solid-state method is found. The sizes of the crystallites have an effect on the cell volume. Table 25 shows the parameters of the cell of each structure.

Table 25. The structural data of the HAP AND HAP-M (M=Ni, Co, Cu and Mn).

Samples	**HAP**	**HAP-Ni**	**HAP-Cu**	**HAP-Co**	**HAP- Mn**
Cristal system	Hexagonal	Monoclinic	Monoclinic	Monoclinic	Monoclinic
S.Group	P 6/m mm	P 2/m	P 2/m	P 2/m	P 2/m
a(Å)	12.06	14.10	10.93	19.39	12.28
b(Å)	12.06	16.17	12.04	3.64	13.86
c(Å)	16.84	8.74	5.49	12.45	6.47
v(Å)	2123.37	1984.69	718.66	881.15	1100.52
Alpha(°)	90	90.00	90.00	90.00	90.00
Beta(°)	90	96.07	96.58	91.26	93.29
Gama(°)	120	90.00	90.00	90.00	90.00
D(nm)	3,60	4,53	2,70	4,77	5,30

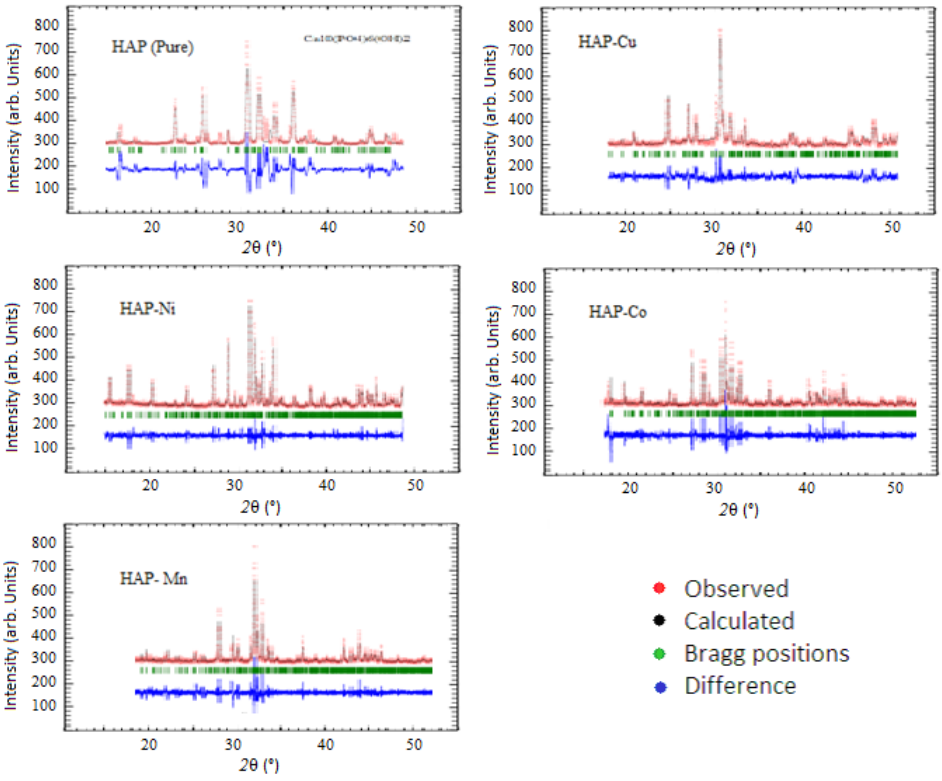

Figure 68. The XRD spectra HAP and HAP-M (M=Ni, Cu, Co, Mn).

The grain size of the different Samples was determined using the spectra of the DRX and the debye-Scherrer formula (11) [426]:

$$D=k*\lambda/B.\cos(\theta) \qquad (11)$$

D (nm): the grain size=1 the constant λ: the beam wavelength of the X-rays used, B the width at mid-height of the most peak, θ the diffraction angle expressed in radian. The width at half height and the size of the grains are inversely proportional and their variation as a function of the doping rate. The steric influence of the M^{2+} (Mn^{2+}, Co^{2+}, Ni^{2+}, Cu^{2+}) cation can be studied comparing the cell parameters.

The compounds HAP crystallize in the hexagonal cristal system with the P6/mmm space group like the work in reference [427], and all other HAP-M (M=Ni, Cu, Co, Mn) crystallize in the monoclinic cristal system with the P2/m space group like the work in reference [428].

This change of crystal system has an influence on the structural parameters of each HAP [429], which also have an influence on the optical and electronic properties of each HAP [430, 431]

according to the incorporated metal Ni, Cu, Co and Mn. We see that each cell of HAP has a unique structural parameter values different to others according to the inserted metal. To have more structural stability, the atoms reorganize themselves for minimizing interatomic vibration [432] and electrical interactions [433]. In this case, the pure HAP stabilizes in the hexagonal system, but after the incorporation of the metal ions in its structure, the HAP is stabilized in the monoclinic system with unique cell volume for each HAP-M product. These cell volume variation results for each product can explain the variation in urbach energy [434]. Less the cell volume of HAP decreases after the metal inserter, the structural disorder is lower, and the urbach energy remains small and near to that of the initial HAP phase. The greatest urbach energies in this study are those of HAP-Co and HAP-Cu which have the smallest cell volume which causes a great variation of the structural parameters a, b and c of the cell of HAP, this variation is shown in Figure. 69. This parameter variation has an influence on the diameter of the HAP's grains as shown in Figure. 70 and shows that the grain size of all HAP-M has increased compared to the initial size of pure HAP except in the case of HAP-Cu which has the smallest grain size with smaller cell volume.

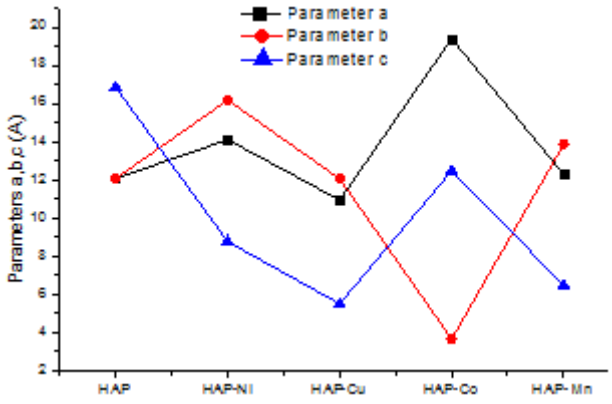

Figure 69. A Variation of the lattice parameters of HAP and HAP-M (M=Ni, Cu, Co, Mn).

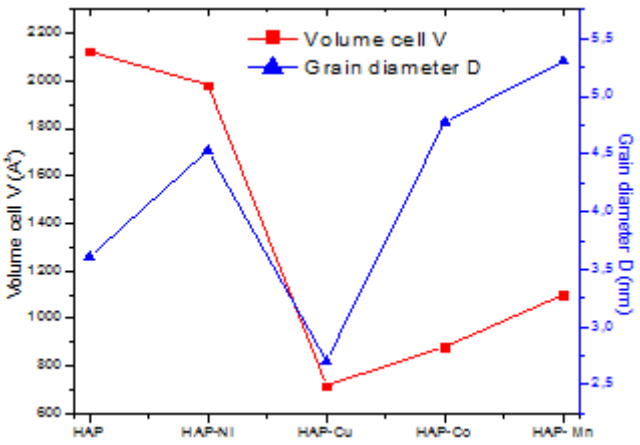

Figure 70. Volume cell and grain diameter of HAP and HAP-M (M=Ni, Cu, Co, Mn).

V.3.2 FTIR: Band assignments and Descriptions of vibrations mode in HAP-M (M= Ni, Cu, Co, Mn)

FTIR spectroscopy is an optical technique that detects molecular bond vibrations and rotations upon absorption of infrared light. Because different chemical functional groups absorb IR light at different frequencies [435], FTIR spectroscopy can be used for chemical structure analysis, chemical fingerprinting and chemical imaging [436]. This absorption has shown the existence of the bonds of samples, the infrared spectrum represents the transmittance (T) on the ordinate; it is expressed as a percentage (%) according to the waves number, and is expressed in (cm^{-1}). We can see that the absorption strips are pointing downwards a low transmission value corresponds to a high absorption and each band is characterized by its position, width and intensity [435]. FTIR spectroscopy thus provides both qualitative and quantitative information and is shown to be an effective companion technique to X-ray diffraction, The FTIR spectra show the bands arising from inter atomic vibrations.

The FTIR spectrum was scanned from 4000-400 cm^{-1} by FTIR Perkin Elmer apparatus using the KBr-disc method for identified the functional groups of the HAP. The broadband at 3250 and 1500 cm^{-1} were attributed at absorbed water, while sharp peak at 3500 cm^{-1} was attributable to the stretching vibration of the lattice HO^- ion and medium sharp peak at 700cm^{-1} was assigned to the OH deformation mode. The characterization band for PO_4^{3-} appear at 470, 610, 1030 and 1070 cm^{-1} and 1350cm^{-1} for samples substituted by transition elements. The observation of the asymmetric P-O stretching vibration at the PO_4^{3-} band at 1070cm^{-1} for HAP no substituted and 1350 cm^{-1} as a distinguishable peak, together while the sharp peaks at 700,610 and 470 cm^{-1}

correspond to the triple degenerate bending vibration of PO_4^{3-} in HAP. Our FTIR results were similar to those reported [425,437]. All FTIR spectrums of all our samples are shown in (Fig. 71) and the band shape and assigned vibration mode function frequency as reported in Table 26.

Table 26. The FT-IR band assignments for HAP and HAP-M (M= Ni, Cu, Co, Mn).

Number of peaks	Frequency ν (cm^{-1})	Assigned vibration mode	Band shape HAP (Pure)	Band shape HAP-Ni	Band shape HAP-Cu	Band shape HAP-Co	Band shape HAP-Mn
1	470	PO_4^{-3}	low intense	low intense	low intense	low intense	low intense
2	610	PO_4^{-3}	Intense	wide	wide	wide	wide
3	700	OH^- out – of – plane bending	low intense	low intense	low intense	low intense	low intense
4	1030	PO_4^{-3}	Intense	wide	wide	wide	wide
5	1070	PO_4^{-3}	low intense	low intense	low intense	low intense	low intense
6	1350	PO_4^{-3}	low intense	low intense	low intense	low intense	low intense
7	1500	H_2O	low intense	low intense	low intense	low intense	low intense
8	1625	H_2O	Intense	intense	intense	intense	intense
9	2010	H_2O	low intense	low intense	low intense	low intense	low intense
10	2375	H_2O	low intense	low intense	low intense	low intense	low intense
11	2880	H_2O	low intense	low intense	low intense	low intense	low intense

12	3250	H_2O	low intense	low intense	low intense	low intense	low intense
13	3500	H_2O and HO^{-1}	Wide	wide	wide	wide	wide
14	3800	structural stretching	low intense	low intense	low intense	low intense	low intense

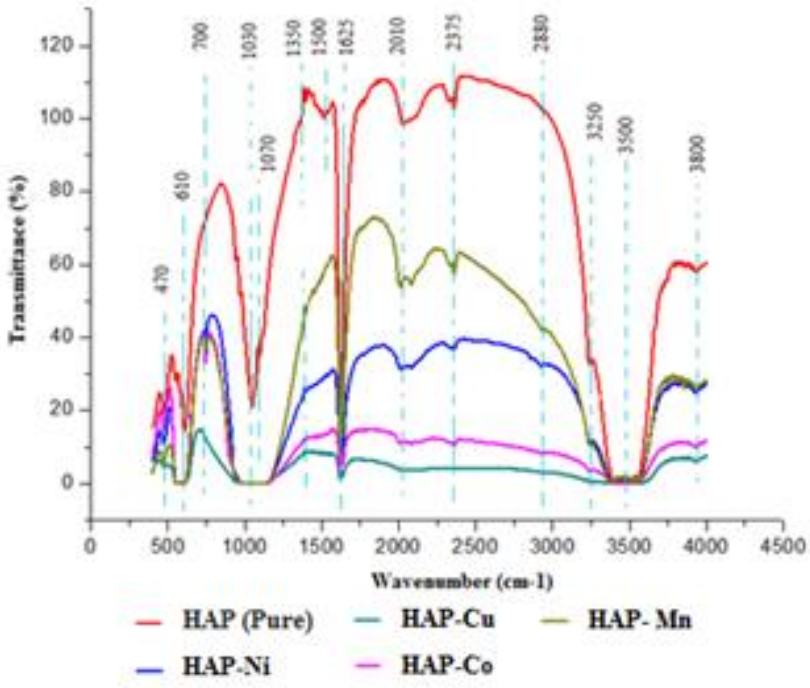

Figure 71. The FTIR spectra of pure HAP and HAP substituted by transition elements (Ni, Cu, Co and Mn).

V.3.3 **Optical properties**

- Uv-visible light transmission and absorbtion spectrum of HAP-M (M=Ni, Cu, Co, Mn).

The optical properties of the pure HAP and HAP-M were determined from the transmittance measurement in the range of wavelength 200-850 nm as shown in Figure.72. The transmittance spectra of our samples are very significatif. As for solid samples, are not the same absorption bands. For the pure HAP, the absorption band is not found, However , the absorption bands have been found in the case of the substituted HAP-M, these bands are related to charge transfer phenomena between metals ions transition element Cu^{2+}, Co^{2+}, Ni^{2+}, Mn^{2+} and Ca^{2+} ion of HAP

Figure. 73. In the case of copper Cu^{2+} ion there are two bands centered on 450 and 750 nm, cobalt Co^{2+} ion found three bands around 750, 550 and 610 nm. High intensity and width are observed may explain the probability of transition [438]. The UV–visible absorption of the HAP-Co is greatly enhanced compared with that of HAP. This remarkable absorption of HAP-Co is attributed to Co in different coordination environments which is caused by substitution of Co for Ca in HAP crystal .Meanwhile, these doped Co ions can introduce an energy level into the electronic band structures of HAP-Co, which leads to the photocatalytic activity under visible light [439].

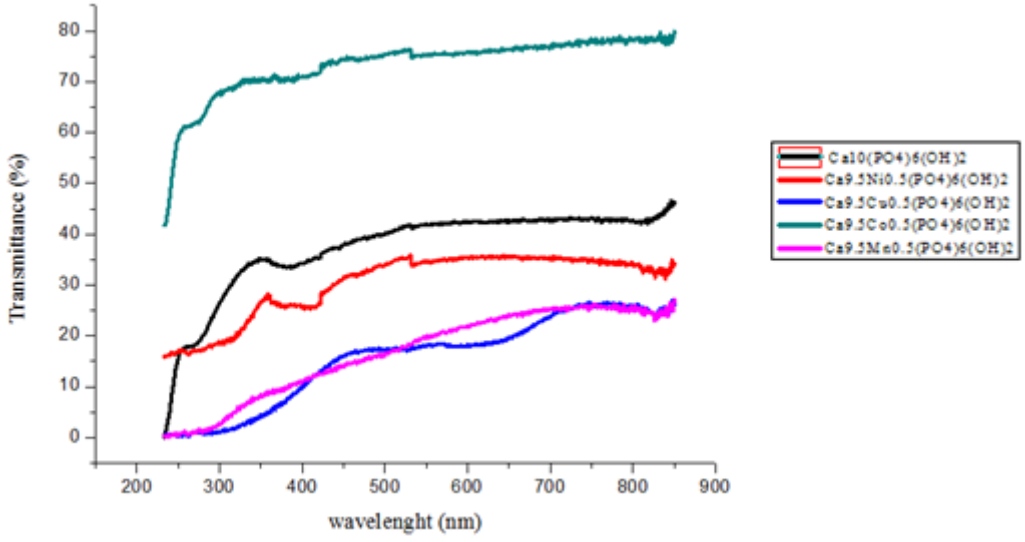

Figure 72. The Transmission spectra of HAP and HAP-M (M=Ni, Cu, Co, Mn).

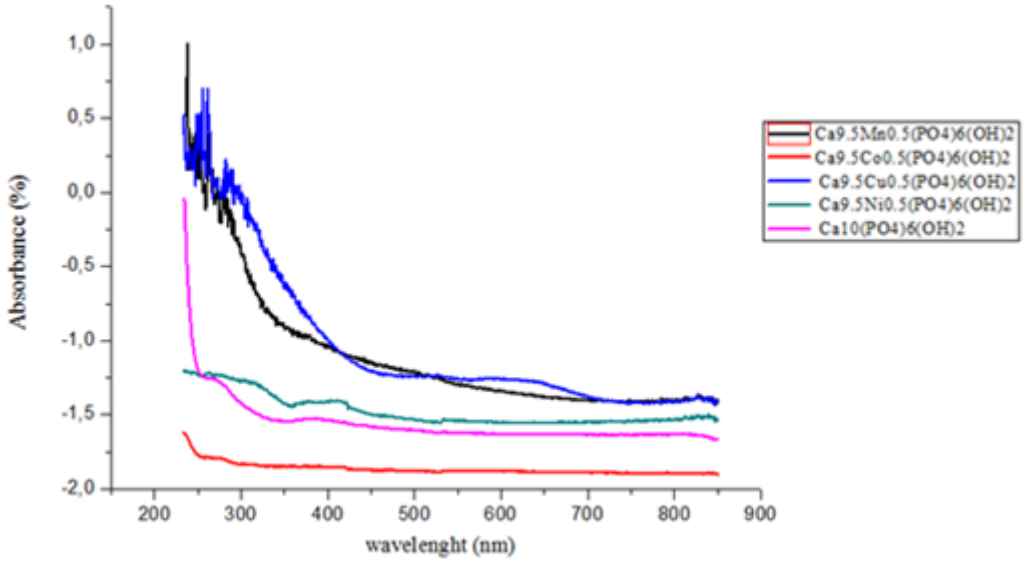

Figure 73. The absorption spectra of HAP and HAP-M (M=Ni, Cu, Co, Mn).

- Opto-electronial properties

- Gap energies of HAP-M (M=Ni, Cu, Co, Mn)

The optical gap for all our samples has been deduced by transmittance spectra using the Tauc's relationship (12) [439] :

$$\alpha h\nu = \alpha_0 (h\nu - E_g)^n \qquad (12)$$

α: absorption coefficient, h: Planck constant, α_0: constant; E_g: gap energy; n = 2 in the case of a direct gap. We plot $(\alpha h\nu)^2$ function $h\nu$, the value of the gap energy is obtained by the extrapolation of the linear part of the curve on the abscissa axis ($h\nu$). All spectrum of dependence of $(\alpha h\nu)^2$ On energy (eV) of HAP and HAP-M as shown in Figure. 74.

- Urbach Energy of HAP-M (M=Ni, Cu, Co, Mn)

The Urbach energy (Eu) reflects the disorder state of the material [440]; it is related to the absorption coefficient by the following relationship (13) [441]:

$$\alpha = \alpha_0 e^{(h\nu/Eu)} \qquad (13)$$

Where (α) absorption coefficient and photon energy ($h\nu$) and Eu is energy of Urbach. We plot Ln(α) function energy ($h\nu$). The Urbach energy (E_U) was deduced by calculate the inverse slope of linear part extrapolation of spectra for each sample. All results as showns in figure 75.

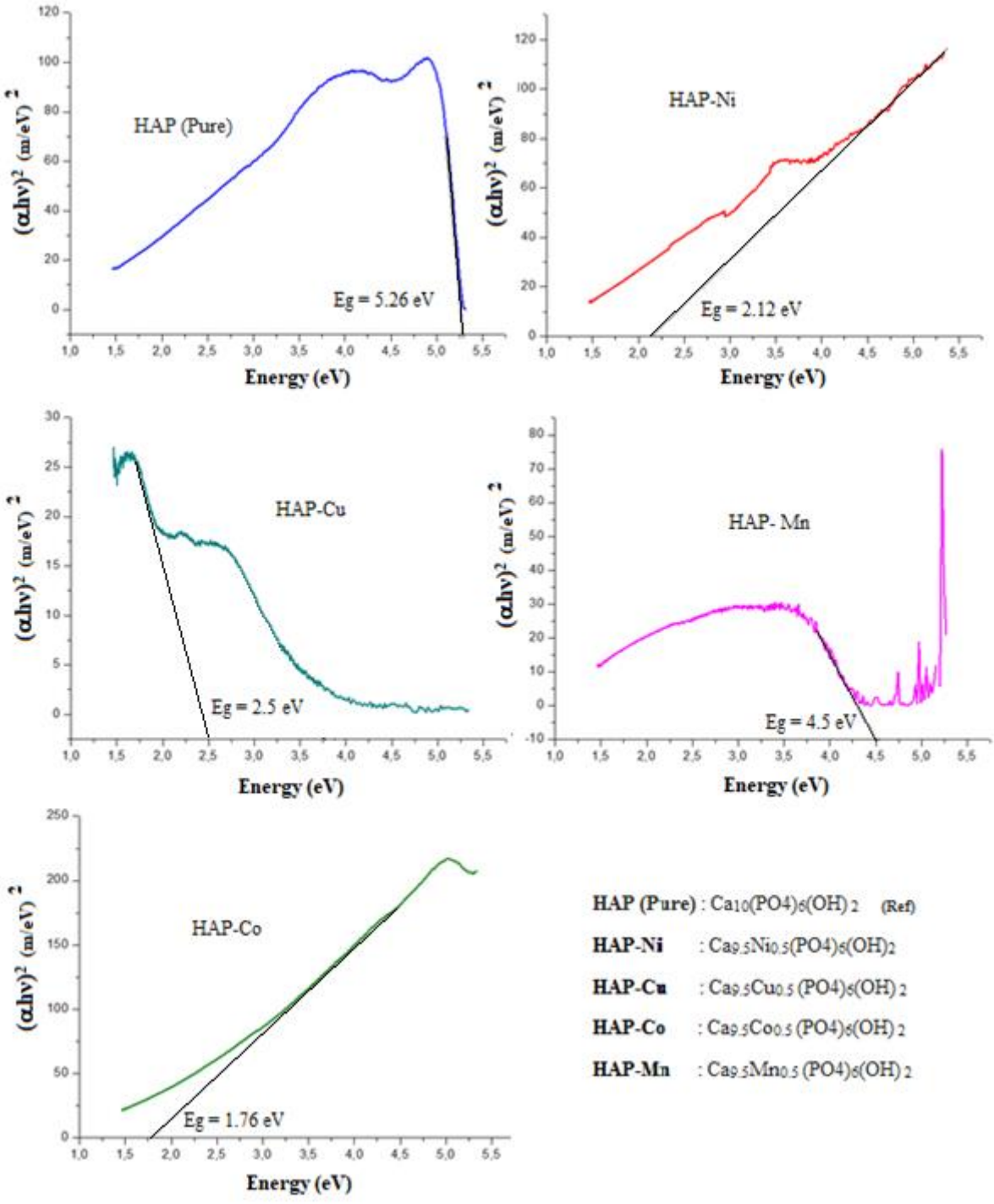

Figure 74. The dependence of (ahv)2 on energy (eV) of HAP and HAP-M (M=Ni, Cu, Co, Mn).

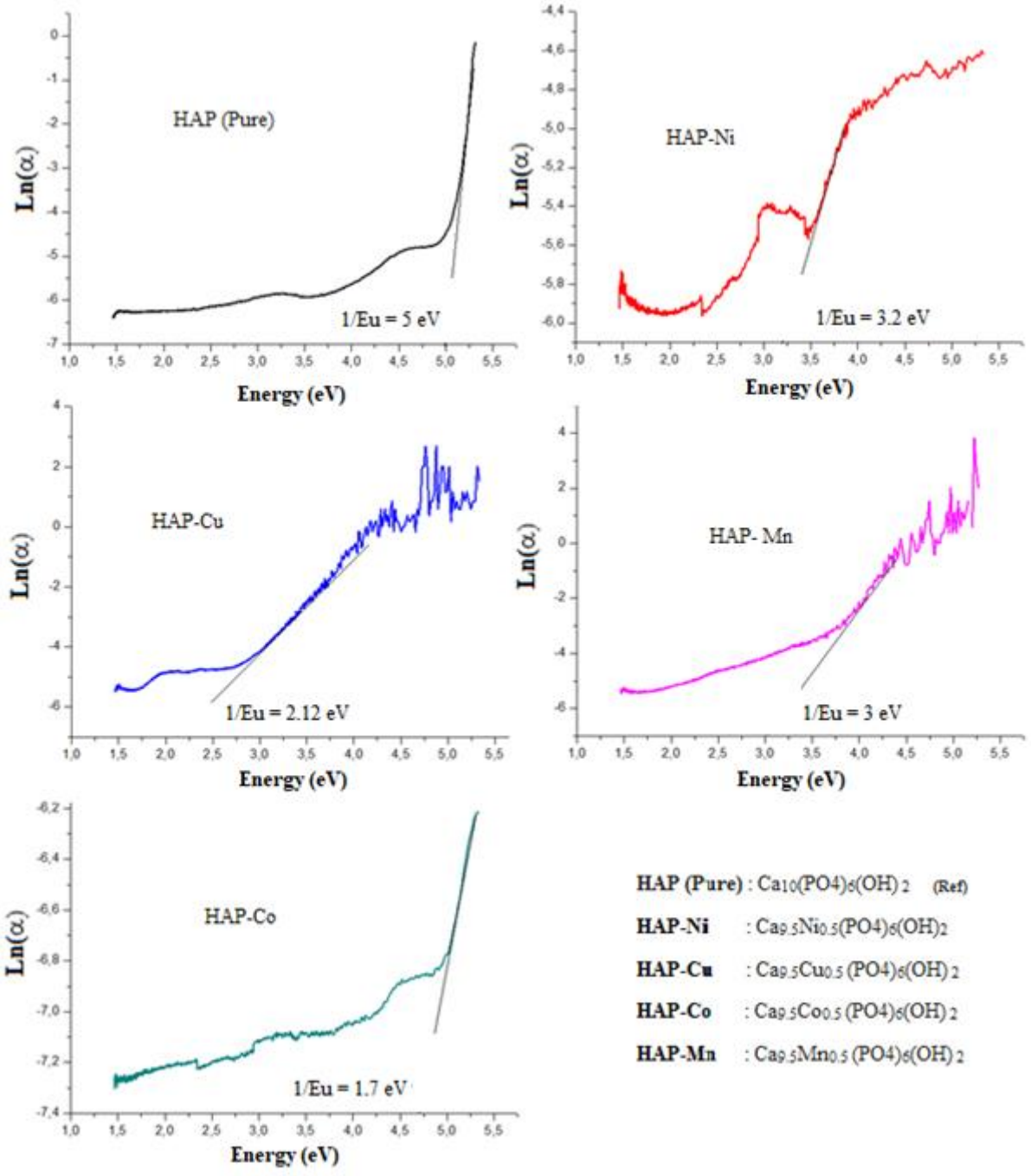

Figure 75. Determination of the Urbach energy of HAP and HAP-M (M=Ni, Cu, Co, Mn).

In the case of crystalline materials, the energy separating the valence band from the conduction band is perfectly defined by Ev and Ec. The energy Ec - Ev corresponds to the energy of the

forbidden band [442]. The shape of the distribution functions of the energy states is a parabola [443]. see Figure 76.

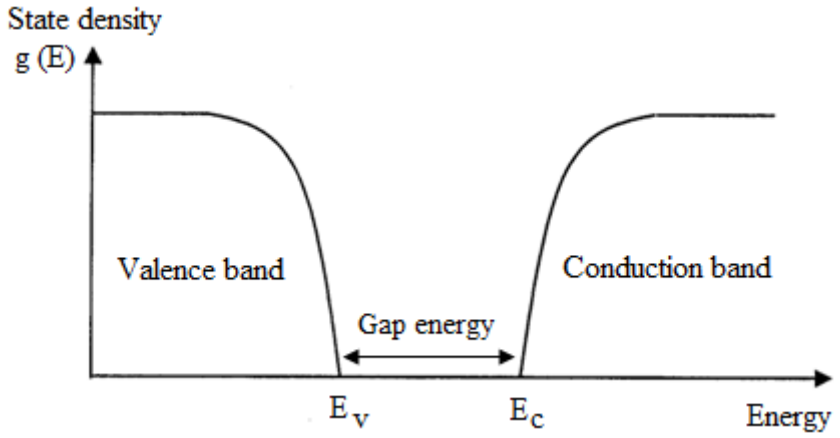

Figure 76. The State density function as energy for HAP pure before incorporing metals [525].

When in a material occur variations of interatomic distances, lengths or angles of connection, there appears what is called a "disorder". In this case, the band edges described in the case of crystal lattices and delimited by Ev and Ec may disappear. We observe what are called localized states formed at strip tails at the boundaries of the forbidden band in the valence and conduction band [444]. For energies higher than Ec and lower than Ev, are the extended states (Figure 77).

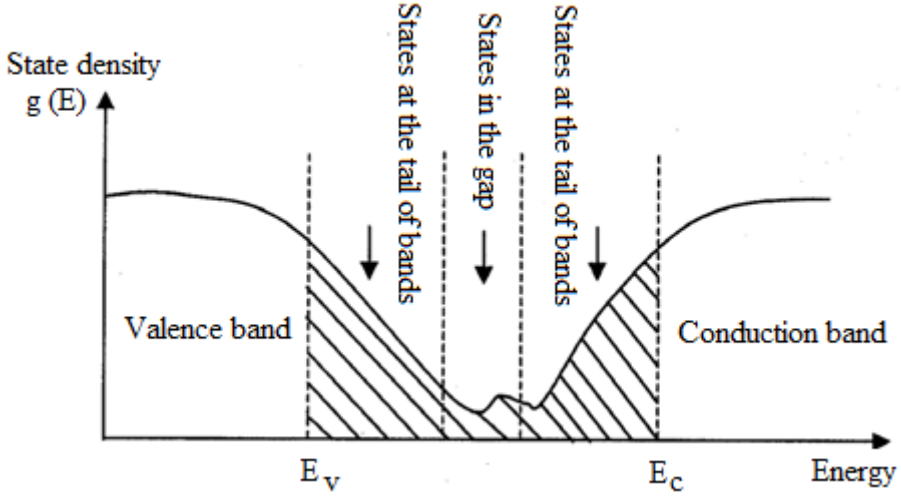

Figure 77. The State density function as energy for HAP after incorporing Metals ions [525].

When the disorder becomes too important (for example with the appearance of links dangling or impurities in the material), the tails may become entangled. Caused by Urbach parameter (E_u) which corresponds to transitions between the extended states of the valence band and the localized states of the conduction band. The decrease or increase of the energy of Urbach is translated successively by the decrease or increase of the structural disorder and the improvement of the stoichiometry [445], which is due in this case to the incorporation of the metal ion in the structure of HAP. Urbach energies as showns in table 27 presents the disorder of the material.

Table 27. The value of the gap energy and Urbach energy for HAP

Samples	**HAP**	**HAP-Ni**	**HAP-Cu**	**HAP-Co**
Optical Gap energy (eV)	5.26	2.12	2.5	1.76
Urbach energy (eV)	0.20	0.25	0.47	0.57

It is found that the Urbach energy has increased after the incorporation of the metal ions in the HAP matrix, because these metal ions are considered as impurities in the HAPs and present more structure disorder of the initial cell of hydroxyapatie. See figure 78.

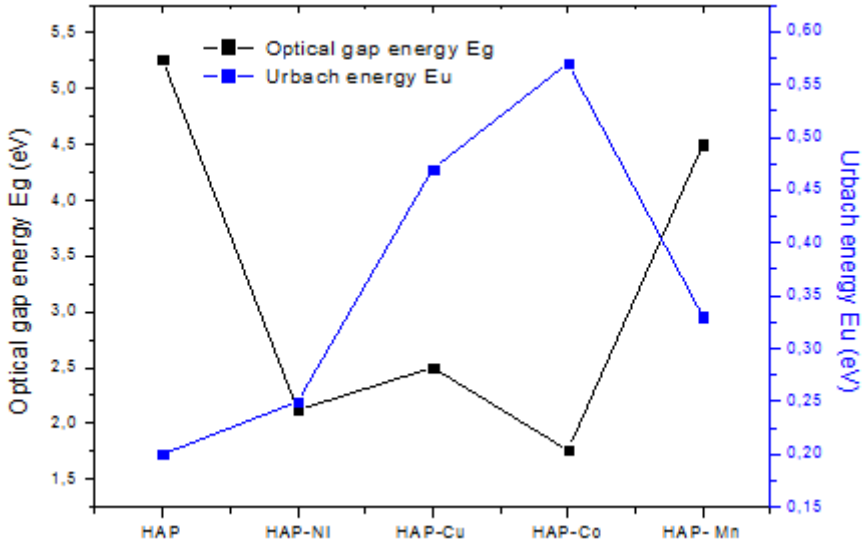

Figure 78. Optical gap energy and Urbach energy of HAP and HAP-M (M=Ni, Cu, Co, Mn).

V.4 Conclusion

The results obtained from the characterization of X-ray diffraction made it possible to observe the presence of the single phases of the HAP powder. The substitution of Ca^{2+} by M^{2+} (M^{2+} = Mn^{2+}, Co^{2+}, Ni^{2+}, Cu^{2+}) exhibit a decrease in the cell volume of all powders HAP-M (M= Mn^{2+}, Co^{2+}, Ni^{2+}, Cu^{2+}) and a decrease in transmittance of infrared light. The most striking aspect of the set of samples is their high crystallinity, preferential orientation of the crystallographic planes powders powders HAP-M (M= Mn^{2+}, Co^{2+}, Ni^{2+}, Cu^{2+}) influenced by the preparation technique itself and the operating conditions (chemicals, annealing temperature, etc.). It should also be noted, the widening of the feet of diffraction lines for all the powders explored. The incorporation of Co, Ni, Cu and Mn metal ions in HAP gave us four biomaterials for the use in dental amalgams, with more mechanical and electronic performance, and less risk of toxicity compared to metal amalgams that cause problems of toxicity and inflammation. These results can also be used in the orthopedic application to solve the problem of increasing concentration of cobalt after installation cobalt chromium alloy of Hip metal implant that causes inflammation problems. The incorporation of Co, Ni, Cu and Mn metal ions in HAP gave us four biomaterials for use in solar panels, with more mechanical and electronic performance, and less risk of the environment pollution due to its biodegradable properties. The decrease of the electrical gap energy of all our samples HAP-M (M = Co, Ni, Cu, Mn) compared to the pure HAP, gives the possibility to its use as semiconductor materials with high photovoltaic activity. The samples of HAPs HAP-M (M = Co, Ni, Cu, Mn) are sparsely colored and their colors can be exploit fo esthetic reason, for product the solar panels with different colors. The low Urbach energy value of all our HAP-M (M = Co, Ni, Cu, Mn) exhibit a high stcuctural stability wich result a long lifespan of our powder and solar panels.

Chapter VI:

EXTRACTION, OPTIMISATION AND CHARACTERISATION OF CHITOSAN FROM SHRIMP SHELLS

VI.1 Introduction

The chitosan and chitin are the most important substances in the fabric of medicines [446] and products with anti-microbial [447] and anti-bacterial properties [448], they provide anticancer activity against human monocyte leukaemia cell line [449]. Also, M. Bouhenna et al demonstrated in 2015 that chitin and its derivatives have a dose-dependent cytotoxic effect against Human larynx carcinoma cell lines and Human embryo rhabdomyosarcoma cell lines, indicating that there are several types of interactions between the charged groups of molecules and tumor cells such as electrostatic interactions between the negative charges of tumor cells groups and the positive charges of groups tested and interactions between hydrophobic groups and tumor cells derived molecules [450].

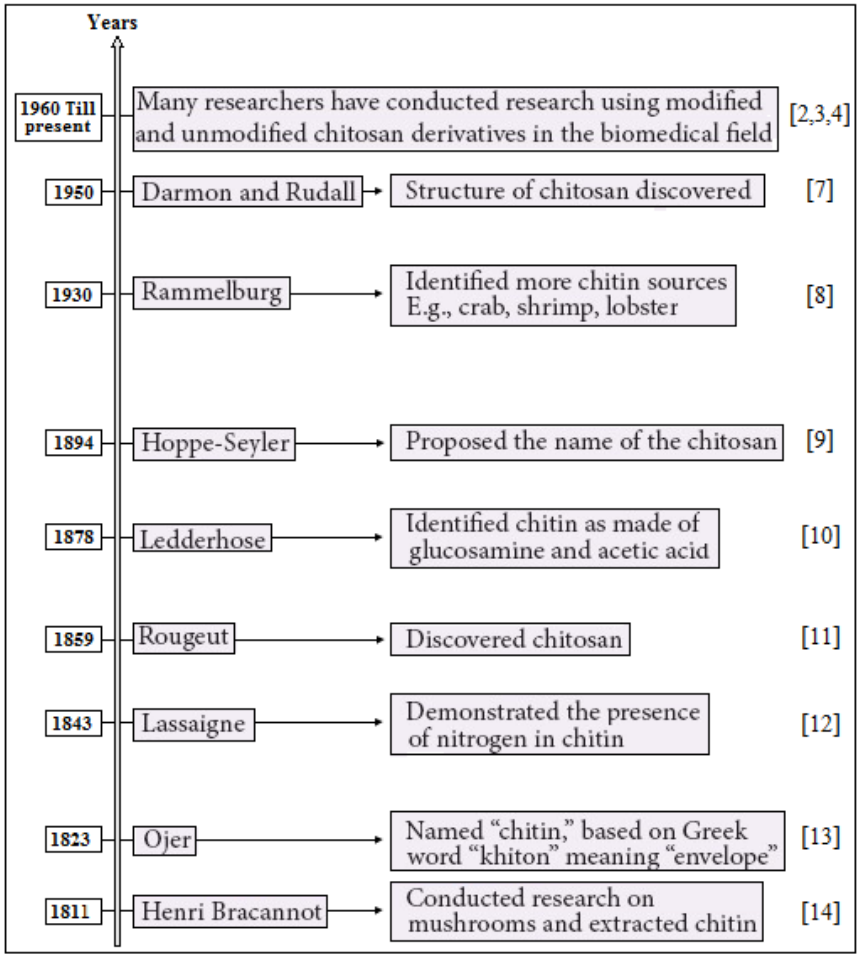

Figure 79. History of the most important events that have been achieved for chitin and chitosan between the years 1811-1950s.

Total global production of captured and farmed shrimp reached 6 million tons in 2006 (FAO, 2009), with only 60% being used as food, leaving 2.3 million tones for non-food uses. Shrimp waste, which is rich in chitin, proteins, lipids, pigments and flavor compounds, has potential commercial value in the food industry [461]. Since their first discovery by Henri Bracannot in 1811 through their research on mushrooms till present, several major events have occurred for chitin and chitosan materials. We summarize in Fig.79, the most important events that have been achieved for chitin and chitosan by different scientists around the world in different research fields between the years 1811-1950s [452, 453, 454, 455, 456, 457, 458, 459].

Furthermore, in 1993 Rane et al [460] evaluated the alkali and acid treatments for chitosan extraction from Fungi, using sodium hydroxide with varying extraction times at 95 °C and 121 °C as alkali treatment and chloric, formic and acetic acids as acid treatment at 95 C with various extraction time durations. They concluded that the highest yields of chitosan under alkaline extraction is at 121 °C for 30 min and chloric acid extraction at 95 °C for 12 h with effects on the degree of deacetylation and viscosity of chitosan. Another study by Percot et al in 2003 [461] defined the optimal conditions to extract chitin from shrimp shells, showing the role of temperature on remains of calcium and proteins on chitin, the weight of molecules, and degrees of acetylation (DA). According to them, the elimination of minerals is complete in time duration around 15 min at home temperature with excess of chloric acid 0.25 M. The deproteinization is well obtained in 1 M of sodium hydroxide within 24 h at 70 °C without effect on the molecular weight or the DA. In this case, the remains of calcium in chitin are under 0.01%, and the DA is about 95%. Besides, Burrows et al in 2007 [462] extracted chitosan from crab exoskeleton as a seed fungicide, using either 0.5%, chloric acid 1.0% and acetic acid 5%. The chitosan extracted with 0.5% chloric acid had the most effect in eliminating fungus and plants growth enhancer. Recently, from several studies [463, 464, 465], waste fungal biomass that results from various pharmaceutical and biotechnological industries set out a potential source of chitosan and must be considered. From the review of Kaur et al In 2013 [466], chitosan was extracted from waste fungal mycelium, using 0.5M of NaOH for alkali treatment at 121°C between 30 and 45 min time duration under agitation. The acidic treatment was carried out by 0.1-0.2M of sulfuric acid under centrifugation at the same temperature and time duration of alkali treatment. The

deacetylation step was performed in a basic solution with pH 8-10 by 1N of NaOH and finished by cleaning with acetone, ethanol and distilled water.

The chitosan is elicited worldwide from shrimp shells, lobsters or crabs by the classical method through generally adding acids for demineralization and bases for deproteinization then sodium hydroxide for deacetylation [461, 466]. Currently, chitin and chitosan are extracted mainly from shrimp shells, with industrial production mostly concentrated in Asia with limited production and strong global demand. The demand for chitin in 2015 was more than 60,000 T, but the world production that year was about 28,000 T. according to a report by Global Industry Analysts Inc. (chitin and chitosan derivatives market report - 2015) which shows an insufficient global production on chitin and chitosan. Global applications of the chitosan market include water treatment, food and beverages, cosmetics, bioplastics, biomedicine, agrochemicals and others. All of this previous information indicates the importance of chitin and chitosan materials. In this study, we tried to highlight the effect of a high concentration of acidity and basicity on the extraction of chitosan from shrimp shells. For this reason, we focused in this study on comparing between the effect of diluted and concentrated chloric acid. Sometimes we introduce the concentrated nitric acid and sulphuric acid for showing the effect of other acids and indicate the best acid for chitosan production. We used the diluted chloric acids 1M (usually used in chitosan production) and chloric acid 20% (CA20%), nitric acid 70% (NA70%), sulphuric acid 98% (SA98%). We employed ammonia 20% as a base for deproteinization and deacetylation in the case of concentrated acids, instead of sodium hydroxide NaOH used in case of diluted chloric acid. The first reason to use ammonia NH_4OH as a base instead of NaOH is to remove proteins in the first step and radical's acetyl group in the second, without remains of Na^+ in chitosan product. Laribi-Habchi et al in 2015 used ammonium sulphate for chitin proteins purification [467] since ammonium sulphate is an ionic chemical compound of formula $(NH_4)_2SO_4$ with ammonium salt NH_4^+ and sulphuric acid H_2SO_4. We are looking for changes that have occurred on chitosan in this production. All chitosan products are well characterized by different X-ray diffraction (XRD) spectroscopy, X-ray fluorescence (XRF) analysis, UV-Visible spectroscopy, Fourier Transformed Infra-Red (FTIR), Raman Spectroscopy, Thermogravimetry and Derivative thermogravimetry (TG/DTG), Scanning Electron Microscopy (SEM), Energy-dispersive X-ray spectroscopy (EDX) analysis, in order to have

maximum information about the physical properties, to be referred and compared to those of commercial chitosan purchased from Fluka Chemika Comp. We also studied the optical properties, absorbance, transmittance and reflectance of visible and ultraviolet light just for raw Shrimp ShP and chitosan extracted by concentrated and diluted chloric acid. We claimed the gap energy (E_g) and Urbach energy (E_u) for disorder determination. We attempt whether the concentration of acids and bases affected the degree of deacetylation (DD), the crystal structure and optical properties.

In all of this manuscript, we noted the Shrimp ShP by (Shrimp ShP), chitosan obtained by diluted chloric acid by (Chitosan DCA), chitosan obtained by concentrated chloric acid by (Chitosan CA), chitosan obtained by concentrated sulphuric acid by (Chitosan SA) and chitosan obtained by concentrated nitric acid by (Chitosan NA), commercial chitosan purchased from Fluka Chemika comp by (Chitosan FC).

VI.2 Experimental processes

VI.2.1 Process of extraction of chtiosan diluted hydrochloric acid

To prepare chitosan DCA, we proceed by taking shrimp shells and rinsing it in water and then dry it in sunlight for 8 hours. We add the chloric acid 1M and mix it for 4h at 80°C, then rinse it again in water. The second part kicks off by adding the base of sodium hydroxide 1M following the same process (4 hours mix in 80°C). Once finished, we rinse it with distillate water and grind it. After that, we put it in the oven for 8h at 100°C. Then, we immerse the product powder in sodium hydroxide solution (pH=12) for 4h at 80°C for deacetylation. The product is then ready after one last grind with porcelain mortar. We end by the whitening process with oxygenated water for 2h at 80°C.

VI.2.2 Process of extraction of chitosan by concentrated acid and base

For the production of Chitosan CA, Chitosan NA, and Chitosan SA, we start as the process for Chitosan DCA by preparing the shell shrimps firstly by rinsing it with water, and then leave it to be dried at sunlight for 8 hours. We grind the dried shrimp shells and put them separately in three 100 ml beakers, then we add in excess the chloric acid 20%, sulphuric acid 98%, nitric acid 70%, each acid in one beaker and we leave them for 2 hours. The grinded shrimp shells completely dissolved in CA20%, NA70%, and SA98%. The second part begins by the separation of products from acids in three steps: filtration, well cleaning with distillate water

and heat drying in order to take the filtrates in a more pure state. Then we add the ammonia 20% in drops until we get to ph=7, and we repeat the same previous filtrations. In this case, our products are chitin. For obtaining the chitosan we add again in each beaker the ammonia 20% in excess and we leave them for 2 hours, we do the same previous filtration to separate chitosan from ammonia. Then we wash them by hydrogen peroxide for 2 hours for bleaching and drying them at 80 °C. The experimental process is summarized in Fig.80.

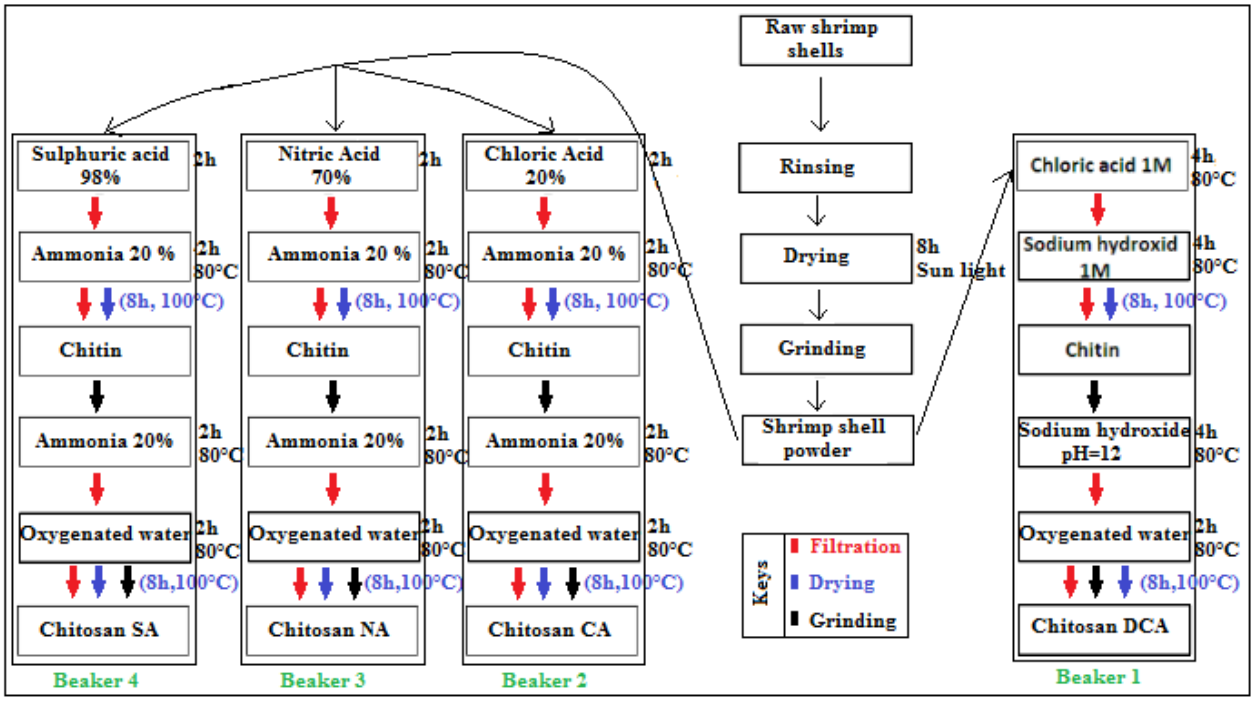

Figure 80. Experimental process of chitin and chitosan extraction.

VI.3 Characterization

VI.3.1 **X-ray fluorescence: Chemical elements concentrations in all chitosan samples**

X-ray fluorescence spectrometry (XRF) is a chemical analysis technique based on the excitation of atoms or molecules by X-Rays. These absorbed rays will be followed immediately by spontaneous secondary emission of another form of energy named fluorescence of X-Rays. The apparatus spectrometer collects all of those secondary emissions and builds the XRF spectrum were each peak corresponds to the quantitative concentration of the chemical elements within materials. This is a non-destructive analysis of the full range of elements from sodium to uranium [468]. The X-ray fluorescence spectrometer is capable of analyzing elements in

concentrations from a high percentage down to ppm level. In our case, the importance of the chemical element analysis is to determine the variation of the mineral elements concentration in shrimp shells after using different acids for its demineralization in order to deduce the acids effect in its mineral part. The XRF patterns of all our products are shown in Fig. 81. We will not give consideration to blue peaks, because this appearance is due to the X-rays reflexion by argon gas used for the functioning of the apparatus. The results show the existence of oligo elements and major elements. Oligo elements in ppm (parts per million) such as Titanium Ti, Zinc Zn, Manganese Mn. We will not consider them in shrimp shells structure, because they do not occupy a major part of its structure and can also be due to background noise. M minerals exist in raw Shrimp ShP. We note the existence of low concentration of chemical elements of magnesium Mg, aluminium Al, silicon Si, Potassium K, Iron Fe, and existence of Calcium Ca and phosphorus in high concentration (41.214% of CaO and 5.046% of P_2O_5). Thus, these are the essential elements that make up the shrimp shells' crystalline structure. Each acid eliminates minerals following its effectiveness. We see the decrease of all elements' concentration in all chitosan samples, but not very much for Chitosan DCA, since its calcium oxide CaO residue is 40.824% (decrease by 0,946%). While, the CaO residues are successively 0.21% Chitosan CA (decrease by 99,49%), 0.24% for Chitosan NA (decrease by 99,417%), 1.244% for Chitosan SA (decrease by 96,988%). All chemical elements' concentrations are summarized in Table 28. We remark that carbon oxide CO and nitrogenous oxide NO which present the polysaccharides family does not appear in XRF analysis results for all chitosan samples because of secondary light interference; but we can easily deduce their concentration by the subtraction of the total concentration of appeared elements from 100% (100% - ∑%elements concentration). The (CO+NO) % concentration for Shrimp ShP, Chitosan DCA, Chitosan CA, Chitosan NA and Chitosan SA are successively 48,417%, 52,464%, 97,976%, 99,021% and 98,12 %. These results show that concentrated acids are good for chitin and chitosan extraction from shrimp shells, due to their higher potential to remove minerals [469]. Therefore, the carbon C, nitrogenous N and oxygen O has been the essential components of our samples. We cannot directly conclude that our products are chitosan or chitin due to their similar components, but we can do it by the degree of deacetylation DD [470-471] (we further discuss it below in FTIR

analysis paragraphs). The border between chitosan and chitin corresponds to a DD of 50 %: Above this value, the compound is called chitosan, if not, the compound is chitin. And the role of the second use of the base is to remove acetyls group from chitin in order to be chitosan.

Table 28. Chemical elements concentrations in Shrimp ShP, Chitosan DCA, Chitosan CA, Chitosan NA, Chitosan SA.

	Samples	**Shrimp ShP**		**Chitosan DCA**		**Chitosan CA**		**Chitosan NA**		**Chitosan SA**	
Major elements	**Compound**	Conc	Unit	Conc	Unit	Conc	Unit	Conc	Unit	Conc	Unit
	MgO	1,373	%	1,344	%	0,028	%	0	ppm	920,2	ppm
	Al_2O_3	0,178	%	0,159	%	0,062	%	0,096	%	0,084	%
	SiO_2	1,549	%	0,325	%	0,972	%	0,227	%	0,177	%
	P_2O_5	5,046	%	4,439	%	0,339	%	0,337	%	0,331	%
	SO_3	0,34	%	0,102	%	0,011	%	0,079	%	0,044	%
	Cl	0,522	%	0,197	%	0,402	%	645,9	ppm	0	ppm
	K_2O	0,293	%	204,2	ppm	893,2	ppm	185,6	ppm	575,1	ppm
	CaO	41,214	%	40,824	%	0,21	%	0,24	%	1,244	%
	Fe_2O_3	0,399	%	937,9	ppm	513	ppm	45,5	ppm	131,7	ppm

	Br	0,117	%	128,5	ppm	350,9	ppm	11,1	ppm	12,8	ppm
	SrO	0,552	%	0,343	%	20	ppm	17,3	ppm	51,2	ppm
Oligo elements	**TiO_2**	680,1	ppm	156,4	ppm	20	ppm	0	ppm	0	ppm
	V_2O_5	18,5	ppm	13,4	ppm	7	ppm	0	ppm	0	ppm
	Cr_2O_3	30	ppm	12	ppm	5	ppm	9	ppm	0	ppm
	MnO	53,9	ppm	44	ppm	12	ppm	0	ppm	9	ppm
	CuO	126,7	ppm	45,2	ppm	95	ppm	51,7	ppm	14,8	ppm
	ZnO	175,7	ppm	90,4	ppm	0,156	ppm	0	ppm	42,5	ppm
	As_2O_3	20,2	ppm	12,7	ppm	13,3	ppm	0	ppm	2,1	ppm
	ZrO_2	1,2	ppm	0	ppm	0	ppm	0	ppm	0	ppm
	Ag_2O	817,6	ppm	0	ppm	0	ppm	0	ppm	0	ppm
	SnO_2	31,7	ppm	27	ppm	0	ppm	0	ppm	25,9	ppm
	Yb_2O_3	25,1	ppm	0	ppm	16,5	ppm	0	ppm	0,5	ppm
	PbO	8,9	ppm	0	ppm	0,366	ppm	0	ppm	2,9	ppm

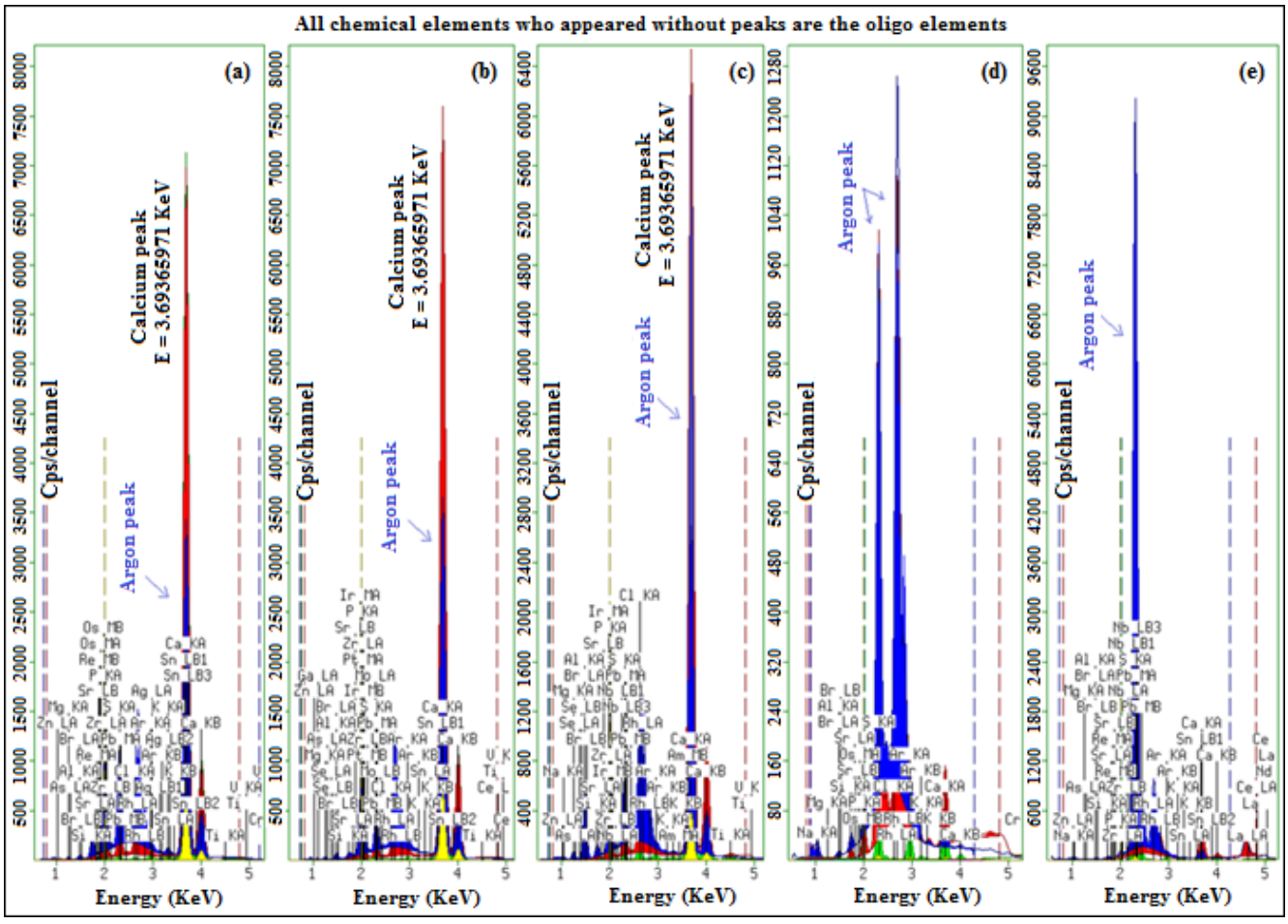

Figure 81. XRF pattern (Cps/channel Vs Energy (KeV)) of (a): Shrimp ShP, (b): Chitosan DCA, (c): Chitosan CA, (d): Chitosan NA, (e): Chitosan SA.

VI.3.2 **X-ray diffraction**

The crystallinity of samples was evaluated by wide angle X-ray diffraction analysis using a Bruker D8 ADVANCE Powder XRD apparatus. Common targets used in X-ray tubes include Cu and Mo, that emit respectively 8 keV and 14 keV X-Ray energies with corresponding wavelengths of 1.54 Å and 0.8 Å. This diffractometer functioned by Cu Kα radiation. The XRD pattern obtained for Shrimp ShP, Chitosan DCA, Chitosan CA, Chitosan NA, Chitosan SA, and Chitosan FC are shown in Fig.82 followed by their Rietveld refinement, aim to deduce the structural parameters of all chitosan samples. The major peaks for all samples extracted by

concentrated acids are similar to this of Chitosan FC with a difference in the degree of crystallinity [472] appeared in the diffraction angle near to 2θ=20° that is the characteristic region of chitosan phases, and near to 2θ=30° for Shrimp ShP and Chitosan DCA, that is the characteristic region of calcite and calcium phosphate family. These primary results show that the use of diluted acid is not the favorite way to extracted chitosan from shrimp shells. It is incapable to remove all minerals from shrimp shells (unlike concentrated acid). The XRD patterns shows the small structural change between shrimp shells and Chitosan DCA, and more structural changes between shrimp shells and chitosan extracted by concentrated acids and Chitosan FC. These changes are due to the mineral removal effectiveness of each acid. In addition, the calcium and phosphorus are the mains minerals components in shrimp shells. The elimination of calcite is not easy by diluted acid, also the presence of calcium and phosphorus in the same time in the aqueous media leads to the formation of HAP crystallite, can't be removed or solved by the diluted acid. For these two reasons, demonstrate that the diluted acids have a small effect and the concentrated acids have a high effect on shrimp shells structure due to easiness removal of calcium and phosphorus mostly for nitric acid that can solve the HAP. Therefore, what's affect bases on shrimp shells crystal structure? Shrimp shells contain proteins as organic part, and it's known that those primary structures, corresponds to the linear succession of the amino acids without reference to their spatial configuration. Thence, proteins are the amino acid polymers, linked together by peptide bonds. The role of the bases is to remove them from shrimp shells, but it does slightly affect its crystallization because these proteins do not form their structure.

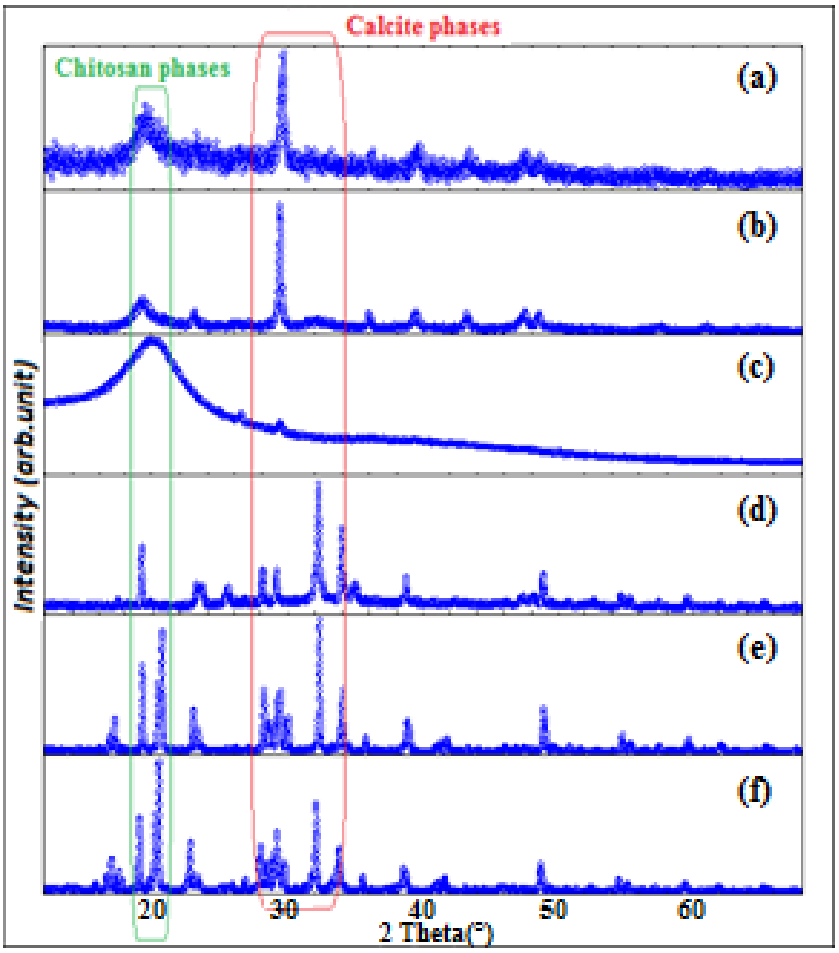

Figure 82. XRD pattern of (a): Shrimp ShP, (b): Chitosan DCA, (c): Chitosan FC, (d): Chitosan NA, (e): Chitosan SA, (f): Chitosan CA.

- Reitveld refinement and Structural parameters of shrimp shells powder, and all chitosan samples

In a view to define the structural parameter variations related to the use of some acid or other, we performed the Rietveld refinement by FullProf software. The structural results are summarized in Table 29, and the FullProf graphs are shown in Fig.83. These graphs show a good Reitveld refinement for all samples, because the calculated pattern and the experimental pattern are almost congruous, with a small difference between them. The major mineral part of shrimp shells crystallizes in tetragonal system with (P 4/m m m) symmetry groups and the same for all chitosan samples that they save these properties after extraction. We remark an increase

in cell parameters of all chitosan samples comparing to those of Shrimp ShP due to the decrease of minerals' concentration that lead to a decrease of number of ionic bonds.

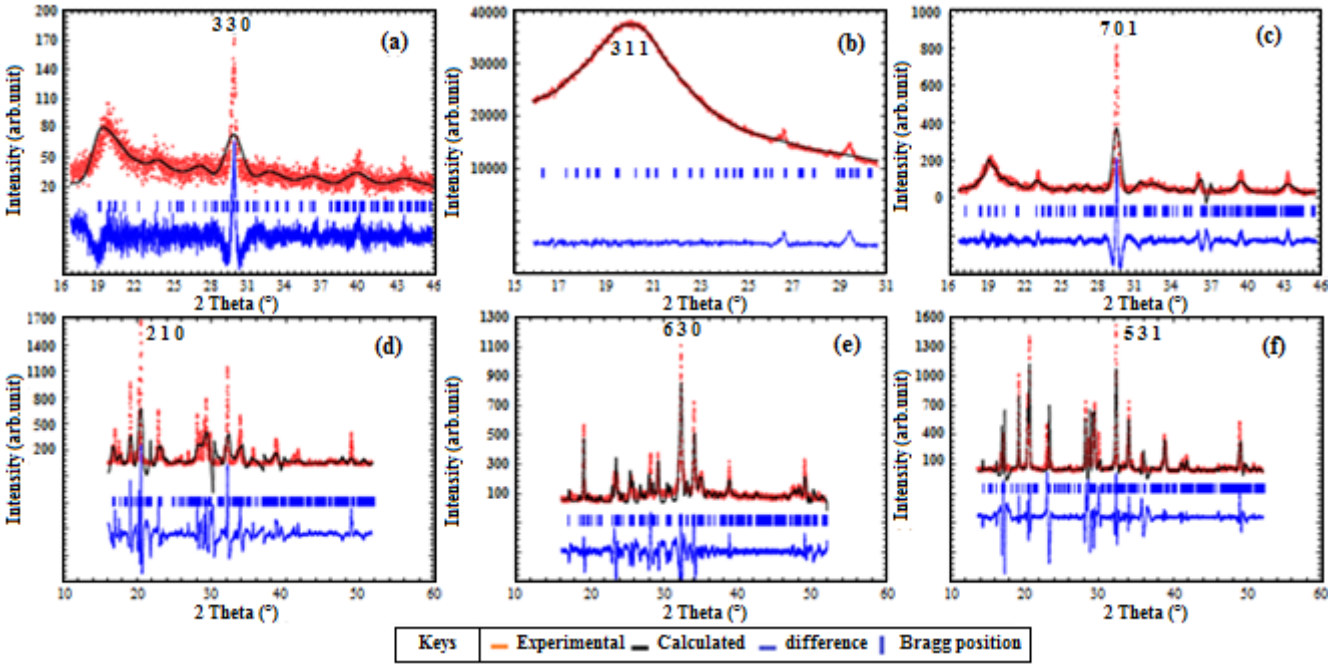

Figure 83. XRD Reitveld refinement of (a): Shrimp ShP, (b): Chitosan FC, (c): Chitosan DCA, (d): Chitosan CA, (e): Chitosan NA, (f): Chitosan SA.

The XRD patterns indicate that the chitosan contains also an amorphous form due to the presence of OH and NH_2 groups which form the intermolecular hydrogen's bond. Thus, this distribution will have some regularity to build easily the crystalline regions. Similarly, to the results reported in the preparation and characterization of the chitosan binary blend [473].

- Grain sizes of shrimp shells powder, and all chitosan samples

The Debye-Scherrer method was used to obtain the grains' size from X-ray diffraction measurements by following relationship (14) [474]:

$$D = \frac{k.\lambda}{B.\cos(\theta)} \qquad (14)$$

Where D is the grin's size diameter, B is the broadening of the diffraction line measured at half-maximum intensity, λ is the wavelength of (Cu Kα), h is the Bragg angle for a given diffraction and k is a constant, in general equal to 0.9 for powders. The grain sizes results are shown in Table 30.

Table 29. Structural parameters of Shrimp ShP, Chitosan DCA, Chitosan FC, Chitosan CA, Chitosan NA and Chitosan SA.

Sample	Crystal System	Symmetry Group	Cell Parameters		2θ (°)	α=β =γ (°)
			a=b(A)	c (A)		
Shrimp ShP	Tetragonal	P 4/m m m	12.76	6.98	29,6	90.00
Chitosan DCA	Tetragonal	P 4/m m m	18.44	7.079	36,35	90.00
Chitosan FC	Tetragonal	P 4/m m m	15.45	10.03	20.19	90.00
Chitosan CA	Tetragonal	P 4/m m m	9.73	25.03	20,37	90.00
Chitosan NA	Tetragonal	P 4/m m m	18.59	4.77	32,26	90.00
Chitosan SA	Tetragonal	P 4/m m m	18.44	5.71	32.32	90.00

Table 30. (a): Shrimp ShP, (b): Chitosan DCA, (c): Chitosan FC, (d): Chitosan CA, (e): Chitosan NA, (f): Chitosan SA.

Sample	A	B	C	D	e	f
D (nm)	4,13	8,51	5,80	9,39	24,61	34,59

We remark an increase in the grain sizes between Shrimp ShP and all our chitosan due to an increase in structural parameters. See Fig.84.

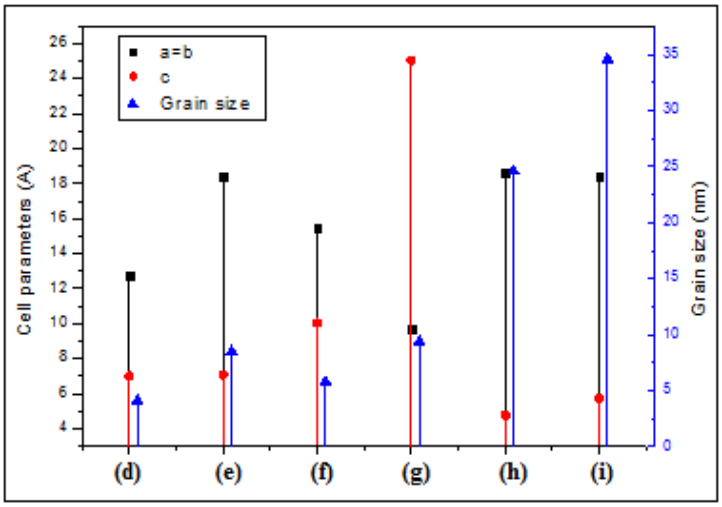

Figure 84. Grain sizes and cell parameters evolution of (d): Shrimp ShP, (e): Chitosan DCA, (f): Chitosan FC, (g): Chitosan CA, (h): Chitosan NA and (i): Chitosan SA.

VI.3.3 **Optical proprieties**

Transmission, Absorbance, Reflectance spectrums of shrimp shells powder, chitosan DCA and chitosan CA in range Uv-Visible

We want to explore the variance in opto-electronic behavior between Shrimp ShP and two types of chitosan. One extracted by diluted acid and the second extracted by concentrated acids. For this objective, we choose Chitosan DCA and Chitosan CA. The Uv-visible spectroscopy analysis was carried out using a T92 + UV-visible spectrophotometer.

The Fig.85 show the optical spectrums of absorbance, transmittance and reflectance as function to the wavelength in the Uv-visible range between 200 and 800 nm. The spectrums indicate that all samples have a high absorption of ultraviolet lights around 90 to 99% in the wavelength range of 200-400 nm with very a low transmission in the absence of reflexion. As well, we remark a darkness between 600 and 800 nm since to the good light absorption by samples circa 45% for Shrimp ShP and and 54% for Chitosan DCA and 57% for Chitosan CA, and transmission nearly 36% for Shrimp ShP and 29% for Chitosan DCA, and 28% for Chitosan CA, and reflexion about 19% for Shrimp ShP and 17% for Chitosan DCA, and 15% for Chitosan CA. This incongruity is due to the elimination of minerals and acetyl groups. The

samples' absorbance above are very important allows us to calculate the coefficient of absorption α which was obtained by dividing the absorbance of each sample by its thickness.

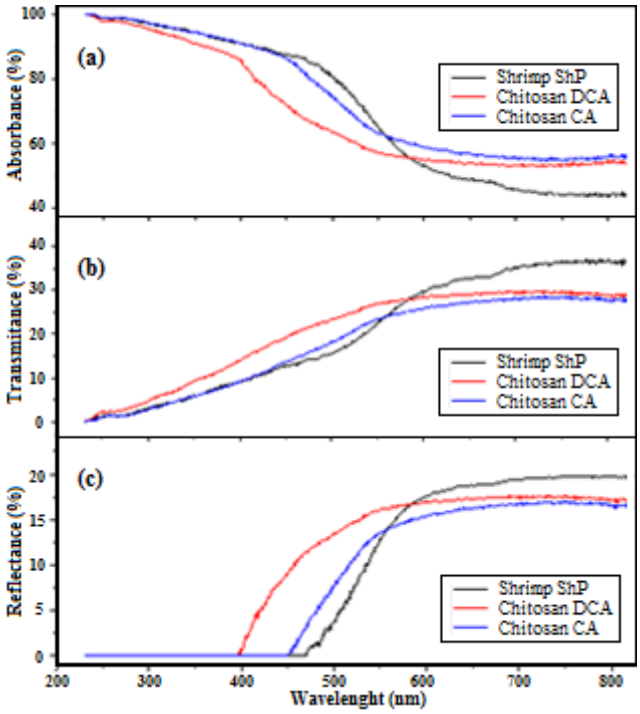

Figure 85. The Uv-Visible spectrums, (a): Absorbance, (b): Transmission (c): Reflectance of Shrimp ShP, Chitosan DCA and Chitosan CA.

- **Dependence of ln (α) and $(ahν)^2$ on energy (eV) and the determination of gap energy and disorder**

As it is shown in Fig.86, the optical gap energy E_g was determined from the absorption coefficient α by the relationship (15) [475-476]. Thus, the E_g is obtained by intersection of the tangent of the linear part of the curve of $(αhν)^2=f(hν)$ with the abscissa axis represents the energy hν.

$$\alpha h\nu = \alpha_0 \cdot \left(h\nu - E_g\right)^n \qquad (15)$$

Where: $α_0$ is a constant and sometimes called the band tailing parameter, it is an energy independent and constant Eg is the gap energy, which is the forbidden zone between the valence band below the Fermi level and conduction band above the Fermi level according to the density

of states model, proposed by Mott and Davis [477-478], n is the power factor of the transition mode equal to 0.5 in our case for the materials that have a direct gap.

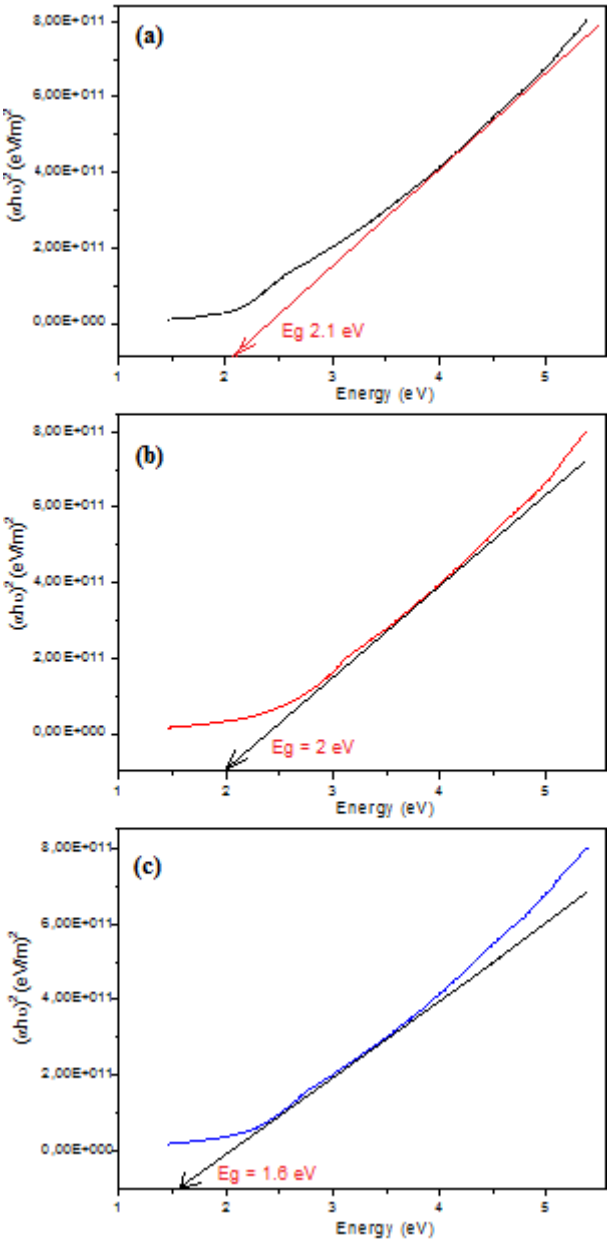

Figure 86. The determination of the optical gap energies of (a): Shrimp ShP, (b): Chitosan DCA, (c): Chitosan CA.

The Urbach energies E_u (Called also the disorder) were deduced from the reciprocal slope of the linear part of the curve of Ln(α)=f(hν) by the Urbach relationship (16). See Fig.87.

$$Ln(\alpha) = Ln(\alpha_0) + \frac{h\nu}{E_u} \qquad (16)$$

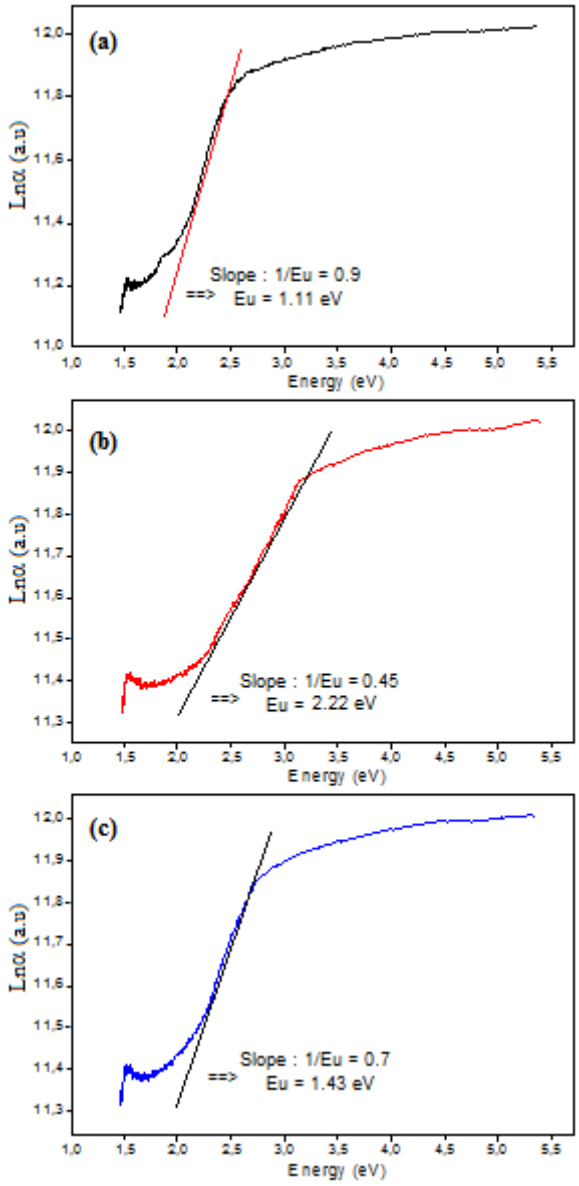

Figure 87. The determination of the Urbach energies (Disorder) of (a): Shrimp ShP, (b): Chitosan DCA, (c): Chitosan CA.

The results show a decrease in the gap energy 2.1 eV for Shrimp ShP, 2 eV for Chitosan DCA and 1.6 eV for Chitosan CA. This decrease is due to the elimination of proteins and all impurities. While, the Chitosan CA is more conductor than Chitosan DCA and Shrimp ShP, thanks to its small gap energy. These products can be candidate to be used in bio-semiconductor, and do not have danger for environment or health. The Urbach energy is the electronic disorder in crystal. We remark that the Urbach energy is lower for Shrimp ShP with value equal to 1.11 eV, this energy increase for Chitosan DCA with value equal to 2.22 eV and for Chitosan CA with value 1.43 eV. These variations depend to the disorder or delocalized states of each sample. After demineralization, and deproteinization, the numbers of defects in structure increase leading to an increase in the electronic disorder for the Chitosan DCA and Chitosan CA which exhibit the increase their Urbach energies value. Consequently, the Shrimp ShP has a low number of defects. The values of the E_g and E_u were summarized in Table 31 and represented in Fig.88.

Table 31. Value of the gap energy and Urbach energy for the Shrimp ShP, Chitosan DCA and Chitosan CA.

Sample	Shrimp ShP	Chitosan DCA	Chitosan CA
Gap energy Eg (eV) (Err ± 0.01 eV)	2.1	2	1.6
Urbach energy E_u (eV) (Err ± 0.01 eV)	1.11	2.22	1.43

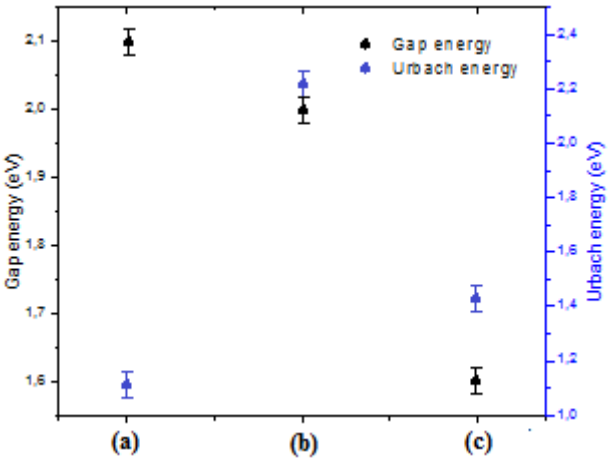

Figure 88. The representation of the optical gap energies and Urbach energies of (a): Shrimp ShP, (b): Chitosan DCA, (c): Chitosan CA.

VI.3.4 **Fourier Transformed Infra-Red (FTIR)**

- Assignment and bands description of FTIR spectrums of shrimp shells, Chitosan DCA, Chitosan CA, Chitosan NA, Chitosan SA and Chitosan FC

The infrared spectrum is obtained by using an infrared spectrophotometer (Perkin Elmer spectrum version 10.4.2). The system is considered well-defined wavelength that can be passed through the sample who being studied. The abscissa axis represents the wavenumbers expressed in (cm^{-1}) equal to the inverse of the wavelength. The magnitude is progressively modified when recording of spectrum and expressed as a percentage (%) in the ordinate axis representing the transmittance (T %). In the absence of all absorptions, the baseline is continuous with a transmittance of 100%. On the other hand, if the sample absorbs an incident beam the vibration of the bonds will altered in the molecules, and the absorption band with a peak pointing downwards appears in the spectrum in the range 400-4000 cm^{-1}. There are several types of vibration, for example: The longitudinal vibration of the bonds where the distance between two atoms varied, and the angular deformation where the nail between the bonds varied. The infrared spectrum provides information concerning the nature of the bonds existed in the material and therefore on its characteristic groups. The FTIR spectrum of the Shrimp ShP showed seven major peaks corresponding to the following wavenumbers 670, 700, 1000, 1175, 1420, 1325 and 1680 cm^{-1} as shown in Fig.(a)-89 and their bands' descriptions are shown in

Table 32. The FTIR analysis showed a specific band appears near to 1320 cm^{-1} for N-acetylglucosamine, and it is often used as the reference band for chitin and chitosan. The amide II band are shown in well-defined peak in 1680 cm^{-1}. The characteristics band of the -OH, -NH_2, -CO groups were appeared respectively in 670, 700, 1000 cm^{-1}, and they are chosen for the calculation of the extent of N-acetylation [479]. The strips in 2170-2200 cm^{-1} correspond to the stretch band of the CH groups. The FT-IR peaks in 690, 700, 1000, 1325, 1680, 2175 and 2200 cm^{-1} are similar to those of chitosans' peaks as shown in Fig.89 where we remark a great similarity between FTIR spectrums of the all chitosan samples obtained in this work and the Chitosan FC, which we regrouped all their functional groups a in Table 32. Besides, we notice that the bands corresponding to the inorganic carbonates are likewise to those of Shrimp ShP, located in 1425 and 874 cm^{-1} even if there is a displacement of the peaks depending on the acid used in the extraction of the chitosan. The peaks in 1175 cm^{-1} corresponding to the stretching vibration of PO_4^{3-} in Shrimp ShP are lost in all chitosans after performing the demineralization. The deproteinization is evidenced by the decrease in the signal intensity and changes in the regions of the CH stretching modes and the angular deformation of the CH_2 groups existing in the proteins. The main signals observed for stretching of C=O band is in 1640.72 cm^{-1}. In addition, the bands located between 1000 and 1150 cm^{-1} is mainly corresponding to the stretching ring of CC and CO groups. Else, the wide bands above 3000 cm^{-1} are related to the overlap of the stretching vibration of the OH and NH bonds [480-481-482].

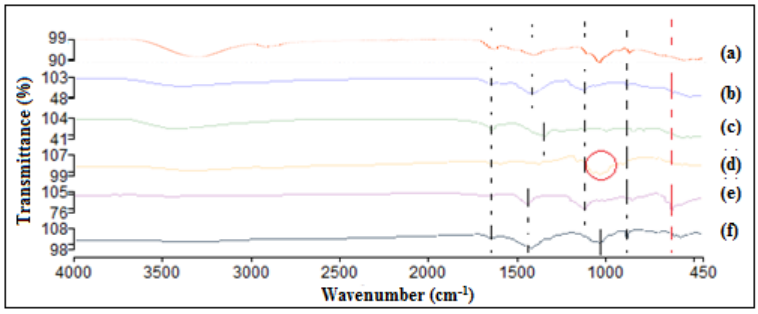

Figure 89. The FTIR spectrums of (a): Shrimp ShP (b): Chitosan CA, (c) Chitosan NA, (d): Chitosan FC, (e): Chitosan SA and (f): Chitosan DCA.

Table 32. Description of IR band of Shrimp ShP, Chitosan CA, Chitosan NA, Chitosan SA, Chitosan DCA and Chitosan FC.

Samples	IR Band cm^{-1}	Transmittance %	Description
Shrimp ShP	3315	92.74	Stretching vibration of OH and N-H group
	2200	96.33	Symmetric CH_3 stretching and asymmetric CH_2 stretching
	2175	96.68	CH stretching
	1680	95.52	($-NH_2$) amide II
	1325	95.61	*s ($-CH_3$) tertiary amide
	1175	93.80	Stretching vibration of PO_4^{3-}
	1000	94.81	*as(C-O-C) and *s(C-O-C)
	700	93.15	NH out – of – plane bending
	670	91.20	OH out – of – plane bending
Chitosan CA	3391,88	81,23	Stretching vibration of OH and N-H group
	1407,54	58,21	Angular deformation of CH2
	1114,38	67,49	C-C and C-O stretching
	874,50	78,55	Antisymmetric stretching of the CO_3^{2-} ion
	514,05	43,97	Vibration of cis C-H
Chitosan NA	2898.73	86,00	CH stretching modes
	1640.72	87,28	Stretching vibration C=O
	1425.67	61,53	Angular deformation of CH_2
	1109.09	62,33	C-C and C-O stretching
	513.90	57,45	Vibration of cis C-H
Chitosan SA	1686.58	100,00	Stretching vibration C=O
	1340.88	87,66	Angular deformation of CH_2
	1110.45	8,39	C-C and C-O stretching
	876.63	92,34	Antisymmetric stretching of the CO_3^{2-} ion
	615.50	76,31	Vibration of cis C-H

Chitosan DCA	1413.15	93,03	Angular deformation of CH_2
	1025.67	10,52	C-C and C-O stretching
	873.14	12,31	Antisymmetric stretching of the CO_3^{2-} ion
	564.13	100	Ibration of cis C-H
Chitosan FC	3300,00	100	Stretching vibration of OH and N-H group
	1640.72	87,28	Stretching vibration C=O
	1425.67	61,53	Angular deformation of CH_2
	1035,86	99,90	C-C and C-O stretching
	513.90	57,45	Vibration of cis C-H

* = stretching vibration, $*_S$ = symmetric stretching vibration and $*_{as}$ = asymmetric stretching vibration.

- Degree of acetylation DA and degree of deacetylation DD of Chitosan DCA, Chitosan CA, Chitosan NA, Chitosan SA and Chitosan FC

The characterization of the chitosan requires the determination of its degree of deacetylation (DD) that is calculated by relationship (18). The degree of deacetylation (DD) of chitosan is more than 50%. FTIR spectroscopy is a rapid technique for qualitatively evaluating the degree of acetylation (DA) from the relationship (17) [460-461] by calculating the absorbance ratios of a characteristic band of an acetyl group on a band common to acetylated and deacetylated units. In a chemical composition of chitin, being the acetyl group with a chemical formula: C_2H_3O and a molar mass: 43.05 $g \cdot mol^{-1}$. But it is not the same for chitosan whose the acetyl group have been previously eliminated by the base. See the Fig.90. The DA and DD are reported in Table 33.

$$DA\% = 31.92.(\frac{A_{1320}}{A_{1420}}) - 12.20 \qquad (17)$$

$$DD\% = 100\% - DA\% \qquad (18)$$

Where A_{1320} and A_{1420} are respectively the absorbance in 1320 and 1420 cm^{-1}. The peak in 1320 cm^{-1} correspond to the characteristic band of amide group (-OH, $-NH_2$, -CO).

Table 33. DA and DD of Chitosan CA, Chitosan NA, Chitosan SA, Chitosan DCA and Chitosan FC

Samples	DA%	DD%
Chitosan CA	19,25	80,74
Chitosan NA	19,26	80,73
Chitosan SA	19,25	80,74
Chitosan DCA	19,14	80,85
Chitosan FC	24,55	75,44

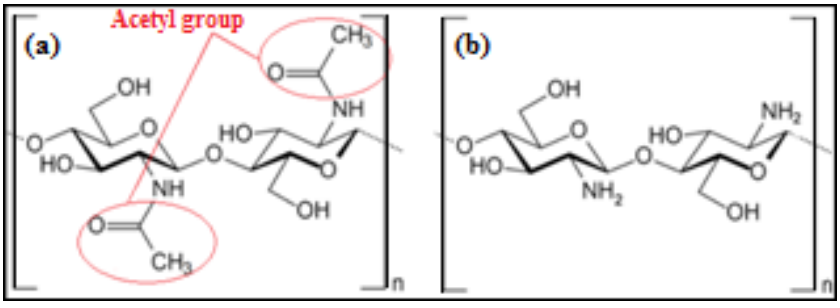

Figure 90. Chemical formula of (a): Chitin and (b): Chitosan.

The degree of deacetylation increases owing to decrease of the number of the acetyl groups due to the protonation of the -NH_2 function on the C-2 position of the repeating unit D-glucosamine, offering chitosan with a high quality.

VI.3.5 Raman Spectroscopy analysis: Spectrums and vibration modes assignments depending to wavenumber for shrimp shells powder, Chitosan NA, Chitosan SA, Chitosan CA, Chitosan DCA, Chitosan FC

Raman Spectroscopy is a non-destructive analysis that provides information about chemical properties and vibrational modes of the molecules. It provides too several information about structure, phase, crystallinity of materials. This technique is based to the excitation of the chemical bonds inside material by laser light in the range of wavenumber typically between 250 and 3500 cm^{-1}. Each chemical bond provides the most assignment response if it is excited by its resonance energy. Generally, this technique is used to determine the vibrational modes of molecules such as pyranoid ring, in-plane or out-plane bending and the stretching vibrations. The Raman spectroscopy analysis for all our chitosan samples was carried out using DRX2

Raman Microscope apparatus. All Raman spectrums are exposed in Fig.91. As can be seen in figure, all essential characteristic peaks of chitosan assignments appeared in each spectrum [473-483]. Whereas the peaks in 470, 1000, 1800, 2630, 3250 cm^{-1} correspond respectively to the stretching vibration of (C-C(=O)-C), the stretching vibration of (C-H), the in-plane bending vibrations of (C=CCOOR) and (C=O), the in-plane bending vibrations of (CH) rings, the stretching vibration of (NH_2). The stretching vibrations in 1000 cm^{-1} and 1800 cm^{-1} are mainly the special peaks of chitosan [484]. We compared our results with those of the literature [485-486], they are congruent. Besides, the Raman analysis results confirm the molecular vibration modes observed in our chitosan samples by FTIR analysis. Moreover, other vibrational modes of low wavenumber frequencies were appeared in Raman spectrums (did not appear in FTIR spectroscopy), some modes are noted in Fig.91 and the majority are regrouped in the Table 34. Our results are congruent to the study of A. ZAJAC et al [487].

Table 34. Raman vibration modes depending to wavenumber for Shrimp ShP, Chitosan DCA, Chitosan FC, Chitosan CA, Chitosan NA and Chitosan SA.

Keys: ϕ, pyranoid ring; ν, stretching; δ, in-plane bending vibrations; γ,ω, out-of plane bending; HB, hydrogen bond.					
Shrimp ShP		**Chitosan DCA**		**Chitosan FC**	
Wavenumber (cm^{-1})	**Assignments**	**Wavenumber (cm^{-1})**	**Assignments**	**Wavenumber (cm^{-1})**	**Assignments**
268 277	δ(C-NH-C)+γ(OH)	276	δ(C-NH-C)+γ(OH)	269 277 301	δ(C-NH-C)+γ(OH)
352 376 396 439 446	γ(OH) + γ(ϕ)	360 369 382 390 402	γ(OH) + γ(ϕ)	349 388 398 412 449	γ(OH) + γ(ϕ)

		420 432 444			
897	ν(ϕ)+ρ(CH_2)	465	ν(ϕ)+ρ(CH_2)	470	δ(COC)
943	ν(CN)	899	ν(ϕ)+ρ(CH_2)	557	ν(NH)+γ(C=O)+ω(CH_3)
993	ν(ϕ)+δ(CH)	928	ν(CN)	702	ω(NH_2)+δ(ϕ)
1102	ν(C-O-C)+ν(ϕ)+ν(C-OH)+ ν(C-CH_2)+δ(CH)+ρ(CH_2)+ρ(CH_3)	991	ν(ϕ)+δ(CH)	944	ν(CN)
1269	δ(OH...O)+ν(C-C)+ν(C-O)+ δ(CH)+ρ(CH_2)	1041	ρ(CH_3)+δ(CH)+ δ(OH)	1140	ν(C-O-C)+ν(ϕ)+ν(C-OH)+ ν(C-CH_2)+δ(CH)+ρ(CH_2) + ρ(CH_3)
1409	δ(CH_3)+δ(CH)	1080 1107 1117 1142	ν(C-O-C)+ν(ϕ)+ν(C-OH)+ ν(C-CH_2)+δ(CH)+ρ(CH_2) + ρ(CH_3)	1255	δ(OH...O)+ν(C-C)+ν(C-O)+ δ(CH)+ρ(CH_2)
1607	δ(NH_2)	3257	ν(OH)HB	1322	ν(CN)+δ(CH)
2760	ν(CH)			1376	δ(CH_2)+δ(CH)+δ(OH)+ν(ϕ)
3284	ν(OH)HB			1407	δ(CH_3)+δ(CH)
				1454	δ(CH)+ω(CH_2)+δ(OH)
				1593	δ(NH_2)
				2809	ν(CH_3)
				2883	ν(CH_2)
				2883	ν(CH_2)
Chitosan CA		**Chitosan NA**		**Chitosan SA**	

Wavenumber (cm^{-1})	**Assignments**	**Wavenumber (cm^{-1})**	**Assignments**	**Wavenumber (cm^{-1})**	**Assignments**
269 277	δ(C-NH-C)+γ(OH)	353 364 387 395 403 414 425 441	γ(OH) + γ(ϕ)	269	δ(C-NH-C)+γ(OH)
363 369 388 398 411 444	γ(OH) + γ(ϕ)	496	δ(CO-NH)+δ(C-CH_3)+ δ(COC)	352 376 385 398 420 427 443	γ(OH) + γ(ϕ)
484	δ(CO-NH)+δ(C-CH_3)+ δ(COC)	567	ν(NH)+γ(C=O)+ω(CH_3)	478	δ(COC)
564	ν(NH)+γ(C=O)+ω(CH_3)	1457	δ(CH)+ω(CH_2)+δ(OH)	497	δ(CO-NH)+δ(C-CH_3)+ δ(COC)
1030	ρ(CH_3)+δ(CH)+ δ(OH)	1661	ν(CO)	568	ν(NH)+γ(C=O)+ω(CH_3)
1092 1102 1109	ν(C-O-C)+ν(ϕ)+ν(C-OH)+ ν(C-CH_2)+δ(CH)+ρ(CH_2)+ ρ(CH_3)	2735	ν(CH)	991	ν(ϕ)+δ(CH)
1381	δ(CH_2)+δ(CH)+δ(OH)+ν(ϕ)	3217	ν(OH)HB	1046	ρ(CH_3)+δ(CH)+ δ(OH)
1407	δ(CH_3)+δ(CH)			1093	ν(C-O-C)+ν(ϕ)+ν(C-OH)+ ν(C-

					CH_2)+δ(CH)+ρ(CH_2) + ρ(CH_3)
1454	δ(CH)+ω(CH_2)+δ(OH)			1450	δ(CH)+ω(CH_2)+δ(OH)
1585	δ(NH_2)			1587	δ(NH_2)
1657	ν(CO)			1657	ν(CO)
2737	ν(CH)			2741	ν(CH)
2822	ν(CH_3)			3229	ν(OH)HB
2883	ν(CH_2)				
2931	ν(CH_3)				
3291	ν(OH)HB				

Furthermore, the effect of diluted or concentrated acids on Shrimp ShP on its crystallinity is more visible by Raman spectroscopy following the shape and intensity of peaks. We note that Shrimp ShP is more crystalline than all our chitosan samples because its build slowly with the growth of shrimp without composition disequilibria or abnormal condition. The crystallinity of the chitosan was affected by its extraction method, especially by acid used. Relying on spectrums intensities, we classify the crystallinity of our chitosan samples in this descending sequence: Chitosan NA, Chitosan SA, Chitosan CA, Chitosan DCA, and Chitosan FC. Because the concentrated acids clean samples from impurity, which give chitosan more opportunities for recrystallization after washing with distilled water and air drying.

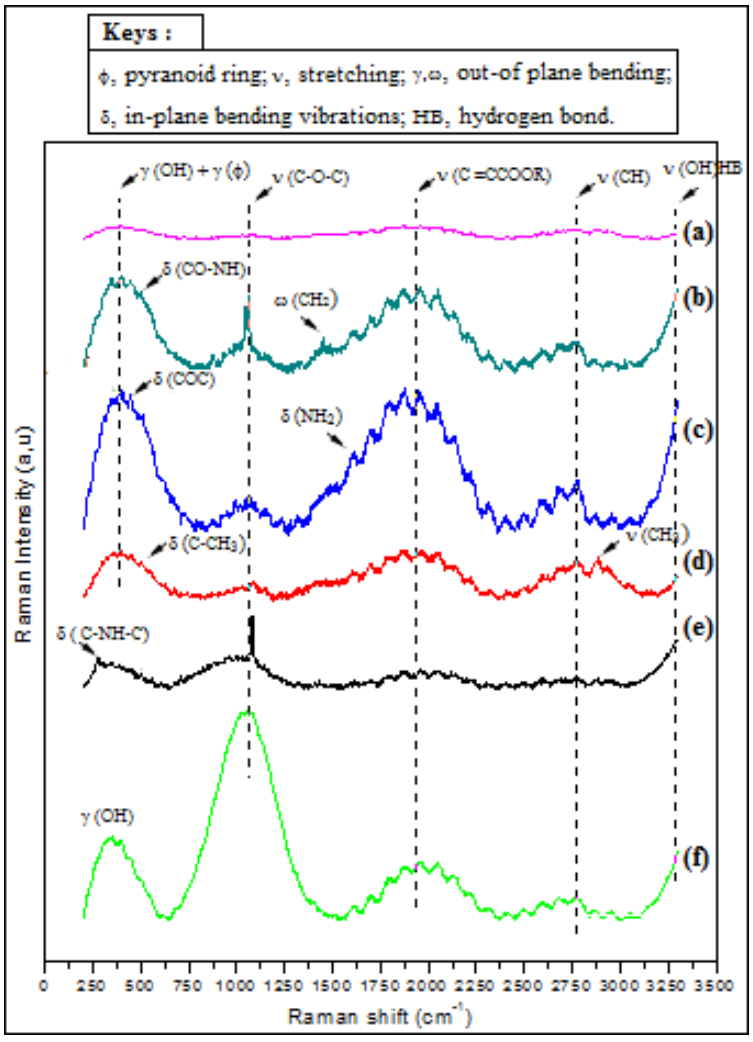

Figure 91. Raman Spectrums of (a): Chitosan FC, (b): Chitosan SA, (c): Chitosan NA, (d): Chitosan CA, (e): Chitosan DCA, (f): Shrimp ShP.

VI.3.6 Thermogravimetry TG and Derivative thermogravimetry DTG for Chitosan FC, Chitosan DCA and Chitosan CA Thermal events observed in Chitosan FC, Chitosan DCA and Chitosan CA in the TG and DTG curves

Thermogravimetric analysis TGA is a thermal analysis that consists of measuring the mass variation of sample in terms of time, through a determined and controlled range of the temperature, with good accuracy of the three measurements: mass, time and temperature. The resulting curve (mass m vs temperature T) provides information about the composition and thermal stability of material [488]. This measurement is often used in research to determine the

characteristics of materials with a view to estimate its kinetics of oxidation at high temperature. Equally to determinate of the temperatures of degradation, the percentage of organic and inorganic parts in material compounds. It can provide other several information on physical phenomena, such as phase transitions, absorption, desorption and thermal decomposition. The Derivative thermogravimetry DTG is the difference thermogravimetry ratio of measurement of weight loss at heating. From the DTG curves, we can determine the number of thermal events to which the substance has been subjected, because each DTG peak, at temperature gives the rate of mass loss (dm/dT in mg/min) within its temperature range [T_i-T_{max}-T_f], where T_i, is the temperature of first mass loss, T_f is the temperature of final mass loss and T_{max} is the temperature of the maximum mass loss rate. In 1954, Paulik – Erdey developed the first thermobalance able to record TG and DTG curves at the same time [489].

Thermogravimetric analysis (TG-DTG) were performed by NETZSCH STA 449F3 Thermogravimeter apparatus, using arbitrarily 24.8 mg of Chitosan FC, 28.8 mg of Chitosan DCA and 31.9 mg of Chitosan CA with heating ratio of 10 °C/min in nitrogen atmosphere with 20.0 mL/min as flow rate of protective gas and 70.0 mL/min as flow rate of purge gas in sample port of platinum until temperature range of 1200 °C. The TG and DTG curves for Chitosan FC, Chitosan DCA and Chitosan CA are shown in Fig.92. The Chitosan FC displays two stages of thermal degradation. The first stage of thermal decomposition started from 62 °C to 145 °C. The peak at the DTG at 100 °C showed an initial mass loss of 3.63 %, referring to the physically adsorbed water surface of the polymer. The second stage of mass loss is subdivided in two parts, the first part for rapid mass loss 51.26 % between 226 and 500 °C with maximum peak of 297 °C in the DTG curve and the second part for slow mass loss 6.35 % between 500 and 813 °C without range of mass stabilization, referring to the decomposition of the polysaccharide structure. The Chitosan DCA undergoes three stages of mass loss. The first stage starting from 75 °C to 150 °C with a maximum peak at 114 °C showed an initial mass loss of 2.27 %, due to release of water in surface and inside polymer. The second step of mass loss 26.93 % is in the range of temperature from 196 to 516 °C with maximum peak of 367 °C according to the first degradation of polymeric carbohydrate molecules whish are consisting of carbon (C), hydrogen (H) and oxygen (O) atoms. The third round of mass loss by 24.65 % with

maximum peak of 775 °C between 606 and 1001 °C, after crystal structure destruction and liberation of the last polysaccharide composed of randomly distributed β-(1→4)-linked D-glucosamine (deacetylated unit) and N-acetyl-D-glucosamine (acetylated unit). Chitosan CA had five parts of thermal degradation on account of his composition and crystalline structure. The first mass loss by 3.86 % from 40 °C to 170 °C with DTG maximum peak at 110 °C, due to water clearance. Then from 184 to 385 °C with DTG maximum peak at 304 °C and mass loss by 14.08 %. The next round of mass loss is by 8.65 % between 390 and 530 °C with maximum peak of 450 °C, due to polysaccharides decomposition. Afterward, the mass decrease by 18.43 % between 530 and 840 °C with DTG maximum peak at 724 °C due to degradation of polymeric carbohydrate after crystal structure destruction. Finally, the mass is lost by 2.65% in range of temperature 840 and 1030 °C with DTG maximum peak at 1000 °C, after mineral part recrystallization due to rest of calcium and phosphorus and liberation of last organic substances. Those all analysis shows that a method of chitosan extraction has an effect on their thermal stability. The Chitosan CA is more thermally stable than Chitosan DCA and Chitosan FC, because he loses his mass slowly, after five degradations showing more thermal inertia. All thermal events remarked in TG and DTG analysis are reported in Table 35. All our TG/DTG curves of chitosan are on concordance with those studies of following authors PEREIRA et al [490], ZHENG et al [491] and SAFDAR et al [492].

Table 35. Thermal events observed in Chitosan FC, Chitosan DCA and Chitosan CA in the TG and DTG curves

Range	Thermal events	**Samples**		
		Chitosan FC	Chitosan DCA	Chitosan CA
1°	Temperature range T_i-T_f (°C)	62–145	75–150	40–170
	DTG T_{max} (°C)	100	114	110
	Mass loss (%)	3.63	2.27	3.86
2°	Temperature range T_i-T_f (°C)	226–500	196–516	184–385

	DTG T_{max}	297	367	304
	Mass loss (%)	51.26	26.93	14.08
3°	Temperature range			
	T_i-T_f (°C)	500–813	606–1001	390–530
	DTG T_{max}	–	775	450
	Mass loss (%)	6.35	24.65	8.65
4°	Temperature range			
	T_i-T_f (°C)	–	–	530–840
	DTG T_{max}	–	–	724
	Mass loss (%)	–	–	18.43
5°	Temperature range			
	T_i-T_f (°C)	–	–	840–1030
	DTG T_{max}	–	–	1000
	Mass loss (%)	–	–	2.65

Table Keys : T_i: Initial temperature, T_f: Final temperature, T_{max}: Temperature of the maximum mass loss rate

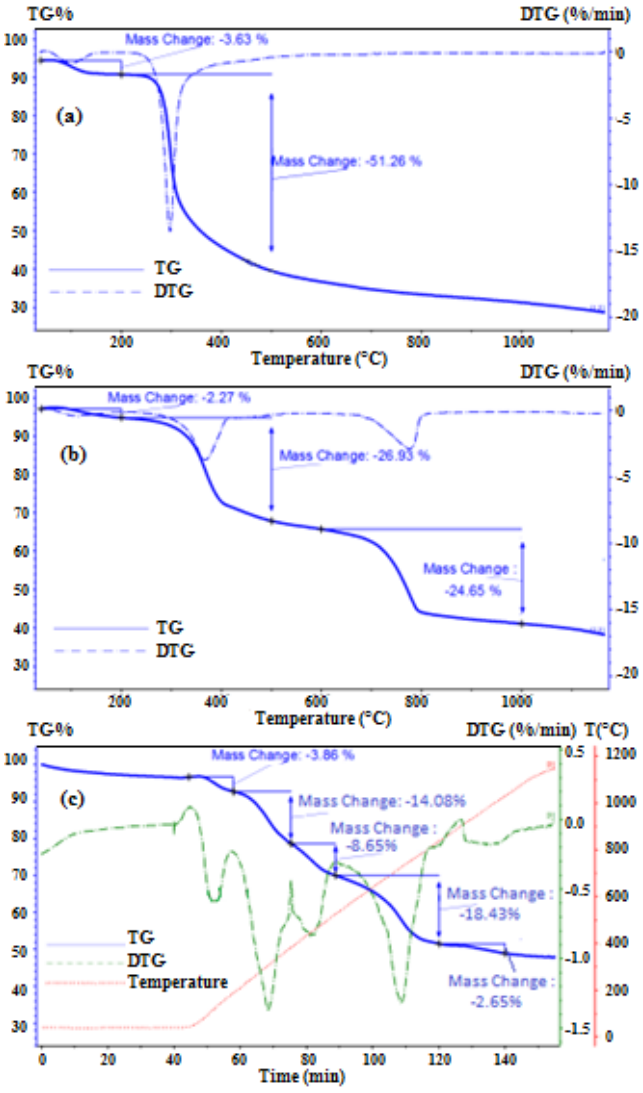

Figure 92. Thermogravimetry TG and Derivative thermogravimetry DTG for (a): Chitosan FC, (b): Chitosan DCA and (c): Chitosan CA.

VI.3.7 Scanning Electron Microscope (SEM) analysis: Microstructures and irregularities in Chitosan FC, Chitosan DCA, Chitosan CA and Chitosan NA.

Scanning Electron Microscope SEM is one of most analysis to observe the surface morphology, particles sizes and microstructure of the materials crystals or amorphous polymers. This microscope produces images after scanning the surface of the sample by intense and focused beam of electrons that interact with atoms of materials, producing various signals containing several information concerning the surface topography.

In our case, scanning electron microscopy (VEGA3 TESCAN, Cadi Ayyad University, Marrakech, Morocco) was used to observe the morphological changes and differences in structure between Chitosan FC, Chitosan DCA, Chitosan CA and Chitosan NA. The surface morphology was taken at an acceleration voltage of 10 kV, by almost working distance (WD) for our samples such as 9.73mm for Chitosan FC, 9.98mm for Chitosan DCA, 10.02mm for Chitosan CA, and 10.05mm for Chitosan NA, with same magnifications: 5 µm, 10 µm and 20 µm respectively for each chitosan samples. All SEM images are regrouped in Fig.93.

The SEM analysis results show an irregularity in Chitosan FC microstructure and its surface morphology: Smooth surface with some rough, irregular membrane fissures, irregular pattern, no pores and no existence of chitosan nanoparticles. The image of the Chitosan DCA reveals that the surface is rough, disordered, disorganized with distorted microstructure with some cracks and very small pores. We notice the appearance also of some smooth and homogenous isolated surface in few areas indicating formation of unacetylated chitosan. The absence of homogeneity in Chitosan DCA surface with smooth part and rough part both is the signs of phase separation indicate the incomplete extraction of the chitosan from shrimp shells. For Chitosan CA and Chitosan NA, we noticed almost similar morphology: Rough surface, irregular block, crystalline cluster with some porosity due to use of ammonium like results of TOLESAet al [493], and an appearance of chitosan nanoparticles. However, we observed some differences between them such as: Appearance of few nanometric threads in Chitosan CA structures, some small smooth and flat zone in Chitosan NA (The same for Chitosan CA but not a lot). We still notice that Chitosan CA nanoparticles sizes are smaller than those of Chitosan NA. Similar results were obtained by S. Salamat et al using sulfuric acid, acetic acid [494].

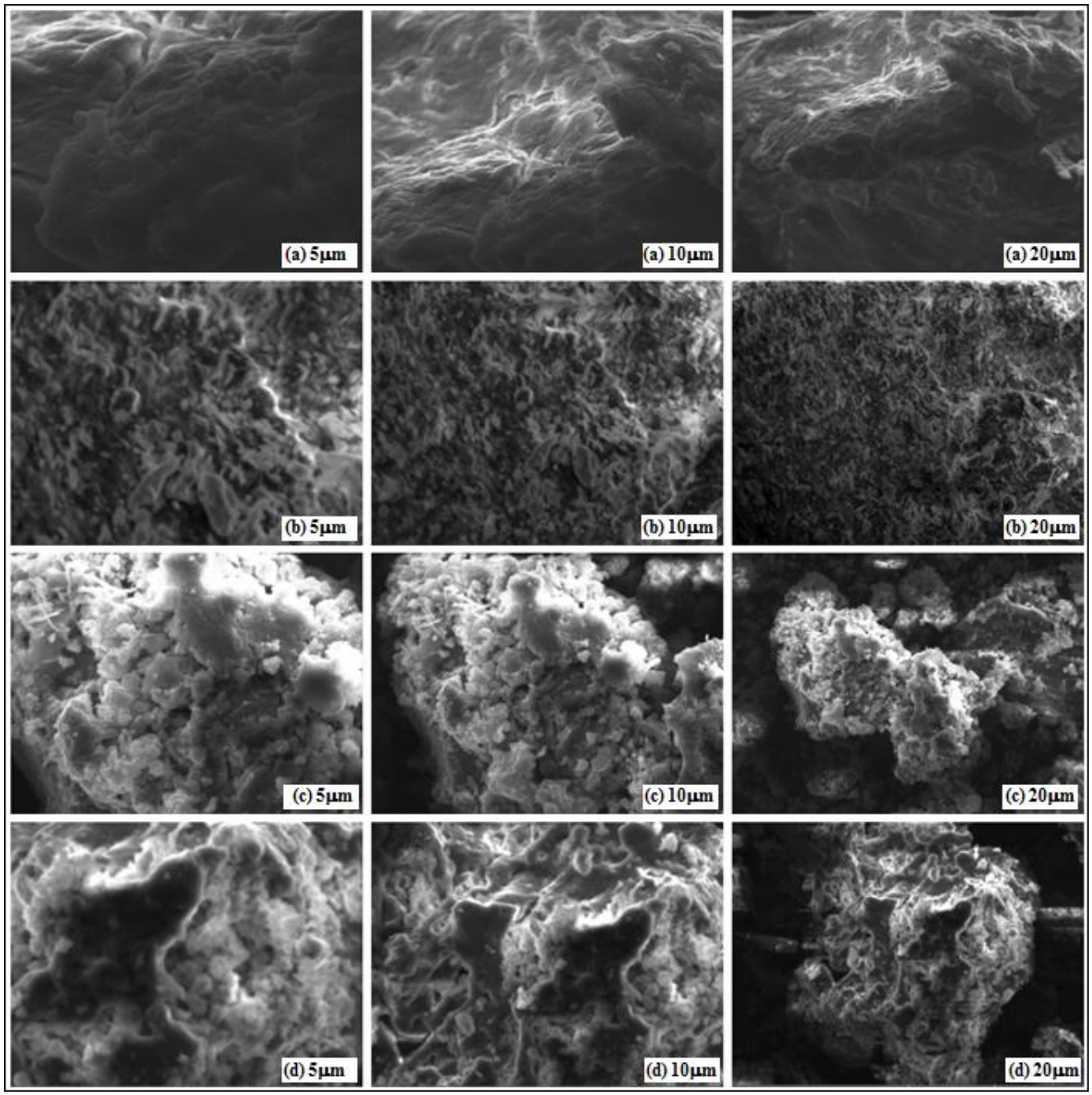

Figure 93. Scanning Electron Microscope (SEM) analysis with magnification 5µm, 10µm and 20µm for (a): Chitosan FC, (b): Chitosan DCA, (c): Chitosan CA and (d): Chitosan NA.

Generally, we notice that the extraction method of chitosan exhibit changes in the shape and morphology. The chitosan samples which were prepared by concentration acids have a higher specific surface area compared to chitosan prepared by diluted acid or Chitosan

FC. Reason that the concentrated acids remove all minerals and impurities from the shrimp shells and forces it for total dissolution in order to generate a lot of chitosan nanoparticles.

VI.3.8 Energy-dispersive X-ray spectroscopy (EDX) analysis of Chitosan DCA, (c): Chitosan CA and (d): Chitosan NA.

Energy Dispersive X-Ray spectroscopy EDX, also noted EDS or EDAX, is an X-Ray non destructive analysis used to identify the elemental composition of materials. Its principle based to convey an external X-ray stimulation on electrons of K bands within atoms, in order to one or more this electron leaves its orbit and will be replaced by an electron from L band, with emission of radiation energy k_α, this last electron will be also replaced by an electron from M band with emission of L_α radiation energy. Furthermore, the electron of K band can be replaced directly by electron from M band with emission of K_β radiation energy. All of these energies' radiation will be captured by the device's collector and processed in order to display a spectrum with different peaks. Each peak corresponds to a unique chemical element with its atomic and weight concentration [495].

Table 36. Elementary EDX analysis for Chitosan DCA, Chitosan FC, Chitosan CA, Chitosan NA

Sample	Chitosan DCA		Chitosan FC		Chitosan CA		Chitosan NA	
Element	Weight %	Atomic %	Weight %	Atomic %	Weight %	Atomic %	Weight %	Atomic %
C	26,26	35,9	45.55	51.92	29,01	35,55	15,02	18,99
N	4,17	4,89	12.28	12.01	5,22	3,91	3,72	3,89
O	49,1	50,41	42.16	36.08	65,76	60,53	81,25	77,11
P	3,4	1,8	0.00	0.00	0.00	0.00	0.00	0.00
Ca	17,06	6,99	0.00	0.00	0.00	0.00	0.00	0.00

All EDX spectrum analysis for Chitosan FC, Chitosan DCA, Chitosan CA and Chitosan NA are shown in Fig.94, and the results of each sample elemental composition are summarized in Table 36, and plotted in Fig.95 in order to compare easily the elemental weight and atomic concentration percentages in each chitosan samples. From the results, we notice the presence of the peaks for following element: the carbon C, the nitrogen N and the oxygen O with a different intensity related to their concentration in each chitosan samples. However, the characteristic peaks of the phosphorus

P, and the calcium Ca appeared only in Chitosan DCA. This result proves the incapacity of diluted acid to remove all minerals from the shrimp shells, contrary to concentrated acids can maybe leave just a few minerals traces.

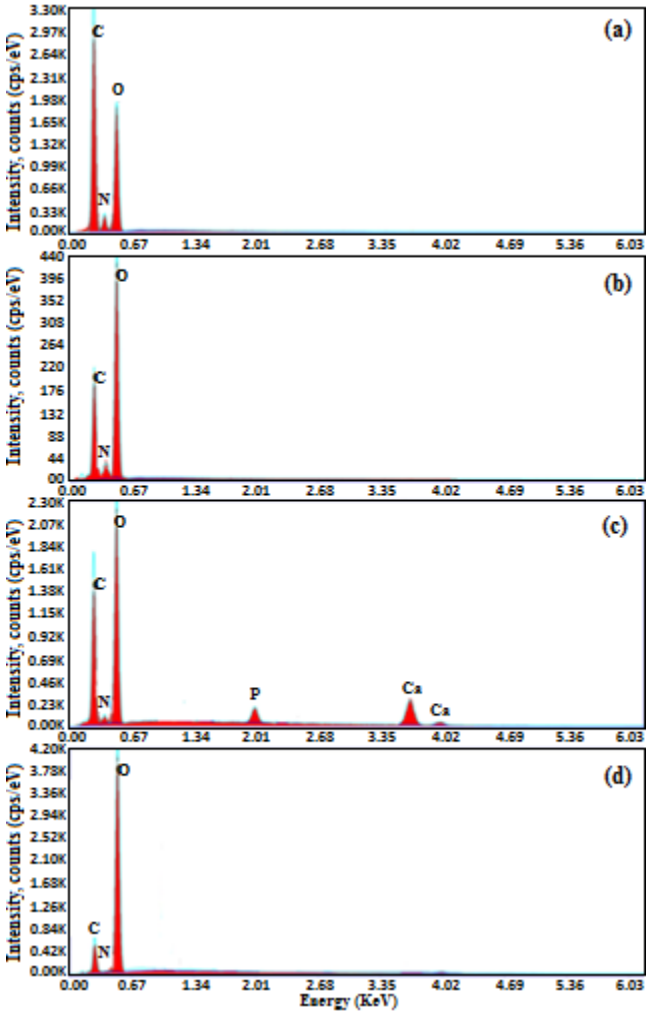

Figure 94. EDX spectrum analysis for (a): Chitosan FC, (b): Chitosan CA, (c): Chitosan DCA and (d): Chitosan NA.

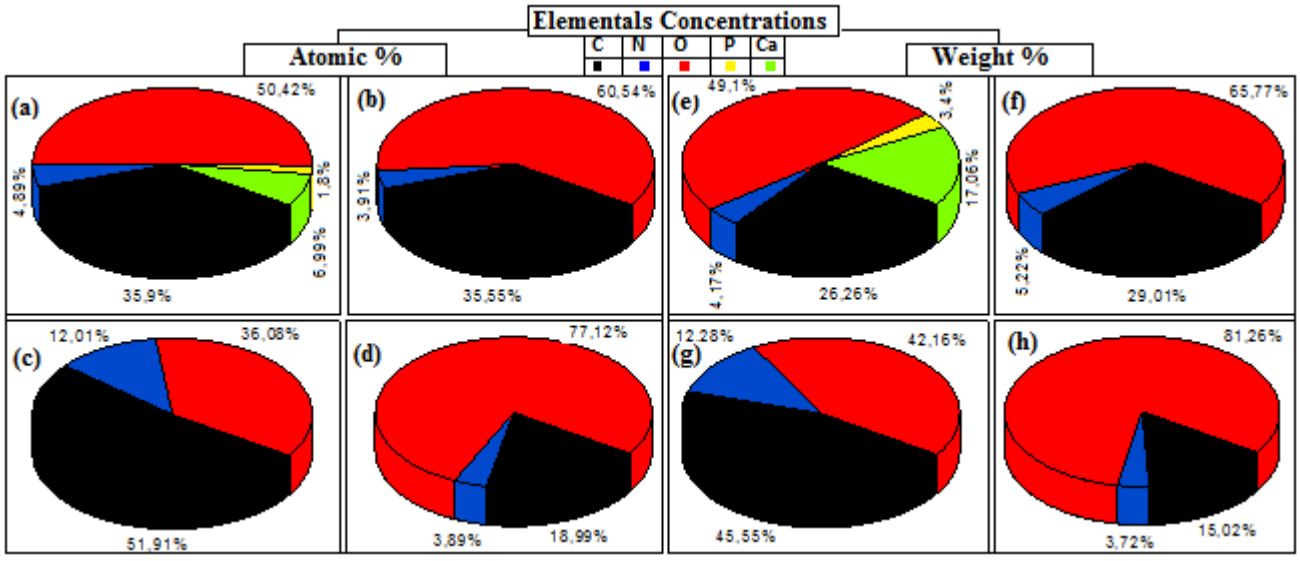

Figure 95. Representation of elemental atomic concentrations for (a): Chitosan DCA, (b): Chitosan CA, (c): Chitosan FC, (d): Chitosan NA. And elementals weight concentrations for (e): Chitosan DCA, (f): Chitosan CA, (g): Chitosan FC, (h): Chitosan NA.

VI.4 Conclusion

We can conclude that our chitosans gained by concentrated acids and base, are pure and ultrafine in nanometer scale 8-30 nm with a very good degree of deacetylation (DD) 80%, splendid for water treatment. Also good on opto-electronic performance with small gap valence as semiconductor, give them a possibility to be used for production of intelligent biodegradable fibers. As well, they provide a different degree of crystallinity towards biodegradable sutures. They offer more heat resistance until 367°C for starting thermal degradation, in comparison to commercial chitosan (from Fluka Chemica Comp) which starts degradation at 297°C.

Our method gives a possibility to produce a big quantity of chitosan in short time duration. It can be also used for treatment of very dirty shrimp shells waste, because the concentrated acids remove all impurity. We recommend to use it only in Laboratories and Factories, and forbidden at home.

Our chitosan samples present are suitable for pharmaceutical applications, due to their purity and high degree of deacetylation.

The grains size obtained of chitosan in our work, is offering good perspective which can be used easily on coating based on carbon nanotube and graphene.

Moreover, these materials can be used as a wound-healing material for the prevention of opportunistic infection and for enabling wound healing, as antibacterial agents, gene delivery vectors and carriers for protein release and drugs.

Chapter VII:

CARBON-CHITOSAN-HYDROXYAPATITE HYBRID PARTICLES SYNTHESIS; USING GRAPHENE, MW CARBON NANOTUBES AND SW CARBON NANOHORNS

VII.1 Introduction

Historically, Human search always to develops their capacity, materials, and tools to treat damage, weakness, or degradation in health. In this way, a lot of scientists from the worldwide try to give solutions for the damage of bone and teeth [496] coming from several diseases such as pathologic [497], physiologic [498] or cause to imprudence [499]. For a long time, the metallic implants were used for partial or total substitution for tooth, hip, knee, and other bones [500,501]. From the historical point of view, the metallic implants are based on mercury, cobalt, and nickel or their alloys [502] since to their mechanical properties, stability, and resistance against external stress [503]. The metallic implant on mercury, cobalt, and nickel provides good mechanical strengths and it is being satisfactory in point [504]. However, these metals display low biocompatibility, without a self-link or growth with bone [505], and their linkage with bone is assured only by screws. Thus, after a certain time duration, great dislocations appear towards bone-metal links [506, 507], which cause a novel weakness and incapacity of normal life for patients. On the other side, the metals display anti-bacterial and anti-microbial activities excessively [508]. Therefore; neighboring areas still suffer inflammation [509]. Also, the ionic exchanges between metallic implants and ions in blood coming from nutrients are highly probable via substitution and/or abrasion phenomenon [510] which can exhibit an increase of heavy metal ions in blood [511] which generate other health complications. Consequently, the world health organization has limited the uses of metals and principally mercury, cobalt, and nickel since their toxicities [512]. Also, the titanium metal was used in orthopedic prosthesis since to their good biocompatibility, mechanical, and chemical stability [513] with very low toxicity risk [514]. But the Titanium as bulk material is expensive and challenging/costly to machine [515] and not able to be convenient by everybody. Thence, the ceramic amalgams and implants based on HAP become more used as material for dental and orthopedic prosthesis [516] due to its high osteoconductivity and biocompatibility [517] in fact that it is naturally the major compound of inorganic part of bone and teeth [518], and due also to its easiness to be synthesized or extracted from abandoned bovine bone or certain shell sea. The HAP material provides good mechanical properties where its structure undergoes no changed phase up to 4 GPa as Young's modulus and it reverts to the original structure when the pressure was released to ambient pressure [519], and high chemical stability [520]. Furthermore, various study and experiment were carried for HAP to increase their mechanical [421], chemical [522] and biological [523] properties by incorporating some metal ions by low concentration in HAP cell to increase its electrical properties with or without changes in its structure

[524,525], or by doping by Titanium that gives HAP some antibacterial activity [526] where this synthesis or Titanium deposition requires energy and tools to perform the electrophoresis deposition (EDP). Recently, Chitosan (CS) was exploited with HAP for produced new biopolymers with osteoconductivity and antibacterial behavior [527] using also the EDP [528], or the chemical vapor deposition [529]. Since, CS is natural product material extracted from shrimp shells, crabs, fungi, or other natural sources [530], displays remarkable antibacterial and antimicrobial activities without risk of toxicity or contamination for human health [531]. At the last time, carbons nanoscale materials as Carbon nanotubes (CNT), Carbon Nanohorns (CNH), fluorine, and Graphene were deposited alone or with CS or chitin into HAP for synthesized hybrids particles displaying very good properties to be used for dental or orthopedic prosthesis [532]. Although several studies, the EDP and Chemical vapor deposition CVD are widely used for coat HAP by CS, GNPs, CNT, and/or CNH. While, those hybrids materials products included two, three, or multi superposed layers [533,534], and not one united homogenate layer. For this reason, we tried to develop the chemical method deposition using acid and organic solvent for HAP, CS, Multiwall Carbon nanotubes (MWCNT), Single-wall Carbon Nanohorns (SWCNH), Graphene nanoplatelets grade C90 (GNPs_C90) and Graphene nanoplatelets grade C97 (GNPs_C97) for produced homogenous hybrids nanomaterials which combined the osteoconductivity and chemical stability of HAP and anti-microbial and anti-bacterial activity of natural CS and high electrical, mechanical properties of nanoscale carbon materials SWCNH, MWCNT, GNPs_C97, and GNPs_C90. We abbreviate the names of our synthesized hybrids nanoparticles as follow CS-HAP-MWCNT, CS-HAP-SWCNH, CS-HAP-GNPs_C90, and CS-HAP-GNPs_C97 in all this manuscript. All those four hybrids nanoparticles have around the same HAP-CS compound part so same properties for this side, but each hybrids nanoparticle provide some particulars properties following its carbon nanoscale particles used in its synthesis. Our HAP used in this study is synthesized by the co-precipitation method according to a ternary diagram of (CaO, P_2O_5, H_2O) at 30 ° C temperature using phosphorus pentoxide (P_2O_5) and calcium oxide (CaO) as precursors with distilled water [535]. And the CS is extracted from shrimp, and the carbon nanoscale materials MWCNT, SWCNH from Carbolex Comp, GNPs_C90, and GNPs_C97 are received from Nanoinnova Technologies SL Comp. To keep our materials solubles, we used the solvents of HAP, CS, and each carbon nanoscale material simultaneously and progressively in one beaker with heath and spin agitation in target to give maximal homogeneity for each solution. At this point, all our materials are in nanometer scales which produce very homogenate nanopowders without subdivision

by layers. This method offers more possibility of external and internal linkage between HAP, CS, and carbon nanoscale materials that we more discussed amongst this manuscript. The MWCNT set out remarkable properties which we illustrate just brief information. It provides tensile strengths as high as 63 GPa, and thermal conductivities higher than 3000 $W.m^{-1}. K^{-1}$ at room temperature, and powerful electronic transport [536]. The other type of nanocarbon used in this study is the SWCNH; it is one type of carbon material family similar to SWCNT with conic closure in the edge with the resemblance in the atomic arrangement of CNT. This new form of nanocarbon attracted increasing attention due to their unique morphology and structure. A single Nanohorn consists of a cone of sp^2-bonded carbon atoms with 2 - 5 nm in diameter and 40 - 80 nm in length. CNH inherits the physicochemical features of CNT and exhibits great potentials in energy conversion, chemical engineering, catalysts, fuel cell, and electronic applications [537]. Numerous monomers Nanohorn about 2000 units get together during synthesis to form a spherical aggregate with diameters about 80 -100 nm [538]. Graphene Nanoplatelets GNPs are unique nanoparticles consisting of short stacks of Graphene sheets having a platelet shape typically consist of aggregates of sub-micron platelets that have a particle diameter fewer than two microns and a typical particle thickness of a few nanometers, depending on the surface area [539]. Grade C particles can be ordered with average surface areas of 300, 500, 750 m^2/g. Recently the GNPs Grade C 900 and 970 m^2/g are available and we used them in this study, we abbreviate their name successively by GNPs_C90 and GNPs_C97. The goodness of GNPs is displayed in their low-cost price and high continuous surface versus Graphene [540]. Besides, GNPs provide all chemical and physical properties of Graphene. Natural graphite is inert and insoluble. Thus, graphite does not present significant environmental risk and consequently, its derivatives GNPs, CNH, CNT ...etc are generally safe towards the environment and human health with proper consideration and controlled functionalization that can potentially reduce their toxicity [541,542,543]. Recently, CNH, CNT, and GNPs were used for advanced polymer composites for biomedical applications [544, 545].

VII.2 Experimental processes

VII.2.1 HAP Synthesis

Our objective is to elaborate HAP according to a ternary diagram (CaO, P_2O_5, H_2O) at 30 ° C temperature

Chemical equation: $3P_2O_5 + 10CaO + H_2O \rightarrow Ca_{10}(PO_4)_6(OH)_2$

Required tools: one thermostat, one beaker 100 ml, Electronic scale, and spatula.

Required reagents: 5.2762 g of calcium oxide (CaO), 4,0066 g of phosphorus pentoxide (P_2O_5), and 90,7172 g distilled water (H_2O) to have a stoichiometric mixture with a total mass of 100 g. According to the ternary diagram, the HAP appearance domain is too thin [546]. After weighing by the electronic accuracy balance, all reagents were put and mixed manually by spatula in a beaker glass of 100 ml before being put in the thermostat at 30 °C constant temperature. During the time of reaction, the solution was shaken manually by spatula after every 24 hours for 144 hours (6 days). The reaction ends after water disappearance. Who will disappear without reaching 100 °C, it is disappearance under reaction and not under vaporization. The gained powder was ground manually with mortar and pestle then put in the oven at 100 °C for 24 hours for residue water evaporation. This chemical process is outlined in figure 96.

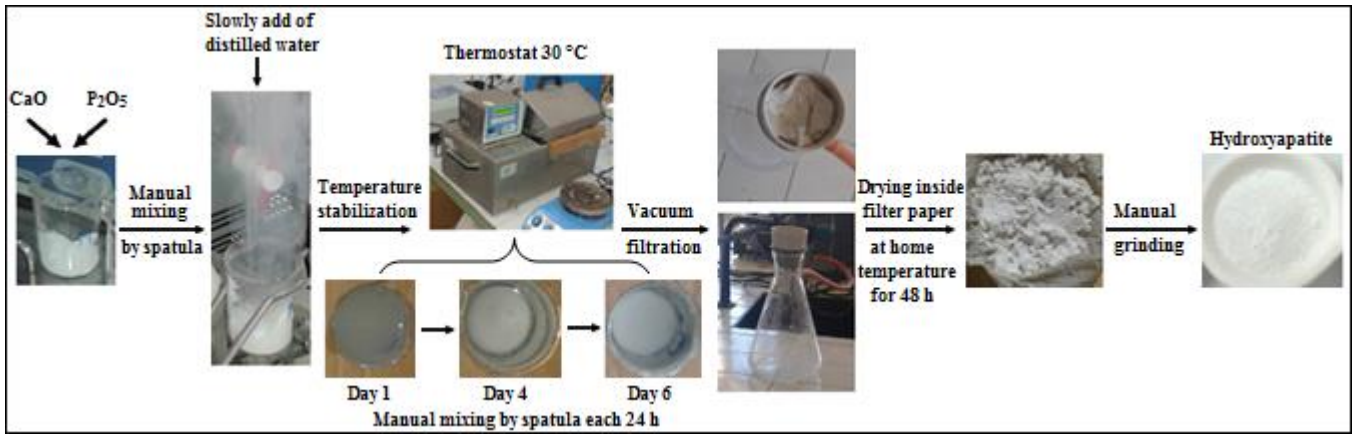

Figure 96. Experimental process of Synthesis of HAP

VII.2.2 **Chtiosan extraction:**

The CS was extracted from shrimp shell by traditional method using nitric acid 1M for demineralization, and ammonia base for deproteinization 1M, then sodium hydroxide NaOH solution with pH=12 for deacetylation. Firstly, the shrimp shells were well rinsed in water, dried until full drought, then ground. In the second step, we add the nitric acid 1M and mixed them for 4h at 80°C. Then, we rinse it by distilled water. In the third part, we add the ammonia 1M following the same process (4 hours mix in 80°C). Once finished, we rinse it also by distillate water. After, we put it in the oven for 8h at 100°C. For deacetylation, we make the product powder in sodium hydroxide solution (pH=12) for 4h at 80°C. The product then is ready for the whitening process by oxygenated

water for 2h at 80°C. We finished by grinding manually our product by porcelain mortar and pestle. This chemical process is schematized in figure 97.

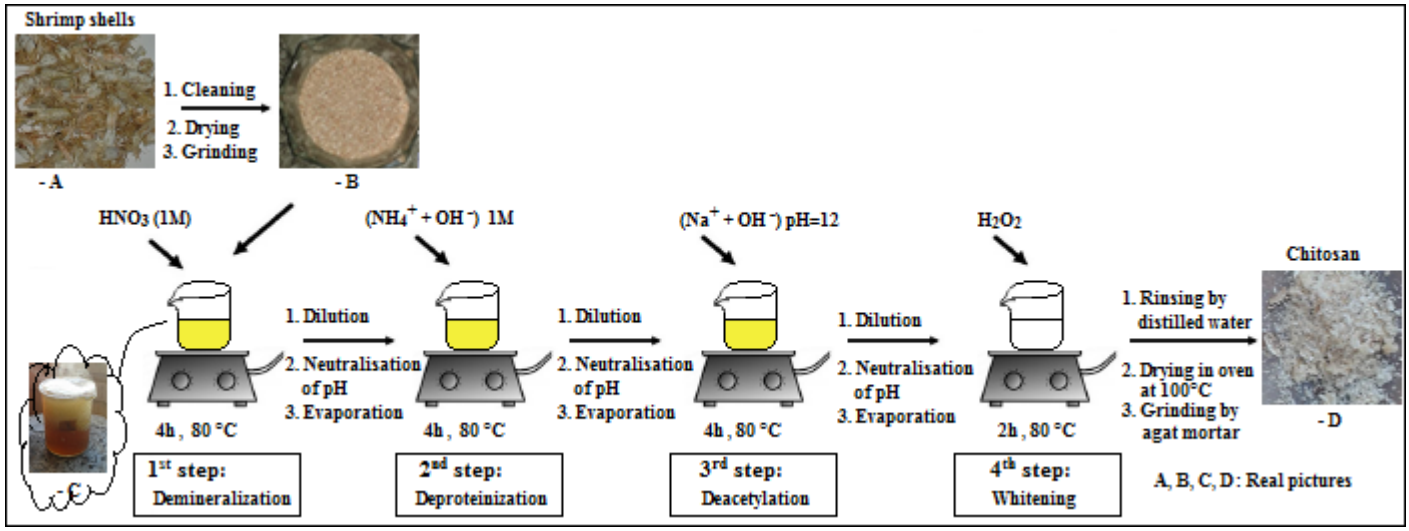

Figure 97. Experimental process of Chitosan extraction

VII.2.3 **Chitosan -Hydroxyapatite-Carbon hybrids nanoparticles synthesis**

Heating under reflux is recommended with a glass flask coupled with a condenser to prevent reagents from escaping. If the necessary condenser or its tools for make heat under reflux are not available like our case, the few quantities of distilled water must be added on a reactive solution once the primitive water quantities have been evaporated. This reaction must be carried under laboratory hood. The experimental process was adapted from K.A.B Pereira et al. [547] and Gomez et al. [548]. 0.3 g of HAP were dispersed in 62 ml Ethanol-nitric acid mixture with 30 ml of ethanol, 2 ml of concentrated nitric acid, and 30 ml of distilled water, using a glass flask. The mixture was kept at 80 C, under mechanical stirring, during 2h. After that, we added in each flask 0.15 g of CS, and 1ml of concentrated acetic acid and we continued the mechanical stirring, during 2 h. Then we added 0.03g of SWCNH in flask 1, 0.03g of MWCNT in flask 2, 0.03g of GNPs_C97 in flask 3, 0.03g of GNPs_C90 in flask 4 and we add in each beaker 2 ml of concentrated hydrochloric acid under mechanical stirring for 2 h duration too. Once finished, the reaction medium must be diluted and neutralized until getting the pH neutralization for total acid removal. Finally, we achieved the filtration, then we make the four obtained powder in the oven for 2 h at 100 °C for the last liquid evaporation. Then we ground manually each powder by agate mortar. This chemical process is summarized in figure 98.

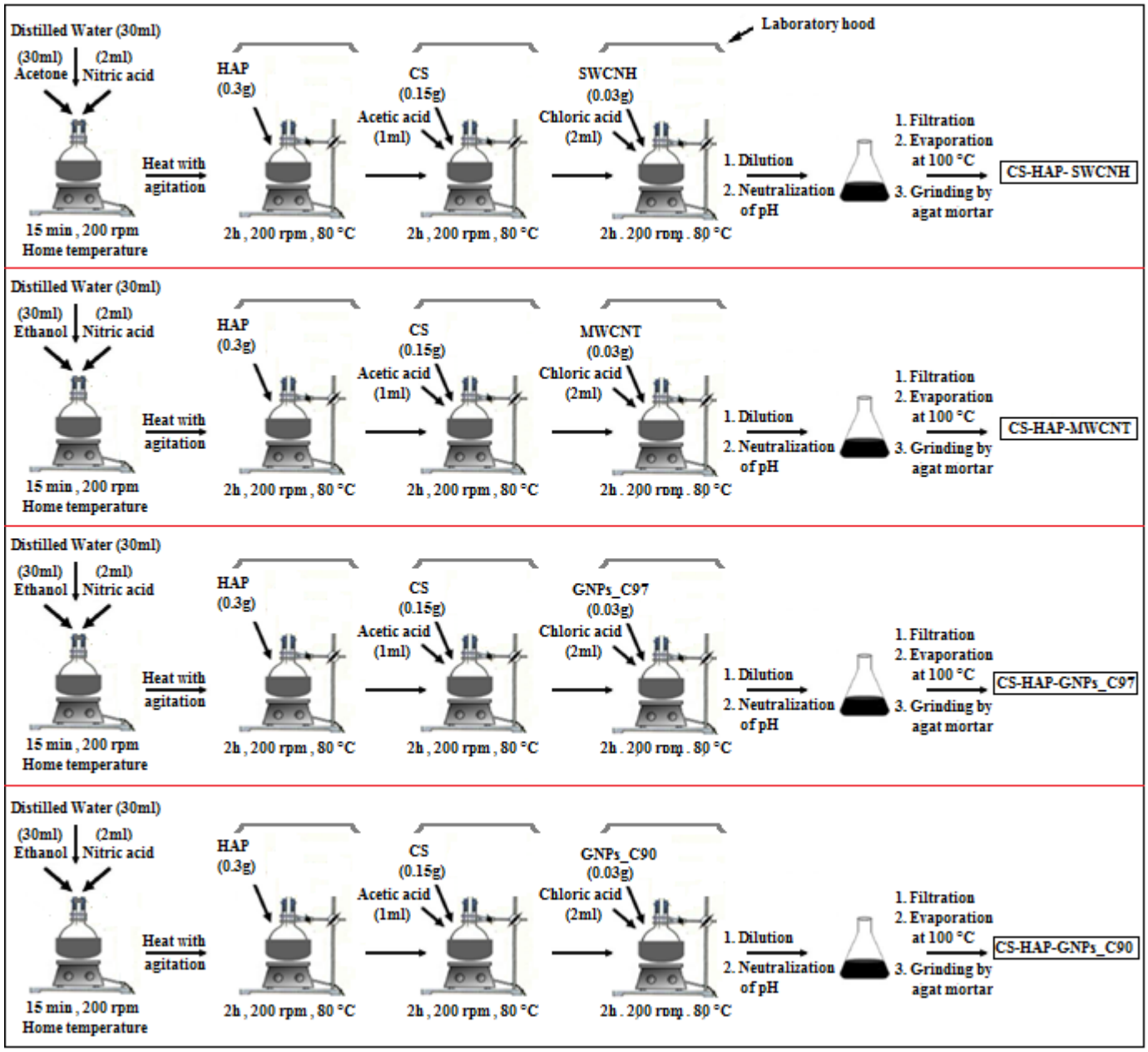

Figure 98. Experimental process of synthesis: CS-HAP-SWCNH, CS-HAP-MWCNT, CS-HAP-GNPs_C97, CS-HAP-GNPs_C90 hybrids nanoparticles

VII.3 Characterization

VII.3.1 X-ray fluorescence analysis: Chemical elements concentrations in of: HAP, CS, CS-HAP-SWCNH, CS-HAP-MWCNT, CS-HAP-GNPs_C97, CS-HAP-GNPs_C90.

X-ray fluorescence XRF is the emission of characteristic "secondary" X rays from a material that has been excited by bombarding with high energy X rays or gamma rays The phenomenon is widely used for elemental analysis and chemical analysis particularly in the investigation of metals glass ceramics

and building materials and for research in geochemistry forensic science archaeology and art objects such as paintings and murals This is a non-destructive analysis of the full range of elements from sodium to uranium [549]. The X-ray fluorescence spectrometer is capable of analyzing elements in concentrations from a high percentage down to ppm-level. Thus, it is very important to clean highly the crucibles that support the samples, because the XRF analysis is very sensitive, and it's highly probable to get some impurity concentration in analysis results due to the residue of materials of previous analysis. Although, if some materials not suitable for the experience appear amidst analysis values, the results must be rectified by the cancellation of the impurity values and distribute them proportionally to major theoretical compounds of samples, and this is our process in this XRF and EDX elemental analysis. In our case, the importance of chemical elemental analysis is to know the concentration variation of Chemical element after synthesis of our four hybrids nanoparticles by chemical deposition, for objective to know the carbon nanoscales materials effect in the mineral part and crystalline structure of HAP. The XRF patterns of all our products are shown in figure .99. We will give consideration of oligo-elements in ppm (parts per million) such as Sodium Na, Manganese Mn, Silicon Si and we cannot count of them in the description of crystallization of the structure of our cells because they do not enter in there build. The existence of these oligo-elements in all our hybrids materials in ppm is due just to the background noise [550] despite our weariness. The important result in this analysis is the percentages of Phosphorus P and Calcium in all our hybrids nanoparticles because they are the essential elements in the structure of HAP [551], and the variation of their concentration lead to change and development in their structural properties such as crystal systems [552], reticular planes [553], lattice parameters [554], coordination [555], and hybridization [556]. The results show the existence of two major mineral elements Ca and P with considerable values. The concentrations of (P , Ca) for HAP, CS, CS-HAP-SWCNH, CS-HAP-MWCNT, CS-HAP-GNPs_C97, CS-HAP-GNPs_C90 successively are (10.368 % , 44.069 %), (0.337 % , 0.240%), (8.034 % , 26.465%), (1.485 % , 11.164%), (5.062 % , 19.015 %), and (9.635 % , 24.839%). We notice that the concentration of Ca and P decreases for all samples and this is evident due to increase of concentration of Carbon C, Oxygen O, Nitrogen N, and Hydrogen H. The concentration of elements C, O, N and H does not appear directly in the XRF patterns, but we can conclude them by simple subtraction by 100% - ∑% appeared elements. The concentration in % (C% + O% + N% +H%) for HAP, CS, CS-HAP-SWCNH, CS-HAP-MWCNT, CS-HAP-GNPs_C97, CS-HAP-GNPs_C90 are successively 45.563 %, 99.423 %, 65.501 %, 87.351 %, 75.923 % and 65.526 %.

These results show a low %Ca and %P concentration of our CS which proves its quality because naturally the CS is composed essentially by C, O N, and H. For HAP we remark that the level of %Ca is higher than the perfect %Ca concentration but a good % P concentration. Since, the perfect theoretical values of elemental concentration of Ca, P, O, H of HAP are successively 22.73 %, 13.64 %, 59.09 %, 4.55% so (O% + H% = 63.64%) owing to its chemical formula $Ca_{10}(PO_4)_6(OH)_2$. Thus, all our synthesized hybrids particles display good concordance those values, which show that these hybrids particles saved the HAP composition and its biocompatibility with a gain of antibacterial and antimicrobial activity due to doping by CS. Although it was being an inequality in the concentration of %(C+O+N+H), this result exhibits some divergence among our hybrids particles. For CS-HAP-SWCNH we notice small decreases of % Ca and P successively by 3.735% and 5.606% and small increases in %(C+O+N+H) by 1.861% which show an increase in the electrical, thermal chemical and structural properties due to doping by SWCNH [557]. Similarly for CS-HAP-MWCNT, it was HAPpened considerable decreases of % Ca by 11.566% and P 12.155% and important increases in %(C+O+N+H) by 23.711% which prove a large permeation betwixt compounds of HAP, CS, and MWCNT leading to a great increase in the mechanical properties due to the effect of MWCNT [558].

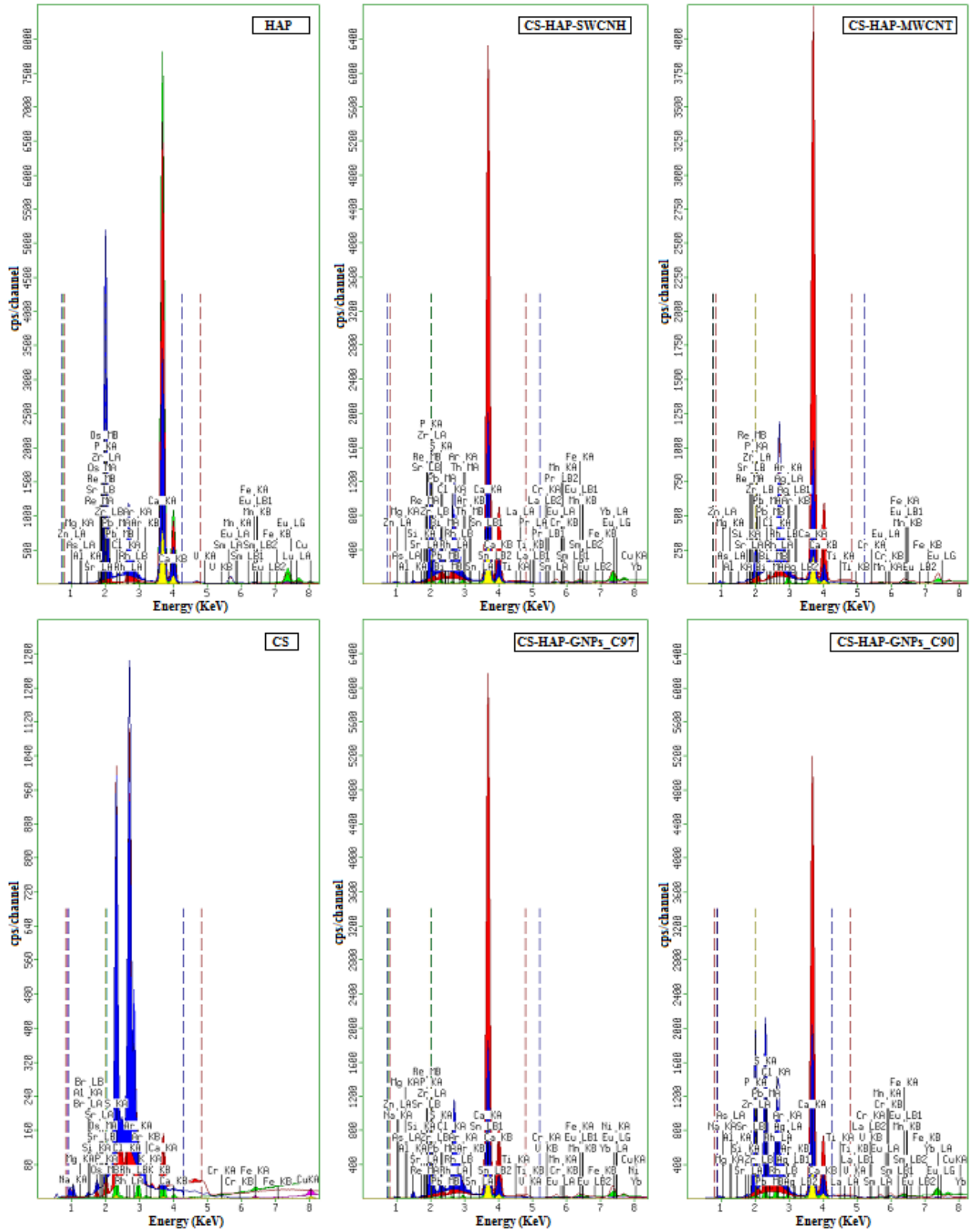

Figure 99. XRF pattern of: HAP, CS, CS-HAP-SWCNH, CS-HAP-MWCNT, CS-HAP-GNPs_C97, CS-HAP-GNPs_C90.

For CS-HAP-GNPs_C90 unlikely to other hybrids particles, we behold a few raises of % Ca by 2.109% and decrease of P by 4.005% and small increases of % (C+O+N+H) by 1.886%. For CS-HAP-GNPs_C97 we notice a decrease of % Ca and P successively by 3.715% and 8.578% and an increase in %(C+O+N+H) by 12.283%, this differences between these two CS-HAP-GNPs is due to the difference in the specific surfaces between GNPs_C90 and GNPs_C97, since the specific surface of GNPs_C97 is bigger than this of GNPs_C90 leading increase in the mechanical, electrical and optoelectronic properties in accordance to high mechanical, electrical and thermal properties of GNPs_C90 and GNPs_C97 in both [559, 560, 561].

Table 37. Chemical elements concentrations in of: HAP, CS, CS-HAP-SWCNH, CS-HAP-MWCNT, CS-HAP-GNPs_C97, CS-HAP-GNPs_C90:

Samples		HAP		CS		CS-HAP-SWCNH		CS-HAP-GNPs_C97		CS-HAP-MWCNT		CS-HAP-GNPs_C90	
Compound		Conc	Unit	Conc	Unit	Conc	Unit	Conc	Unit	Conc	Unit	Conc	Unit
P		10,36	%	0,33	%	8,03	%	5,06	%	1,48	%	9,63	%
Ca		44,06	%	0,24	%	26,46	%	19,01	%	11,16	%	24,83	%
Oligo elements	Na	0	ppm	6,40	Ppm	0	ppm	0	ppm	0	ppm	5,70	ppm
	Mg	607,3	ppm	0	Ppm	361,7	ppm	800,7	ppm	0	ppm	803,20	ppm
	Al	468,2	ppm	0,14	Ppm	0,66	ppm	1,26	ppm	0,12	ppm	0,26	ppm
	Si	0	ppm	0,22	Ppm	0,11	ppm	0,15	ppm	820,7	ppm	0,17	ppm
	S	0	ppm	4,07	Ppm	1,87	ppm	0,70	ppm	0	ppm	7,84	ppm
	Cl	133,3	ppm	645,9	Ppm	0,39	ppm	0,36	ppm	72,3	ppm	2,83	ppm
	K	0	ppm	185,6	Ppm	0	ppm	0	ppm	0	ppm	0	ppm
	V	14,7	ppm	0	Ppm	0	ppm	14,3	ppm	0	ppm	16,1	ppm
	Cr	0	ppm	9	Ppm	53,5	ppm	99,2	ppm	18,9	ppm	43,2	ppm
	Mn	136,2	ppm	0	Ppm	107,3	Ppm	51,2	ppm	22,4	ppm	59	ppm
	Fe	315,9	ppm	45,5	Ppm	403,8	ppm	434,2	ppm	128,5	ppm	492,9	ppm
	Cu	267,4	ppm	51,7	Ppm	23,9	ppm	19,8	ppm	0	ppm	48,3	ppm
	Zn	144,3	ppm	0	Ppm	23,8	ppm	81,8	ppm	12,7	ppm	0	ppm
	As	29	ppm	0	Ppm	21,6	ppm	12,9	ppm	8,5	ppm	12,4	ppm
	Sr	249,7	ppm	17,3	Ppm	193,3	ppm	134,3	ppm	93,9	ppm	158,3	ppm
	Zr	3,3	ppm	0	Ppm	0,4	ppm	7,2	ppm	2,7	ppm	1,8	ppm

VII.3.2 EDX analysis: elemental and weight concentrations of: HAP, CS, CS-HAP-SWCNH, CS-HAP-MWCNT, CS-HAP-GNPs_C97, CS-HAP-GNPs_C90.

Energy-dispersive X-ray spectroscopy EDX is an analytical technique used for the elemental analysis of sample It relies on the interaction of some source of X-ray excitation and a sample Its characterization capabilities are due in large part to the fundamental principle that each element has a unique atomic structure allowing a unique set of peaks on its electromagnetic emission spectrum.

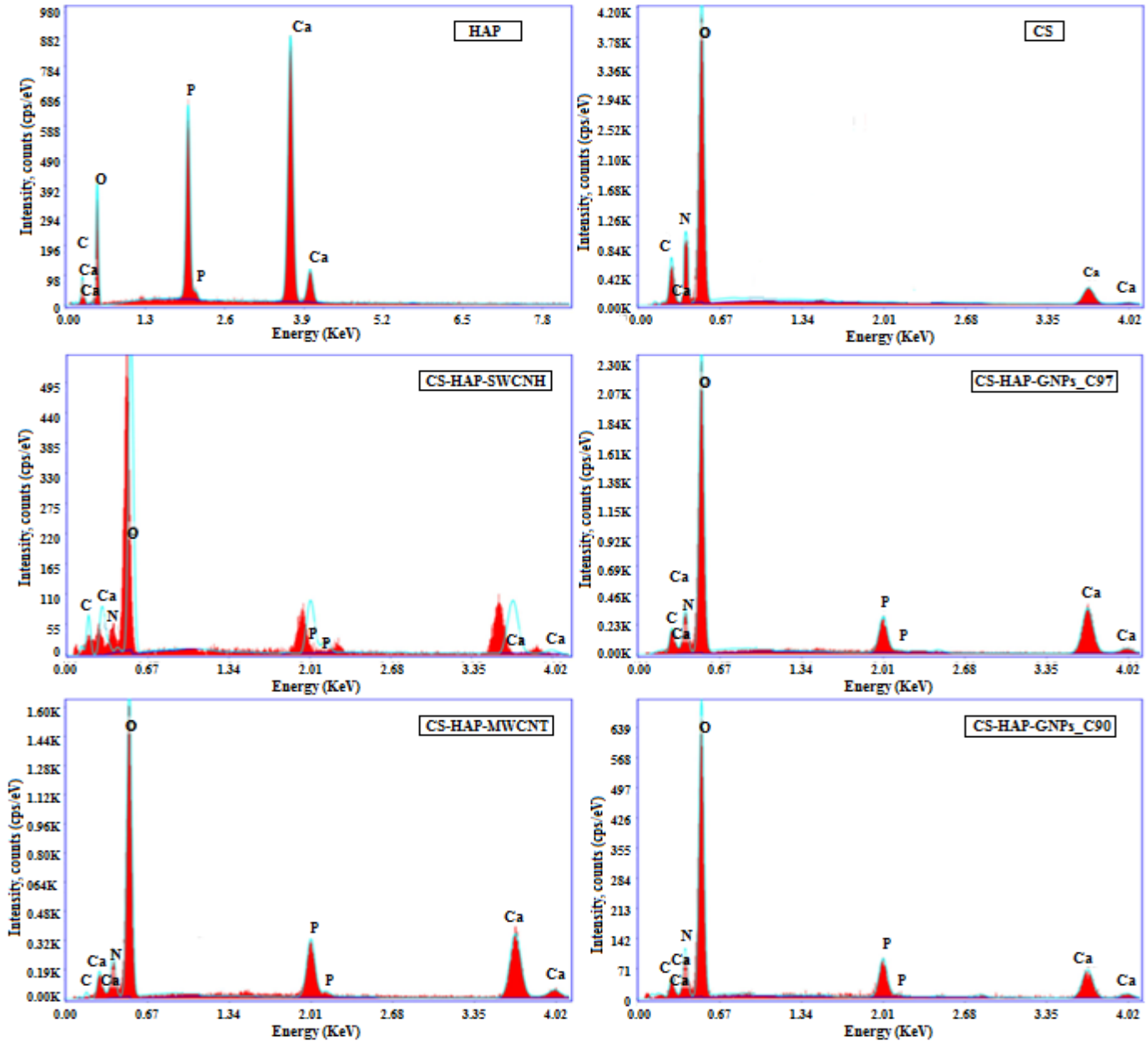

Figure 100. EDX spectrum analysis of: HAP, CS, CS-HAP-SWCNH, CS-HAP-MWCNT, CS-HAP-GNPs_C97, CS-HAP-GNPs_C90.

All EDX spectrum analysis for HAP, CS, CS-HAP-SWCNH, CS-HAP-GNPs_C97, CS-HAP-MWCNT, CS-HAP-GNPs_C90 are shown in figure. 100, and the results of each sample elemental composition are summarized in table 38 and plotted in figure. 101, to compare easily the elemental weight and atomic concentration percentages in each hybrid nanoparticles. The EDX analysis results show a good purity of all our samples, and all EDX results displayed a good correlation with those of XRF results. Thus, we observe in the EDX pattern of HAP the existence peaks of Ca, P, and O which are the essential chemical elements of HAP. The appearance of the peak of C in HAP pattern is due to the metallization of the sample to be an electrical conductor to be analyzed by SEM and EDX apparatus. For CS, We remark the appearance of major peaks of C, N, O with 99.64% weight concentration (wt%) and 99.87% atomic concentration (at%) of (C+N+O) and a minor peak of Ca 0.35 wt% and 0.12 at%, which prove the quality of our extracted CS, because it is already known that C, N, and O are the essentials compounds of CS [562] with an allowance of few existences of Ca and P [563].

Table 38. Elementary EDX analysis of: HAP, CS, CS-HAP-SWCNH, CS-HAP-MWCNT, CS-HAP-GNPs_C97, CS-HAP-GNPs_C90.

	Samples											
	HAP		CS		CS-HAP-SWCNH		CS-HAP-MWCNT		CS-HAP-GNPs_C97		CS-HAP-GNPs_C90	
Element	Weight %	Atomic %	Weight %	Atomic %	Weight %	Atomic %	Weight %	Atomic %	Weight %	Atomic %	Weight %	Atomic %
C	6,9	12,38	12,86	16,19	4,82	8,13	2,55	4,16	2,66	4,16	3,52	5,27
N	0	0	17,25	17,95	2,16	1,91	12,94	18,14	14,2	19,03	16,79	21,58
O	43,6	58,78	69,53	65,73	54,71	69,26	47,63	58,46	52,46	61,59	53,77	60,48
P	13,9	9,68	0	0	9,04	5,91	8,11	5,14	6,04	3,66	7,78	4,52
Ca	35,6	19,16	0,35	0,12	29,26	14,79	28,77	14,1	24,64	11,56	18,14	8,15

For all our hybrids particles CS-HAP-SWCNH, CS-HAP-MWCNT, CS-HAP-GNPs_C97, and CS-HAP-GNPs_C90, we notice the existence of peaks of following elements C, N, O, Ca and P as essentials elements, with appearances of very small peaks of impurity and background noises that we do not count on them. We remark that wt% and at% in both of Ca and P for HAP are higher than those of all hybrid particles contrary to the wt% and at% of C, N, O, and H in evidence.

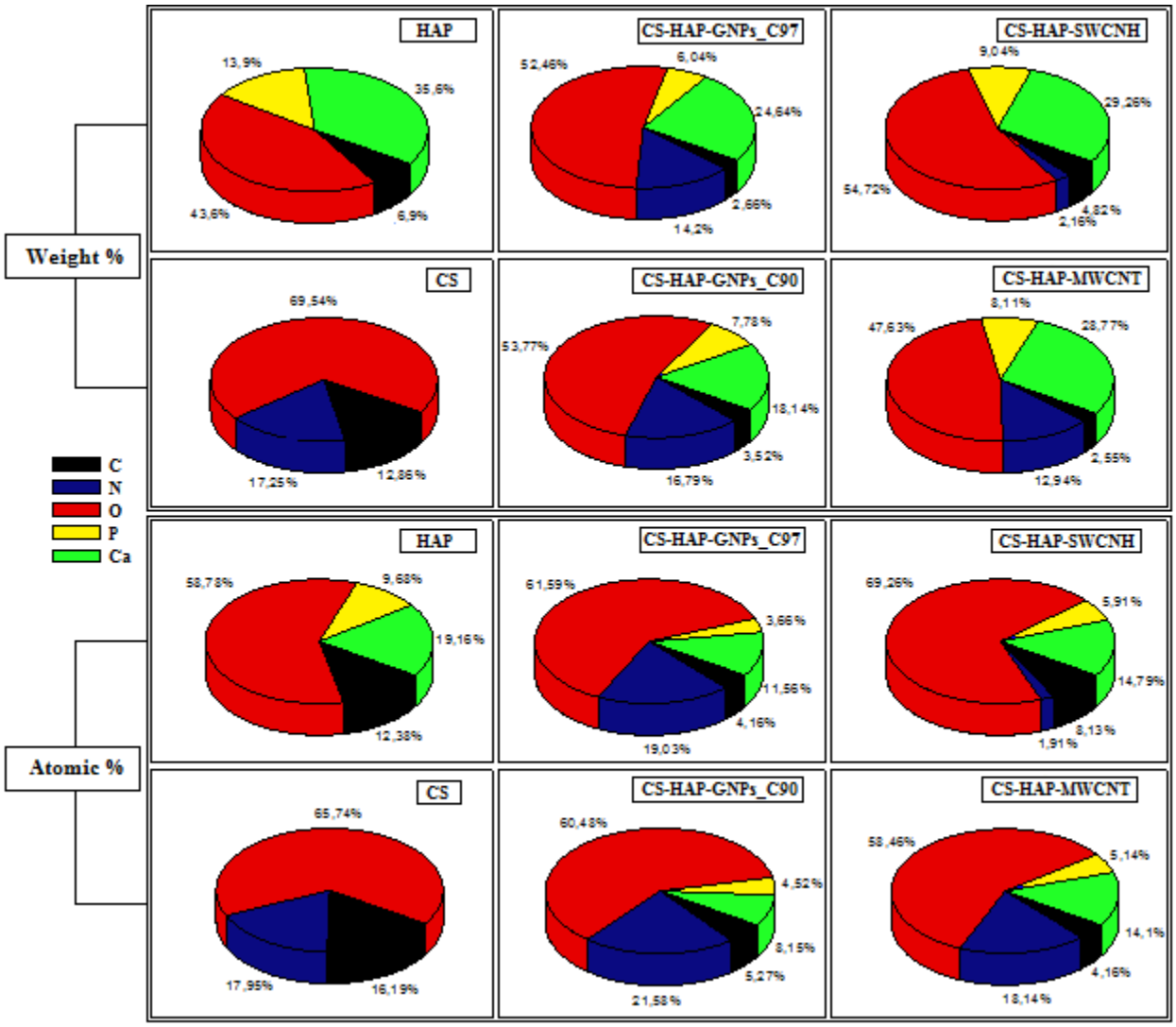

Figure 101. Elementals atomic and weight concentrations of: HAP, CS, CS-HAP-SWCNH, CS-HAP-MWCNT, CS-HAP-GNPs_C97, CS-HAP-GNPs_C90.

Consequently, the (wt% ; at%) of Ca were decreased for CS-HAP-SWCNH, CS-HAP-GNPs_C97, CS-HAP-MWCNT, CS-HAP-GNPs_C90 successively by (6.34wt% ; 4.37at%), (10.96wt% ; 7.60at%), (6.83wt% ; 5.06at%), (17.46wt% ;11.01 at%) and in the same order we note the decreases of P by (4.86wt% ; 3.77at%), (7.86wt% ; 6.02at%), (5.79wt% ; 4.54at%) and (6.12wt% ;5.16at%). This decrease of wt% and at% of Ca and P in both for each hybrid particle is due to the fixation of CS and some Carbon nanoscale materials among SWCNH, MWCNT, GNPs_C97or GNPs_C90. Similar results were observed by Enrico Bertoni et al in the synthesis of HAP nanocrystals in the presence of polyacrylic acid in solution [564]. Whereof, the increases of (wt% ; at%) of {C+N}

between our hybrids particles in same previous sequence by (6.98 wt% ; 10.04 at%), (16.86 wt% ; 23.19 at%), (15.49 wt% ; 22.30 at%) and (20.31 wt% ; 26.85 at%) and finally the increases of (wt% ; at%) of O by (11.11 wt% ; 10.48 at%), (8.86 wt% ; 2.81 at%), (4.03wt% ; - 0.32 at%) and (10.17 wt% ; 1.70 at%). These increases of C, N, and O in our hybrid particles yielded the various possibility of linkage between HAP, CS, and Carbon nanoscale materials as the same as the study of Monika Szlachta et al [565]. The appeared bonds observed in this study $\_C^1\_O\_C^2\_$, where C^1 come from CS, O belong to HAP and C^2 belong to carbon nanoscale particles or C=O were C and O does not belong same particle type and by bonding between Ca, PO_4, OH hydroxyl groups, and C, O from GNPs, MWCNT or SWCNH similarly as the study of Milena Stevanović et al [566] which demonstrate good combine between HAP, CS and someone of carbon nanomaterial SWCNH, MWCNT, GNPs_C97or GNPs_C90 in one hybrid particle which we discussed quantitatively this in FTIR paragraph.

VII.3.3 X-ray diffraction, Reitveld refinement and Structural parameters of: HAP, CS, CS-HAP-SWCNH, CS-HAP-GNPs_C97, CS-HAP-MWCNT, CS-HAP-GNPs_C90.

The structural analysis X-ray diffraction of HAP, CS, CS-HAP-SWCNH, CS-HAP-GNPs_C97, CS-HAP-MWCNT, CS-HAP-GNPs_C90 powders was carried out by a Bruker D8 ADVANCE Powder XRD apparatus, with copper anticathode $\lambda_{CuK\alpha}$ = 1.54 Å. The recording condition is 0.010142°/ (automatic time in s) for 2θ taken between 10° and 80°. The crystallographic parameters of all samples were refined from the experimental positions of the diffraction lines using the Fullprof software. The XRD patterns obtained for HAP, CS, CS-HAP-SWCNH, CS-HAP-GNPs_C97, CS-HAP-MWCNT, CS-HAP-GNPs_C90 are shown in figure 102, and there Rietveld refinement in figure 103, aims to deduce the structural parameters of all samples.

The XRD patterns of HAP display good homogeneity due to the appearance of one major peak and low numbers of minor peaks with bass intensities. Else, the major peak at 2θ = 31.612° is wide which signifies a medium degree of crystallinity for HAP with a reticular plan (0 2 3) as preferred orientation.

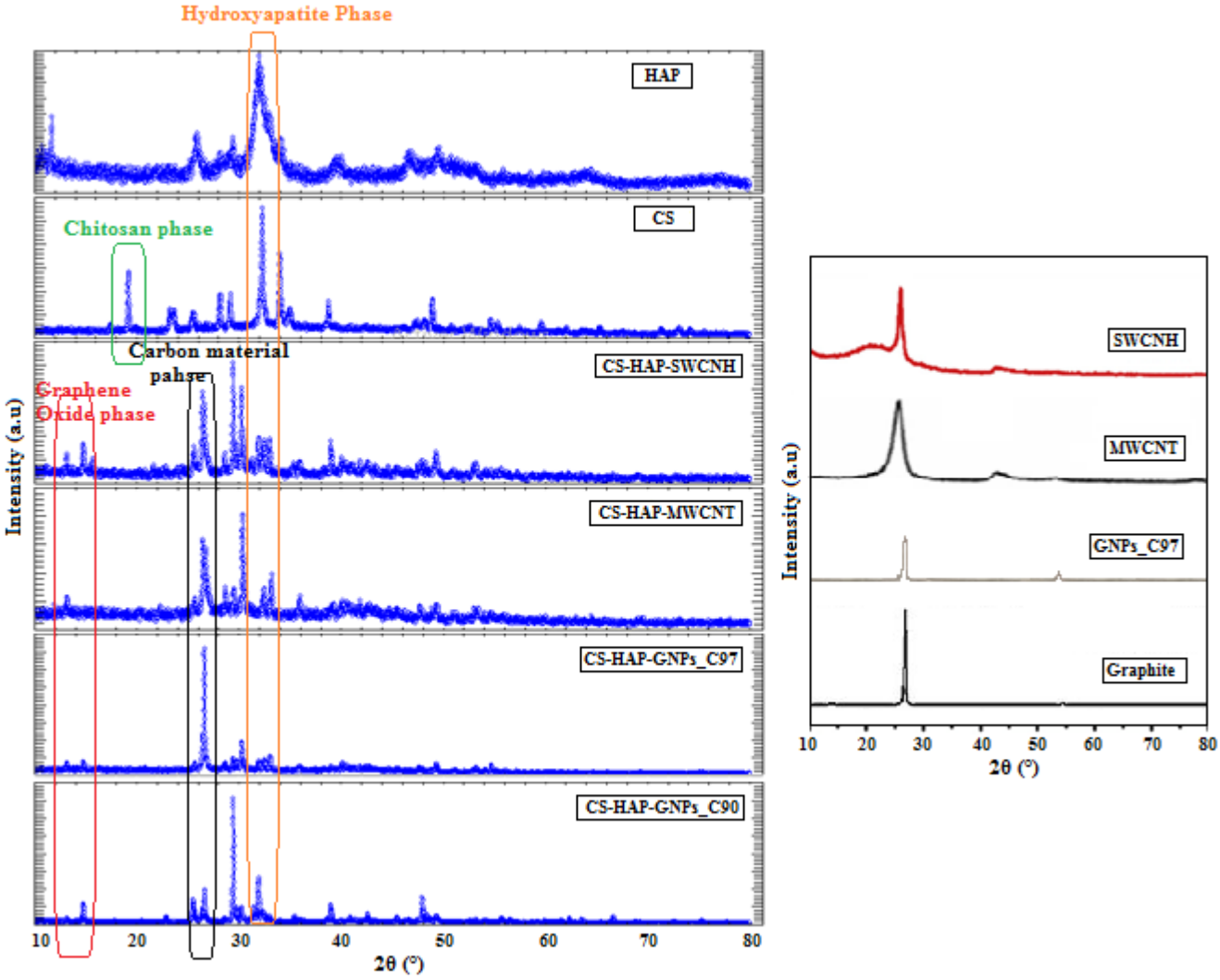

Figure 102. XRD pattern of: HAP, CS, CS-HAP-SWCNH, CS-HAP-MWCNT, CS-HAP-GNPs_C97, CS-HAP-GNPs_C90.

We note that this middle crystallinity of our HAP powder is due to ambient temperature 30 °C of crystallization and consequently the raise of crystallinity of HAP if desired can be gutted by heat treatment at high temperature since 600 °C until 1000 °C or more [567]. But in our case, we required middle crystallinity of HAP to be solved easily, due to the absorption of solvent [568] for the next step of the experiment. For CS samples, we remark a presence of two essentials phases; the CS phase is presented by a peak at $2\theta = 19.111°$ with preferred orientation (3 0 0), and the second phase is presented by peaks at $2\theta = 32.228°$ and its neighboring with preferred orientation (4 0 2) which indicate the calcite due to the existence of calcium and phosphorus which lead to the formation of the calcites by few quantities in CS powder. For our hybrid particles, we observe the common fact that

all those particles are in a high degree of crystallinity because all appeared peaks for each particle are very thins, and the disappearance of CS peaks which signify the total integration of CS into HAP structure.

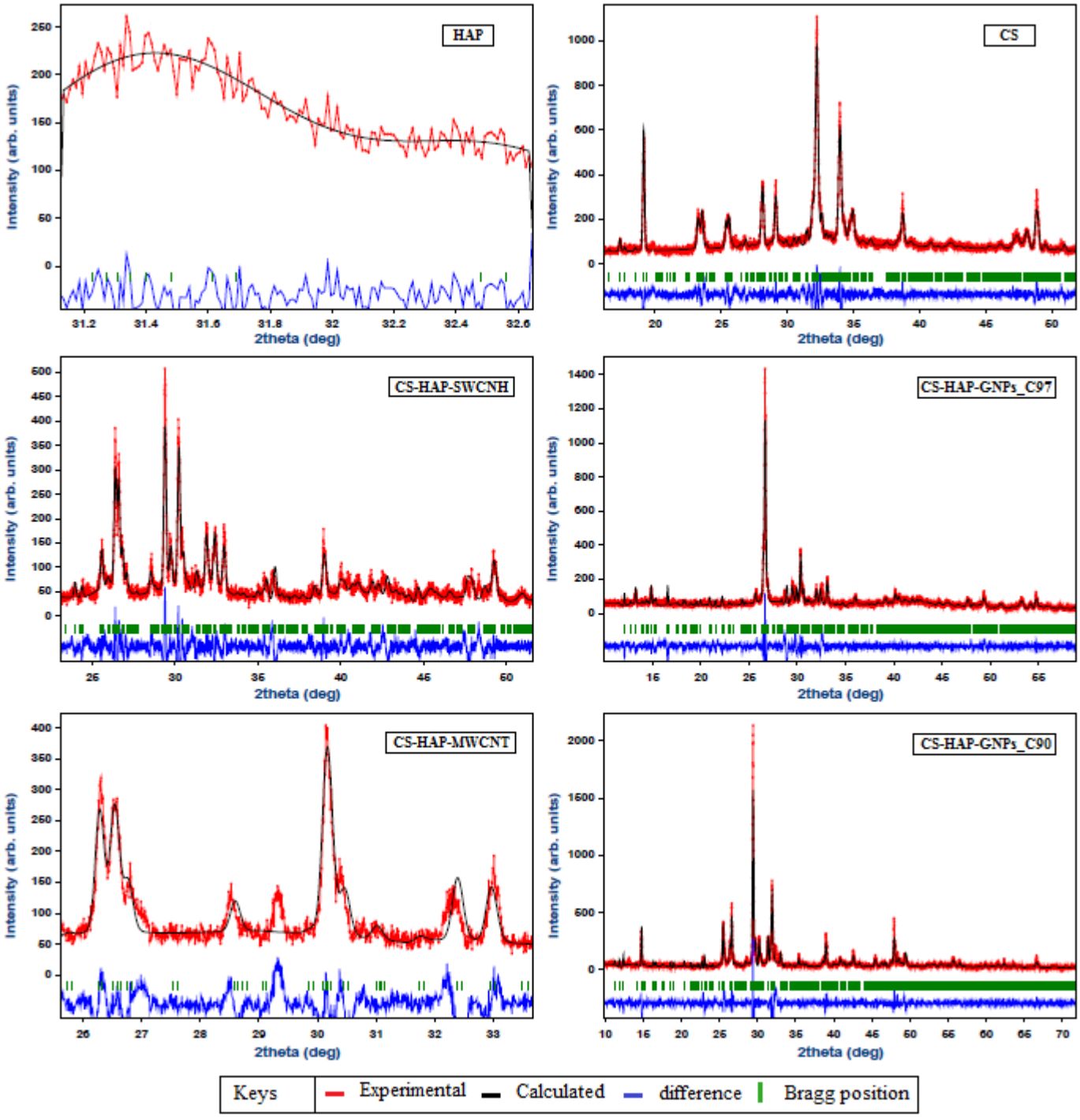

Figure 103. Rietveld refinement graphs of: HAP, CS, CS-HAP-SWCNH, CS-HAP-MWCNT, CS-HAP-GNPs_C97, CS-HAP-GNPs_C90.

We observe a displacement on the left of HAP peak toward pure GNPs peaks position at 2θ = 26.5° and the appearance of small peaks near 2θ =12° which indicate the oxidation of carbon [569]. But we notify too, some differences between there crystalline structures. Thus, the hybrids particles based on GNPs are more homogeneous than those based on CNT and CNH; since existence just of one major peak for CS-HAP-GNPs_C97 at 2θ = 26.648° with preferred reticular plans orientation (-4 0 2) and a minor peak at 2θ = 30.329° which mention a few being of HAP phase with preferred orientation (3 0 2). Likewise, for CS-HAP-GNPs_C90, we see only single major peak appeared at 2θ = 29.392° with (-1 2 2) as preferred orientation for reticular plans and a minor peak at 2θ = 31.893 ° with preferred orientation (1 2 2). Elsewhere, we observed one major peak for CS-HAP-SWCNH at 2θ = 29.368° which indicate the formation of new structure based on its of HAP with preferred reticular plans orientation (0 3 1) and other considerable peaks at 2θ = 26.360° which mention being of SWCNH phase in its originality with preferred orientation (1 1 1), and the second considerable peak at 2θ = 30.206° which mention the HAP phase with preferred orientation (2 6 0). Similarly for CS-HAP-MWCNT, we see one major peak at 2θ = 30.148° with (3 0 1) as preferred orientation for reticular plans, and other considerable peaks at 2θ = 26.267° which prove the existence of MWCNT phase with preferred orientation (2 1 0) and a minor peak at 2θ = 32.368° with preferred orientation (3 0 3). We achieved the Rietveld refinement trough Fullprof software for all our particles. As it is shown in figure 103, the Rietveld graphs demonstrate a good refinement for all our particles, because the experimental line is in good correlation with the calculated line with a small difference indicated by the blue line.

Table 39. Reliabilities factors of Rietveld refinement of: HAP, CS, CS-HAP-SWCNH, CS-HAP-MWCNT, CS-HAP-GNPs_C97, CS-HAP-GNPs_C90.

Sample	Rp	Rwp	Re	Chi2	GoF
HAP	8.46	10.5	10.3	1.02	1.0
CS	28.3	28.3	20.3	1.95	1.4
CS-HAP-SWCNH	38.9	42.1	26.5	2.52	1.6
CS-HAP-MWCNT	43.3	42.7	22.3	3.65	1.9
CS-HAP-GNPs_C97	46.7	50.6	28.5	3.14	1.8
CS-HAP-GNPs_C90	39.3	48.0	21.8	4.82	2.2

This remark is approved also by the reliabilities factors regrouped in table 39, where the GoF-index (Goodness of fit) is lower than 2 for each particle except CS-HAP-GNPs_C90 where this Gof-index value equal to 2.2, and it is known that the refinement is considered good if the Gof-index is lower than 2.

Table 40. Structural parameters of: HAP, CS, CS-HAP-SWCNH, CS-HAP-MWCNT, CS-HAP-GNPs_C97, CS-HAP-GNPs_C90.

Sample	Crystal System	Symmetry Group	Cell Parameters			Cell Volume (A^3)	2θ (°)	α (°)	β (°)	γ (°)	hkl	d_{hkl}
			a(A)	b(A)	c (A)							
HAP	Hexagonal	P 6/m m m	11.91	11.91	10.14	1247.07	31.61	90	90	120	2 0 3	2.82
CS	Orthorhombic	P m m m	13.92	13.23	9.19	1695.01	32.22	90	90	90	4 0 2	2.77
CS-HAP-SWCNH	Orthorhombic	P m m m	19.93	18.57	3.48	1291.64	29.36	90	90	90	0 3 1	3.03
CS-HAP-MWCNT	Hexagonal	P 6/m m m	10.35	10.35	21.73	2018.94	30.14	90	90	120	3 0 1	2.96
CS-HAP-GNPs_C97	Monoclinic	P 2/m	13.63	6.96	12.41	1097.83	26.64	90	111.29	90	-4 0 2	3.34
CS-HAP-GNPs_C90	Monoclinic	P 2/m	12.85	10.05	7.64	964.24	29.39	90	102.66	90	-1 2 2	3.03

We elicited from this refinement several data about the structural properties for each particle, such as crystal system, lattice parameters, and the symmetry groups as it is summarized in table 40. We find that HAP and CS-HAP-MWCNT were crystallized in both in the hexagonal system with growth on the cell volume for CS-HAP-MWCNT which can indicate that this hybrids particle is built superimposed the HAP structure. The crystal system of two particles CS and CS-HAP-SWCNH is Orthorhombic. The hybrids particles based on Graphene; CS-HAP-GNPs_C97 and CS-HAP-GNPs_C90 crystallizes in Monoclinic which indicate a novel crystallization by increases of beta angle.

The Debye-Scherrer method is used to obtain the grain's size from X-ray diffraction measurements by following relationship (19) [570]:

$$D = \frac{k*\lambda}{B*\cos(\theta)} \qquad (19)$$

Where D is the grain's size diameter, B indicate the FWHM, it is the broadening of the diffraction line measured at half-maximum intensity, l is the wavelength (Cu Kα), k is a constant in general, equal to 0.9 for powders. The grain size results are shown in table 41.

Table 41. FWHM and Grain size evolution of: HAP, CS, CS-HAP-SWCNH, CS-HAP-MWCNT, CS-HAP-GNPs_C97, CS-HAP-GNPs_C90.

Product	HAP	CS	CS-HAP-SWCNH	CS-HAP-MWCNT	CS-HAP-Gr(C97)	CS-HAP-Gr(C90)
FWHM (°)	0.85	0.20	0.16	0.18	0.15	0.15
D (nm)	9,60	40,85	49,35	44,85	51,97	52,86

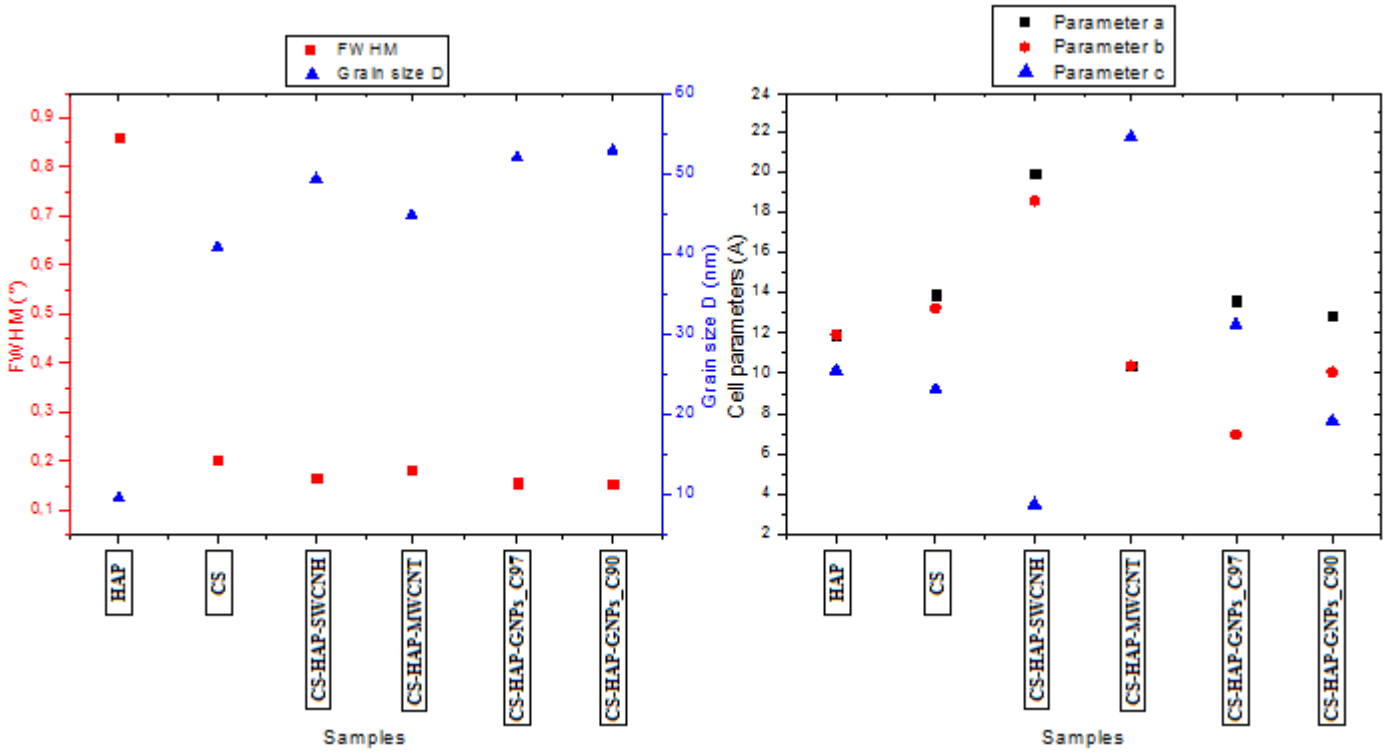

Figure 104. Grain sizes and cell parameters evolution of: HAP, CS, CS-HAP-SWCNH, CS-HAP-MWCNT, CS-HAP-GNPs_C97, CS-HAP-GNPs_C90.

We have plotted the FWHM and the grain sizes D in figure 104-a, and cell parameters in figure 104-b, to facilitate the visualization and comparison between our particles simultaneously. We observe decreases of FWHM and increases in the grain sizes D which can be described by increases in lattice

parameters a, b, and c which carries to increase of cell volume that lead to increases in grain sizes. The sizes of our hybrid particles are about 44 to 52 nm scale which approves their nanometric nature [571]. The difference between grain sizes of our hybrids nanoparticles is related principally to the rate of confusion between HAP, CS, and each one from SWCNH, MWCNT, GNPs_C97, and GNPs_C90.

VII.3.4 FTIR analysis: FTIR spectrums Assignment description of HAP, CS, CS-HAP-SWCNH, CS-HAP-MWCNT, CS-HAP-GNPs_C97, CS-HAP-GNPs_C90).

The FTIR spectroscopic analysis for all our particles was carried out utilizing the Perkin Elmer spectrum version 10.4.2 spectrophotometer. This is a good track to know the bonds' vibration of all our particles and especially to well define the differences between internal linkage and bonding between our hybrid particles. The FTIR spectrums of all our particles are exposed in figure 105, and the descriptions of their assignments are regrouped in table 42 for HAP and CS samples and in table 43 for the samples CS-HAP-SWCNH, CS-HAP-MWCNT, CS-HAP-GNPs_C97, and CS-HAP-GNPs_C90. The FTIR spectrum of HAP shows the presence of the stretching vibration of the free OH- groups at 3445 cm^{-1} and the vibrational mode of the structural hydroxide OH- group appeared at 630 cm^{-1}. We see also the PO_4 bending at 1039 cm^{-1}, PO_4 stretching vibrations at 950 cm^{-1} as a first mode, and at 473cm^{-1} that are the characteristic peaks of HAP [572].

The FTIR spectrum of the CS powder showed nine remarkable peaks at the ranges of 518, 613, 876, 1108, 1335, 1427, 1572, 1640 and 2851 cm^{-1} as shown in figure.105-b and table 42 shows their band's description. Among these peaks, the strip at 2187 cm^{-1} corresponds to the C≡C stretch band and the specific bands appeared near 1320 cm^{-1} at 2900 cm^{-1} indicating respectively the N-acetylglucosamine and the _CH backbone vibrations frequently used to check the CS kind [573]. The FTIR spectrums of our four hybrids particles display two common peaks as HAP particles 3400 cm^{-1} and 1050 cm^{-1} indicating respectively the stretching vibrations of hydroxyl groups and the bending mode of PO_4^{3-}, which prove that our hybrids particles provide the HAP phase. We observe also the common band near 1630 cm^{-1} indicate the stretching vibration of C=C and C=O groups in both, and the stretch of NO_2 group caused by linked C_H/N_H near 1320 cm^{-1} as a characteristic peak of CS which evince that all our hybrids particles contain the CS phase.

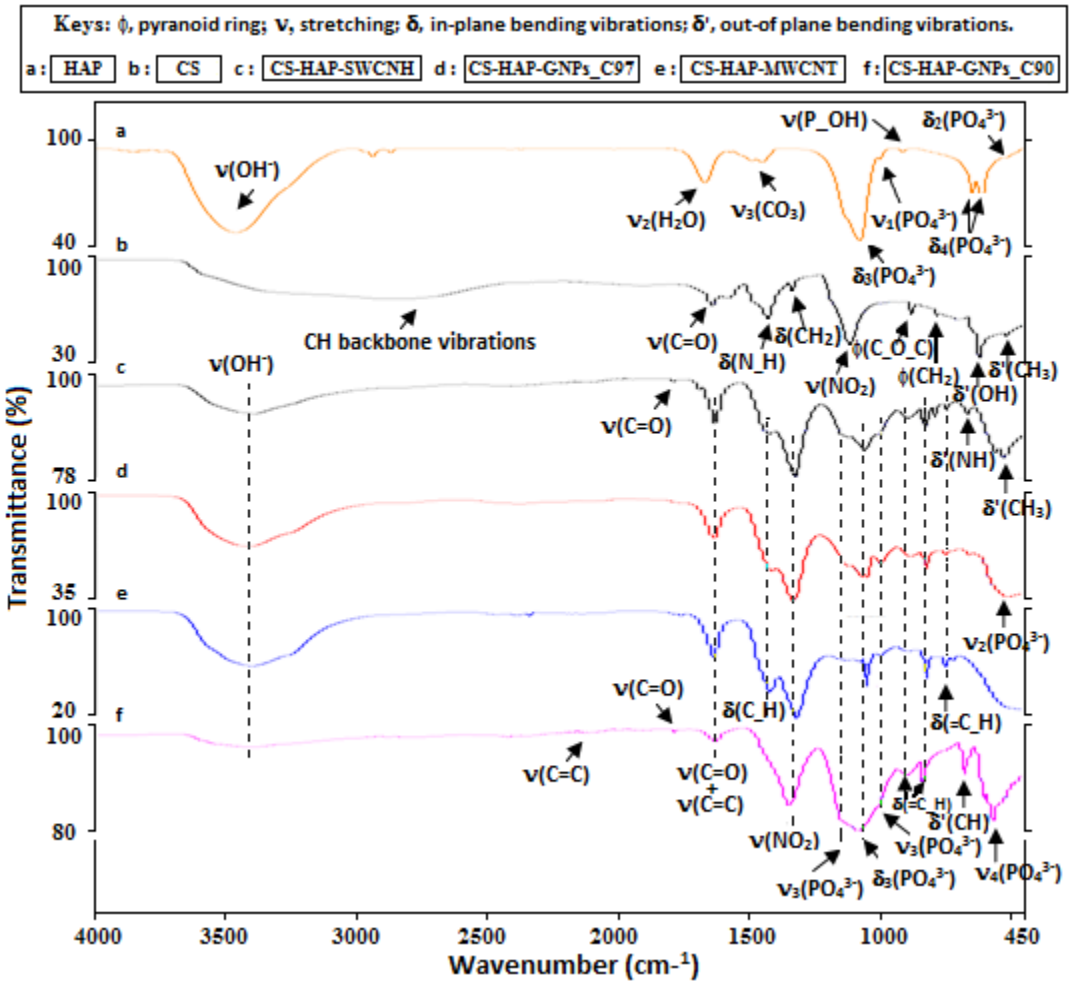

Figure 105. The FTIR spectra of: HAP, CS, CS-HAP-SWCNH, CS-HAP-MWCNT, CS-HAP-GNPs_C97, CS-HAP-GNPs_C90.

Unlikely, they appeared new assignments own for each hybrid particle. Thus, the C≡C stretch as alkynes at 2102 cm^{-1}, C=O stretch at 1768 cm^{-1}, and =C-H bend at 672 cm^{-1} as Alkenes structure disubstituted, cis appeared for CS-HAP-GNPs_C90. Besides, we observe the appearance of the =C-H bend as Phenyl structure disubstituted, para at 819 cm^{-1}, and the =C-H bend as Phenyl structure disubstituted, ortho at 741 cm^{-1} for CS-HAP-GNPs_C97. Uniquely for CS-HAP-SWCNH, we remark the appearance of C=O stretch as ketones at 1687 cm^{-1} and the out-of-plane bending of CH_3 at 516 cm^{-1}. We see the outstanding peaks for CS-HAP-MWCNT the =C-H bend as phenyl structure mono-substituted at 713 cm^{-1} [574]. Those particular assignments bear out the new linkage between HAP, CS, and the considered carbon nanomaterial used. And prove also that the GNPs_C90 or GNPs_C97 fixed oxygen to turn into Graphene oxide with their famous assignments C=O carbonyl/carboxyl and

C=C aromatics about 1632 cm^{-1} due to oxygen functional groups fixed on carbon in a different possible position [575] after the formation of these hybrid nanoparticles.

Table 42. Assignment of FTIR spectra of HAP and CS .

HAP			CS		
IR Band cm^{-1}	T %	Description	IR Band cm^{-1}	T %	Description
3445	46,07	stretching vibration of the free OH^- group	2851	73,21	_CH backbone vibrations
1640	78,21	H_2O adsorbed ν_2	2187	86.09	C≡C stretch
1452	92,3	CO_3 group ν_3 asymmetrical stretching vibration	1640	68,38	amide I band (stretching vibration of the C=O group)
			1572	73,77	N_H bending vibration
1418	91,19	CO_3 group ν_3 asymmetrical stretching vibration	1427	58,3	asymmetrical C_H bending vibration of the CH_2 group
1039	40,83	PO_4 bend ν_3	1335	78,14	Amide III band, NO_2 stretch, caused by linked C_H/N_H deformation vibrations
950	95,91	PO4 stretch n1	1108	39,72	pyranose ring __C__O__C__
873	97,76	CO_3 group and P_(OH) stretching vibration	895	57,96	deformation of the b -glycosidic linkage
630	78.11	Vibrational mode of the OH^- group in the HAP structure	876	61,68	pyranoid ring CH_2
			780	60,51	NH out – of – plane bending
603	71,07	PO_4 bend ν_4	613	30,71	out-of plane bending of (OH…O)
567	66,95	PO_4 bend ν_4			
473	94,1	PO_4 bend ν_2 vibrational mode	518	46,24	out-of plane bending of CH_3

Table 43. Assignment of FTIR spectra of: CS-HAP-SWCNH, CS-HAP-MWCNT, CS-HAP-GNPs_C97, CS-HAP-GNPs_C90.

Samples	CS-HAP-SWCNH		CS-HAP-GNPs_C97		CS-HAP-MWCNT		CS-HAP-GNPs_C90	
Description	IR Band cm^{-1}	T %	IR Band cm^{-1}	T %	IR Band cm^{-1}	T %	IR Band cm^{-1}	T %
stretching vibrations of hydroxyl groups	3396	93, 46	3418	67, 02	3409	58, 44	3395	96, 4
C≡C stretch (as alkynes)	-	-	-	-	-	-	2102	99. 11

C=O stretch (as acides chlories)	-	-	-	-	-	-	1768	99.23
C=O stretch (as ketones)	1687	99.21	-	-	-	-	-	-
C=C stretch and (stretching vibration of the C=O group)	1632	91,05	1633	72,3	1632	65,28	1626	97,46
asymmetrical C_H bending vibration of the CH_2 group	1411	89.53	1413	51,63	1415	38,46	-	-
NO_2 stretch and is caused by linked C_H/N_H deformation vibrations	1323	77,78	1327	33,21	1313	18,38	1344	84,61
PO_4^{3-} ν_3		-	1064	47,86	1067	61,8	1068	79,5
PO_4 bend ν_3 and C-C, C-OH, C-H ring and side group vibrations	1048	84,27	1044	47,86	1043	43,12	-	-
PO_4 stretch ν_1	-	-	992	56,42	992	66,79	-	-
deformation of the β -glycosidic linkage	886	92,26	880	60,74	-	-	875	90.82
=C-H bend (as phenyl structure disubstituted, para)	834	90,92	-	-	-	-	834	87,39
=C-H bend (as phenyl structure disubstituted, para)	819	90,39	819	53,07	818	49,05	-	-
NH out – of – plane bending	788	92,52	-	-	-	-	-	-
=C-H bend (as phenyl structure disubstituted, ortho)	-	-	741	61,91	746	57,94	-	-
=C-H bend (as phenyl structure mono-substituted)	-	-	-	-	713	63.02	-	-
=C-H bend (as alkenes structure disubstituted, cis)	-	-	-	-	-	-	672	90,9
C-OH out-of-plane bending	-	-	656	61,61	-	-	-	-
PO_4 bending ν_4	-	-	-	-	-	-	558	81,65
out-of plane bending of CH_3	516	82,57	-	-	-	-	-	-
PO_4 bend ν_2 vibrational mode	-	-	499	35,49	-	-	-	-

VII.3.5 SEM analysis: Microstructures and irregularities of HAP, CS, CS-HAP-SWCNH, CS-HAP-MWCNT, CS-HAP-GNPs_C97, CS-HAP-GNPs_C90).

Scanning Electron Microscope (SEM) is a most convenient technique to observe the surface morphology, physical state, particle sizes, and microstructure of materials crystals or amorphous polymers. This is a type of electron microscope that produces images of a sample by scanning the surface with a focused beam of electrons. The electrons interact with atoms in the sample, producing various signals that contain information about the surface topography and composition of the sample. The electron beam is scanned in a raster scan pattern, and the position of the beam is combined with the intensity of the detected signal to produce an image. In our case, scanning electron microscopy VEGA3 TESCAN was used to observe the morphological changes and differences in structure between HAP, CS, CS-HAP-SWCNH, CS-HAP-MWCNT, CS-HAP-GNPs_C97, CS-HAP-GNPs_C90. The surface morphology was taken at an acceleration voltage of 10 kV, by almost working distance (WD) for our samples such as 9.88 mm for HAP, 10.05mm for CS, 10.55 mm for CS-HAP-SWCNH, and 10.36 mm for CS-HAP-GNPs_C97, 10.27 mm for CS-HAP-MWCNT, and 10.05 mm for CS-HAP-GNPs_C90 with same magnifications: 20 μm, 10 μm and 5 μm respectively for each sample.

All SEM images are regrouped in the figure. 106. The SEM images display an inequality in HAP grain's sizes, with divergences in shapes and roughness between micro bulk zones without pores that someone is smooth and evidently can be subdivided into m smaller nanoparticles because we know already the size of this HAP grains from XRD analysis by Debye-Scherrer method about 9.6 nm.Besides, we see also certain rough surfaces in HAP images due to posture of very small HAP grain on micro bulk zones which occurs an irregularity in microstructure and surface morphology and irregularity in interface boundaries. But we remark a great similarity in shape and size between nanoparticles which are apparent in the left of the 20 μm image of HAP. For the CS sample, we observe an irregularity of microstructure and surface morphology so smooth surface with similar string with pores about 50 nm in unpredictable positions between sample blocks and some rough areas in depth that's deposit similar CS nanoparticles on the verge of bulk micro surfaces.

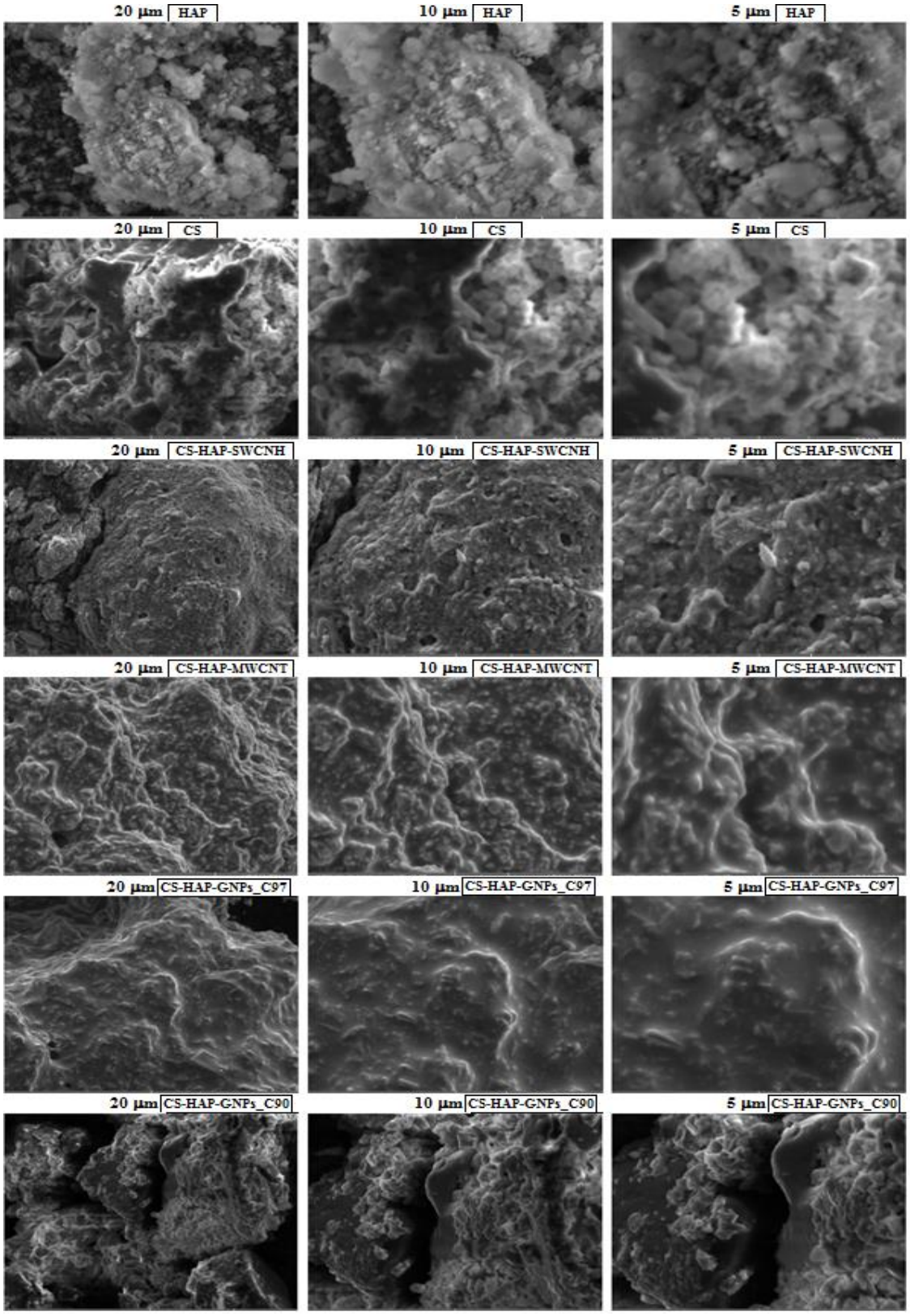

Figure 106. Scanning Electron Microscope (SEM) analysis for HAP, CS, CS-HAP-SWCNH, CS-HAP-MWCNT, CS-HAP-GNPs_C97, CS-HAP-GNPs_C90.

We notice the existence of the nanoparticles of CS by different sizes around 40 to 50 nm faithfully to the size value funded in the XRD analysis part. We note that the porosity in the irregular block and the crystalline cluster gives a good possibility to the penetration of other nanoparticles smaller than 40 nm like our HAP nanoparticles gained in this study. The SEM images of CS-HAP-SWCNH reveals that the materials are homogenous with a rough surface, disordered, disorganized, distorted in microstructure with some cracks, and very small pores. Irregular fissures, irregular pattern, the existence of HAP ‘s nanoparticles and some string of CS strongly linked between them by CNH, as a form of a spherical aggregate of CNH [576]. Also, we notice for CS-HAP-GNPs_C97 the appearance of a very smooth and homogenous surface of carbon coat the nanoparticles of HAP, nanoparticles, and string of CS. With some regularity in blocks without pores but three appeared in the 20 μm image resolution in all analyzed surface, which we observe insight the homogeneity of the materials which prove that this hybrids nanoparticle is homogenous in surface and depth like a deposition in one layer by EDP [577] or by sonocoating a polymer surface with nano-HAP [578]. For CS-HAP-MWCNT, we noticed almost similar morphology of other hybrids materials due to the similarity of the nature of carbon nanomaterial used. We notice the roughness of macroscopic surfaces and smoothing between blocks with irregularity due to string of CS that’s appeared clearly in the edge of blocks in 5 μm resolution with uniform repartition of HAP nanoparticles. From the CS-HAP- GNPs_C90 SEM images, we unveil two important views. The majority of three materials HAP, CS, and GNPs_C90 are largely molten to outcome bulk micro materials with smooth surfaces and deposition of solved CS and HAP nanoparticles which exhibit certain roughness in interfaces of crystalline blocks, with certain discontinuance between hybrid materials units observed in 20 μm resolutions. Generally, we notice that carbon nanoscale materials SWCNH, GNPs_C97, MWCNT, or GNPs_C90 used in the synthesis of our hybrid nanoparticles are the principle factor of changes in the shape and morphology since the chemical method and CS-HAP are identical for all our hybrids particles.

VII.4 Conclusion

In summary, this study tried to contribute to the development of synthesis and characterization of nanoscale biomaterials for biomedical applications for amelioration and regeneration of the skeletal system, especially for bone and teeth which are highly recommended in modern therapeutics and surgery. The synthesis of CS-HAP-SWCNH, CS-HAP-GNPs_C97, CS-HAP-MWCNT, CS-HAP-GNPs_C90 hybrids particles well carried due to the intrinsic accessibilities of linkage between HAP,

CS and carbon nanoscale materials, and each hybrids particles provides common properties of HAP and CS and others typical properties since the carbon material amid SWCNH, GNPs_C97, MWCNT or GNPs_C90. The sizes of Hybrids particles around 50 nm indicate that the CS with size circa 40nm is the foundation of our four hybrids particles, and the SEM analysis proves that HAP nanoparticles with sizes near 9 nm have been deposited upon CS interfaces strongly linked within carbon materials with some divergence of the link according to the type of carbon and for this reason, we signaled some difference in assignments such as C=C, C=O, and _C_C_ for bonded HAP and CS. The goodness in crystallinity and depth homogeneity of all our hybrids materials offers divers' possibilities of uses in various applications in dental and orthopedics fields for coat, regeneration, and partial or total substitution.

Chapter VIII:

APPLICATION: BIO-CERAMIC AMALGAMS BASED ON HYDROXYAPATITE DOPED BY LOW METAL (Co, Ni, Cu, Mn) CONCENTRATION AND THEIR TOXICITY DISCUSSION

VIII.1 Introduction

The sensation is an essential element to live reacting with the outside world and knowing what surrounds us. In the case where a natural tooth is replaced by an artificial tooth, this sensation takes place no longer, nor to feel cold or hot, because the materials currently used for the manufacture of dental prostheses are insulating materials. It is desired by this study to increase the sensation by dental prosthesis by increasing the electrical and thermal conductivity of HAP by doping at a concentration of the metal element nickel, copper, cobalt and manganese. For a dental prosthesis to be similar to a natural tooth from an electrical and thermal point of view. After our good result on structural and vibrational properties in our previous word obout this subject [579], We report also to continue study of their thermic and electric propertises. Around the world, m studies and substitution experiments have been carried out on HAPs to increase its physical, chemical and biological properties [580, 581, 582, 583]. The synthetic HAP used for orthopedic and dental application may be satisfactory in terms of mechanical properties [584, 585], but it remains too far to meet the thermal and electronic need to give a sensation of cold or heat to the patient after dental replacement. By this study, we want to see the effect of weak Ca substitution of HAP by a metal ion (M = Mn, Co, Ni, Cu) on the optical, electronic and structural properties to increase the electrical conductivity of HAP. When the atoms come together to form a solid, their valence electrons interact because of Coulomb forces, and they also sense the electric field produced by their own nucleus and that of the other atoms. In addition, two specific quantum mechanical effects occur. First, by Heisenberg's principle of uncertainty, constraining electrons to a small volume increases their energy, this is called promotion. The second effect, due to Pauli's exclusion principle, limits the number of electrons that can have the same property (which includes energy). According to these effects and therefore, the valence electrons of the atoms form broad valence bands when they form a solid. The bands are separated by spaces, where the electrons can not exist. The precise location of bands and bands depends on the type of atom [586]. The gap energy of the pure HAP is often greater than 5 eV [587, 588] and has a wide band gap that does not allow easy passage of electrons from the valence band to the conduction band [589, 590]. The incorporation of these metal ions (Mn, Co, Ni, Cu) by low concentration could decrease the gap energy by significant values to give more thermal and electrical conductivity to the HAP.

VIII.2 Synthesis process

Crystalline powders of HAP with general chemical formula $Ca_{10}(PO_4)_6(OH)_2$ were prepared by ceramic route. All reagents are in the solid state. We mix and grind the reagents directly and manually with mortar and pestle. The Synthesis process as resumed in graphical representation as shown in Figure 107.

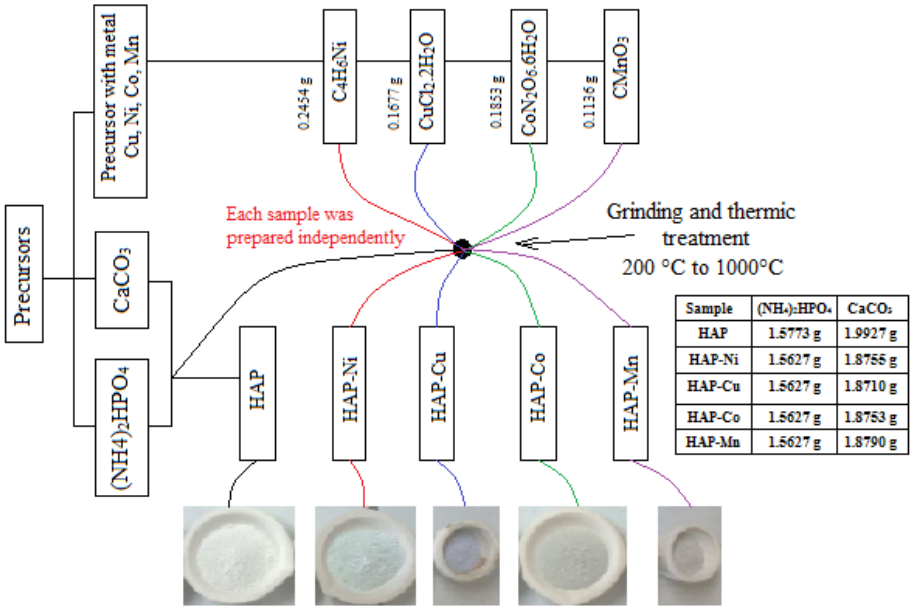

Figure 107. Synthesis process for HAP, HAP-M (M=Ni, Cu, Co, Mn) by solid state method.

VIII.3 Optoelectronic properties

Optical properties were studied by optical transmittance measurements in the UV / Visible range using a T92 + UV-visible spectrophotometer at room temperature. The aim of these measurements is to deduce the electrical and thermal conductivity via gap energies of each sample by Tauc's law. The spectra of the following compounds: HAP and HAP-M (M=Ni, Cu, Co, Mn) were recorded in the visible range between 200 and 400 nm. The experimental results show the different absorbance, transmittance spectra of all samples function of the wavelength. The spectra show low transparency in the visible range (400 - 800 nm) with a transmittance around 20% for HAP-Cu and HAP-Mn, 30% for HAP-Ni, 40% for HAP and 70% for HAP-Co. This difference comes from metal ions incorporate into HAP matrix. Also, the optical absorbance is reciprocally depending on transmittance spectra for each sample. The study of the different transmittance spectra in the zone of high absorption leads to the calculations of the absorption coefficient of the samples whose results have been represented in

figure 108. The energy of the optical band (Eg) can be determined from the absorption coefficient (α), which can be calculated from the transmittance, [591, 592]. By following relationship (20):

$$\alpha h\nu=\alpha_0(h\nu-Eg)^n \qquad (20)$$

Where α_0 is a constant and sometimes called the band tailing parameter and it is an energy independent constant. E_g is the optical gap energy, which situated between the localized states near the mobility edges according to the density of states model, proposed by Mott and Davis [593, 594]. In the equation (2), there is another constant (n), which is called the power factor of the transition mode.

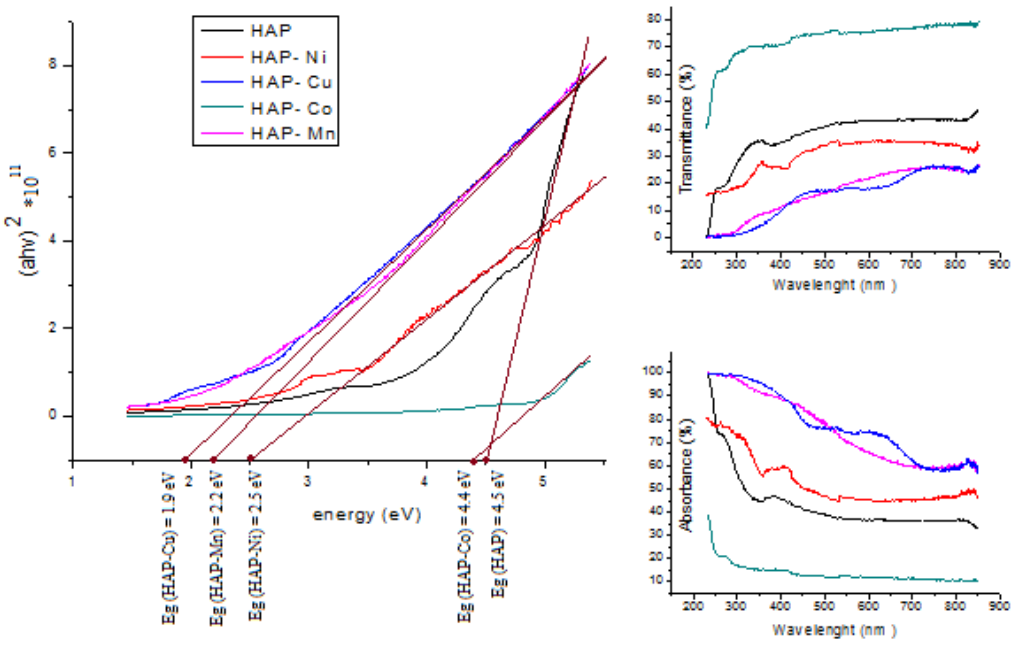

Figure 108. Transmittance, absorbance measurements and gap energies plot for HAP, HAP-M (M=Ni, Cu, Co, Mn).

It is said that these products are not conductors of electricity; it limits the exchanges of exchange between two systems. The table 44 showed the values of the gap energy. These gap energies value will be used in electrical and thermal properties calculations of these samples.

Table 44. The gap energies value of HAP and HAP-M (M=Ni, Cu, Co, Mn).

Samples	HAP	HAP-CO	HAP-Ni	HAP-Mn	HAP-Cu
Gap energy (eV)	4.5	4.4	2.5	2.2	1.9

VIII.4 Electrical conductivity

It is noted that the gap energy has decreased after the insertion of the metal ions in the HAP matrix according to each metal, the values of new gap energies are shown in Table 44. We see that the gap energy has greatly decreased after the incorporation of nickel, copper and cobalt and slightly decreases after incorporation of manganese. This decrease variation is related to the nature of valence band and conductivity of each metal inserted into the HAP matrix. The conductivity of manganese is lower compared to that of other metals nickel, copper and cobalt used in this study [595] that is the reason of the gap energy of HAP-Mn is reduced. The conductivities of the nickel, copper and cobalt are too great which gives more free electrons that can move easily in the HAP matrix to fill the conduction layer and decreases the gap between the valence energy level and the conduction energy level to give a lower gap energy. The Electrical conductivity of pure metals nickel, copper and cobalt as showns in table 45.

Table 45. Electrical conductivity of pure metals for temperatures between 273 and 300 K.

Pure Metal	Ca	Ni	Cu	Co	Mn
Electric Conductivity (10^8 S/m)	0.28985	0.13888	0.57971	0.17857	0.00694

For the calculation of HAP conductivity, we use the relationship (21), (22) [596]:

$$\sigma=\sigma_0 \exp(-E_g/k_B T) \quad (21)$$

$$\log \sigma=\log \sigma_0 -(E_g/k_B T) \quad (22)$$

Where σ is the electrical conductivity, Eg is the gap energy, k_B is the Booltzman constant, T is the temperature in kelvin degrees, σ_0 is the pre-factor exponential and represente the maximal conductivity that the materials can have it, this is constant for same materials.

For determination of log σ_0 counstant, we use the experimental result in the work of laghzizil et al [597] and we us it for empirical calculation of our HAPs conductivity in this work.

The results clearly show that electrical conductivity increases if gap energy decreases, see Figure 109. Thus, the electrical conductivity increases with temperature, see figure 110. The variation of the logarithm of the electrical conductivity of our samples was plotted in the temperature range of 0 ° C to 100 ° C. as shown in figure 111, since it is often the temperature range of the beverages or foods that may be in contact with the substituted teeth. that we want given by this work the possibility of transmitting the electrical or thermal sensation to the patient as natural teeth. The table 46 summarize

the values of log σ and σ increase at 25 °C for samples HAP-M (M=Ni, Cu, Co, Mn) compared by pure HAP at 25 °C.

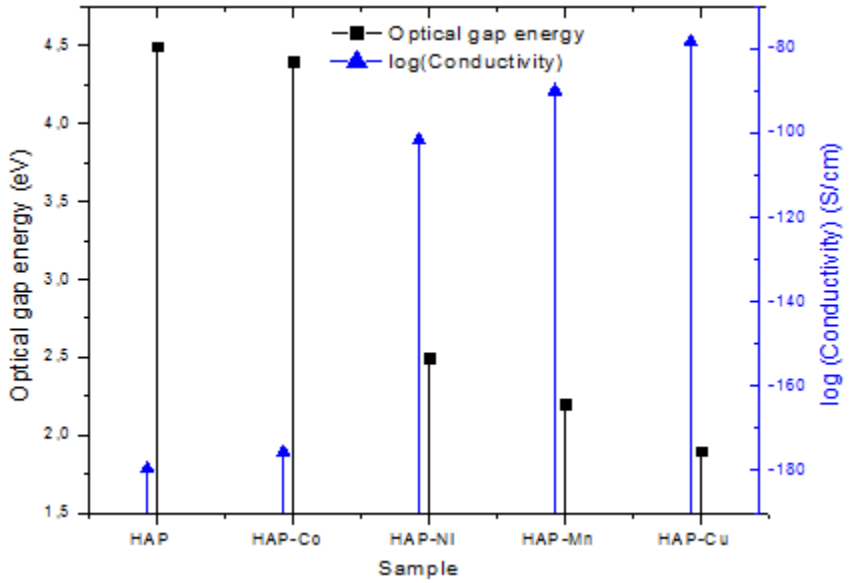

Figure 109. Optical gap energy and Conductivity of HAP and HAP-M (M=Ni, Cu, Co, Mn).

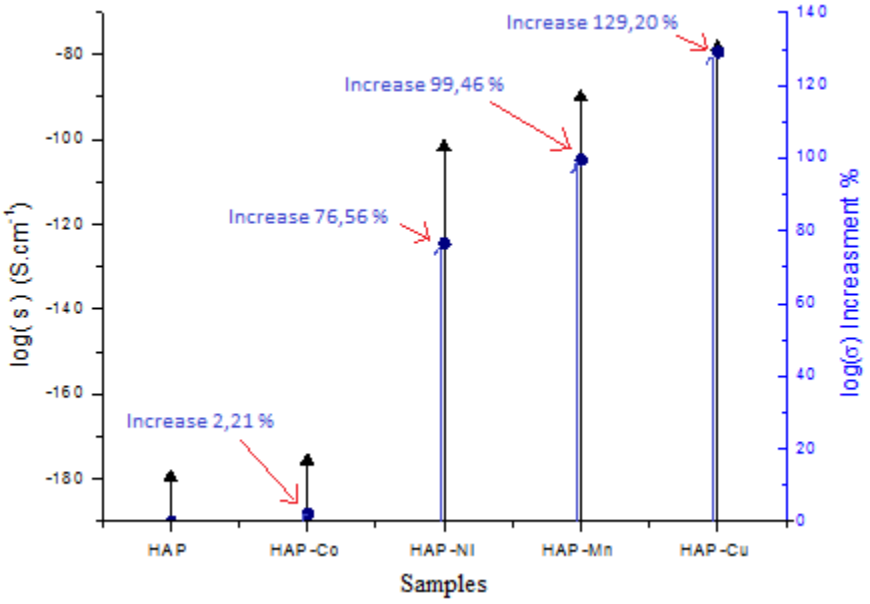

Figure 110. log σ increasement of samples HAP-M (M=Ni, Cu, Co, Mn) compared by pure HAP at 25 °C.

Table 46. Statistical value of log s and s increase at 25 °C for samples HAP-M (M=Ni, Cu, Co, Mn) compared by pure HAP at 25 °C.

Sample	Temperature	log(σ) (S/cm)	Increase (%) log σ	σ (S/cm)	Increase σ (%)

HAP	0 °C	-195,55	-	$1,18*10^{-85}$	-
HAP-Co		-191,30	2,220	$8,29*10^{-84}$	69,99
HAP-Ni		-110,58	76,83	$9,43*10^{-49}$	$7,96*10^{+36}$
HAP-Mn		-97,83	99,87	$3,23*10^{-43}$	$2,73*10^{+42}$
HAP-Cu		-85,09	129,81	$1,10*10^{-37}$	$9,36*10^{+47}$
HAP	25 °C	-179,51	-	$1,08*10^{-78}$	-
HAP-Co		-175,62	2,216	$5,32*10^{-77}$	49,01
HAP-Ni		-101,67	76,56	$6,95*10^{-45}$	$6,41*10^{+33}$
HAP-Mn		-89,99	99,46	$8,19*10^{-40}$	$7,55*10^{+38}$
HAP-Cu		-78,32	129,20	$9,65*10^{-35}$	$8,89*10^{+43}$
HAP	50 °C	-167,99	-	$1,09*10^{-73}$	-
HAP-Co		-164,35	2,21	$4,16*10^{-72}$	37,94
HAP-Ni		-95,27	76,32	$4,19*10^{-42}$	$3,82*10^{+31}$
HAP-Mn		-84,36	99,12	$2,29*10^{-37}$	$2,08*10^{+36}$
HAP-Cu		-73,45	128,69	$1,25*10^{-32}$	$1,14*10^{+41}$
HAP	75 °C	-154,36	-	$9,11*10^{-68}$	-
HAP-Co		-151,03	2,20	$2,55*10^{-66}$	28,02
HAP-Ni		-87,70	76,01	$8,15*10^{-39}$	$8,94*10^{+28}$
HAP-Mn		-77,70	98,66	$1,79*10^{-34}$	$1,97*10^{+33}$
HAP-Cu		-67,70	128,00	$3,95*10^{-30}$	$4,33*10^{+37}$
HAP	100 °C	-144,31	-	$2,10*10^{-63}$	-
HAP-Co		-141,20	2,20	$4,72*10^{-62}$	22,41
HAP-Ni		-82,11	75,74	$2,16*10^{-36}$	$1,02*10^{+27}$
HAP-Mn		-72,78	98,26	$2,44*10^{-32}$	$1,15*10^{+31}$
HAP-Cu		-63,45	127,41	$2,75*10^{-28}$	$1,30*10^{+35}$

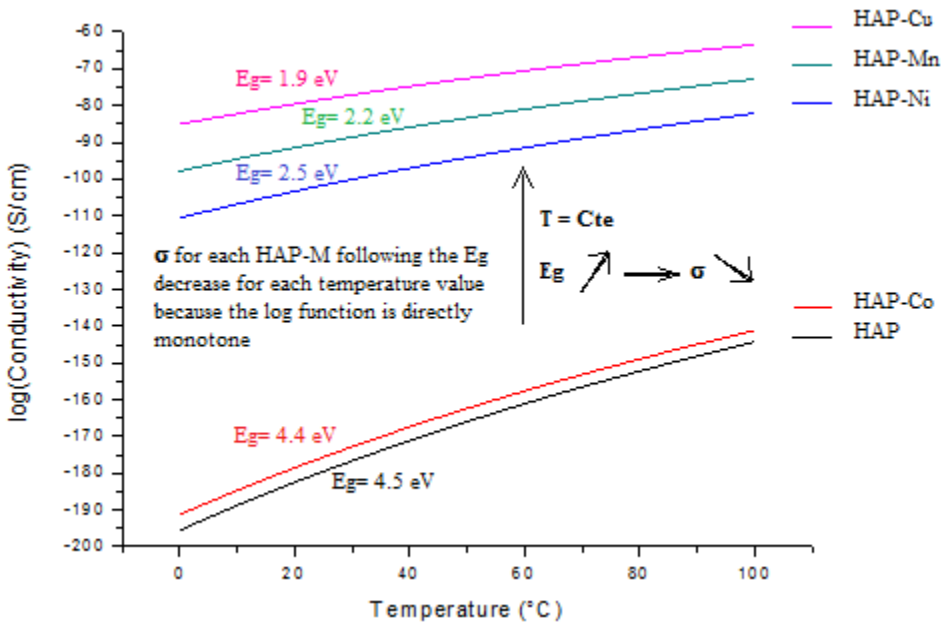

Figure 111. Variation of electrical conductivity of HAP and HAP-M (M=Ni, Cu, Co, Mn) function temperature

VIII.5 Thermal conductivity

Thermal conduction is a mode of heat transfer caused by a difference in temperature between two regions of the same medium, or between two media in contact, and occurring without overall material displacement (macroscopically) as opposed to convection which is another heat transfer. It can be interpreted as the transmission, step by step, of the thermal agitation: an atom or a molecule transfer part of its kinetic energy to the neighboring atoms.

Thermal conduction is a process of internal energy transport linked to molecular agitation and due to heterogeneity of the medium on a macroscopic scale. It is an irreversible phenomenon similar to the phenomenon of diffusion. So, thermal conduction is the movement of thermal energy from hot parts of a system to cold parts. As the energy diffuses into a system, temperature differences decrease and entropy increases. In solids, the translational motion takes the form of phonons. Phonons are elementary quantities of vibration energy moving in a solid at the speed of the substance's own sound. The way in which phonons interact in the solid determines their properties, such as thermal diffusion. Electrical insulators generally have low thermal conductivity and these solids are considered thermal insulators (such as glass, plastics, rubber, ceramics and stone). This is because in solids, atoms and molecules are not free to move. Metals, however, have a high thermal conductivity. Indeed, their structure allows a diffusion of the kinetic energy by conduction electrons, light and extremely mobile. This is why in metals there is an almost perfect correlation between electrical conductivity and

thermal conductivity. Electron conductivity predominates in metals because electrons are delocalised, that is, they are not bonded to an atom and behave like a quantum gas.

From an atomic point of view, thermal conductivity is related to two types of behavior: the movement of charge carriers, ions, electrons and holes, and oscillation of atoms around their equilibrium position. In metals, the movement of free electrons is preponderant whereas in the case of non-metals, the vibration of ions is the most important. The thermal conductivity is therefore linked on the one hand to the electrical conductivity (movement of the charge carriers) and on the other hand to the very structure of the material (vibrations of the atoms. Indeed, in a solid, the vibrations of the atoms are not random and independent of each other, but correspond to Eigen modes of vibration, "phonons». This contribution will be more important in a crystal, ordered [595]. The incorporation of the Ni, Cu, Co, Mn metal ions in the HAP matrix acts directly on its thermal conductivity [598] because these metals have a very important thermal conductivity [595], see table 47.

Table 47. Thermal conductivity of pure metals at temperature 27 °C.

Pure Metal	Ca	Ni	Cu	Co	Mn
Thermal Conductivity (W·cm−1·K−1)	2	0.907	4.01	1	0.0782

Also, the increase of the electrical conductivity contributes to the increase of the thermal conductivity of our samples, because it presents the contribution of the load carriers to the thermal conduction.

Mathematically, the thermal conductivity λ can thus be written as the sum of two contributions as figured in relationships (23) and (24) [598]:

$$\lambda = \lambda e + \lambda p \qquad (23)$$

$$\text{When: } \lambda_e = LT\sigma \qquad (24)$$

Where λe is the contribution of charge carriers (electrons or holes), λp is the contribution of the vibrations of atoms (phonons), L is the Lorentz factor, this is constant positive value for the same materials, T is the temperature, σ is the electrical conductivity. See figure 112 and table 48.

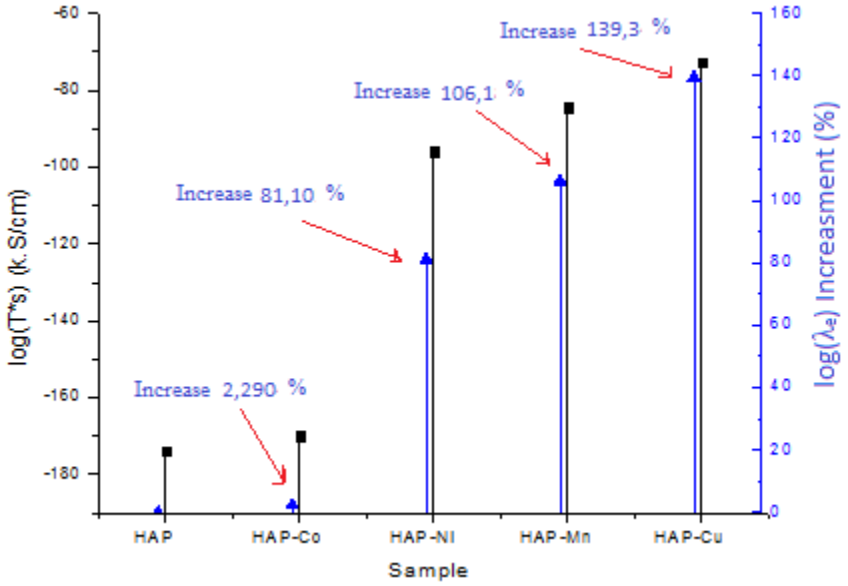

Figure 112. log λ_e increasement of samples HAP-M (M=Ni, Cu, Co, Mn) compared by pure HAP at 25 °C.

Table 48. Statistical value of log T*s and T*s increase at 25 °C for samples HAP-M (M=Ni, Cu, Co, Mn) compared by pure HAP.

Sample	Temperature	log(T*σ) (K.S/cm)	Increase (%) logT* σ	T*σ (K.S/cm)	Increase T*σ (%)
HAP	0 °C	-189,94	-	$3,24*10^{-83}$	-
HAP-Co		-185,69	2,287	$2,27*10^{-81}$	$7,01*10^{+01}$
HAP-Ni		-104,97	80,94	$2,58*10^{-46}$	$7,96*10^{+36}$
HAP-Mn		-92,22	105,94	$8,84*10^{-41}$	$2,73*10^{+42}$
HAP-Cu		-79,48	138,97	$3,03*10^{-35}$	$9,35*10^{+47}$
HAP	25 °C	-173,82	-	$3,24*10^{-76}$	-
HAP-Co		-169,92	2,29	$1,59*10^{-74}$	$4,91*10^{+01}$
HAP-Ni		-95,97	81,10	$2,07*10^{-42}$	$6,39*10^{+33}$
HAP-Mn		-84,30	106,18	$2,44*10^{-37}$	$7,53*10^{+38}$
HAP-Cu		-72,62	139,34	$2,88*10^{-32}$	$8,89*10^{+43}$
HAP	50 °C	-160,19	-	$2,69*10^{-70}$	-
HAP-Co		-156,60	2,293	$9,76*10^{-69}$	$3,63*10^{+01}$
HAP-Ni		-88,37	81,27	$4,18*10^{-39}$	$1,55*10^{+31}$
HAP-Mn		-77,59	106,44	$2,00*10^{-34}$	$7,43*10^{+35}$
HAP-Cu		-66,82	139,72	$9,52*10^{-30}$	$3,54*10^{+40}$
HAP		-148,51	-	$3,17*10^{-65}$	-

HAP-Co	75 °C	-145,17	2,29	$8,90*10^{-64}$	$2,81*10^{+01}$
HAP-Ni		-81,84	81,44	$2,84*10^{-36}$	$8,96*10^{+28}$
HAP-Mn		-71,84	106,70	$6,25*10^{-32}$	$1,97*10^{+33}$
HAP-Cu		-61,84	140,11	$1,38*10^{-27}$	$4,35*10^{+37}$
HAP	100 °C	-138,39	-	$7,87*10^{-61}$	-
HAP-Co		-135,28	2,29	$1,76*10^{-59}$	$2,24*10^{+01}$
HAP-Ni		-76,19	81,62	$8,09*10^{-34}$	$1,03*10^{+27}$
HAP-Mn		-66,86	106,96	$9,12*10^{-30}$	$1,16*10^{+31}$
HAP-Cu		-57,53	140,52	$1,03*10^{-25}$	$1,31*10^{+35}$

VIII.6 Toxicity discussion

We discuss also in this part, the Origin, production and applications of Coblat (Co) and Nickel (Ni). The Ni in free state constitutes 5 to 50% by weight of meteorites. It is found in several ores associated with sulfur, oxygen, antimony, arsenic or silica. The most important nickel ores are oxides (eg laterite containing mixed nickel / iron oxides) and sulphides. Pentlandite ($(NiFe)_9S_8$), which is the most important sulphide, is usually found associated with pyrrhotite (Fe_7S_6), chalcopyrite ($CuFeS_2$) and small amounts of cobalt, selenium, tellurium, silver, gold and platinum. Large deposits of nickel are found in Canada, Russia, Australia, New Caledonia, Indonesia and Cuba.

Since nickel, copper and iron occur as distinct minerals in sulphide deposits, mechanical concentration processes, such as flotation, and magnetic separation, after crushing and grinding of the gas, are used. The nickel concentrate is transformed into sulphurous matte by roasting or sintering. The matte is refined by electrolytic extraction or by the Mond process. In this process, the matte is ground, calcined and treated with carbon monoxide at 50 ° C to form nickel carbonyl ($Ni(CO)_4$) gas, which then decomposes at a temperature of 200 to 250 ° C to form deposit in the form of nickel powder. Global nickel production is around 70,000 t / year.

The industry produces more than 3,000 nickel alloys and compounds. The most popular are stainless steel and Ni-Cr-Fe alloys, the main applications of which are heat-resistant equipment and kitchen utensils. Monel metal and other Ni-Cu alloys are used in the manufacture of coins, equipment for the dairy industry and the food industries. Ni-Al alloys are used for the production of magnets and catalysts (Raney nickel, for example). Ni-Cr alloys are used in heating elements, gas turbines and jet engines. Nickel alloys formed with precious metals are used in jewelry. Nickel metal, its compounds

and alloys have many other applications: electroplating, magnetic tapes and computer components, arc welding filler rods, surgical and dental prostheses, nickel batteries. cadmium, pigments for paints (e.g. yellow nickel titanate), molds for ceramic and glass vessels and catalysts for hydrogenation reactions, organic synthesis and the final methanation step in gasification coal. Occupational nickel exposures can also occur in recycling operations, as materials comprising nickel, particularly those in the steel industry, are typically melted, refined and used for the preparation of alloys with a composition similar to that of the initial alloy.

The risks to human health from occupational exposure to nickel compounds can be divided into three main categories:

- Allergies;
- Rhinitis, sinusitis and respiratory ailments;
- Cancers of the nasal cavities, lungs and other organs.

The health risks from nickel carbonyl are described above in the article on metal carbonyls.

Allergies. Nickel and its compounds are the most common cause of allergic contact skin disease. They are not only found in people occupationally exposed to nickel compounds, but also in the general population after contact with coins, jewelry, watch cases, suspender-type clothing attachments, etc., which contain nickel. In people exposed to nickel, nickel dermatitis usually begins with erythema papular on the hands. The skin gradually becomes eczematous; in the chronic stage, lichenification is often observed. Sensitization to nickel sometimes causes conjunctivitis, pulmonary eosinophilia, and local or systemic reactions to implants containing nickel (for example in intraosseous pins, dental implants, prosthetic heart valves, and pacemaker leads. cardiac). Ingestion of drinking water contaminated with nickel or foods rich in nickel can increase eczema on the hands of people sensitized to nickel.

Rhinitis, sinusitis and respiratory ailments. People employed in nickel refineries and nickel-plating shops, who are highly exposed to inhalation of nickel dust or aerosols of soluble nickel compounds, are often prone to chronic upper respiratory diseases, such as hypertrophic rhinitis, nasal sinusitis, anosmia, nasal polyposis, and perforation of the nasal septum. Chronic conditions of the lower respiratory tract (eg bronchitis, pulmonary fibrosis) have also been described, but such cases are less common. Rendall, Phillips and Renton (1994) reported a fatal case of acute worker exposure to inhalation of nickel particles in an arc welding process; the authors stress the importance of wearing personal protective equipment in arc welding processes with electrodes containing nickel.

Cancers. Epidemiological studies of workers employed in nickel refineries in Canada, Wales, Germany, Norway and Russia have described increased mortality from cancers of the lungs and nasal cavities. It has also been reported that certain groups of workers employed in nickel refineries have more frequent malignancies, such as carcinomas of the larynx, kidneys, prostate or stomach, and soft tissue sarcomas, but the statistical significance of these observations is not sufficiently reliable. The increased risk of cancers of the lungs and nasal cavities exists primarily in those employed in refining operations that involve high exposure to nickel, such as roasting, casting and electrolysis. Although these cancer risks are generally related to exposure to insoluble nickel compounds, such as nickel sub-sulfide and nickel oxide, exposure to soluble nickel compounds has also been reported in patients workers assigned to electrolysis.

The results of many epidemiological studies on cancer risks among workers employed in industries using nickel have been generally negative, but recent facts suggest a slightly increased cancer risk among welders, grinders, workers employed in the industry, electrolytic plating and those manufacturing batteries. These occupational groups are often exposed to vapors and fumes which contain mixtures of carcinogenic metals (nickel and chromium or nickel and cadmium, for example). Based on an assessment of epidemiological studies, the International Agency for Research on Cancer (IARC) concluded in 1990 that there is sufficient evidence for the carcinogenicity, in humans, of nickel sulfate and combinations of sulfides. and nickel oxides encountered in the nickel refining industry, but that the indications concerning the carcinogenicity of nickel and its alloys (always in humans) are insufficient. Nickel compounds have been classified as carcinogenic to humans (Group 1) and nickel metal, among those possibly carcinogenic to humans (Group 2B).

For the renal effects in workers with high exposure to soluble nickel compounds, renal tubular dysfunction may be observed, evidenced by increased renal excretion of β2-microglobulin (β2M) and N-acetyl-glucosaminidase (NAG).

The metal carbonyls correspond to the general formula Mex (CO) y. They are formed by the combination of a metal (Me) with carbon monoxide (CO). Most are solid at room temperature, but nickel carbonyl, iron pentacarbonyl, and ruthenium pentacarbonyl are liquid, while cobalt hydrocarbonyl is gaseous. This article focuses on nickel carbonyl which, due to its volatility, is exceptionally toxic and which, due to its industrial importance, deserves special attention. Since pentacarbonyl iron and hydrocarbonyl cobalt also have high vapor pressures and can form accidentally, they also deserve serious consideration as potential toxic compounds professionally.

Most metal carbonyls react vigorously with oxygen and oxidizing substances, and some ignite spontaneously. On exposure to air and light, carbonyl nickel breaks down to carbon monoxide and particulate nickel metal; hydrocarbonyl cobalt decomposes into octacarbonyl cobalt and hydrogen, and pentacarbonyl iron decomposes into nonacarbonyl iron and carbon monoxide.

The toxicity of a given carbonyl metal depends on the toxicity of carbon monoxide and that of the metal from which it is derived, as well as the volatility and instability of the carbonyl itself. The main route of exposure is inhalation, but absorption through the skin can also occur with liquid carbonyls. The relative acute toxicities (LD50 for the rat) of nickel carbonyl, cobalt hydrocarbonyl and iron pentacarbonyl are in the ratio 1: 0.52: 0.33. Inhalation of these substances by laboratory animals causes acute interstitial pneumonia, accompanied by pulmonary edema and hair damage, as well as damage to the brain, liver and kidneys.

Judging by the meager literature regarding their toxicity, hydrocarbonyl cobalt and pentacarbonyl iron rarely cause health hazards to workers in industry. However, pentacarbonyl iron can be accidentally formed when carbon monoxide, or a gas mixture containing it, is stored in pressurized steel cylinders or passes through steel conduits, during the production of lighting gas. by reforming petroleum, or during a gas welding operation. The presence of carbon monoxide in the releases from blast furnaces, electric arc furnaces or foundry furnaces in the manufacture of steel can also lead to the formation of pentacarbonyl iron.

The metal alloy was used in dental amalgam for years 1929 [599], but the side effects and toxicity of some metal ions such as mercury have led the scientific community to limit or prohibit the use of mercury-based dental amalgam [600, 601], because the mercury is a major factor that can cause Alzheimer's disease to the patient [602, 603]. Also, the high concentrations of cobalt Co and nickel Ni in dental amalgams and implants cause increased concentration of metal ions in the blood [604, 605] which can result from ill effects to the normal functioning of the human body and cardiovascular problems [606]. Since the 1985's, dental implants and amalgams have become more based on ceramic biomaterials [607] and HAPs [608], because it does not present risk of toxicity to health [609], since HAP is the essential component in the mineral part of bone and teeth [610, 611]. Generally, ceramic-based implants are more secure to health than metal-based implants [612], but they have a shorter lifespan compared to metallic implant [613, 614]. The incorporation of low percentage metal ions concentration into the HAP matrix increases its mechanical properties [615] and electrical to give a longer lifespan of bio-ceramic dental amalgams and dental implant based on HAPs and greatly

reduces the toxicity risk to use metallic dental amalgam and implants [616]. The HAP (HAP) with general formula Ca10 (PO4) 6(OH) 2 is a phosphorus apatite which crystallizes natural state in the hexagonal system [617, 618]. It is the main constituent of bones and teeth; it has excellent affinity with bone tissue. So, its advantage is to create strong chemical bond with the bone [619]. The HAP can be used also for the purification of aqueous media [620, 621] and the immobilization of uranium in nuclear waste [622].

Among the metal ions used in this work, Copper Cu and manganese Mn present Low risk of toxicity [623]. However, the Cobalt Co and Nickel Ni presents a major factor of toxicity if their weight concentration is high. M studies have been realized to know the damaging and side effect of use the metalic ions in orthopedic [624, 625, 626] and dental application [627, 628], but there is no ceiling limit for the use of Cobalt and Nickel in dental amalgam based on nickel or cobalt, since several amalgams containing up to 67% cobalt and 71.5% nickel [629] because the risk of toxicity and inflammation arises after the penetration of Co2 + and Ni2 + inside the body through the dental roots via abrasion and corrosion phenomenon [630, 631]. the work of Arne Hansen-Petersen, showed side effects of using dental implants with a high concentration of Cobalt and Nickel [632], is the increase ions of cobalt and nickel in the blood which causes inflammations in the neighboring tissue of the dental implant, and more risks of toxicity [633]. The human body can receive up to 250 ug/day of Cobalt, and 400 ug/day of Nickel via nutrition (food and drink) [634], this concentration decreases over the days because the human body needs cobalt for vitamin B_{12} production [633] which is essential for normal brain function [635]. The Cobalt and Nickel transfer into the body via abrasion and corrosion [636] is too inferior to the intake of Cobalt and Nickel via air and nutrition [629]. But the problem arises because of the daily accumulation of Cobalt and Nickel via abrasion plus nutrition which can cause dangerous consequences after 5 years [637]. To determine the weight concentration of Cobalt and Nickel elements in our HAP-Co and HAP-Ni samples, we use the X-ray fluorescence spectroscopy (XRF) where the experimental spectra as it is shown in figure 113.

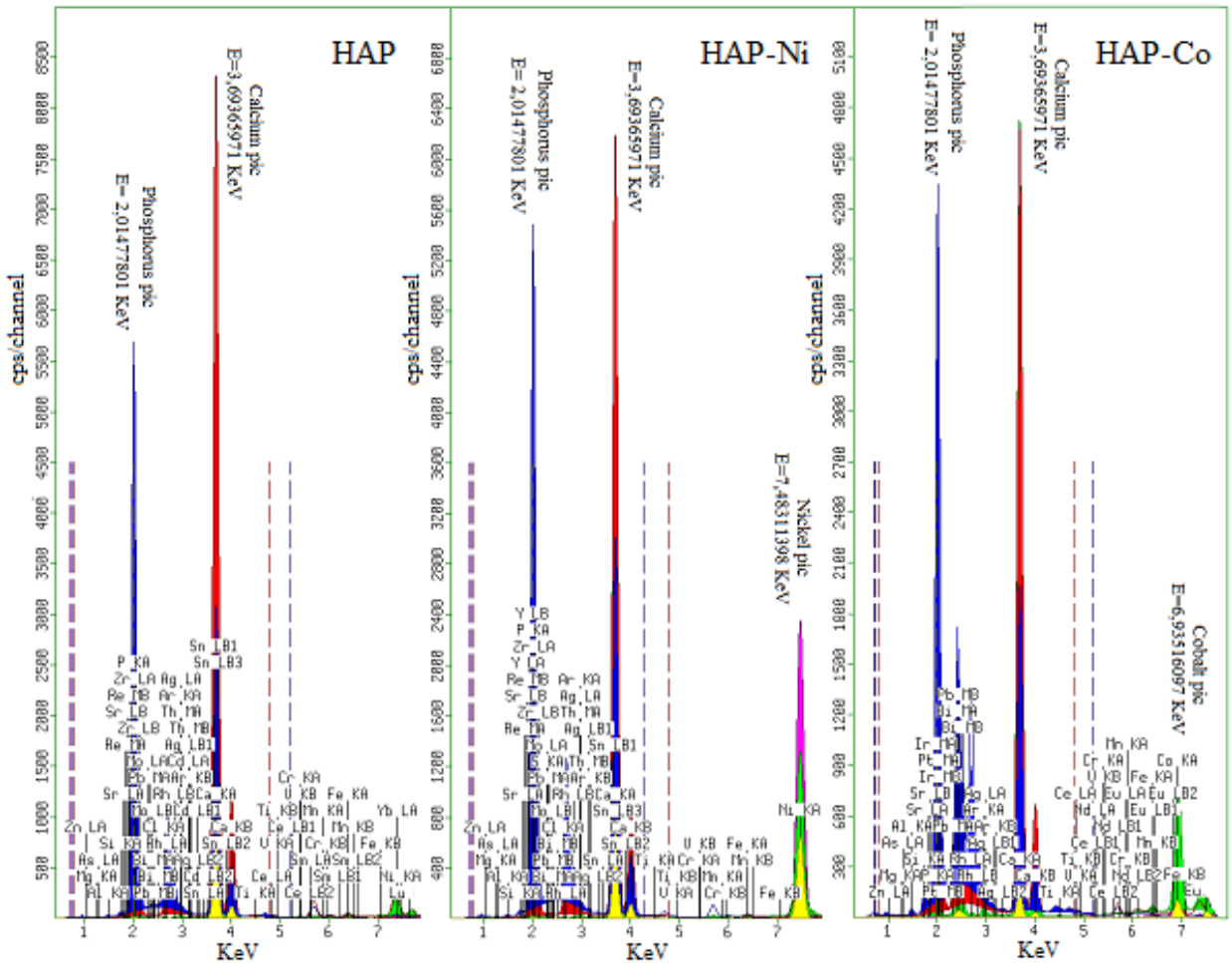

Figure 113. XRF analysis spectrum for HAP, HAP-Ni and HAP-Co

Our HAP-Co samples contain only 1.46 wt% Cobalt that is strongly bound to the HAP matrix [638], which reduces the Cobalt transfer from HAP-Co to body via abrasion and corrosion. The weight percentage of Co in our HAP-Co samples is closed to the value given by Zeeshan Qamar et al fornatural dental substitution 1.35 wt% Ca by Co in natural teeth via nutrition (food and drink) [639]. The mass percentage of Ni in our samples HAP-Ni 2.68 wt% which is lower than the value given by Anu Priya et al 2.97 wt% so that the nickel is strongly bound to the HAP matrix. the low weight concentration of Cobalt and Nickel in our samples reduces the risk of toxicity, because the human body can eliminate up to 5ug /L of Cobalt and Nickel by Urination. Which is larger than the amount of Co and Ni transferred to the body via abrasion and corrosion. and all this reduce the risk of toxicity by our HAP-M samples (M = Co, Ni). All results of theorical (Th) and experimental (Exp) weight concentration of chemicals elements of our samples HAP-Co and HAP-Ni as reported in table 49.

Table 49. Concentration of P, Ca, Ni and Co Chemical elements in HAP, HAP-Ni and HAP-Co.

Elements Sample	wt% P2O5	wt% P		wt % CaO	wt% Ca		wt% NiO	wt% Ni		wt% Co3O4	wt% Co	
		Th	Exp		Th	Exp		Th	Exp		Th	Exp
HAP	39.34	18.49	17.16	57.73	39.89	41.25	123,5ppm	0	97ppm	0	0	0
HAP-Ni	38.14	18.32	16.64	50.22	37.55	35.89	3,411	2.8	2.68	0	0	0
HAP-Co	41.57	18.32	18.14	49.79	37.54	35.58	0	0	0	1,991	2.9	1.46

Those results are also ploted and showns in figure 114, for easy comparison between theorical and experimental values of weight concentration element in HAP, HAP-Ni and HAP-Co. Those result showd that experimental valus are near of theorical values.

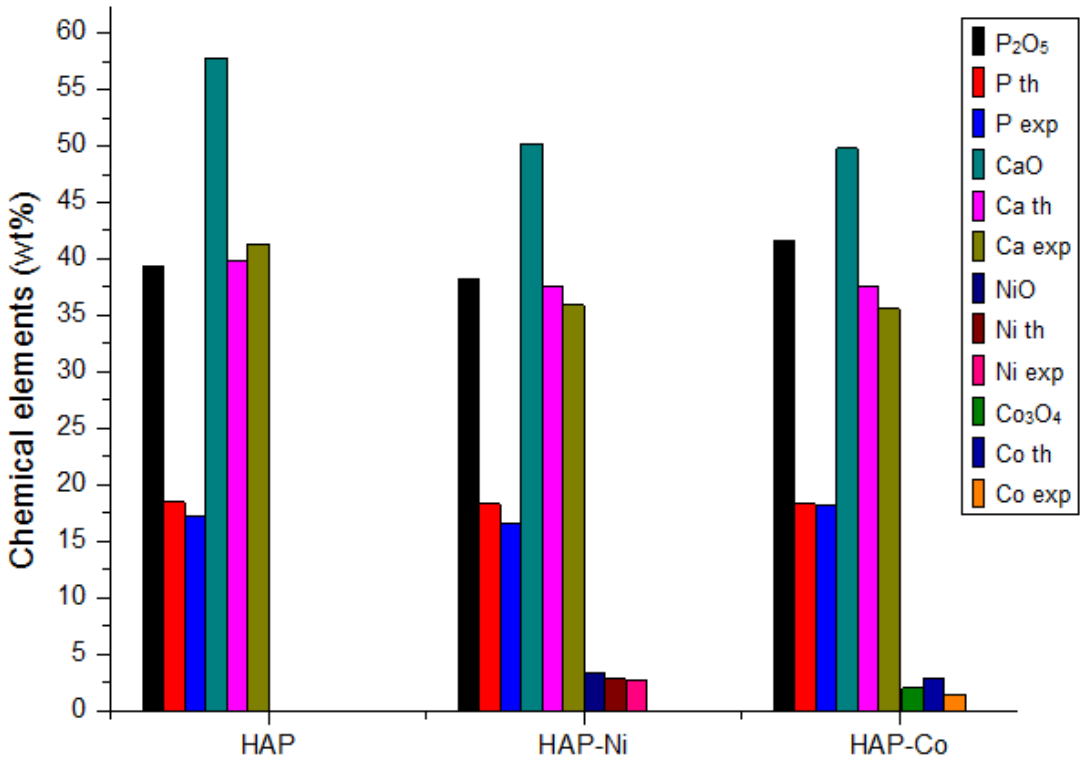

Figure 114. Concentration of P, Ca, Ni and Co Chemical elements in HAP, HAP-Ni and HAP-Co

VIII.7 Conclusion

The incorporation of Co, Ni, Cu and Mn metal ions in HAPs decrease their gap energy following nature of each metal ion, and increase the thermal and electrical conductivities. For this reason, these powders are similar to natural bon on thermal and electrical conductivities,

The increase of the electrical and thermal conductivities of our samples HAP-M (M = Co, Ni, Cu, Mn) compared to the pure HAP, gives the possibility of sensation to the heat and the cold to the patient unlike the ceramics used currently gives no feeling of hot or cold to the patient.

Samples of HAPs HAP-M (M = Co, Ni, Cu, Mn) are sparsely colored and their colors are near to white due to the absorption power of HAPs and also due to the low weight concentration of metal ions in our samples. This presents an important factor from an aesthetic point of view because our samples have a white color near to that of natural teeth.

To repair bone and tooth damage without toxicity we used the appropriate concentration of doped heavy metal ions. Cobalt is an oligo element essential for human's life, and used by the body for the composition of cobalamins necessary for brain functions. The cobalt and nickel intakes to the general population are mainly dietary and range of 250 μg/day of Cobalt, and 400 μg/day of Nickel through nutrition, food and drink. The Cobalt and Nickel used are strongly bonded on HAP structure, and cannot attack blood directly even by abrasion phenomenon which is very slow reaction where human body can eliminate up to 5μg/L of Cobalt and Nickel by urination. For this reason, we conclude the risk of toxicity by this bio-ceramic is unlikely.

Chapter IX:

CONCLUSIONS AND PERSPECTIVES

IX.1 Thesis Conclusions

The pure HAP was successfully synthesized by a novel sol-gel method using albumin from egg's white for an offering a media's growth of HAP similar to this for natural bone HAP. The comparison with the classical method shows that this method provides more purity and homogeneity with the fixation of very small quantities of minerals existing in egg's white which are very good because the natural HAP contains few concentrations of minerals. The incorporation of the transition metals of Cu, Co, Ni, and Mn with small concentration by substitution of 5% of Calcium which displays a total substitution of 1.13% into HAP cell, was carried out successfully via ceramic route method. This metal doping gave HAP new optoelectronic properties by increasing their optical and electrical properties which lead to a restriction in the optical gap. Hence, the doped HAP became semiconductors and can be used as biomaterials semiconductors in dental and orthopedic fields. Also, the increases in the electrical conductivities for all doped HAP until 140% can be exploited for dental amalgams to ensure the thermal and electrical conduction and give a sensation of cold and hot for patients for more tasting foods and drinks likewise natural teeth. The toxicities of Nickel and Cobalt were carefully discussed. It was being that this concentration provides no risk of toxicity due to strong bonding of Co and Ni into HAP cell, and it's very low potential penetration into the body via substitution or abrasion phenomenon are smaller than quotidian quantities of Co, and Ni coming from nutrition and consequently, the body can use them for production for some vitamins like B_{12} vitamin that require the Co. Their residues will be easily eliminated by the body via their biological mechanisms for body cleaning. As well, these doped HAP can be used as semiconductors materials, for manufacturing of solar panels due to their small gap bands to be used in the areas where the silicon is not favorable or not adequate, like areas of Sulphuric acid production where the solar panels based on silicon are not appealed due to its quick corrosion of silicon due to the few quantities of Sulphuric acids attached in the atmospheric air. The Chitosan samples were successfully extracted from shrimp shells by diluted and concentrated hydrochloric acids, and also by concentrated Nitric and Sulphuric acids. The results showed a difference in chitosan properties following the acids used in its demineralization; they provide a different degree of crystallinity towards biodegradable sutures, also the concentrated acid minimizes the time duration of decimalization and produces more quantities. The grains size reached of chitosan in this research, suggesting a considerable prospect; they can be handled easily on coating based on carbon material nanoscales. Our chitosan samples are advantageous for pharmaceutical purposes, due to their purity and a high degree of deacetylation.

Four different hybrids nanoparticles (CS-HAP-SWCNH, CS-HAP-GNPs_C97, CS-HAP-MWCNT, CS-HAP-GNPs_C90) were prepared and characterized successfully. All hybrids nanoparticles were synthesized by a developed method of chemical deposition carried by common solvents between HAP, Chitosan, and Carbon nanomaterials. The differences in linkage, structure, surfaces are owing to the type of carbon nanomaterials used that present 6.67 wt% for the first time, but the real carbon wt% into nanohybrids particles does also varied according to the carbon nanomaterials kinds and its ability to be linked with HAP and Chitosan nanoparticles. The characterization based on XRF, EDX, XRD, FTIR, SEM shows that the synthesized nano-HAP displayed the properties of HAP present in the bone, chemically, and morphologically. These nanocomposites get consequently an increase in the strength, thermal and electrical properties due to the presence of MWCNT, SWCNH, and GNPs grade C which provide very higher mechanical, thermal, and electrical properties. Also, the bioactivity of these hybrids nanoparticles is coming from coupling with Chitosan nanoparticles that provide very excellent bioactivity and antimicrobial and antibacterial activities. Most agglomeration is observed for CS-HAP-SWCNH due to the combination of carbon nanohorns, which lead to a decrease in mechanical properties. The quality in crystallization and profound homogeneity of all our hybrids nanocomposite gives divers' potentialities for its applications in dental and orthopedics domains for the coat, recovery, and partial or total replacement.

Finally, the outcome of this research so notably proposes to develop nanocomposites that engaged the mechanical strength and biocompatibility requirements of the natural HAP which are achieved successfully. Consequently, to contribute to the current knowledge of bones and teeth to develop materials designed for teeth and bone amalgams and implants.

IX.2 Recommendation for future works

IX.2.1 **Bio-Material development for orthopedic application**

The materials for dental or orthopedic implants are improved to function in the body as tools capable to maintain and influence bone reconstruction. These bone implants must be biocompatible to blend completely within the tissue host without causing immune resistance and biodegradable into forms of carbon dioxide and water. Besides, bone implants should own an allowable pore opening, and entirely interconnected with very porous structures which are the significant thing for giving accessible space for the cells to live through, grow, and adapt. Moreover, the higher surface area to volume rate gives more possibility for cell interactions. Subsequently, bone implants should additionally possess enough mechanical strength to maintain its structure subsequent implantation,

until achieving principally the bone endurance. Hence, it is necessary to choose the best material for bone implant application. For increasing the biodegradability and biocompatibility of materials meant for bone implants, polymers are largely investigated. The weak hardness of some polymers is treated by reinforcement by some ceramic. As a consequence, the polymer-ceramic nanocomposites have introduced an alternative to the extant metals-ceramic or metals-polymers nanocomposites for the orthopedic implants. Also, the manufacturing of orthopedic implants from nanocomposites of polymer-ceramic proved to be a smart way to defeat the undesirable effects of minerals nanocomposites such as toxicity and absence of biocompatibility.

The results of this study recommend that the prepared polymer-ceramic (CS-HAP-SWCNH, CS-HAP-GNPs_C97, CS-HAP-MWCNT, CS-HAP-GNPs_C90) hybrids nanocomposites satisfy the fundamental requirements of orthopedic implants; mechanical strength and biocompatibility. Therefore, the recommendations for future works are considered according to these results. The biocompatibility of the orthopedic implant counts largely on its spatial porous microstructure with inter-connecting pores or without connecting. The being of these openings permits cells to enter within the bone-implant and intensify the rehabilitation process of bones. Meantime, the presence of pores can lead to a change and decrease in the mechanical strength of the bone implants. Thus, tridimensional print of porous orthopedic implant with controlled pore dimension using the synthesized CS-HAP-SWCNH, CS-HAP-GNPs_C97, CS-HAP-MWCNT, CS-HAP-GNPs_C90 hybrids nanopowders, can give a solution and optimization of porosity and save the mechanical strength and biocompatibility.

IX.2.2 **Development of solar panels**

Solar energy is radiant light and heat from the Sun that is harnessed using a range of ever-evolving technologies such as solar heating, photovoltaics, solar thermal energy, solar architecture, molten salt power plants and artificial photosynthesis. It is an important source of renewable energy and its technologies are broadly characterized as either passive solar or active solar depending on how they capture and distribute solar energy or convert it into solar power. Active solar techniques include the use of photovoltaic systems, concentrated solar power and solar water heating to harness the energy. Passive solar techniques include orienting a building to the Sun, selecting materials with favorable thermal mass or light-dispersing properties, and designing spaces that naturally circulate air.

A solar cell, or photovoltaic cell, is an electrical device that converts the energy of light directly into electricity by the photovoltaic effect, which is a physical and chemical phenomenon. It is a form of photoelectric cell, defined as a device whose electrical characteristics, such as current, voltage, or resistance, vary when exposed to light. Individual solar cell devices can be combined to form modules, otherwise known as solar panels. In basic terms a single junction silicon solar cell can produce a maximum open-circuit voltage of approximately 0.5 to 0.6 volts.

Also, HAP can be used for energy production by conversion of sunligh energy to electrical energy since its high photovoltaic activity after doping by metals transition elements. Also, HAP can be used in the areas when silicon is not applicable due to its low resistance of corrrosion by acids like areas of phosphate manufacturing. The optimisation of concentration of metal transition element and theirs and combinition into HAP cell must be studied.

IX.2.3 **Pigment and microscopic dyes eliminations**

A pigment is a colored chemical substance insoluble into the medium that it colors. It is possible to associate, by etching, with a metal salt, to form an insoluble pigment. The pigments are largely used in art and industry as powders. They can be: used as a liquid in order to obtain a paint or ink; applied to a material, textile or leather, on which they are fixed on the surface; or incorporated into bulk material such as plaster or plastic to color it. A pigment can be natural or synthetic form mineral or organic origin. The Figure. 115. show some examples of powder pigments.

Numerous pigments are based on transition metal ions such as Cu, Co, Ni and Mn. In the other side, the waste of these pigments presents important menace toward the environment and human health if it not eliminated correctly.

In this study, we have successfly fixed these chromophore ions into HAP cell. So, we look that we can use this finding to fixed all pigment and microscopic dyes based on those metalic ions into HAP cell to eliminate them from the aqueous media. Langmuir and Freundlich adsorption isotherm must be appleid and disscussess in these cases to see the capacity of our HAP powders to adsorbe pigments and microscopic dyes.

Figure 115. Examples of powder pigments

IX.2.4 **Combinition with spinels oxide for applications on energies fields.**

Photocatalysis is based on the principle of activating a semiconductor using the energy provided by light. While, semiconductor is considered as a catalyst and its principle is close to heterogeneous catalysis where the oxidation-reduction reaction takes place on its surface. Spinels oxide with a chemical formula of A2+B23+O4 are considered as good semiconductor photocatalysis. They are a large class of compounds of mixed-metal oxides crystallizing into cubic structure, where A2+ ions occupy the tetrahedral sites and all B3+ ions occupy the octahedral sites. These systems have an immense technological importance due to their diverse applications in sensors, transducers, microelectronics, magnetoelectric devices, telecommunication systems, and industrially important catalytic and photocatalytic reactions.

A variety of approaches have been explored to enhance the photocatalytic activity of photocatalysts, including composite, morphological control, chemisorption of industrial gases ion doping, surface sensitization, noble metal loading, fuel and Li-air cells as electrocatalysts of oxygen or H_2O_2 reduction, and hetero structure constructing.

We notice that the spinel oxide has common properties with HAP like photocatalytic activities and accessibility to fixation pf metal ions for increasing their physic-chemical properties. For this reason, we want to bring up the possibility to combine HAP with spinels oxide to develop the fuel cell materials for batteries application.

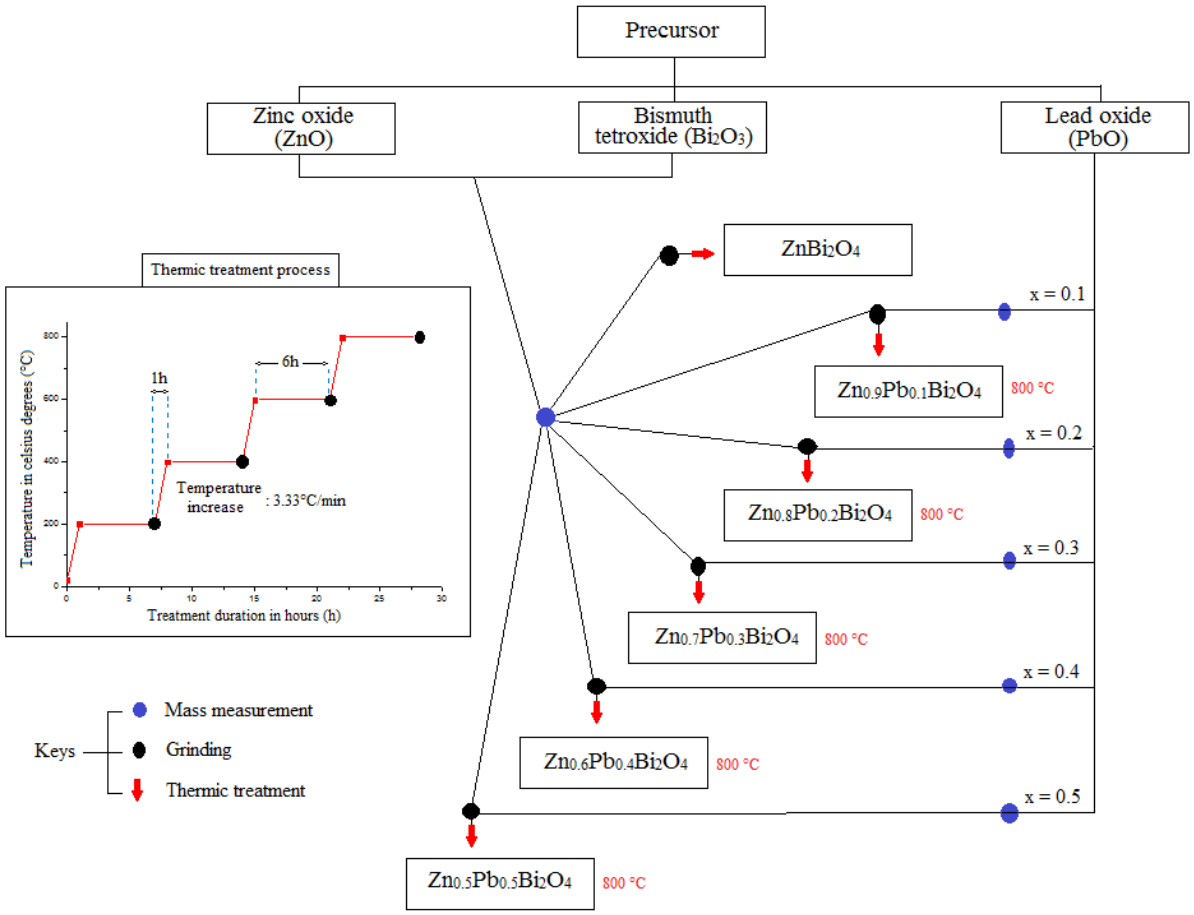

Figure 116. Synthesis process for the elaboration of various $Zn_{1-x}Pb_xBi_2O_4$ (x=0.0, 0.1, 0.2, 0.3, 0.4 and 0.5) spinels by solid state method.

We are started by synthesizing and characterizing the $Zn_{1-x}Pb_xBi_2O_4$ (x=0.1, 0.2, 0.3, 0.4, 0.5) spinel oxides, where A^{2+} present Zn^{2+} or Pb^{2+} ions after substitution, and B^{3+} present Bi^{3+} ions. We substituted the Zn^{2+} of $ZnBi_2O_4$ spinel oxide by Pb^{2+} with different concentration (10%, 20%, 30%, 40 and 50%) to see the effect on the structural parameters and bonds assignments this spinels oxide. The Figure .116 schematize the synthesis process for the elaboration of various $Zn_{1-x}Pb_xBi_2O_4$ (x=0.0, 0.1, 0.2, 0.3, 0.4 and 0.5) spinels by solid state method. We want to optimize the grain sizes of this spinels oxide to choose the most dimensions to be coupled with all our HAP nanomaterials produced in this study. Theirs exploitation into environment protection, and heavy metal ions eliminations from aqueous media and micro dyes eliminations must be also investigated.

REFERENCES

[1] ROSER, Max, RITCHIE, Hannah, et ORTIZ-OSPINA, Esteban. World population growth. Our World in Data, 2013.
[2] ADELEKE, Oluwatoyin Ayotomilola. Porous and Non-Porous Metallic Biomaterials. Unfolding the Biopolymer Landscape, vol. 2, p. 38, 2016.
[3] ROBERTS, W. Eugene et HARTSFIELD JR, James K. Bone development and function: genetic and environmental mechanisms. In : Seminars in Orthodontics. WB Saunders, p. 100-122, 2004.
[4] ROOBAN, Thavarajah, KRISHNASWAMY, Nathamuni Rengarajan, MANI, Karthik, et al. Root damage and repair in patients with temporary skeletal anchorage devices. American journal of orthodontics and dentofacial orthopedics, vol. 141, no 5, p. 547-555, 2012.
[5] CHEN, Fa-Ming et LIU, Xiaohua. Advancing biomaterials of human origin for tissue engineering. Progress in polymer science, vol. 53, p. 86-168, 2016.
[6] NAAHIDI, Sheva, JAFARI, Mousa, EDALAT, Faramarz, et al. Biocompatibility of engineered nanoparticles for drug delivery. Journal of controlled release, vol. 166, no 2, p. 182-194, 2013.
[7] GOMEZ, Pablo F. et MORCUENDE, Jose A. A historical and economic perspective on Sir John Charnley, Chas F. Thackray Limited, and the early arthroplasty industry. The Iowa orthopaedic journal, vol. 25, p. 30, 2005.
[8] WINTER, George D. Tissue reaction to metallic wear and corrosion products in human patients. Journal of Biomedical Materials Research, vol. 8, no 3, p. 11-26, 1974.
[9] CHEN, Qizhi et THOUAS, George A. Metallic implant biomaterials. Materials Science and Engineering: R: Reports, vol. 87, p. 1-57, 2015.
[10] DUAN, Wei, CHEN, Cong, HAQUE, Masudul, et al. Polymer-mineral scaffold augments in vivo equine multipotent stromal cell osteogenesis. Stem cell research & therapy, vol. 9, no 1, p. 60, 2018.
[11] BARRY, Mikayla, PEARCE, Hannah, CROSS, Lauren, et al. Advances in Nanotechnology for the Treatment of Osteoporosis. Current osteoporosis reports, vol. 14, no 3, p. 87-94, 2016.
[12] https://fr.wikipedia.org/wiki/Liste_des_pays_par_esp%C3%A9rance_de_vie#Historique_1950-2015.
[13] PRAKASAM, Mythili, LOCS, Janis, SALMA-ANCANE, Kristine, et al. Biodegradable materials and metallic implants—a review. Journal of functional biomaterials, vol. 8, no 4, p. 44, 2017.
[14] DE SCHEERDER, Ivan K., WILCZEK, Krzysztof L., VERBEKEN, Eric V., et al. Biocompatibility of biodegradable and nonbiodegradable polymer-coated stents implanted in porcine peripheral arteries. Cardiovascular and interventional radiology, vol. 18, no 4, p. 227-232, 1995.
[15] WOLFE, D. et SINGH, Jogender. Functionally gradient ceramic/metallic coatings for gas turbine components by high-energy beams for high-temperature applications. Journal of materials science, vol. 33, no 14, p. 3677-3692, 1998.
[16] JARZĄBEK, Dariusz M., MILCZAREK, Michał, WOJCIECHOWSKI, Tomasz, et al. The effect of metal coatings on the interfacial bonding strength of ceramics to copper in sintered Cu-SiC composites. Ceramics International, vol. 43, no 6, p. 5283-5291, 2017.
[17] CORDEIRO, Jairo M. et BARÃO, Valentim AR. Is there scientific evidence favoring the substitution of commercially pure titanium with titanium alloys for the manufacture of dental implants?. Materials Science and Engineering: C, vol. 71, p. 1201-1215, 2017.
[18] ZHANG, Yuqing, SUN, Danni, CHENG, Jun, et al. Mechanical and biological properties of Ti–(0–25 wt%) Nb alloys for biomedical implants application. Regenerative Biomaterials, vol. 7, no 1, p. 119-127.
[19] MOHAMMAD, Kaif. Customised Cranioplasty Implant for Decompressive Craniectomy Patients–A Technical Note. Turkish neurosurgery, 2019, vol. 29, no 1, 2020.
[20] SENGUPTA, Biswajit, SHEKHAR, Shashank, et KULKARNI, Kaustubh N. A novel ultra-high strength and low-cost as-cast titanium alloy. Materials Science and Engineering: A, vol. 696, p. 478-481, 2017.
[21] LI, Mei, ZHANG, Chi, CHENG, Mengjie, et al. Small intestinal submucosa: A potential osteoconductive and osteoinductive biomaterial for bone tissue engineering. Materials Science and Engineering: C, vol. 75, p. 149-156, 2017.

[22] MEHRALI, Mehdi, THAKUR, Ashish, PENNISI, Christian Pablo, et al. Nanoreinforced hydrogels for tissue engineering: Biomaterials that are compatible with load-bearing and electroactive tissues. Advanced Materials, vol. 29, no 8, p. 1603612, 2017.
[23] BADAWY, Mohamed EI et RABEA, Entsar I. Chitosan and its modifications as biologically active compounds in different applications. Adv. Physicochem. Prop. Biopolym, 2017.
[24] MARKOVIC, Milenko, FOWLER, Bruce O., et TUNG, Ming S. Preparation and comprehensive characterization of a calcium hydroxyapatite reference material. Journal of research of the National Institute of Standards and Technology, vol. 109, no 6, p. 553, 2004.
[25] SAUER, G. R., ZUNIC, W. B., DURIG, J. R., et al. Fourier transform Raman spectroscopy of synthetic and biological calcium phosphates. Calcified tissue international, vol. 54, no 5, p. 414-420, 1994.
[26] REY, C., COMBES, C., DROUET, C., et al. 1.11 Bioactive Calcium Phosphate Compounds: Physical Chemistry. Comprehensive biomaterials II, vol. 244, 2017.
[27] TSUCHIDA, Takashi, KUBO, Jun, YOSHIOKA, Tetsuya, et al. Reaction of ethanol over hydroxyapatite affected by Ca/P ratio of catalyst. Journal of Catalysis, vol. 259, no 2, p. 183-189, 2008.
[28] WU, Yu-Shiang, LEE, Yuan-Haun, et CHANG, Hou-Cheng. Preparation and characteristics of nanosized carbonated apatite by urea addition with coprecipitation method. Materials Science and Engineering: C, vol. 29, no 1, p. 237-241, 2009.
[29] TSUCHIDA, Takashi, KUBO, Jun, YOSHIOKA, Tetsuya, et al. Influence of preparation factors on Ca/P ratio and surface basicity of hydroxyapatite catalyst. Journal of the Japan Petroleum Institute, vol. 52, no 2, p. 51-59, 2009.
[30] OGIWARA, H., YAMADA, Y., SATOU, M., et al. HS LIU, TS CHIN, LS LAI, SY CHIU, KH CHUNG, CS CHANG &. Ceramics International, vol. 23, p. 545-549, 1997.
[31] EARL, J. S., WOOD, D. J., et MILNE, S. J. Hydrothermal synthesis of hydroxyapatite. In : Journal of Physics: Conference Series. IOP Publishing, p. 268, 2006.
[32] ANDRES-VERGES, M., FERNANDEZ-GONZALEZ, C., et MARTÍNEZ-GALLEGO, M. Hydrothermal synthesis of calcium deficient hydroxyapatites with controlled size and homogeneous morphology. Journal of the European Ceramic Society, vol. 18, no 9, p. 1245-1250, 1998.
[33] LIU, J. Ye, x. Wang, H., Zhu, M., Wang, B., Yan, H, p. 629-633, 2003.
[34] ZHANG, Xing et VECCHIO, Kenneth S. Hydrothermal synthesis of hydroxyapatite rods. Journal of Crystal Growth, vol. 308, no 1, p. 133-140, 2007.
[35] DU, Xingwei, CHU, Ying, XING, Shuangxi, et al. Hydrothermal synthesis of calcium hydroxyapatite nanorods in the presence of PVP. Journal of materials science, vol. 44, no 23, p. 6273-6279, 2009.
[36] KEE, Chia Ching, ISMAIL, Hanafi, et NOOR, Ahmad Fauzi Mohd. Effect of synthesis technique and carbonate content on the crystallinity and morphology of carbonated hydroxyapatite. Journal of Materials Science & Technology, vol. 29, no 8, p. 761-764, 2013.
[37] KALITA, Samar J. et VERMA, Saurabh. Nanocrystalline hydroxyapatite bioceramic using microwave radiation: Synthesis and characterization. Materials Science and Engineering: C, vol. 30, no 2, p. 295-303, 2010.
[38] LIU, Dean-Mo, TROCZYNSKI, T., et TSENG, Wenjea J. Water-based sol–gel synthesis of hydroxyapatite: process development. Biomaterials, vol. 22, no 13, p. 1721-1730, 2001.
[39] JILLAVENKATESA, A. et CONDRATE SR, R. A. Sol–gel processing of hydroxyapatite. Journal of materials science, vol. 33, no 16, p. 4111-4119, 1998.
[40] LIVAGE, J., BARBOUX, Ph, VANDENBORRE, M. T., et al. Sol-gel synthesis of phosphates. Journal of non-crystalline solids, vol. 147, p. 18-23, 1992.
[41]. RAO, R. Ramachandra, ROOPA, H. N., et KANNAN, T. S. Solid state synthesis and thermal stability of HAP and HAP–β-TCP composite ceramic powders. Journal of Materials Science: Materials in Medicine, vol. 8, no 8, p. 511-518, 1997.
[42] LAZIĆ, S., KATANIĆ-POPOVIĆ, J., ZEC, Slavica, et al. Properties of hydroxyapatite crystallized from high temperature alkaline solutions. Journal of Crystal Growth, vol. 165, no 1-2, p. 124-128, 1996.
[43] CABANES, Frédéric. Déphosphatation des effluents: Précipitation et valorisation du phosphore. Thèse de doctorat, 2006.

[44] OKTAR, F. N. Microstructure and mechanical properties of sintered enamel hydroxyapatite. Ceramics international, vol. 33, no 7, p. 1309-1314, 2007.
[45] ELLIOTT, J. C., WILSON, R. M., et DOWKER, S. E. P. Apatite structures. Advances in X-ray Analysis, vol. 45, p. 172-181, 2002.
[46] EANES, E. D. Enamel apatite: chemistry, structure and properties. Journal of Dental Research, vol. 58, no 2_suppl, p. 829-836, 1979.
[47] KAY, Me I., YOUNG, R. A., et POSNER, A. S. Crystal structure of hydroxyapatite. Nature, vol. 204, no 4963, p. 1050-1052, 1964.
[48] SCHMITT, Michel. Contribution a l'elaboration de nouveaux materiaux biphases en phosphates de calcium (doctorat: chimie des biomateriaux). Thèse de doctorat. Nantes, 2000.
[49] GARCIA, Sarah Diallo. Les Hydroxyapatites, un système basique atypique modulable par la synthèse: vers l'identification des sites actifs. Thèse de doctorat. Université Pierre et Marie Curie-Paris VI, 2012.
[50] GOODSHIP, A. E., CUNNINGHAM, J. L., OGANOV, V., et al. Bone loss during long term space flight is prevented by the application of a short term impulsive mechanical stimulus. Acta astronautica, vol. 43, no 3-6, p. 65-75, 1998.
[51] SETO, H., AOKI, K., KASUGAI, S., et al. Trabecular bone turnover, bone marrow cell development, and gene expression of bone matrix proteins after low calcium feeding in rats. Bone, vol. 25, no 6, p. 687-695, 1999.
[52] SODEK, K. L., TUPY, J. H., SODEK, J., et al. Relationships between bone protein and mineral in developing porcine long bone and calvaria. Bone, vol. 26, no 2, p. 189-198, 2000.
[53] SU, X., SUN, K., CUI, F. Z., et al. Organization of apatite crystals in human woven bone. Bone, vol. 32, no 2, p. 150-162, 2003.
[54] HELLMICH, Christian, ULM, Franz-Josef, et DORMIEUX, Luc. Can the diverse elastic properties of trabecular and cortical bone be attributed to only a few tissue-independent phase properties and their interactions?. Biomechanics and modeling in mechanobiology, vol. 2, no 4, p. 219-238, 2004.
[55] RHO, Jae-Young, KUHN-SPEARING, Liisa, et ZIOUPOS, Peter. Mechanical properties and the hierarchical structure of bone. Medical engineering & physics, vol. 20, no 2, p. 92-102, 1998.
[56] PALMER, Liam C., NEWCOMB, Christina J., KALTZ, Stuart R., et al. Biomimetic systems for hydroxyapatite mineralization inspired by bone and enamel. Chemical reviews, vol. 108, no 11, p. 4754-4783, 2008.
[57] KUSMANTO, Febe, WALKER, G., GAN, Q., et al. Development of composite tissue scaffolds containing naturally sourced mircoporous hydroxyapatite. Chemical Engineering Journal, vol. 139, no 2, p. 398-407, 2008.
[58] MURUGAN, R. et RAMAKRISHNA, S. Production of ultra-fine bioresorbable carbonated hydroxyapatite. Acta Biomaterialia, vol. 2, no 2, p. 201-206, 2006.
[59] CHEN, Liang, MCCRATE, Joseph M., LEE, James CM, et al. The role of surface charge on the uptake and biocompatibility of hydroxyapatite nanoparticles with osteoblast cells. Nanotechnology, vol. 22, no 10, p. 105708, 2011.
[60] ZHOU, Hongjian et LEE, Jaebeom. Nanoscale hydroxyapatite particles for bone tissue engineering. Acta biomaterialia, vol. 7, no 7, p. 2769-2781, 2011.
[61] LU, Xiong et LENG, Yang. Theoretical analysis of calcium phosphate precipitation in simulated body fluid. Biomaterials, vol. 26, no 10, p. 1097-1108, 2005.
[62] SAKAI, Susumu, ANADA, Takahisa, TSUCHIYA, Kaori, et al. Comparative study on the resorbability and dissolution behavior of octacalcium phosphate, β-tricalcium phosphate, and hydroxyapatite under physiological conditions. Dental Materials Journal, vol. 35, no 2, p. 216-224, 2016.
[63] HASSAN, Mohamad Nageeb, MAHMOUD, Morsi Mohamed, ABD EL-FATTAH, Ahmed, et al. Microwave-assisted preparation of Nano-hydroxyapatite for bone substitutes. Ceramics International, vol. 42, no 3, p. 3725-3744, 2016.
[64] LI, Ming, WANG, Yanbo, LIU, Qian, et al. In situ synthesis and biocompatibility of nano hydroxyapatite on pristine and chitosan functionalized graphene oxide. Journal of Materials Chemistry B, vol. 1, no 4, p. 475-484, 2013.

[65] MONDAL, Sudip, HOANG, Giang, MANIVASAGAN, Panchanathan, et al. Nano-hydroxyapatite bioactive glass composite scaffold with enhanced mechanical and biological performance for tissue engineering application. Ceramics International, vol. 44, no 13, p. 15735-15746, 2018.
[66] IGNJATOVIĆ, Nenad, WU, Victoria, AJDUKOVIĆ, Zorica, et al. Chitosan-PLGA polymer blends as coatings for hydroxyapatite nanoparticles and their effect on antimicrobial properties, osteoconductivity and regeneration of osseous tissues. Materials Science and Engineering: C, vol. 60, p. 357-364, 2016.
[67] SINGH, Sushma, PAL, Abhisek, et MOHANTY, Sangeeta. Nano Structure of Hydroxyapatite and its modern approach in Pharmaceutical Science. Research Journal of Pharmacy and Technology, vol. 12, no 3, p. 1463-1472, 2019.
[68] RAMESH, Niranjan, MORATTI, Stephen C., et DIAS, George J. Hydroxyapatite–polymer biocomposites for bone regeneration: A review of current trends. Journal of Biomedical Materials Research Part B: Applied Biomaterials, vol. 106, no 5, p. 2046-2057, 2018.
[69] YANG, Guo-li, HE, Fu-ming, HU, Ji-an, et al. Effects of biomimetically and electrochemically deposited nano-hydroxyapatite coatings on osseointegration of porous titanium implants. Oral Surgery, Oral Medicine, Oral Pathology, Oral Radiology, and Endodontology, vol. 107, no 6, p. 782-789, 2009.
[70] RODRIGUES, Bruno VM, LEITE, Nelly CS, DAS NEVES CAVALCANTI, Bruno, et al. Graphene oxide/multi-walled carbon nanotubes as nanofeatured scaffolds for the assisted deposition of nanohydroxyapatite: characterization and biological evaluation. International journal of nanomedicine, vol. 11, p. 2569, 2016.
[71] HUANG, Di, XU, Mengjie, NIU, Lulu, et al. In situ biomimetic formation of nano-hydroxyapatite crystals on chitosan microspheres. Polymers for Advanced Technologies, 2020, vol. 31, no 1, p. 36-43.
[72] NIE, Wei, PENG, Cheng, ZHOU, Xiaojun, et al. Three-dimensional porous scaffold by self-assembly of reduced graphene oxide and nano-hydroxyapatite composites for bone tissue engineering. Carbon, vol. 116, p. 325-337, 2017.
[73] HRUSCHKA, Veronika, TANGL, Stefan, RYABENKOVA, Yulia, et al. Comparison of nanoparticular hydroxyapatite pastes of different particle content and size in a novel scapula defect model. Scientific reports, vol. 7, no 1, p. 1-11, 2017.
[74] HSU, Hsueh-Chuan, WU, Shih-Ching, HSU, Shih-Kuang, et al. Bone-like nano-hydroxyapatite coating on low-modulus Ti–5Nb–5Mo alloy using hydrothermal and post-heat treatments. Thin Solid Films, vol. 687, p. 137463, 2019.
[75] BAYANI, Mojtaba, TORABI, Sepehr, SHAHNAZ, Aysan, et al. Main properties of nanocrystalline hydroxyapatite as a bone graft material in treatment of periodontal defects. A review of literature. Biotechnology & Biotechnological Equipment, vol. 31, no 2, p. 215-220, 2017.
[76] CHANG, Hao-Chieh, YANG, Connie, FENG, Fang, et al. Bone morphogenetic protein-2 loaded poly (D, L-lactide-co-glycolide) microspheres enhance osteogenic potential of gelatin/hydroxyapatite/β-tricalcium phosphate cryogel composite for alveolar ridge augmentation. Journal of the Formosan Medical Association, vol. 116, no 12, p. 973-981, 2017.
[77] HANAFY, Ahmed Khaled, SHINAISHIN, Souzy F., ELDEEN, Ghada Nour, et al. Nano Hydroxyapatite & Mineral Trioxide Aggregate Efficiently Promote Odontogenic Differentiation of Dental Pulp Stem Cells. Open access Macedonian journal of medical sciences, vol. 6, no 9, p. 1727, 2018.
[78] MAJHOOLL, Alhussein Arkan, ZAINOL, Ismail, JAAFAR, Che Nor Aiza, et al. A Brief Review on Biomedical Applications of Hydroxyapatite Use as Fillers in Polymer. J. Chem, vol. 13, p. 112-119, 2019.
[79] DA SILVA, Ranna CaStRo, DE MELO ALENCAR, CRiStiane, SILVA, BeatRiz Helena RoDRigueS, et al. A Clinical, Randomised, Double-Blind Study on the Use of Nano-Hydroxyapatite and Arginine During at-Home Tooth Bleaching. Journal of Clinical & Diagnostic Research, vol. 12, no 12, 2018.
[80] ESTEVES-OLIVEIRA, M., SANTOS, N. M., MEYER-LÜCKEL, Hendrik, et al. Caries-preventive effect of anti-erosive and nano-hydroxyapatite-containing toothpastes in vitro. Clinical oral investigations, vol. 21, no 1, p. 291-300, 2017.
[81] MANCHERY, Nithin, JOHN, Joseph, NAGAPPAN, Nagappan, et al. Remineralization potential of dentifrice containing nanohydroxyapatite on artificial carious lesions of enamel: A comparative in vitro study. Dental research journal, vol. 16, no 5, p. 310, 2019.

[82] LIU, Ying, TANG, Yuxia, WU, Jiang, et al. Facile synthesis of biodegradable flower-like hydroxyapatite for drug and gene delivery. Journal of Colloid and Interface Science, 2020.
[83] ZHAO, Lina, ZHAO, Wenhui, LIU, Ye, et al. Nano-hydroxyapatite-derived drug and gene co-delivery system for anti-angiogenesis therapy of breast cancer. Medical Science Monitor: International Medical Journal of Experimental and Clinical Research, vol. 23, p. 4723, 2017.
[84] WANG, Shengrui, ZHANG, Le, CHEN, Wendy, et al. Rapid regeneration of enamel-like-oriented inorganic crystals by using rotary evaporation. Materials Science and Engineering: C, p. 111141, 2020.
[85] HAN, S. X., NING, Z. W., CHEN, K., et al. Preparation and tribological properties of Fe-hydroxyapatite bioceramics. Biosurface and Biotribology, vol. 3, no 2, p. 75-81, 2017.
[86] HABIBAH, Tutut Ummul et SALISBURY, Herb G. Hydroxyapatite dental material. In : StatPearls [Internet]. StatPearls Publishing, 2019.
[87] LIU, Naiqiang, AI, Fei, WANG, Weikun, et al. Nano-hydroxyapatite as an Efficient Polysulfide Absorbent for High-performance Li-S Batteries. Electrochimica Acta, vol. 215, p. 162-170, 2016.
[88] LI, Heng, WU, Dabei, WU, Jin, et al. Flexible, high-wettability and fire-resistant separators based on hydroxyapatite nanowires for advanced lithium-ion batteries. Advanced Materials, vol. 29, no 44, p. 1703548, 2017.
[89] YANG, Chun-Chen, LI, Yingjeng James, CHIU, Shwu-Jer, et al. A direct borohydride fuel cell based on poly (vinyl alcohol)/hydroxyapatite composite polymer electrolyte membrane. Journal of power sources, vol. 184, no 1, p. 95-98, 2008.
[90] PICCIRILLO, C. et CASTRO, P. M. L. Calcium hydroxyapatite-based photocatalysts for environment remediation: Characteristics, performances and future perspectives. Journal of environmental management, vol. 193, p. 79-91, 2017.
[91] NASR-ESFAHANI, Mojtaba et FEKRI, Sahar. Alumina/TiO2/hydroxyapatite interface nanostructure composite filters as efficient photocatalysts for the purification of air. Reaction Kinetics, Mechanisms and Catalysis, vol. 107, no 1, p. 89-103, 2012.
[92] OCHANDO-PULIDO, Javier Miguel, STOLLER, Marco, DI PALMA, Luca, et al. Spinning Disk Reactor Technology in Photocatalysis: Nanostructured Catalysts Intensified Production and Applications. In : Nanophotocatalysis and Environmental Applications. Springer, Cham, p. 303-333, 2019.
[93] NAYAK, Bishnupriya, SAMANT, Amruta, MISRA, Pramila K., et al. Nanocrystalline hydroxyapatite: a potent material for adsorption, biological and catalytic studies. Materials Today: Proceedings, vol. 9, p. 689-698, 2019.
[94]. KHAN, Sana et MALIK, Abdul. Environmental and health effects of textile industry wastewater. In : Environmental deterioration and human health. Springer, Dordrecht, p. 55-71, 2014.
[95] CHEN, Zhenzhen, LIU, Yiling, MAO, Lianzhen, et al. Effect of cation doping on the structure of hydroxyapatite and the mechanism of defluoridation. Ceramics International, vol. 44, no 6, p. 6002-6009, 2018.
[96] JIA, Jinping, YANG, Ji, LIAO, Jun, et al. Treatment of dyeing wastewater with ACF electrodes. Water Research, vol. 33, no 3, p. 881-884, 1999.
[97] XIAO, Senbo, STACKLIES, Wolfram, CETINKAYA, Murat, et al. Mechanical response of silk crystalline units from force-distribution analysis. Biophysical journal, vol. 96, no 10, p. 3997-4005, 2009.
[98] GUAN, Yebin, CAO, Weicheng, WANG, Xiaohong, et al. Hydroxyapatite nano-rods for the fast removal of congo red dye from aqueous solution. Materials Research Express, vol. 5, no 6, p. 065053, 2018.
[99] CIOBANU, Gabriela, HARJA, Maria, RUSU, Lacramioara, et al. Acid Black 172 dye adsorption from aqueous solution by hydroxyapatite as low-cost adsorbent. Korean Journal of Chemical Engineering, vol. 31, no 6, p. 1021-1027, 2014.
[100] EL-ZAHHAR, Adel A. et AWWAD, Nasser S. Removal of malachite green dye from aqueous solutions using organically modified hydroxyapatite. Journal of environmental chemical engineering, vol. 4, no 1, p. 633-638, 2016.
[101] REYNARD, Bruno, LÉCUYER, Christophe, et GRANDJEAN, Patricia. Crystal-chemical controls on rare-earth element concentrations in fossil biogenic apatites and implications for paleoenvironmental reconstructions. Chemical Geology, vol. 155, no 3-4, p. 233-241, 1999.

[102] POLLARD, A. Mark et HERON, Carl. Preface to Second Edition. In : Archaeological Chemistry.p. P009-P010, 2008.
[103] ROCHE, Damien, SÉGALEN, Loïc, BALAN, Etienne, et al. Preservation assessment of Miocene–Pliocene tooth enamel from Tugen Hills (Kenyan Rift Valley) through FTIR, chemical and stable-isotope analyses. Journal of Archaeological Science, vol. 37, no 7, p. 1690-1699, 2010.
[104] SUZUKI, Takashi, HATSUSHIKA, Toshiaki, et HAYAKAWA, Yasumasa. Synthetic hydroxyapatites employed as inorganic cation-exchangers. Journal of the Chemical Society, Faraday Transactions 1: Physical Chemistry in Condensed Phases, vol. 77, no 5, p. 1059-1062, 1981.
[105] SCHUBERT, Sven et FREITAG, Ruth. Comparison of ceramic hydroxy-and fluoroapatite versus Protein A/G-based resins in the isolation of a recombinant human antibody from cell culture supernatant. Journal of Chromatography A, vol. 1142, no 1, p. 106-113, 2007.
[106] DATTOLO, Laura, KELLER, Emily L., et CARTA, Giorgio. pH Transients in hydroxyapatite chromatography columns—effects of operating conditions and media properties. Journal of Chromatography A, vol. 1217, no 48, p. 7573-7578, 2010.
[107] OPRE, Z., GRUNWALDT, J.-D., MALLAT, T., et al. Selective oxidation of alcohols with oxygen on Ru–Co-hydroxyapatite: A mechanistic study. Journal of Molecular Catalysis A: Chemical, vol. 242, no 1-2, p. 224-232, 2005.
[108] JUN, Jin Hyuk, LIM, Tae Hoon, NAM, Suk-Woo, et al. Mechanism of partial oxidation of methane over a nickel-calcium hydroxyapatite catalyst. Applied Catalysis A: General, vol. 312, p. 27-34, 2006.
[109] VENUGOPAL, Akula et SCURRELL, Mike S. Hydroxyapatite as a novel support for gold and ruthenium catalysts: Behaviour in the water gas shift reaction. Applied Catalysis A: General, vol. 245, no 1, p. 137-147, 2003.
[110] SEBTI, Saïd, TAHIR, Rachid, NAZIH, Rachid, et al. Comparison of different Lewis acid supported on hydroxyapatite as new catalysts of Friedel–Crafts alkylation. Applied Catalysis A: General, vol. 218, no 1-2, p. 25-30, 2001.
[111] SMAHI, Abdellatif, SOLHY, Abderrahim, EL BADAOUI, Hanane, et al. Potassium fluoride doped fluorapatite and hydroxyapatite as new catalysts in organic synthesis. Applied Catalysis A: General, vol. 250, no 1, p. 151-159, 2003.
[112] MORIN-CRINI, Nadia, LICHTFOUSE, Eric, TORRI, Giangiacomo, et al. Applications of chitosan in food, pharmaceuticals, medicine, cosmetics, agriculture, textiles, pulp and paper, biotechnology, and environmental chemistry. Environmental Chemistry Letters, p. 1-26, 2019.
[113] SAMUELS, Robert Joel. Solid state characterization of the structure of chitosan films. Journal of polymer science: polymer physics edition, vol. 19, no 7, p. 1081-1105, 1981.
[114] SANTOS, Vanessa P., MARQUES, Nathália SS, MAIA, Patrícia CSV, et al. Seafood Waste as Attractive Source of Chitin and Chitosan Production and Their Applications. International Journal of Molecular Sciences, vol. 21, no 12, p. 4290, 2020.
[115] BATISTA, Anabelle Camarotti de Lima, SOUZA NETO, Francisco Ernesto de, et PAIVA, Weslley de Souza. Review of fungal chitosan: past, present and perspectives in Brazil. Polímeros, vol. 28, no 3, p. 275-283, 2018.
[116] ARANAZ, Inmaculada, MENGÍBAR, Marian, HARRIS, Ruth, et al. Functional characterization of chitin and chitosan. Current chemical biology, vol. 3, no 2, p. 203-230, 2009.
[117] YADAV, Monika, GOSWAMI, Priynshi, PARITOSH, Kunwar, et al. Seafood waste: a source for preparation of commercially employable chitin/chitosan materials. Bioresources and Bioprocessing, vol. 6, no 1, p. 8, 2019.
[118] FABRITIUS, Helge, SACHS, C., RAABE, D., et al. Chitin in the exoskeletons of arthropoda: From ancient design to novel materials science. In : Chitin. Springer, Dordrecht, p. 35-60, 2011.
[119] LIMAM, Zouhour, SELMI, Salah, SADOK, Saloua, et al. Extraction and characterization of chitin and chitosan from crustacean by-products: Biological and physicochemical properties. African journal of biotechnology, vol. 10, no 4, p. 640-647, 2011.

[120] CONDRON, Leo, STARK, Christine, O'CALLAGHAN, Maureen, et al. The role of microbial communities in the formation and decomposition of soil organic matter. In : Soil microbiology and sustainable crop production. Springer, Dordrecht, p. 81-118, 2010.
[121] JAYATHILAKAN, K., SULTANA, Khudsia, RADHAKRISHNA, K., et al. Utilization of byproducts and waste materials from meat, poultry and fish processing industries: a review. Journal of food science and technology, vol. 49, no 3, p. 278-293, 2012.
[122] HAMED, Imen, ÖZOGUL, Fatih, et REGENSTEIN, Joe M. Industrial applications of crustacean by-products (chitin, chitosan, and chitooligosaccharides): A review. Trends in food science & technology, vol. 48, p. 40-50, 2016.
[123] YOUNES, Islem et RINAUDO, Marguerite. Chitin and chitosan preparation from marine sources. Structure, properties and applications. Marine drugs, vol. 13, no 3, p. 1133-1174, 2015.
[124] BAXTER, Shari, ZIVANOVIC, Svetlana, et WEISS, Jochen. Molecular weight and degree of acetylation of high-intensity ultrasonicated chitosan. Food Hydrocolloids, vol. 19, no 5, p. 821-830, 2005.
[125] MAHMOUD, Nesreen S., GHALY, Abdel E., et ARAB, Fereshteh. Unconventional approach for demineralization of deproteinized crustacean shells for chitin production. Am. J. Biochem. Biotechnol, vol. 3, no 1, p. 1-9, 2007.
[126] SMITH, J. Keaton, MOSHREF, Abteen R., JENNINGS, Jessica A., et al. Chitosan sponges for local synergistic infection therapy: a pilot study. Clinical Orthopaedics and Related Research®, vol. 471, no 10, p. 3158-3164, 2013.
[127] ARBIA, Wassila, ARBIA, Leila, ADOUR, Lydia, et al. Chitin extraction from crustacean shells using biological methods–a review. Food Technology and Biotechnology, vol. 51, no 1, p. 12-25, 2013.
[128] KAUR, Surinder et DHILLON, Gurpreet Singh. Recent trends in biological extraction of chitin from marine shell wastes: a review. Critical reviews in biotechnology, vol. 35, no 1, p. 44-61, 2015.
[129] YOUNES, Islem, GHORBEL-BELLAAJ, Olfa, NASRI, Rim, et al. Chitin and chitosan preparation from shrimp shells using optimized enzymatic deproteinization. Process Biochemistry, vol. 47, no 12, p. 2032-2039, 2012.
[130] HAARD, N. F., FELTHAM, L. A. W., HELBIG, N., et al. Modification of proteins with proteolytic enzymes from the marine environment.
[131] BAIANO, Antonietta. Recovery of biomolecules from food wastes—a review. Molecules, vol. 19, no 9, p. 14821-14842, 2014.
[132] BHATNAGAR, Sonal et KUMARI, Reeta. Bioremediation: a sustainable tool for environmental management–a review. Annual Research & Review in Biology, p. 974-993, 2013.
[133] PHROMRAKSA, Panthitra, NAGANO, Hiroko, KANAMARU, Yoshihiro, et al. Characterization of Bacillus subtilis isolated from Asian fermented foods. Food science and technology research, vol. 15, no 6, p. 659-666, 2009.
[134] MEENA, Pukhraj, TRIPATHI, Abhishek Dutt, SRIVASTAVA, S. K., et al. Utilization of agro-industrial waste (wheat bran) for alkaline protease production by Pseudomonas aeruginosa in SSF using Taguchi (DOE) methodology. Biocatalysis and Agricultural Biotechnology, vol. 2, no 3, p. 210-216, 2013.
[135] HUGH, R. et RYSCHENKOW, Ewdokia. Pseudomonas maltophilia, an alcaligenes-like species. Microbiology, vol. 26, no 1, p. 123-132, 1961.
[136] JUNG, W. J., JO, G. H., KUK, J. H., et al. Production of chitin from red crab shell waste by successive fermentation with Lactobacillus paracasei KCTC-3074 and Serratia marcescens FS-3. Carbohydrate Polymers, vol. 68, no 4, p. 746-750, 2007.
[137] GUIBAL, Eric. Interactions of metal ions with chitosan-based sorbents: a review. Separation and purification technology, vol. 38, no 1, p. 43-74, 2004.
[138] THARANATHAN, Rudrapatnam N. et KITTUR, Farooqahmed S. Chitin—the undisputed biomolecule of great potential. 2003.
[139] PENICHE, C., ARGÜELLES-MONAL, W., et GOYCOOLEA, F. M. Chitin and chitosan: major sources, properties and applications. In : Monomers, polymers and composites from renewable resources. Elsevier, p. 517-542, 2008.

[140] LOPES, SELMA A., VEIGA, ITIARA G., et MORAES, ÂNGELA M. Desenvolvimento de dispositivo de quitosana e xantana para a liberação tópica ou em tecidos moles de indometacina. Blucher Chemical Engineering Proceedings, vol. 1, no 2, p. 13205-13212, 2015.
[141] JAYAKUMAR, R., PRABAHARAN, M., NAIR, S. V., et al. Novel carboxymethyl derivatives of chitin and chitosan materials and their biomedical applications. Progress in Materials Science, vol. 55, no 7, p. 675-709, 2010.
[142] KUMARASWAMY, R. V., KUMARI, Sarita, CHOUDHARY, Ram Chandra, et al. Engineered chitosan based nanomaterials: bioactivities, mechanisms and perspectives in plant protection and growth. International journal of biological macromolecules, vol. 113, p. 494-506, 2018.
[143] MORGANTI, Pierfrancesco et COLTELLI, Maria-Beatrice. A new carrier for advanced cosmeceuticals. Cosmetics, vol. 6, no 1, p. 10, 2019.
[144] FALCONER, K. E. Managing diffuse environmental contamination from agricultural pesticides: an economic perspective on issues and policy options, with particular reference to Europe. Agriculture, ecosystems & environment, vol. 69, no 1, p. 37-54, 1998.
[145] DUHAN, Joginder Singh, KUMAR, Ravinder, KUMAR, Naresh, et al. Nanotechnology: The new perspective in precision agriculture. Biotechnology Reports, vol. 15, p. 11-23, 2017.
[146] ROSETI, Livia, PARISI, Valentina, PETRETTA, Mauro, et al. Scaffolds for bone tissue engineering: state of the art and new perspectives. Materials Science and Engineering: C, vol. 78, p. 1246-1262, 2017.
[147] IKADA, Yoshito. Challenges in tissue engineering. Journal of the Royal Society Interface, vol. 3, no 10, p. 589-601, 2006.
[148] KARANDE, Tejas S., ONG, Joo L., et AGRAWAL, C. Mauli. Diffusion in musculoskeletal tissue engineering scaffolds: design issues related to porosity, permeability, architecture, and nutrient mixing. Annals of biomedical engineering, vol. 32, no 12, p. 1728-1743, 2004.
[149] BARANWAL, Anupriya, KUMAR, Ashutosh, PRIYADHARSHINI, A., et al. Chitosan: an undisputed bio-fabrication material for tissue engineering and bio-sensing applications. International Journal of Biological Macromolecules, vol. 110, p. 110-123, 2018.
[150] KONG, Ming, CHEN, Xi Guang, XING, Ke, et al. Antimicrobial properties of chitosan and mode of action: a state of the art review. International journal of food microbiology, vol. 144, no 1, p. 51-63, 2010.
[151] AHSAN, Saad M., THOMAS, Mathai, REDDY, Kranthi K., et al. Chitosan as biomaterial in drug delivery and tissue engineering. International journal of biological macromolecules, vol. 110, p. 97-109, 2018.
[152] CASETTARI, Luca, VLLASALIU, Driton, CASTAGNINO, Enzo, et al. PEGylated chitosan derivatives: Synthesis, characterizations and pharmaceutical applications. Progress in Polymer Science, vol. 37, no 5, p. 659-685, 2012.
[153] JIA, Zhishen, XU, Weiliang, et al. Synthesis and antibacterial activities of quaternary ammonium salt of chitosan. Carbohydrate research, vol. 333, no 1, p. 1-6, 2001.
[154] HU, Ying, DU, Yumin, YANG, Jianhong, et al. Synthesis, characterization and antibacterial activity of guanidinylated chitosan. Carbohydrate polymers, vol. 67, no 1, p. 66-72, 2007.
[155] RIVA, Raphaël, RAGELLE, Heloise, DES RIEUX, Anne, et al. Chitosan and chitosan derivatives in drug delivery and tissue engineering. In : Chitosan for biomaterials II. Springer, Berlin, Heidelberg, p. 19-44, 2011.
[156] GUO, Zhong, XING, Ronge, LIU, Song, et al. Synthesis and hydroxyl radicals scavenging activity of quaternized carboxymethyl chitosan. Carbohydrate Polymers, vol. 73, no 1, p. 173-177, 2008.
[157] IMRAN, Mohd, SAJWAN, Meenakshi, ALSUWAYT, Bader, et al. Synthesis, characterization and anticoagulant activity of chitosan derivatives. Saudi Pharmaceutical Journal, vol. 28, no 1, p. 25-32, 2020.
[158] RAAFAT, Dina et SAHL, Hans-Georg. Chitosan and its antimicrobial potential–a critical literature survey. Microbial biotechnology, vol. 2, no 2, p. 186-201, 2009.
[159] KROEMER, Guido, GALLUZZI, Lorenzo, et BRENNER, Catherine. Mitochondrial membrane permeabilization in cell death. Physiological reviews, vol. 87, no 1, p. 99-163, 2007.
[160] VINSOVA, Jarmila et VAVRIKOVA, Eva. Chitosan derivatives with antimicrobial, antitumour and antioxidant activities-a review. Current pharmaceutical design, vol. 17, no 32, p. 3596-3607, 2011.

[161] ZIVANOVIC, S., BASURTO, C. C., CHI, S., et al. Molecular weight of chitosan influences antimicrobial activity in oil-in-water emulsions. Journal of food protection, vol. 67, no 5, p. 952-959, 2004.
[162] HOSSEINNEJAD, Mahmoud et JAFARI, Seid Mahdi. Evaluation of different factors affecting antimicrobial properties of chitosan. International journal of biological macromolecules, vol. 85, p. 467-475, 2016.
[163] YOUNES, Islem, SELLIMI, Sabrine, RINAUDO, Marguerite, et al. Influence of acetylation degree and molecular weight of homogeneous chitosans on antibacterial and antifungal activities. International journal of food microbiology, vol. 185, p. 57-63, 2014.
[164] KUMAR, Santosh, KOH, Joonseok, KIM, Hyerim, et al. A new chitosan–thymine conjugate: Synthesis, characterization and biological activity. International journal of biological macromolecules, vol. 50, no 3, p. 493-502, 2012.
[165] RABEA, Entsar I., BADAWY, Mohamed E.-T., STEVENS, Christian V., et al. Chitosan as antimicrobial agent: applications and mode of action. Biomacromolecules, vol. 4, no 6, p. 1457-1465, 2003.
[166] XING, Ke, ZHU, Xiao, PENG, Xue, et al. Chitosan antimicrobial and eliciting properties for pest control in agriculture: a review. Agronomy for Sustainable Development, vol. 35, no 2, p. 569-588, 2015.
[167] DUTTA, P. K., TRIPATHI, Shipra, MEHROTRA, G. K., et al. Perspectives for chitosan based antimicrobial films in food applications. Food chemistry, vol. 114, no 4, p. 1173-1182, 2009.
[168] TRIPATHI, Shipra, MEHROTRA, G. K., et DUTTA, P. K. Chitosan based antimicrobial films for food packaging applications. e-Polymers, vol. 8, no 1, 2008.
[169] TURNER, R. Kerry, GEORGIOU, Stavros, CLARK, Rebecca, et al. Economic valuation of water resources in agriculture: From the sectoral to a functional perspective of natural resource management. Food & Agriculture Org., 2004.
[170] KANU, Ijeoma, ACHI, O. K., et al. Industrial effluents and their impact on water quality of receiving rivers in Nigeria. Journal of applied technology in environmental sanitation, vol. 1, no 1, p. 75-86, 2011.
[171] ZEMNUKHOVA, L., KHARCHENKO, U., et BELENEVA, I. Biomass derived silica containing products for removal of microorganisms from water. International journal of environmental science and technology, vol. 12, no 5, p. 1495-1502, 2015.
[172] AL-MANHEL, Alaa Jabbar, AL-HILPHY, Asaad Rehman Saeed, et NIAMAH, Alaa Kareem. Extraction of chitosan, characterisation and its use for water purification. Journal of the Saudi Society of Agricultural Sciences, vol. 17, no 2, p. 186-190, 2018.
[173] SEWVANDI, G. A. et ADIKARY, S. U. Removal of heavy metals from wastewater using chitosan. 2011.
[174] JAMIL, S. M., ALI, M. W., RIPIN, A., et al. Metals removal from recovered base oil using chitosan biopolymers. Journal of Applied Sciences(Faisalabad), vol. 10, no 21, p. 2725-2728, 2010.
[175] HOSSEINNEJAD, Mahmoud et JAFARI, Seid Mahdi. Evaluation of different factors affecting antimicrobial properties of chitosan. International journal of biological macromolecules, vol. 85, p. 467-475, 2016.
[176] CRINI, Gregorio et BADOT, Pierre-Marie. Application of chitosan, a natural aminopolysaccharide, for dye removal from aqueous solutions by adsorption processes using batch studies: A review of recent literature. Progress in polymer science, vol. 33, no 4, p. 399-447, 2008.
[177] NO, H. K., MEYERS, Samuel P., PRINYAWIWATKUL, Witoon, et al. Applications of chitosan for improvement of quality and shelf life of foods: a review. Journal of food science, vol. 72, no 5, p. R87-R100, 2007.
[178]. ZARGAR, Vida, ASGHARI, Morteza, et DASHTI, Amir. A review on chitin and chitosan polymers: structure, chemistry, solubility, derivatives, and applications. ChemBioEng Reviews, vol. 2, no 3, p. 204-226, 2015.
[179] KUMAR, Majeti NV Ravi. A review of chitin and chitosan applications. Reactive and functional polymers, vol. 46, no 1, p. 1-27, 2000.
[180] SORIA, Ana Cristina et VILLAMIEL, Mar. Effect of ultrasound on the technological properties and bioactivity of food: a review. Trends in food science & technology, vol. 21, no 7, p. 323-331, 2010.

[181] NO, H. K., MEYERS, Samuel P., PRINYAWIWATKUL, Witoon, et al. Applications of chitosan for improvement of quality and shelf life of foods: a review. Journal of food science, vol. 72, no 5, p. R87-R100, 2007.
[182] NIEDERHOFER, Andreas et MÜLLER, Bernd W. A method for direct preparation of chitosan with low molecular weight from fungi. European Journal of Pharmaceutics and Biopharmaceutics, vol. 57, no 1, p. 101-105, 2004.
[183] HADWIGER, Lee A., OGAWA, Tomoya, KUYAMA, Hiroki, et al. Chitosan polymer sizes effective in inducing phytoalexin accumulation and fungal suppression are verified with synthesized oligomers. MPMI-Molecular Plant Microbe Interactions, vol. 7, no 4, p. 531-533, 1994.
[184] SKJÅK-BRÆK, Gudmund, ANTHONSEN, Thorleif, et SANDFORD, Paul (ed.). Chitin and chitosan. London : Elsevier applied science, 1989.
[185] NO, H. K., MEYERS, Samuel P., PRINYAWIWATKUL, Witoon, et al. Applications of chitosan for improvement of quality and shelf life of foods: a review. Journal of food science, vol. 72, no 5, p. R87-R100, 2007.
[186] VELICKOVA, Elena, WINKELHAUSEN, Eleonora, KUZMANOVA, Slobodanka, et al. Impact of chitosan-beeswax edible coatings on the quality of fresh strawberries (Fragaria ananassa cv Camarosa) under commercial storage conditions. LWT-Food Science and Technology, vol. 52, no 2, p. 80-92, 2013.
[187] HERNÁNDEZ-MUÑOZ, Pilar, ALMENAR, Eva, OCIO, María José, et al. Effect of calcium dips and chitosan coatings on postharvest life of strawberries (Fragaria x ananassa). Postharvest Biology and Technology, vol. 39, no 3, p. 247-253, 2006.
[188] NO, H. K., MEYERS, Samuel P., PRINYAWIWATKUL, Witoon, et al. Applications of chitosan for improvement of quality and shelf life of foods: a review. Journal of food science, vol. 72, no 5, p. R87-R100, 2007.
[189] YANG, W., FORTUNATI, E., BERTOGLIO, Federico, et al. Polyvinyl alcohol/chitosan hydrogels with enhanced antioxidant and antibacterial properties induced by lignin nanoparticles. Carbohydrate polymers, vol. 181, p. 275-284, 2018.
[190] PAI, Shraddha, KINI, M. Srinivas, et SELVARAJ, Raja. A review on adsorptive removal of dyes from wastewater by hydroxyapatite nanocomposites. Environmental Science and Pollution Research, p. 1-15, 2019.
[191] NGAH, WS Wan, TEONG, L. C., et HANAFIAH, M. A. K. M. Adsorption of dyes and heavy metal ions by chitosan composites: A review. Carbohydrate polymers, vol. 83, no 4, p. 1446-1456, 2011.
[192] SIRIPATRAWAN, Ubonrat et VITCHAYAKITTI, Wara. Improving functional properties of chitosan films as active food packaging by incorporating with propolis. Food Hydrocolloids, vol. 61, p. 695-702, 2016.
[193] DUAN, Chao, MENG, Xin, MENG, Jingru, et al. Chitosan as a preservative for fruits and vegetables: a review on chemistry and antimicrobial properties. Journal of Bioresources and Bioproducts, vol. 4, no 1, p. 11-21, 2019.
[194] MAHATO, Neelima, SHARMA, Kavita, KOTESWARARAO, Rakoti, et al. Citrus essential oils: Extraction, authentication and application in food preservation. Critical reviews in food science and nutrition, vol. 59, no 4, p. 611-625, 2019.
[195] MUJTABA, Muhammad, MORSI, Rania E., KERCH, Garry, et al. Current advancements in chitosan-based film production for food technology; A review. International journal of biological macromolecules, vol. 121, p. 889-904, 2019.
[196] CORREA-PACHECO, Zormy Nacary, BAUTISTA-BAÑOS, Silvia, DE LORENA RAMOS-GARCÍA, Margarita, et al. Physicochemical characterization and antimicrobial activity of edible propolis-chitosan nanoparticle films. Progress in Organic Coatings, vol. 137, p. 105326, 2019.
[197] PACKIRISAMY, Rajiv Gandhi, GOVINDASAMY, Chandramohan, SANMUGAM, Anandhavelu, et al. Synthesis of novel Sn1-xZnxO-chitosan nanocomposites: Structural, morphological and luminescence properties and investigation of antibacterial properties. International journal of biological macromolecules, vol. 138, p. 546-555, 2019.
[198] ALAVI, Mehran et RAI, Mahendra. Recent progress in nanoformulations of silver nanoparticles with cellulose, chitosan, and alginic acid biopolymers for antibacterial applications. Applied Microbiology and Biotechnology, vol. 103, no 21-22, p. 8669-8676, 2019.

[199] AZIZI, Susan, AHMAD, Mansor Bin, HUSSEIN, Mohd Zobir, et al. Preparation and properties of poly (vinyl alcohol)/chitosan blend bionanocomposites reinforced with cellulose nanocrystals/ZnO-Ag multifunctional nanosized filler. International journal of nanomedicine, vol. 9, p. 1909, 2014.
[200]. GEORGAKILAS, Vasilios, PERMAN, Jason A., TUCEK, Jiri, et al. Broad family of carbon nanoallotropes: classification, chemistry, and applications of fullerenes, carbon dots, nanotubes, graphene, nanodiamonds, and combined superstructures. Chemical reviews, vol. 115, no 11, p. 4744-4822, 2015.
[201] ZHANG, Pengfei, QIAO, Zhen-An, ZHANG, Zhiyong, et al. Mesoporous graphene-like carbon sheet: high-power supercapacitor and outstanding catalyst support. Journal of Materials Chemistry A, vol. 2, no 31, p. 12262-12269, 2014.
[202] MUKESH, Tiwary et JHA, Ashok Kumar. A review on: carbon nanotubes are vital for plant growth. Am. J. Agric. For, vol. 5, no 5-1, p. 1-9, 2017.
[203] GIULIANINI, Michele et MOTTA, Nunzio. Polymer self-assembly on carbon nanotubes. In : Self-Assembly of Nanostructures. Springer, New York, NY, p. 1-72, 2012.
[204] FLAHAUT, E., PEIGNEY, A., et LAURENT, Ch. CCVD Synthesis of Single-and Double-Walled Carbon Nanotubes. Nanoengineered and Nanofibrous Materials, 2003.
[205] IIJIMA, Sumio. Synthesis of carbon nanotubes. Nature, vol. 354, no 6348, p. 56-58, 1991.
[206] ZHU, Shuyun et XU, Guobao. Single-walled carbon nanohorns and their applications. Nanoscale, vol. 2, no 12, p. 2538-2549, 2010.
[207] ZHAI, Yunpu, DOU, Yuqian, ZHAO, Dongyuan, et al. Carbon materials for chemical capacitive energy storage. Advanced materials, vol. 23, no 42, p. 4828-4850, 2011.
[208] ZHU, Shuyun et XU, Guobao. Single-walled carbon nanohorns and their applications. Nanoscale, vol. 2, no 12, p. 2538-2549, 2010.
[209] SERBAN, Bogdan-Catalin, BUMBAC, Marius, BUIU, Octavian, et al. Carbon nanohorns and their nanocomposites: Synthesis, properties and applications. A concise review. Ann. Acad. Rom. Sci. Ser. Math. Appl, vol. 11, p. 5-18, 2018.
[210] VARSHNEY, Kalpna, et al. Carbon nanotubes: a review on synthesis, properties and applications. International journal of engineering research and general science, vol. 2, no 4, p. 660-677, 2014.
[211] ARORA, Neha et SHARMA, N. N. Arc discharge synthesis of carbon nanotubes: Comprehensive review. Diamond and related materials, vol. 50, p. 135-150, 2014.
[212] HOU, Pengxiang, LIU, Chang, TONG, Yu, et al. Purification of single-walled carbon nanotubes synthesized by the hydrogen arc-discharge method. Journal of Materials Research, vol. 16, no 9, p. 2526-2529, 2001.
[213] CHRZANOWSKA, Justyna, HOFFMAN, Jacek, MAŁOLEPSZY, Artur, et al. Synthesis of carbon nanotubes by the laser ablation method: Effect of laser wavelength. physica status solidi (b), vol. 252, no 8, p. 1860-1867, 2015.
[214] SAKAKIBARA, Youichi, TATSUURA, Satoshi, KATAURA, Hiromichi, et al. Near-infrared saturable absorption of single-wall carbon nanotubes prepared by laser ablation method. Japanese journal of applied physics, vol. 42, no 5A, p. L494, 2003.
[215] CHENG, H. M., LI, Feng, SU, Ge, et al. Large-scale and low-cost synthesis of single-walled carbon nanotubes by the catalytic pyrolysis of hydrocarbons. Applied Physics Letters, vol. 72, no 25, p. 3282-3284, 1998.
[216] MAHANANDIA, P., VISHWAKARMA, P. N., NANDA, K. K., et al. Multiwall carbon nanotubes from pyrolysis of tetrahydrofuran. Materials research bulletin, vol. 41, no 12, p. 2311-2317, 2006.
[217] KONG, Jing, CASSELL, Alan M., et DAI, Hongjie. Chemical vapor deposition of methane for single-walled carbon nanotubes. Chemical Physics Letters, vol. 292, no 4-6, p. 567-574, 1998.
[218] WEI, Dacheng, LIU, Yunqi, WANG, Yu, et al. Synthesis of N-doped graphene by chemical vapor deposition and its electrical properties. Nano letters, vol. 9, no 5, p. 1752-1758, 2009.
[219] MANAWI, Yehia M., SAMARA, Ayman, AL-ANSARI, Tareq, et al. A review of carbon nanomaterials' synthesis via the chemical vapor deposition (CVD) method. Materials, vol. 11, no 5, p. 822, 2018.

[220] WANG, Chundong, ZHOU, Yungang, HE, Lifang, et al. In situ nitrogen-doped graphene grown from polydimethylsiloxane by plasma enhanced chemical vapor deposition. Nanoscale, vol. 5, no 2, p. 600-605, 2013.
[221] ZHANG, Guangyu, MANN, David, ZHANG, Li, et al. Ultra-high-yield growth of vertical single-walled carbon nanotubes: Hidden roles of hydrogen and oxygen. Proceedings of the National Academy of Sciences, vol. 102, no 45, p. 16141-16145, 2005.
[222] HARRIS, Peter JF et HARRIS, Peter John Frederich. Carbon nanotube science: synthesis, properties and applications. Cambridge university press, 2009.
[223] KOMAROV, F. F. et MIRONOV, A. M. Carbon nanotubes: present and future. Phys. Chem. Solid State, vol. 5, no 3, p. 411-429, 2004.
[224] MUBARAK, N. M., ABDULLAH, E. C., JAYAKUMAR, N. S., et al. An overview on methods for the production of carbon nanotubes. Journal of Industrial and Engineering Chemistry, vol. 20, no 4, p. 1186-1197, 2014.
[225] KUMAR, Mukul et ANDO, Yoshinori. Chemical vapor deposition of carbon nanotubes: a review on growth mechanism and mass production. Journal of nanoscience and nanotechnology, vol. 10, no 6, p. 3739-3758, 2010.
[226] DANAFAR, Firoozeh, FAKHRU'L-RAZI, A., SALLEH, Mohd Amran Mohd, et al. Fluidized bed catalytic chemical vapor deposition synthesis of carbon nanotubes—a review. Chemical Engineering Journal, vol. 155, no 1-2, p. 37-48, 2009.
[227] WEI, Fei, ZHANG, Qiang, QIAN, Wei-Zhong, et al. The mass production of carbon nanotubes using a nano-agglomerate fluidized bed reactor: A multiscale space–time analysis. Powder Technology, vol. 183, no 1, p. 10-20, 2008.
[228] SU, Ming, ZHENG, Bo, et LIU, Jie. A scalable CVD method for the synthesis of single-walled carbon nanotubes with high catalyst productivity. Chemical Physics Letters, vol. 322, no 5, p. 321-326, 2000.
[229] YARBROUGH, Walter A. et MESSIER, Russell. Current issues and problems in the chemical vapor deposition of diamond. Science, vol. 247, no 4943, p. 688-696, 1990.
[230] SOMORJAI, G. A. et RIOUX, R. M. High technology catalysts towards 100% selectivity: Fabrication, characterization and reaction studies. Catalysis Today, vol. 100, no 3-4, p. 201-215, 2005.
[231] CORTIAL, Guillaume, SIUTKOWSKI, Magali, GOETTMANN, Frédéric, et al. Metallic nanoparticles hosted in mesoporous oxide thin films for catalytic applications. Small, vol. 2, no 8-9, p. 1042-1045, 2006.
[232] SINGH, Inderbir, REHNI, Ashish K., KUMAR, Pradeep, et al. Carbon nanotubes: synthesis, properties and pharmaceutical applications. Fullerenes, Nanotubes and Carbon Nanostructures, vol. 17, no 4, p. 361-377, 2009.
[233] PITKETHLY, Michael J. Nanomaterials–the driving force. Materials today, vol. 7, no 12, p. 20-29, 2004.
[234] MELECHKO, Anatoli Vasilievich, MERKULOV, Vladimir I., MCKNIGHT, Timothy E., et al. Vertically aligned carbon nanofibers and related structures: controlled synthesis and directed assembly. Journal of applied physics, vol. 97, no 4, p. 3, 2005.
[235] WEI, Dacheng, PENG, Lan, LI, Menglin, et al. Low temperature critical growth of high quality nitrogen doped graphene on dielectrics by plasma-enhanced chemical vapor deposition. ACS nano, vol. 9, no 1, p. 164-171, 2015.
[236] GEIM, Andre K. et NOVOSELOV, Konstantin S. The rise of graphene. In : Nanoscience and technology: a collection of reviews from nature journals.p. 11-19, 2010.
[237] DUBOIS, SM-M., ZANOLLI, Zeila, DECLERCK, Xavier, et al. Electronic properties and quantum transport in Graphene-based nanostructures. The European Physical Journal B, vol. 72, no 1, p. 1-24, 2009.
[238] RITTER, Kyle A. et LYDING, Joseph W. The influence of edge structure on the electronic properties of graphene quantum dots and nanoribbons. Nature materials, vol. 8, no 3, p. 235-242, 2009.
[239] CHEN, Zhihong, DU, Xu, DU, Mao-Hua, et al. Bulk separative enrichment in metallic or semiconducting single-walled carbon nanotubes. Nano Letters, vol. 3, no 9, p. 1245-1249, 2003.

[240] RAO, C. N. R., VOGGU, Rakesh, et GOVINDARAJ, A. Selective generation of single-walled carbon nanotubes with metallic, semiconducting and other unique electronic properties. Nanoscale, vol. 1, no 1, p. 96-105, 2009.
[241] MA, Liang, WANG, Jinlan, et DING, Feng. Recent progress and challenges in graphene nanoribbon synthesis. ChemPhysChem, vol. 14, no 1, p. 47-54, 2013.
[242] KOSYNKIN, Dmitry V., HIGGINBOTHAM, Amanda L., SINITSKII, Alexander, et al. Longitudinal unzipping of carbon nanotubes to form graphene nanoribbons. Nature, vol. 458, no 7240, p. 872-876, 2009.
[243] BARHOUM, Ahmed, SHALAN, Ahmed Esmail, EL-HOUT, Soliman I., et al. A broad family of carbon nanomaterials: classification, properties, synthesis, and emerging applications. Handbook of Nanofibers; Springer International Publishing: New York City, NY, USA, p. 1-40, 2019.
[244] VARSHNEY, Kalpna, et al. Carbon nanotubes: a review on synthesis, properties and applications. International journal of engineering research and general science, vol. 2, no 4, p. 660-677, 2014.
[245] WANG, Nan. Functionalization and Characterization of Carbon Based Nanomaterials for Electronics, Composite and Biomedical Applications. Chalmers Tekniska Hogskola (Sweden), 2017.
[246] KIM, Kyung Tae et JO, Won Ho. Noncovalent functionalization of multiwalled carbon nanotubes using graft copolymer with naphthalene and its application as a reinforcing filler for poly (styrene-co-acrylonitrile). Journal of Polymer Science Part A: Polymer Chemistry, vol. 48, no 19, p. 4184-4191, 2010.
[247] CHEN, Robert J., BANGSARUNTIP, Sarunya, DROUVALAKIS, Katerina A., et al. Noncovalent functionalization of carbon nanotubes for highly specific electronic biosensors. Proceedings of the National Academy of Sciences, vol. 100, no 9, p. 4984-4989, 2003.
[248] ZHAO, Jijun, LU, Jian Ping, HAN, Jie, et al. Noncovalent functionalization of carbon nanotubes by aromatic organic molecules. Applied physics letters, vol. 82, no 21, p. 3746-3748, 2003.
[249] SINGER, Gerald, SIEDLACZEK, Philipp, SINN, Gerhard, et al. Acid free oxidation and simple dispersion method of MWCNT for high-performance CFRP. Nanomaterials, vol. 8, no 11, p. 912, 2018.
[250] SHOJAOSADATI, S. A., GANJI, F., ZAHEDI, B., et al. Effect of different CNT's oxidation methods on thiocoline detection by surfactant modified graphite electrodes. International Journal of Nanoscience and Nanotechnology, vol. 6, no 4, p. 195-204, 2010.
[251] WANG, Hong, LIU, Fucai, FU, Wei, et al. Two-dimensional heterostructures: fabrication, characterization, and application. Nanoscale, vol. 6, no 21, p. 12250-12272, 2014.
[252] YAO, Yao et PING, Jianfeng. Recent advances in graphene-based freestanding paper-like materials for sensing applications. TrAC Trends in Analytical Chemistry, vol. 105, p. 75-88, 2018.
[253] LIU, Wenjun, CAI, Jingyu, et LI, Zhaohui. Self-assembly of semiconductor nanoparticles/reduced graphene oxide (RGO) composite aerogels for enhanced photocatalytic performance and facile recycling in aqueous photocatalysis. ACS Sustainable Chemistry & Engineering, vol. 3, no 2, p. 277-282, 2015.
[254] LIU, Jinlong, ZHANG, Yaqian, LI, Yaping, et al. In situ chemical synthesis of sandwich-structured MnO2/graphene nanoflowers and their supercapacitive behavior. Electrochimica Acta, vol. 173, p. 148-155, 2015.
[255] DONG, Xiaochen, CAO, Yunfa, WANG, Jing, et al. Hybrid structure of zinc oxide nanorods and three dimensional graphene foam for supercapacitor and electrochemical sensor applications. RSC advances, vol. 2, no 10, p. 4364-4369, 2012.
[256] PATIL, U. M., LEE, Su Chan, SOHN, J. S., et al. Enhanced symmetric supercapacitive performance of Co (OH) 2 nanorods decorated conducting porous graphene foam electrodes. Electrochimica Acta, vol. 129, p. 334-342, 2014.
[257] YANG, Cheng, DENNO, Madelaine E., PYAKUREL, Poojan, et al. Recent trends in carbon nanomaterial-based electrochemical sensors for biomolecules: A review. Analytica chimica acta, vol. 887, p. 17-37, 2015.
[258] BIANCO, Alberto, KOSTARELOS, Kostas, PARTIDOS, Charalambos D., et al. Biomedical applications of functionalised carbon nanotubes. Chemical Communications, no 5, p. 571-577, 2005.
[259] ZHAO, Fuli, YAO, Dan, GUO, Ruiwei, et al. Composites of polymer hydrogels and nanoparticulate systems for biomedical and pharmaceutical applications. Nanomaterials, vol. 5, no 4, p. 2054-2130, 2015.

[260] WANG, Ying, LI, Zhaohui, WANG, Jun, et al. Graphene and graphene oxide: biofunctionalization and applications in biotechnology. Trends in biotechnology, vol. 29, no 5, p. 205-212, 2011.
[261] ZHANG, Lu, WANG, Zhipeng, XU, Chen, et al. High strength graphene oxide/polyvinyl alcohol composite hydrogels. Journal of Materials Chemistry, vol. 21, no 28, p. 10399-10406, 2011.
[262] ZHENG, Ming, JAGOTA, Anand, SEMKE, Ellen D., et al. DNA-assisted dispersion and separation of carbon nanotubes. Nature materials, vol. 2, no 5, p. 338-342, 2003.
[263] JACUNSKI, Mark D., SHUR, Michael S., et HACK, Michael. Threshold voltage, field effect mobility, and gate-to-channel capacitance in polysilicon TFTs. IEEE Transactions on Electron Devices, vol. 43, no 9, p. 1433-1440, 1996.
[264] LIU, Qian, LIU, Zunfeng, ZHANG, Xiaoyan, et al. Polymer photovoltaic cells based on solution-processable graphene and P3HT. Advanced Functional Materials, vol. 19, no 6, p. 894-904, 2009.
[265] KAEMPGEN, Martti et ROTH, Siegmar. Transparent and flexible carbon nanotube/polyaniline pH sensors. Journal of Electroanalytical Chemistry, vol. 586, no 1, p. 72-76, 2006.
[266] DE VOLDER, Michael FL, TAWFICK, Sameh H., BAUGHMAN, Ray H., et al. Carbon nanotubes: present and future commercial applications. science, vol. 339, no 6119, p. 535-539, 2013.
[267] IONESCU, Adrian M. et RIEL, Heike. Tunnel field-effect transistors as energy-efficient electronic switches. nature, vol. 479, no 7373, p. 329-337, 2011.
[268] IONESCU, Adrian M. et RIEL, Heike. Tunnel field-effect transistors as energy-efficient electronic switches. nature, vol. 479, no 7373, p. 329-337, 2011.
[269] PARK, Hongsik, AFZALI, Ali, HAN, Shu-Jen, et al. High-density integration of carbon nanotubes via chemical self-assembly. Nature nanotechnology, vol. 7, no 12, p. 787-791, 2012.
[270] FRANKLIN, Aaron D., LUISIER, Mathieu, HAN, Shu-Jen, et al. Sub-10 nm carbon nanotube transistor. Nano letters, vol. 12, no 2, p. 758-762, 2012.
[271] RUECKES, Thomas, KIM, Kyoungha, JOSELEVICH, Ernesto, et al. Carbon nanotube-based nonvolatile random access memory for molecular computing. science, vol. 289, no 5476, p. 94-97, 2000.
[272] JUNG, Minhun, KIM, Jaeyoung, NOH, Jinsoo, et al. All-printed and roll-to-roll-printable 13.56-MHz-operated 1-bit RF tag on plastic foils. IEEE Transactions on Electron Devices, vol. 57, no 3, p. 571-580, 2010.
[273] SUN, Dong-ming, TIMMERMANS, Marina Y., TIAN, Ying, et al. Flexible high-performance carbon nanotube integrated circuits. Nature nanotechnology, vol. 6, no 3, p. 156-161, 2011.
[274] CHAE, Sang Hoon et LEE, Young Hee. Carbon nanotubes and graphene towards soft electronics. Nano Convergence, vol. 1, no 1, p. 15, 2014.
[275] DE VOLDER, Michael FL, TAWFICK, Sameh H., BAUGHMAN, Ray H., et al. Carbon nanotubes: present and future commercial applications. science, vol. 339, no 6119, p. 535-539, 2013.
[276] SADEGH, Hamidreza, ALI, Gomaa AM, MAKHLOUF, Abdel Salam Hamdy, et al. MWCNTs-Fe_3O_4 nanocomposite for Hg (II) high adsorption efficiency. Journal of Molecular Liquids, vol. 258, p. 345-353, 2018.
[277] ARABI, Seyed Masoud Seyed, LALEHLOO, Rahman Shakibaei, OLYAI, Mohamad Reza Talei Bavil, et al. Removal of congo red azo dye from aqueous solution by ZnO nanoparticles loaded on multiwall carbon nanotubes. Physica E: Low-dimensional Systems and Nanostructures, vol. 106, p. 150-155, 2019.
[278] CHENG, Qian, TANG, Jie, MA, Jun, et al. Graphene and carbon nanotube composite electrodes for supercapacitors with ultra-high energy density. Physical Chemistry Chemical Physics, vol. 13, no 39, p. 17615-17624, 2011.
[279] SATHTHASIVAM, Jayaprakash, YIMING, Wubulikasimu, WANG, Kui, et al. A novel architecture for carbon nanotube membranes towards fast and efficient oil/water separation. Scientific reports, vol. 8, no 1, p. 1-6, 2018.
[280] YANG, Hui Ying, HAN, Zhao Jun, YU, Siu Fung, et al. Carbon nanotube membranes with ultrahigh specific adsorption capacity for water desalination and purification. Nature communications, vol. 4, no 1, p. 1-8, 2013.
[281] SUTASINPROMPRAE, Juthawan, JITJAICHAM, Sujinda, NITHITANAKUL, Manit, et al. Preparation and characterization of ultrafine electrospun polyacrylonitrile fibers and their subsequent pyrolysis to carbon fibers. Polymer International, vol. 55, no 8, p. 825-833, 2006.

[282] ARSHAD, Salman N., NARAGHI, Mohammad, et CHASIOTIS, Ioannis. Strong carbon nanofibers from electrospun polyacrylonitrile. Carbon, vol. 49, no 5, p. 1710-1719, 2011.
[283] DE VOLDER, Michael FL, TAWFICK, Sameh H., BAUGHMAN, Ray H., et al. Carbon nanotubes: present and future commercial applications. science, vol. 339, no 6119, p. 535-539, 2013.
[284] PORTET, Cristelle, YUSHIN, G., et GOGOTSI, Yuri. Electrochemical performance of carbon onions, nanodiamonds, carbon black and multiwalled nanotubes in electrical double layer capacitors. Carbon, vol. 45, no 13, p. 2511-2518, 2007.
[285] PALMA, Matteo, WANG, Wei, PENZO, Erika, et al. Controlled formation of carbon nanotube junctions via linker-induced assembly in aqueous solution. Journal of the American Chemical Society, vol. 135, no 23, p. 8440-8443, 2013.
[286] CHEN, Wufeng, LI, Sirong, CHEN, Chunhua, et al. Self-assembly and embedding of nanoparticles by in situ reduced graphene for preparation of a 3D graphene/nanoparticle aerogel. Advanced materials, vol. 23, no 47, p. 5679-5683, 2011.
[287] LIU, Chenguang, YU, Zhenning, NEFF, David, et al. Graphene-based supercapacitor with an ultrahigh energy density. Nano letters, vol. 10, no 12, p. 4863-4868, 2010.
[288] HU, Chenxi, GUO, Shimei, LU, Guixia, et al. Carbon coating and Zn2+ doping of magnetite nanorods for enhanced electrochemical energy storage. Electrochimica Acta, vol. 148, p. 118-126, 2014.
[289] DE LAS CASAS, Charles et LI, Wenzhi. A review of application of carbon nanotubes for lithium ion battery anode material. Journal of Power Sources, vol. 208, p. 74-85, 2012.
[290] KUMAR, G. Gnana, REDDY, K., NAHM, Kee Suk, et al. Synthesis and electrochemical properties of SnS as possible anode material for lithium batteries. Journal of Physics and Chemistry of Solids, vol. 73, no 9, p. 1187-1190, 2012.
[291] KUMAR, G. Gnana, REDDY, K., NAHM, Kee Suk, et al. Synthesis and electrochemical properties of SnS as possible anode material for lithium batteries. Journal of Physics and Chemistry of Solids, vol. 73, no 9, p. 1187-1190, 2012.
[292] SHENG, Zhen-Huan, GAO, Hong-Li, BAO, Wen-Jing, et al. Synthesis of boron doped graphene for oxygen reduction reaction in fuel cells. Journal of Materials Chemistry, vol. 22, no 2, p. 390-395, 2012.
[293] YANG, Zhi, YAO, Zhen, LI, Guifa, et al. Sulfur-doped graphene as an efficient metal-free cathode catalyst for oxygen reduction. ACS nano, vol. 6, no 1, p. 205-211, 2012.
[294] LI, Yanguang, ZHOU, Wu, WANG, Hailiang, et al. An oxygen reduction electrocatalyst based on carbon nanotube–graphene complexes. Nature nanotechnology, vol. 7, no 6, p. 394-400, 2012.
[295] BORIS, Malishev. Stabilized form of phosphorus pentoxide. U.S. Patent No 2,005,944, 25 juin 1935.
[296] CASEY, M., LEONARD, J., LYGO, B., et al. Purification and drying of solvents. In : Advanced Practical Organic Chemistry. Springer, Boston, MA,p. 28-42, 1990.
[297] WESTHEIMER, F. H. The role of phosphorus in chemistry and biochemistry: an overview.
[298] SMITH, James P., BROWN, Walter E., et LEHR, James R. Structure of crystalline phosphoric acid. Journal of the American Chemical Society, vol. 77, no 10, p. 2728-2730, 1955.
[299] BOERSTOEL, H., MAATMAN, H., WESTERINK, J. B., et al. Liquid crystalline solutions of cellulose in phosphoric acid. Polymer, vol. 42, no 17, p. 7371-7379, 2001.
[300] DRIVER, J., LIJMBACH, D., et STEEN, I. Why recover phosphorus for recycling, and how?. Environmental technology, vol. 20, no 7, p. 651-662, 1999.
[301] YAMADA, Hisashi, KAYAMA, Mitsu, SAITO, Kazuo, et al. A fundamental research on phosphate removal by using slag. Water research, vol. 20, no 5, p. 547-557, 1986.
[302] TAYIBI, Hanan, CHOURA, Mohamed, LÓPEZ, Félix A., et al. Environmental impact and management of phosphogypsum. Journal of environmental management, vol. 90, no 8, p. 2377-2386, 2009.
[303] POLUEKTOV, Pavel P., SCHMIDT, Olga V., KASCHEEV, Vladimir A., et al. Modelling aqueous corrosion of nuclear waste phosphate glass. Journal of Nuclear Materials, vol. 484, p. 357-366, 2017.
[304] ZIMMERMANN, Herbert, ZEBISCH, Matthias, et STRÄTER, Norbert. Cellular function and molecular structure of ecto-nucleotidases. Purinergic signalling, vol. 8, no 3, p. 437-502, 2012.
[305] GILMOUR, Rodney. Phosphoric acid: purification, uses, technology, and economics. CRC Press, 2013.

[306] MIZANE, Abbes et REHAMNIA, Rabah. Study of some parameters to obtain the P2O5 water-Soluble from partially acidulated phosphate rocks (PAPRs) by sulfuric acid. Phosphorus Research Bulletin, vol. 27, p. 18-22, 2012.
[307] MATHIAS, Paul M., CHEN, Chau-Chyun, et WALTERS, Marten. Modeling the complex chemical reactions and mass transfer in a phosphoric acid reactor. In : Proceeedings of the Third Joint China/USA Chemical Engineering Conference (CUChE-3). 2000.
[308] LEYSHON, David W., LUTZ, William A., OLIVER, Robert H., et al. Manufacture of phosphoric acid. U.S. Patent No 3,192,014, 29 juin 1965.
[309] FORNÉS, Ignacio Villalón, DOROSEVAS, Viktoras, VAICIUKYNIENE, Danute, et al. The Investigation of Phosphogypsum Specimens Processed by Press-Forming Method. WASTE AND BIOMASS VALORIZATION, 2020.
[310] TERADAL, Nagappa L., MARX, Sharon, MORAG, Ahiud, et al. Porous graphene oxide chemi-capacitor vapor sensor array. Journal of Materials Chemistry C, vol. 5, no 5, p. 1128-1135, 2017.
[311] LIN, Geng-Min et CHYANG, Chien-Song. Removal of HCl in flue gases by calcined limestone at high temperatures. Energy & Fuels, vol. 31, no 11, p. 12417-12424, 2017.
[312] JERRAM, Dougal, SCARTH, Alwyn, et TANGUY, Jean-Claude. Volcanoes of Europe. Dunedin Academic Press Ltd, 2017.
[313] PATNAIK, Amar, BHAT, I., et GANGWAR, Swati. Manufacturing and characterization of quicklime (CaO) filled ZA-27 metal alloy composites for single-row deep groove ball bearing. Handbook of Composites from Renewable Materials, Design and Manufacturing, vol. 2, p. 133, 2017.
[314] POSSAN, Edna, THOMAZ, William A., ALEANDRI, Gustavo A., et al. CO2 uptake potential due to concrete carbonation: A case study. Case Studies in Construction Materials, vol. 6, p. 147-161, 2017.
[315] OUNOUGHENE, Ghania, BUSKENS, Ellen, SANTOS, Rafael M., et al. Solvochemical carbonation of lime using ethanol: Mechanism and enhancement for direct atmospheric CO_2 capture. Journal of CO_2 Utilization, vol. 26, p. 143-151, 2018.
[316] MOH'D, Basem K. THE COLOR OF SOME JORDANIAN BUILDING LIMESTONES IN THE DRY AND WET STATES. Technology, vol. 8, no 3, p. 337-343, 2017.
[317] MACÊDO, Juliana, FERREIRA JÚNIOR, Jair A., NASCIMENTO, Karla A., et al. Skin burn and ocular damage by calcium oxide (virgin lime) in swines. Pesquisa Veterinária Brasileira, vol. 38, no 11, p. 2088-2091, 2018.
[318] BARTSCH, R., MICHAELSEN, S., HARTWIG, A., et al. Calcium hydroxide [MAK Value Documentations, 2013]. The MAK-Collection for Occupational Health and Safety: Annual Thresholds and Classifications for the Workplace, vol. 1, no 1, p. 12-25, 2002.
[319] COPSEY, Nigel. Traditional hot mixed lime mortars for conservation and repair. Journal of Building Survey, Appraisal & Valuation, vol. 8, no 1, p. 9-30, 2019.
[320] BIAN, Xue, WU, W. Y., ZHENG, Qiang, et al. Study on decomposition of mixed rare earth concentrate by Ca (OH) 2-NaOH. Chin. Rare Earths, vol. 35, no 4, p. 30-34, 2014.
[321] MWITI, Marangu Joseph. Pozzolanicity, Chloride Ingress and Compressive Strength of Laboratory made Kenya Clay-Portland Cement Blends. PhD diss., Kenyatta University, 2013.
[322] FREITAS, A. A., SANTOS, R. L., COLAÇO, R., et al. From lime to silica and alumina: systematic modeling of cement clinkers using a general force-field. Physical Chemistry Chemical Physics, vol. 17, no 28, p. 18477-18494, 2015.
[323] JIMOH, Onimisi A., OTITOJU, Tunmise A., HUSSIN, Hashim, et al. Understanding the precipitated calcium carbonate (PCC) production mechanism and its characteristics in the liquid–gas system using milk of lime (MOL) suspension. South African Journal of Chemistry, vol. 70, p. 1-7, 2017.
[324] TANG, Jia et WANG, Jie. Catalytic steam gasification of coal char with alkali carbonates: A study on their synergic effects with calcium hydroxide. Fuel Processing Technology, vol. 142, p. 34-41, 2016.
[325] GREGORY, Thomas M., MORENO, Edgard C., et BROWN, Walter E. Solubility of $CaHPO_4 \cdot 2H_2O$ in the system Ca (OH) 2-H3PO4-H2O at 5, 15, 25, and 37.5 C. Journal of Research of the National Bureau of Standards. Section A, Physics and Chemistry, vol. 74, no 4, p. 461, 1970.

[326] GALYEAN, R. D. et COTTERILL, O. J. Chromatography and electrophoresis of native and spray-dried egg white. Journal of food science, vol. 44, no 5, p. 1345-1349, 1979.
[327] WELLMAN-LABADIE, O., PICMAN, J., et HINCKE, M. T. Comparative antibacterial activity of avian egg white protein extracts. British poultry science, vol. 49, no 2, p. 125-132, 2008.
[328] FEVOLD, Harry L. Egg proteins. In : Advances in protein chemistry. Academic Press, p. 187-252, 1951.
[329] ANTON, M., NAU, Francoise, et LECHEVALIER, V. Egg proteins. In : Handbook of hydrocolloids. Woodhead Publishing, p. 359-382, 2009.
[330] GUHA, Snigdha, MAJUMDER, Kaustav, et MINE, Yoshinori. Egg proteins. Reference Module in Food Science, 2018.
[331] STADELMAN, William J., NEWKIRK, Debbie, et NEWBY, Lynne. Egg science and technology. CRC Press, 2017.
[332] MAO, Xiangzhao, GUO, Na, SUN, Jianan, et al. Comprehensive utilization of shrimp waste based on biotechnological methods: A review. Journal of Cleaner Production, vol. 143, p. 814-823, 2017.
[333] https://www.newindianexpress.com/states/odisha/2018/jun/26/odisha-illegal-dumping-of-shrimp-waste-continues-unabated-in-port-town-1833828.html
[334] JURCZYK, M. et NOWAK, M. Introduction to hydrogen based chemical agents for hydrogen technology. In : Hydrogen Storage Materials. Springer, Berlin, Heidelberg, p. 486-491, 2018.
[335] NORDSTROM, Darrell Kirk, ALPERS, Charles N., PTACEK, Carol J., et al. Negative pH and extremely acidic mine waters from Iron Mountain, California. Environmental Science & Technology, vol. 34, no 2, p. 254-258, 2000.
[336] PENG, Peng, LANG, Yin-Hai, et WANG, Xiao-Mei. Adsorption behavior and mechanism of pentachlorophenol on reed biochars: pH effect, pyrolysis temperature, hydrochloric acid treatment and isotherms. Ecological Engineering, vol. 90, p. 225-233, 2016.
[337] CLARKE, Stephen I. et MAZZAFRO, William J. Nitric acid. Kirk-Othmer Encyclopedia of Chemical Technology, 2000.
[338] TRENT, C. H. et ZUCROW, M. J. Behavior of Liquid Hydrocarbons with White Fuming Nitric Acid. Industrial & Engineering Chemistry, vol. 44, no 11, p. 2668-2673, 1952.
[339] SCHAFFERT, Roland. The infrared absorption spectra of NO2 and N2O4. The Journal of Chemical Physics, vol. 1, no 7, p. 507-511, 1933.
[340] THOMPSON, Darren M. et ALLAN, Barry D. Higher density inhibited red fuming nitric acid (IRFNA) oxidizer gel. U.S. Patent No 6,063,219, 16 mai 2000.
[341] RAY, James D. et OGG JR, Richard A. Kinetics of the nitrogen dioxide catalyzed oxidation of nitric oxide. The Journal of Chemical Physics, vol. 26, no 5, p. 984-988, 1957.
[342] BULLOCK, Kathryn R. Lead/acid batteries. Journal of power sources, vol. 51, no 1-2, p. 1-17, 1994.
[343] HAQUE, Nawshad, HUGHES, Anthony, LIM, Seng, et al. Rare earth elements: Overview of mining, mineralogy, uses, sustainability and environmental impact. Resources, vol. 3, no 4, p. 614-635, 2014.
[344] HSU, Yu-Mei, WU, Chang-Yu, LUNDGREN, Dale A., et al. Chemical characteristics of aerosol mists in phosphate fertilizer manufacturing facilities. Journal of Occupational and Environmental Hygiene, vol. 4, no 1, p. 17-25, 2007.
[345] XUHONG, Mu, DIANZHONG, Wang, YONGRUI, Wang, et al. Nanosized molecular sieves as petroleum refining and petrochemical catalysts. Chinese journal of catalysis, vol. 34, no 1, p. 69-79, 2013.
[346] BHAUMIK, Madhumita, CHOI, Hyoung J., SEOPELA, MatHAPelo P., et al. Highly effective removal of toxic Cr (VI) from wastewater using sulfuric acid-modified avocado seed. Industrial & Engineering Chemistry Research, vol. 53, no 3, p. 1214-1224, 2014.
[347] GREYSON, Jerome C. Carbon, nitrogen, and sulfur pollutants and their determination in air and water. CRC Press, 1990.
[348] SETH, Rohit, CHESTER, D., et MOIEMEN, N. A review of chemical burns. Trauma, vol. 9, no 2, p. 81-94, 2007.
[349] AHMED, Nahed SE et EL-SHISHTAWY, Reda M. The use of new technologies in coloration of textile fibers. Journal of Materials Science, vol. 45, no 5, p. 1143-1153, 2010.

[350] GOTTESMAN, Ronen, SHUKLA, Sourabh, PERKAS, Nina, et al. Sonochemical coating of paper by microbiocidal silver nanoparticles. Langmuir, vol. 27, no 2, p. 720-726, 2011.
[351] HEBERLING, Matthew M., WU, Bian, BARTSCH, Sebastian, et al. Priming ammonia lyases and aminomutases for industrial and therapeutic applications. Current Opinion in Chemical Biology, vol. 17, no 2, p. 250-260, 2013.
[352] CZUPPON, T. A., KNEZ, S. A., et ROVNER, J. M. Ammonia. Kirk-Othmer Encyclopedia of Chemical Technology, 2000.
[353] YOUCAI, Zhao et STANFORTH, R. Extraction of zinc from zinc ferrites by fusion with caustic soda. Minerals Engineering, vol. 13, no 13, p. 1417-1421, 2000.
[354] BURGHER, François, MATHIEU, Laurence, BLOMET, Joël, et al. Damaged skin. In : Chemical Skin Injury. Springer, Berlin, Heidelberg, p. 73-196, 2014.
[355] HOU, Aiqin, ZHANG, Xufang, et ZHOU, Yunxia. Low temperature bleaching of cellulose fabric with (N-[4-triethylammoniomethyl]-benzoyl) caprolactam chloride as novel cationic activator for H_2O_2 bleaching. Carbohydrate polymers, vol. 82, no 3, p. 618-622, 2010.
[356] WOO, Young-Ah, LIM, Hun-Rang, KIM, Hyo-Jin, et al. Determination of hydrogen peroxide concentration in antiseptic solutions using portable near-infrared system. Journal of pharmaceutical and biomedical analysis, vol. 33, no 5, p. 1049-1057, 2003.
[357] KARUPPANAPANDIAN, Thirupathi, MOON, Jun-Cheol, KIM, Changsoo, et al. Reactive oxygen species in plants: their generation, signal transduction, and scavenging mechanisms. Australian Journal of Crop Science, vol. 5, no 6, p. 709, 2011.
[358] ISHIKAWA, Takahiro et SHIGEOKA, Shigeru. Recent advances in ascorbate biosynthesis and the physiological significance of ascorbate peroxidase in photosynthesizing organisms. Bioscience, biotechnology, and biochemistry, vol. 72, no 5, p. 1143-1154, 2008.
[359] DUFFUS, John H. " Heavy metals" a meaningless term?(IUPAC Technical Report). Pure and applied chemistry, vol. 74, no 5, p. 793-807, 2002.
[360] SALZER, A. Nomenclature of organometallic compounds of the transition elements (IUPAC Recommendations 1999). Pure and Applied Chemistry, vol. 71, no 8, p. 1557-1585, 1999.
[361] MUN, Bongjin Simon, WATANABE, Masamitsu, ROSSI, Massimiliano, et al. A study of electronic structures of Pt 3 M (M= Ti, V, Cr, Fe, Co, Ni) polycrystalline alloys with valence-band photoemission spectroscopy. The Journal of chemical physics, vol. 123, no 20, p. 204717, 2005.
[362] TAN, Haiyan, VERBEECK, Jo, ABAKUMOV, Artem, et al. Oxidation state and chemical shift investigation in transition metal oxides by EELS. Ultramicroscopy, vol. 116, p. 24-33, 2012.
[363] CARLIN, Richard Lewis et VAN DUYNEVELDT, Adrianus J. Magnetic properties of transition metal compounds. New York : Springer-Verlag, 1977.
[364] BARCELOUX, Donald G. et BARCELOUX, Donald. Nickel. Journal of Toxicology: Clinical Toxicology, vol. 37, no 2, p. 239-258, 1999.
[365] BARCELOUX, Donald G. et BARCELOUX, Donald. Cobalt. Journal of Toxicology: Clinical Toxicology, vol. 37, no 2, p. 201-216, 1999.
[366] BARCELOUX, Donald G. et BARCELOUX, Donald. Copper. Journal of toxicology: clinical Toxicology, vol. 37, no 2, p. 217-230, 1999.
[367] KABIR, Mukul, MOOKERJEE, Abhijit, et KANHERE, D. G. Structure, electronic properties, and magnetic transition in manganese clusters. Physical Review B, vol. 73, no 22, p. 224439, 2006.
[368] KUMAR, Vipin, SHARMA, Sachin Kr, SHARMA, T. P., et al. Band gap determination in thick films from reflectance measurements. Optical materials, vol. 12, no 1, p. 115-119, 1999.
[369] KHAN, G. A. et HOGARTH, C. A. Optical absorption spectra of evaporated V_2O_5 and co-evaporated V_2O_5/B_2O_3 thin films. Journal of materials science, vol. 26, no 2, p. 412-416, 1991.
[370] http://www.mtheiss.com/ojl_optr.htm.
[371] TAUC, J. et MENTH, A. States in the gap. Journal of non-crystalline solids, vol. 8, p. 569-585, 1972.
[372] TAUC, Jan. Optical properties and electronic structure of amorphous Ge and Si. Materials Research Bulletin, vol. 3, no 1, p. 37-46, 1968.

[373] KRANJČEC, Mladen, STUDENYAK, I. P., et KURIK, M. V. On the Urbach rule in non-crystalline solids. Journal of Non-Crystalline Solids, vol. 355, no 1, p. 54-57, 2009.
[374] SOURI, Dariush et TAHAN, Zahra Esmaeili. A new method for the determination of optical band gap and the nature of optical transitions in semiconductors. Applied Physics B, vol. 119, no 2, p. 273-279, 2015.
[375] TUĞLUOĞLU, Nihat, BARIŞ, Behzad, GÜREL, Hatice, et al. Investigation of optical band gap and device parameters of rubrene thin film prepared using spin coating technique. Journal of alloys and compounds, vol. 582, p. 696-702, 2014.
[376] RAI, R. C. Analysis of the Urbach tails in absorption spectra of undoped ZnO thin films. Journal of Applied Physics, vol. 113, no 15, p. 153508, 2013.
[377] SOLIEMAN, A. et ABU-SEHLY, A. A. Determination of the optical constants of amorphous AsxS100− x films using effective-medium approximation and OJL model. Materials Chemistry and Physics, vol. 129, no 3, p. 1000-1005, 2011.
[378]378. VAN LAAR, Bob et SCHENK, Henk. The development of powder profile refinement at the Reactor Centre Netherlands at Petten. Acta Crystallographica Section A: Foundations and Advances, vol. 74, no 2, p. 88-92, 2018.
[379] YOUNG, Robert Alan (ed.). The rietveld method. Oxford : Oxford university press, 1993.
[380] VASHISTA, M. et PAUL, S. Correlation between full width at half maximum (FWHM) of XRD peak with residual stress on ground surfaces. Philosophical Magazine, vol. 92, no 33, p. 4194-4204, 2012.
[381] SEONG, B.-S., EM, Vyacheslav, MIKULA, Pavol, et al. Optimization of a bent perfect Si (111) monochromator at a small take-off angle for use in a stress instrument. Journal of Applied Crystallography, vol. 43, no 3, p. 654-658, 2010.
[382] CAGLIOTI, G., PAOLETTI, A. t, et RICCI, F. P. Choice of collimators for a crystal spectrometer for neutron diffraction. Nuclear Instruments, vol. 3, no 4, p. 223-228, 1958.
[383] HAGIWARA, Takeshi, KYO, Zuiho, MANABE, Akitaka, et al. Formation of C-type rare earth structures in the $Ce_{1-x}Nd_xO_{2-\delta}$ system: a factor in the decrease in oxide-ion conductivity. Journal of the Ceramic Society of Japan, vol. 117, no 1372, p. 1306-1310, 2009.
[384] PARIKIN, Parikin, DANI, M., JAHJA, A. K., et al. Crystal Structure Investigation of Ferritic 73Fe24Cr2Si0. 8Mn0. 1Ni Steel for Multi-purpose Structural Material Applications. International Journal of Technology (2015) 4, vol. 2018, no 1, p. 78-88, 2017.
[385] MACKAY, A. L. Extensions of space-group theory. Acta Crystallographica, vol. 10, no 9, p. 543-548, 1957.
[386] KAUFMANN, Kevin, ZHU, Chaoyi, ROSENGARTEN, Alexander S., et al. Crystal symmetry determination in electron diffraction using machine learning. Science, vol. 367, no 6477, p. 564-568, 2020.
[387]bAMEH, E. S. A review of basic crystallography and x-ray diffraction applications. The International Journal of Advanced Manufacturing Technology, vol. 105, no 7-8, p. 3289-3302, 2019.
[388] https://www.ill.eu/sites/fullprof/
[389] JANSSENS, Koen, ADAMS, FCV, et RINDBY, A. X-ray fluorescence analysis. Handbook of spectroscopy, vol. 1, p. 365-420, 2003.
[390] SMITH, Brian C. Fundamentals of Fourier transform infrared spectroscopy. CRC press, 2011.
[391] FAIX, O. Fourier transform infrared spectroscopy. In : Methods in lignin chemistry. Springer, Berlin, Heidelberg, p. 83-109, 1992.
[392] LONG, Derek Albert. Raman spectroscopy. New York, p. 1-12, 1977.
[393] YAN, Bing, GREMLICH, Hans-Ulrich, MOSS, Serge, et al. A comparison of various FTIR and FT Raman methods: applications in the reaction optimization stage of combinatorial chemistry. Journal of Combinatorial Chemistry, vol. 1, no 1, p. 46-54, 1999.
[394] COATS, A. W. et REDFERN, J. P. Thermogravimetric analysis. A review. Analyst, vol. 88, no 1053, p. 906-924, 1963.
[395] KIMOTO, S. et RUSS, John C. The characteristics and applications of the scanning electron microscope. American scientist, vol. 57, no 1, p. 112-33, 1969.
[396] CLARK, B. J., FROST, T., et RUSSELL, M. A. (ed.). UV Spectroscopy: Techniques, instrumentation and data handling. Springer Science & Business Media, 1993.

[397] REZWAN, Kurosh, CHEN, Q. Z., BLAKER, J. Ju, et al. Biodegradable and bioactive porous polymer/inorganic composite scaffolds for bone tissue engineering. Biomaterials, vol. 27, no 18, p. 3413-3431, 2006.
[398] ARKIN, V. H., LAKHERA, Meenu, MANJUBALA, I., et al. Solid state synthesis and characterization of calcium phosphate for biomedical application. Int. J. Chem Tech. Res., vol. 8, p. 264-267, 2015.
[399] EL JAZOULI, Abdelaziz, TBIB, B., DEMOURGUES, Alain, et al. Structure and colour of diphosphate pigments with square pyramid environment around chromophore ions (Co^{2+}, Ni^{2+}, Cu^{2+}). Dyes and Pigments, vol. 104, p. 67-74, 2014.
[400] BROWN, Paul Wencil. Phase Relationships in the Ternary System $CaO─P_2O_5─H_2O$ at 25° C. Journal of the American Ceramic Society, vol. 75, no 1, p. 17-22, 1992.
[401] COSTESCU, A., PASUK, I., UNGUREANU, F., et al. PHYSICO-CHEMICAL PROPERTIES OF NANO-SIZED HEXAGONAL HYDROXYAPATITE POWDER SYNTHESIZED BY SOL-GEL. Digest Journal of Nanomaterials & Biostructures (DJNB), vol. 5, no 4, 2010.
[402] BARINOV, S. M., RAU, J. V., CESARO, S. Nunziante, et al. Carbonate release from carbonated hydroxyapatite in the wide temperature rage. Journal of Materials Science: Materials in Medicine, vol. 17, no 7, p. 597-604, 2006.
[403] CIOBANU, C. S., ANDRONESCU, E., VASILE, B. S., et al. Looking for new synthesis of hydroxyapatite doped with europium. Optoelectronics and Advanced Materials, Rapid Communications, vol. 4, no 10, p. 1515-1519, 2010.
[404] BAI, Xiao, MORE, Karren, ROULEAU, Christopher M., et al. Functionally graded hydroxyapatite coatings doped with antibacterial components. Acta biomaterialia, 2010, vol. 6, no 6, p. 2264-2273.
[405] DOAT, A., PELLE, F., GARDANT, N., et al. Synthesis of luminescent bioapatite nanoparticles for utilization as a biological probe. Journal of Solid State Chemistry, vol. 177, no 4-5, p. 1179-1187, 2004.
[406] KHAN, Shamshad A., AL-HAZMI, F. S., AL-HENITI, S., et al. Effect of cadmium addition on the optical constants of thermally evaporated amorphous Se–S–Cd thin films. current applied physics, vol. 10, no 1, p. 145-152, 2010.
[407] MURPHY, Anthony B. Optical properties of an optically rough coating from inversion of diffuse reflectance measurements. Applied optics, vol. 46, no 16, p. 3133-3143, 2007.
[408] ONODA, Hiroaki et OKUMOTO, Kenichi. Department of Informatics and Environmental Sciences. Faculty of Life and Environmental Sciences, Kyoto Prefectural University Kyoto, Japan, vol. 2.
[409] VAN ZEGHBROECK, B. Principles of electronic devices: Principle of Semiconductor Devices. 1997.
[410] GOLAN, Gady, AXELEVITCH, Alex, GORENSTEIN, B., et al. Hot-probe method for evaluation of impurities concentration in semiconductors. Microelectronics journal, vol. 37, no 9, p. 910-915, 2006.
[411] URBACH, Franz. The long-wavelength edge of photographic sensitivity and of the electronic absorption of solids. Physical Review, vol. 92, no 5, p. 1324, 1953.
[412] MA, Guobin et LIU, Xiang Yang. Hydroxyapatite: hexagonal or monoclinic?. Crystal Growth and Design, vol. 9, no 7, p. 2991-2994, 2009.
[413] BAHROLOLOOM, M. E., JAVIDI, M., JAVADPOUR, S., et al. Characterisation of natural hydroxyapatite extracted from bovine cortical bone ash. J. Ceram. Process. Res, vol. 10, no 2, p. 129-138, 2009.
[414] SOPYAN, Iis, MEL, M., RAMESH, S., et al. Porous hydroxyapatite for artificial bone applications. Science and Technology of Advanced Materials, vol. 8, no 1-2, p. 116, 2007.
[415] ZHOU, Hailong, WU, Tao, DONG, Xiuli, et al. Adsorption mechanism of BMP-7 on hydroxyapatite (001) surfaces. Biochemical and biophysical research communications, vol. 361, no 1, p. 91-96, 2007.
[416] RUSU, Viorel Marin, NG, Chuen-How, WILKE, Max, et al. Size-controlled hydroxyapatite nanoparticles as self-organized organic–inorganic composite materials. Biomaterials, vol. 26, no 26, p. 5414-5426, 2005.
[417] AREY, J. Samuel, SEAMAN, John C., et BERTSCH, Paul M. Immobilization of uranium in contaminated sediments by hydroxyapatite addition. Environmental science & technology, vol. 33, no 2, p. 337-342, 1999.

[418] GIBSON, Iain R. et BONFIELD, William. Novel synthesis and characterization of an AB-type carbonate-substituted hydroxyapatite. Journal of Biomedical Materials Research: An Official Journal of The Society for Biomaterials, The Japanese Society for Biomaterials, and The Australian Society for Biomaterials and the Korean Society for Biomaterials, vol. 59, no 4, p. 697-708, 2002.
[419] MIAO, Xigeng, TAN, Dawn Meifang, LI, Jian, et al. Mechanical and biological properties of hydroxyapatite/tricalcium phosphate scaffolds coated with poly (lactic-co-glycolic acid). Acta Biomaterialia, vol. 4, no 3, p. 638-645, 2008.
[420] SUCHANEK, Wojciech et YOSHIMURA, Masahiro. Processing and properties of hydroxyapatite-based biomaterials for use as hard tissue replacement implants. Journal of Materials Research, vol. 13, no 1, p. 94-117, 1998.
[421] ITO, Michio, HIDAKA, Yuichi, NAKAJIMA, Mituharu, et al. Effect of hydroxyapatite content on physical properties and connective tissue reactions to a chitosan–hydroxyapatite composite membrane. Journal of Biomedical Materials Research: An Official Journal of The Society for Biomaterials, The Japanese Society for Biomaterials, and The Australian Society for Biomaterials, vol. 45, no 3, p. 204-208, 1999.
[422] AKAO, Masaru, AOKI, Hideki, et KATO, Kazuo. Mechanical properties of sintered hydroxyapatite for prosthetic applications. Journal of Materials Science, vol. 16, no 3, p. 809-812, 1981.
[423] HEDIA, H. S. et MAHMOUD, Nemat-Alla. Design optimization of functionally graded dental implant. Bio-medical materials and engineering, vol. 14, no 2, p. 133-143, 2004.
[424] PIZZINI, Stefania, ROBERTS, Kevin J., DRING, Ian S., et al. Application of X-ray absorption spectroscopy to the structural characterisation of monodispersed benzotriazole coatings on partly oxidised copper thin films. Journal of Materials Chemistry, vol. 3, no 8, p. 811-819, 1993.
[425] NEJATI, E., FIROUZDOR, V., ESLAMINEJAD, M. B., et al. Needle-like nano hydroxyapatite/poly (l-lactide acid) composite scaffold for bone tissue engineering application. Materials Science and Engineering: C, vol. 29, no 3, p. 942-949, 2009.
[426] HOLZWARTH, Uwe et GIBSON, Neil. The Scherrer equation versus the'Debye-Scherrer equation'. Nature nanotechnology, vol. 6, no 9, p. 534-534, 2011.
[427] ZHOU, Jiming, ZHANG, Xingdong, CHEN, Jiyong, et al. High temperature characteristics of synthetic hydroxyapatite. Journal of materials science: materials in medicine, vol. 4, no 1, p. 83-85, 1993.
[428] ELLIOTT, J. C. Monoclinic space group of hydroxyapatite. Nature Physical Science, vol. 230, no 11, p. 72-72, 1971.
[429] KRAUS, Werner et NOLZE, Gert. POWDER CELL–a program for the representation and manipulation of crystal structures and calculation of the resulting X-ray powder patterns. Journal of applied Crystallography, vol. 29, no 3, p. 301-303, 1996.
[430] ZHU, Manzhou, AIKENS, Christine M., HOLLANDER, Frederick J., et al. Correlating the crystal structure of a thiol-protected Au25 cluster and optical properties. Journal of the American Chemical Society, vol. 130, no 18, p. 5883-5885, 2008.
[431] FRENCH, R. H., GLASS, S. J., OHUCHI, F. S., et al. Experimental and theoretical determination of the electronic structure and optical properties of three phases of ZrO_2. Physical Review B, vol. 49, no 8, p. 5133, 1994.
[432] YOUNG, R. A. et ELLIOTT, J. C. Atomic-scale bases for several properties of apatites. Archives of oral biology, vol. 11, no 7, p. 699-707, 1966.
[433] PEDONE, Alfonso, CORNO, Marta, CIVALLERI, Bartolomeo, et al. An ab initio parameterized interatomic force field for hydroxyapatite. Journal of Materials Chemistry, vol. 17, no 20, p. 2061-2068, 2007.
[434] BENRAMACHE, Said et BENHAOUA, Boubaker. Influence of annealing temperature on structural and optical properties of ZnO: In thin films prepared by ultrasonic spray technique. Superlattices and Microstructures, vol. 52, no 6, p. 1062-1070, 2012.
[435] FU, Baiping, SUN, Xuemei, QIAN, Weixin, et al. Evidence of chemical bonding to hydroxyapatite by phosphoric acid esters. Biomaterials, vol. 26, no 25, p. 5104-5110, 2005.
[436] LING, Yunfeng, RIOS, Hector F., MYERS, Elizabeth R., et al. DMP1 depletion decreases bone mineralization in vivo: an FTIR imaging analysis. Journal of Bone and Mineral Research, vol. 20, no 12, p. 2169-2177, 2005.

[437] WANG, Aili, LIU, Dong, YIN, Hengbo, et al. Size-controlled synthesis of hydroxyapatite nanorods by chemical precipitation in the presence of organic modifiers. Materials Science and Engineering: C, vol. 27, no 4, p. 865-869, 2007.
[438] MORSE, Michael D. Clusters of transition-metal atoms. Chemical Reviews, vol. 86, no 6, p. 1049-1109, 1986.
[439] MOHSENI-SALEHI, Motahare S., TAHERI-NASSAJ, Ehsan, et HOSSEINI-ZORI, Maryam. Effect of dopant (Co, Ni) concentration and hydroxyapatite compositing on photocatalytic activity of titania towards dye degradation. Journal of Photochemistry and Photobiology A: Chemistry, vol. 356, p. 57-70, 2018.
[440]. WASIM, S. M., RINCÓN, C., MARÍN, G., et al. Effect of structural disorder on the Urbach energy in Cu ternaries. Physical Review B, vol. 64, no 19, p. 195101, 2001.
[441] URBACH, Franz. The long-wavelength edge of photographic sensitivity and of the electronic absorption of solids. Physical Review, vol. 92, no 5, p. 1324, 1953.
[442] CARVALHO, A., RIBEIRO, R. M., et NETO, AH Castro. Band nesting and the optical response of two-dimensional semiconducting transition metal dichalcogenides. Physical Review B, vol. 88, no 11, p. 115205, 2013.
[443] STRUTINSKY, V. M. Shell effects in nuclear masses and deformation energies. Nuclear Physics A, vol. 95, no 2, p. 420-442, 1967.
[444] FANCHINI, G. et TAGLIAFERRO, A. Disorder and Urbach energy in hydrogenated amorphous carbon: a phenomenological model. Applied physics letters, vol. 85, no 5, p. 730-732, 2004.
[445] BHATT, R., BHAUMIK, Indranil, GANESAMOORTHY, S., et al. Urbach tail and bandgap analysis in near stoichiometric $LiNbO_3$ crystals. physica status solidi (a), vol. 209, no 1, p. 176-180, 2012.
[446] LI, Xiaoyun, MA, Meihu, AHN, Dong Uk, et al. Preparation and characterization of novel eggshell membrane-chitosan blend films for potential wound-care dressing: From waste to medicinal products. International journal of biological macromolecules, vol. 123, p. 477-484, 2019.
[447] NAGESWARARAO, P. V. et BABU, D. E. Assessment of anti-microbial activity of chitin, chitosan and shrimp shell of Litopenaeus vannamei from bhimavaram farms, west Godavari district, Andhra Pradesh. 2019.
[448] KHATTAK, Shahia, WAHID, Fazli, LIU, Ling-Pu, et al. Applications of cellulose and chitin/chitosan derivatives and composites as antibacterial materials: current state and perspectives. Applied microbiology and biotechnology, vol. 103, no 5, p. 1989-2006, 2019.
[449] SALAH, R., MICHAUD, P., MATI, F., et al. Anticancer activity of chemically prepared shrimp low molecular weight chitin evaluation with the human monocyte leukaemia cell line, THP-1. International journal of biological macromolecules, vol. 52, p. 333-339, 2013.
[450] BOUHENNA, M., SALAH, R., BAKOUR, R., et al. Effects of chitin and its derivatives on human cancer cells lines. Environmental Science and Pollution Research, vol. 22, no 20, p. 15579-15586, 2015.
[451] BENHABILES, M. S., ABDI, N., DROUICHE, N., et al. Protein recovery by ultrafiltration during isolation of chitin from shrimp shells Parapenaeus longirostris. Food Hydrocolloids, vol. 32, no 1, p. 28-34, 2013.
[452] DARMON, S. E. et RUDALL, K. M. Infra-red and X-ray studies of chitin. Discussions of the Faraday Society, vol. 9, p. 251-260, 1950.
[453] WINTEROWD, Jack G. et SANDFORD, Paul A. Chitin and chitosan. FOOD SCIENCE AND TECHNOLOGY-NEW YORK-MARCEL DEKKER-, p. 441-441, 1995.
[454] HOPPE-SEYLER, F. Ueber chitin und cellulose. Berichte der deutschen chemischen Gesellschaft, vol. 27, no 3, p. 3329-3331, 1894.
[455] NWE, Nitar, FURUIKE, Tetsuya, et TAMURA, Hiroshi. Chitosan from aquatic and terrestrial organisms and microorganisms: production, properties and applications. Biodegradable materials: production, properties and applications. Nova Science, Hauppauge, NY, p. 29-50, 2011.
[456] YEUL, Vijay S. et RAYALU, Sadhana S. Unprecedented chitin and chitosan: A chemical overview. Journal of Polymers and the Environment, vol. 21, no 2, p. 606-614, 2013.
[457] LASSAIGNE, J. L. Mémoire sur un Procède Simple pour Constater la Présence de lAzote dans des Quantités Minimes de Matière Organique. Compt Rendus, vol. 16, p. 387-391, 1843.

[458] RAJASREE, R. et RAHATE, K. P. An overview on various modifications of chitosan and it's applications. Int J Pharm Sci Res, vol. 4, no 11, p. 4175, 2013.
[459] MUZZARELLI, Riccardo AA, BOUDRANT, Joseph, MEYER, Diederick, et al. Current views on fungal chitin/chitosan, human chitinases, food preservation, glucans, pectins and inulin: A tribute to Henri Braconnot, precursor of the carbohydrate polymers science, on the chitin bicentennial. Carbohydrate polymers, vol. 87, no 2, p. 995-1012, 2012.
[460] RANE, Kishore D. et HOOVER, Dallas G. An evaluation of alkali and acid treatments for chitosan extraction from fungi. Process Biochemistry, vol. 28, no 2, p. 115-118, 1993.
[461] PERCOT, Aline, VITON, Christophe, et DOMARD, Alain. Optimization of chitin extraction from shrimp shells. Biomacromolecules, vol. 4, no 1, p. 12-18, 2003.
[462] BURROWS, Felicity, LOUIME, Clifford, ABAZINGE, Michael, et al. Extraction and evaluation of chitosan from crab exoskeleton as a seed fungicide and plant growth enhancer. Am. Eurasian J. Agric. Environ. Sci, vol. 2, no 2, p. 103-111, 2007.
[463] TAYEL, Ahmed A., MOUSSA, Shaaban H., WAEL, F., et al. Antimicrobial textile treated with chitosan from Aspergillus niger mycelial waste. International journal of biological macromolecules, vol. 49, no 2, p. 241-245, 2011.
[464] GHORMADE, V., PATHAN, E. K., et DESHPANDE, M. V. Can fungi compete with marine sources for chitosan production?. International journal of biological macromolecules, vol. 104, p. 1415-1421, 2017.
[465] DARWESH, Osama M., SULTAN, Yousef Y., SEIF, Mohamed M., et al. Bio-evaluation of crustacean and fungal nano-chitosan for applying as food ingredient. Toxicology reports, vol. 5, p. 348-356, 2018.
[466] KAUR, Surinder et DHILLON, Gurpreet Singh. The versatile biopolymer chitosan: potential sources, evaluation of extraction methods and applications. Critical reviews in Microbiology, vol. 40, no 2, p. 155-175, 2014.
[467] LARIBI-HABCHI, Hassiba, BOUANANE-DARENFED, Amel, DROUICHE, Nadjib, et al. Purification, characterization, and molecular cloning of an extracellular chitinase from Bacillus licheniformis stain LHH100 isolated from wastewater samples in Algeria. International journal of biological macromolecules, vol. 72, p. 1117-1128, 2015.
[468] BECKHOFF, Burkhard, KANNGIEßER, Birgit, LANGHOFF, Norbert, et al. (ed.). Handbook of practical X-ray fluorescence analysis. Springer Science & Business Media, 2007.
[469] OSTROM, Meredith Eggers. Separation of clay minerals from carbonate rocks by using acid. Journal of Sedimentary Research, vol. 31, no 1, p. 123-129, 1961.
[470] KASAAI, Mohammad R. A review of several reported procedures to determine the degree of N-acetylation for chitin and chitosan using infrared spectroscopy. Carbohydrate polymers, vol. 71, no 4, p. 497-508, 2008.
[471] BRUGNEROTTO, J., LIZARDI, J., GOYCOOLEA, F. M., et al. An infrared investigation in relation with chitin and chitosan characterization. Polymer, vol. 42, no 8, p. 3569-3580, 2001.
[472] ABDEEN, Z. et MOHAMMAD, Somaia G. Study of the adsorption efficiency of an eco-friendly carbohydrate polymer for contaminated aqueous solution by organophosphorus pesticide. Open Journal of Organic Polymer Materials, vol. 2014, 2013.
[473] DAS, N. G., KHAN, P. A., et HOSSAIN, Z. Chitin from the shell of two coastal portunid crabs of Bangladesh. Indian J. Fish, vol. 43, no 4, p. 413-415, 1996.
[474] QAZI, S. Junaid S., RENNIE, Adrian R., COCKCROFT, Jeremy K., et al. Use of wide-angle X-ray diffraction to measure shape and size of dispersed colloidal particles. Journal of colloid and interface science, vol. 338, no 1, p. 105-110, 2009.
[475] THIRUNAVUKKARASU, N. Biology, nutritional evaluation and utilization of mud crab Scylla tranquebarica (Fabricius, 1798). Thèse de doctorat. Ph. D. Thesis, Annamalai University, India, 2005.
[476] ALMQVIST, Nils. Fractal analysis of scanning probe microscopy images. Surface Science, vol. 355, no 1-3, p. 221-228, 1996.
[477] N.R. Taskar, V. Natarajan, I.V. Bhat, S.K. Gandhi, J. Cryst. Growth 86. 288, 1980.
[478] MOTT, Nevill Francis et DAVIS, Edward A. Electronic processes in non-crystalline materials. Oxford university press, 2012.

[479] BAUTISTA-BAÑOS, Silvia, HERNANDEZ-LAUZARDO, Ana Niurka, VELAZQUEZ-DEL VALLE, Miguel Gerardo, et al. Chitosan as a potential natural compound to control pre and postharvest diseases of horticultural commodities. Crop protection, vol. 25, no 2, p. 108-118, 2006.
[480] ZVEZDOVA, Dilyana. Synthesis and characterization of chitosan from marine sources in Black Sea. Annual Proceedings," Angel Kanchev" University of Ruse, vol. 49, no 9.1, p. 65-69, 2010.
[481] SUGUMARAN, P., SUSAN, V. Priya, RAVICHANDRAN, P., et al. Production and characterization of activated carbon from banana empty fruit bunch and Delonix regia fruit pod. Journal of Sustainable Energy & Environment, vol. 3, no 3, p. 125-132, 2012.
[482] SOUNDARRAJAN, M., GOMATHI, T., et SUDHA, P. N. Understanding the adsorption efficiency of chitosan coated carbon on heavy metal removal. Int. J. Sci. Res. Publ, vol. 3, no 1, p. 1-10, 2013.
[483] CARRAPISO, Ana I. et GARCÍA, Carmen. Development in lipid analysis: some new extraction techniques and in situ transesterification. Lipids, vol. 35, no 11, p. 1167-1177, 2000.
[484] ABDOU, Entsar S., NAGY, Khaled SA, et ELSABEE, Maher Z. Extraction and characterization of chitin and chitosan from local sources. Bioresource Technology, vol. 99, no 5, p. 1359-1367, 2008.
[485] OLIVEIRA, L. F. C. et SANTOS, P. S. Chromophore-selective resonance Raman spectra of copper (II) croconate and rhodizonate complexes with nitrogenous counterligands. Journal of molecular structure, vol. 263, p. 59-67, 1991.
[486] JUNQUEIRA, Georgia MA, ROCHA, Willian R., DE ALMEIDA, Wagner B., et al. Theoretical study of oxocarbons: structure and vibrational spectrum of the D6h and C2 forms of the rhodizonate ion. Journal of Molecular Structure: THEOCHEM, vol. 684, no 1-3, p. 141-147, 2004.
[487] ZAJĄC, A., HANUZA, J., WANDAS, M., et al. Determination of N-acetylation degree in chitosan using Raman spectroscopy. Spectrochimica Acta Part A: Molecular and Biomolecular Spectroscopy, vol. 134, p. 114-120, 2015.
[488] VAIMAKIS, Tiverios C. Thermogravimetry (TG) or Thermogravimetric Analysis (TGA). University of Ioannina, 2013.
[489] PAULIK, F. Thermal analysis under quasi-isothermal–quasi-isobaric conditions. Thermochimica acta, vol. 340, p. 105-116, 1999.
[490] PEREIRA, Leudimar Aires, DA SILVA REIS, Luizângela, BATISTA, Felipe Alves, et al. Biological Properties Of Chitosan Derivatives Associated With The Ceftazidime Drug. Carbohydrate Polymers, p. 115002, 2019.
[491] ZHENG, Feng-Yi, LI, Ruisong, HU, Jiadan, et al. Chitin and waste shrimp shells liquefaction and liquefied products/polyvinyl alcohol blend membranes. Carbohydrate polymers, vol. 205, p. 550-558, 2019.
[492] SAFDAR, Rizwan, GNANASUNDARAM, Nirmala, IYYASAMI, Regupathi, et al. Preparation, characterization and stability evaluation of ionic liquid blended chitosan tripolyphosphate microparticles. Journal of Drug Delivery Science and Technology, vol. 50, p. 217-225, 2019.
[493] TOLESA, Leta Deressa, GUPTA, Bhupender S., et LEE, Ming-Jer. Chitin and chitosan production from shrimp shells using ammonium-based ionic liquids. International journal of biological macromolecules, vol. 130, p. 818-826, 2019.
[494] SALAMAT, Samaneh, HADAVIFAR, Mojtaba, et REZAEI, Hassan. Preparation of nanochitosan-STP from shrimp shell and its application in removing of malachite green from aqueous solutions. Journal of Environmental Chemical Engineering, vol. 7, no 5, p. 103328, 2019.
[495] LOVEJOY, T. C., RAMASSE, Q. M., FALKE, M., et al. Single atom identification by energy dispersive X-ray spectroscopy. Applied Physics Letters, vol. 100, no 15, p. 154101, 2012.
[496] SU, Kangning, YUAN, Li, YANG, Jie, et al. Numerical Simulation of Mandible Bone Remodeling under Tooth Loading: A Parametric Study. Scientific reports, vol. 9, no 1, p. 1-12, 2019.
[497] GUPTA, Anant, VENKATESH, Srivas, CHOPRA, Sumit, et al. Generative image translation for data augmentation of bone lesion pathology. arXiv preprint arXiv:1902.02248, 2019.
[498] LI, Jie, BAO, Jun, ZENG, Jian, et al. Iguratimod: a valuable remedy from the Asia Pacific region for ameliorating autoimmune diseases and protecting bone physiology. Bone research, vol. 7, no 1, p. 1-11, 2019.
[499] SHARMA, Tarang, BHATNAGAR, Shinjini, et TIWARI, Ashutosh. Typhoid Diagnostics: Looking Beneath the Surface. Journal of Clinical & Diagnostic Research, vol. 12, no 9, 2018.

[500] PRAKASAM, Mythili, LOCS, Janis, SALMA-ANCANE, Kristine, et al. Biodegradable materials and metallic implants—a review. Journal of functional biomaterials, vol. 8, no 4, p. 44, 2017.
[501] MANAM, N. S., HARUN, W. S. W., SHRI, D. N. A., et al. Study of corrosion in biocompatible metals for implants: A review. Journal of Alloys and Compounds, vol. 701, p. 698-715, 2017.
[502] PIGATTO, Paolo D., BERTI, Emilio, SPADARI, Francesco, et al. Photoletter to the editor: Exfoliative cheilitis associated with titanium dental implants and mercury amalgam. Journal of dermatological case reports, vol. 5, no 4, p. 89, 2011.
[503] SEVILLA, P., APARICIO, C., PLANELL, J. A., et al. Comparison of the mechanical properties between tantalum and nickel–titanium foams implant materials for bone ingrowth applications. Journal of Alloys and Compounds, vol. 439, no 1-2, p. 67-73, 2007.
[504] PARK, B. J. et KIM, Young Kon. Metallic biomaterials. Balance, vol. 1, p. 50, 2003.
[505] MANAM, N. S., HARUN, W. S. W., SHRI, D. N. A., et al. Study of corrosion in biocompatible metals for implants: A review. Journal of Alloys and Compounds, vol. 701, p. 698-715, 2017.
[506] LOGROSCINO, Giandomenico, DONATI, Fabrizio, SARACCO, Michela, et al. Early failure of a locked titanium plate in a proximal humeral fracture: Case report and metallurgic analysis. Trauma case reports, vol. 17, p. 18-22, 2018.
[507] GAILLARD, Romain, KENNEY, Raymond, DELALANDE, Jean-Luc, et al. Ten-to 16-Year Results of a Modern Cementless Dual-Mobility Acetabular Implant in Primary Total Hip Arthroplasty. The Journal of arthroplasty, vol. 34, no 11, p. 2704-2710, 2019.
[508] LEMIRE, Joseph A., HARRISON, Joe J., et TURNER, Raymond J. Antimicrobial activity of metals: mechanisms, molecular targets and applications. Nature Reviews Microbiology, vol. 11, no 6, p. 371-384, 2013.
[509] THOMAS, V., CATLEDGE, S. A., BAKER, P., et al. Ceramic Coatings in Load-Bearing Articulating Joint Implants. In : Materials for Bone Disorders. Academic Press, p. 315-347, 2017.
[510] PECHANCOVÁ, Radka, PLUHÁČEK, Tomáš, GALLO, Jiří, et al. Study of chromium species release from metal implants in blood and joint effusion: Utilization of HPLC-ICP-MS. Talanta, vol. 185, p. 370-377, 2018.
[511] EDDYA, Mohammed et EL-HAMI, Khalil. Bio-Ceramic Amalgams Based on HAP Doped by Cobalt, Nickel and Their Toxicity Discussion. In : International Conference on Advanced Intelligent Systems for Sustainable Development. Springer, Cham, p. 66-71, 2019.
[512] ELINDER, Carl-Gustaf, FRIBERG, Lars, KJELLSTRÖM, Tord, et al. Biological monitoring of metals. World Health Organization, 1994.
[513] GUILLEMOT, Fabien. Recent advances in the design of titanium alloys for orthopedic applications. Expert review of medical devices, vol. 2, no 6, p. 741-748, 2005.
[514] GRANDE, Fedora et TUCCI, Paola. Titanium dioxide nanoparticles: a risk for human health?. Mini reviews in medicinal chemistry, vol. 16, no 9, p. 762-769, 2016.
[515] MACDONALD, D., FERNÁNDEZ, R., DELLORO, F., et al. Cold spraying of armstrong process titanium powder for additive manufacturing. Journal of Thermal Spray Technology, vol. 26, no 4, p. 598-609, 2017.
[516] LIU, Luting et WEBSTER, Thomas J. Nanotechnology for Reducing Orthopedic Implant Infections: Synthesis, Characterization, and Properties. In : Orthopedic Biomaterials. Springer, Cham, p. 31-62, 2017.
[517] KANEKO, Nao, SUZUKI, Yuhei, UMEDA, Ryo, et al. Development of nitrogen-doped HAP ceramics. Journal of Asian Ceramic Societies, p. 1-8, 2020.
[518] RAMALINGAM, Sundar, SUNDAR, Chalini, JANSEN, John A., et al. Alveolar bone science: Structural characteristics and pathological changes. In : Dental Implants and Bone Grafts. Woodhead Publishing, p. 1-22, 2020.
[519] SAILUAM, Wutthigrai, PHACHEERAK, Kanoknan, FONGKAEW, Ittipon, et al. Elastic and mechanical properties of HAP under pressure: A first-principles investigation. Computational Condensed Matter, p. e00481, 2020.

[520] BELAMRI, D., HARABI, A., KARBOUAA, N., et al. The effect of KF on the structural evolution of natural HAP during conventional and microwave sintering. Ceramics International, vol. 46, no 1, p. 1189-1194, 2020.
[521] INDRA, Ade, FIRDAUS, Ridwan, MULYADI, Ismet Hari, et al. Enhancing the physical and mechanical properties of pellet-shaped HAP by controlling micron-and nano-sized powder ratios. Ceramics International, 2020.
[522] LIU, Dan, WU, Yong-hao, LI, Xiang-feng, et al. Effect of nano-scaled surface roughness on the biological properties of HAP ceramics. Chinese Journal of Tissue Engineering Research, vol. 22, no 18, p. 2903-2909, 2018.
[523] GHOLIZADEH, Bahador Safikhani, BUAZAR, Foad, HOSSEINI, Seyed Mehdi, et al. Enhanced antibacterial activity, mechanical and physical properties of alginate/HAP bionanocomposite film. International journal of biological macromolecules, vol. 116, p. 786-792, 2018.
[524] EDDYA, Mohammed et EL-HAMI, Khalil. Thermal and Electrical Conductivities of Bio-Ceramic Amalgams Based on HAP Doped by Low Metal (Co, Ni, Cu, Mn) Concentration for Dental and Orthopedic Engineering. In : International Conference on Advanced Intelligent Systems for Sustainable Development. Springer, Cham, p. 364-374, 2019.
[525] EDDYA, Mohammed, TBIB, Bouazza, et EL-HAMI, Khalil. High photocatalytic activity of hydroxyapatite bio-degradable semiconductor for solar panels and environment protection. *ISTE OpenScience*, 2018.
[526] ZHOU, Jianhong, WANG, Xiaoli, et ZHAO, Lingzhou. Antibacterial, angiogenic, and osteogenic activities of Ca, P, Co, F, and Sr compound doped titania coatings with different Sr content. Scientific reports, vol. 9, no 1, p. 1-11, 2019.
[527] RUPHUY, Gabriela, LOPES, Jose Carlos, DIAS, Madalena Maria, et al. New insights into nanoHAP/CS nanocomposites for bone tissue regeneration. In : Materials for Biomedical Engineering. Elsevier, p. 331-371, 2019.
[528] PAWLIK, Anna, REHMAN, Muhammad Atiq Ur, NAWAZ, Qaisar, et al. Fabrication and characterization of electrophoretically deposited CS-HAP composite coatings on anodic titanium dioxide layers. Electrochimica Acta, vol. 307, p. 465-473, 2019.
[529] LEILEI, Zhang, HEJUN, Li, KEZHI, Li, et al. Multi-layer SiC/Mg and F co-substituted HAP/CS bioactive coating for carbon fibers. Materials Letters, vol. 164, p. 360-363, 2016.
[530] DE FARIAS, Bruna Silva, JUNIOR, Tito Roberto Sant'Anna Cadaval, et DE ALMEIDA PINTO, Luiz Antonio. CS-functionalized nanofibers: A comprehensive review on challenges and prospects for food applications. International journal of biological macromolecules, vol. 123, p. 210-220, 2019.
[531] INANLI, Ayşe Gurel, TÜMERKAN, Elif T. Aksun, ABED, Nariman EL, et al. The impact of CS on seafood quality and human health: A review. Trends in Food Science & Technology, 2020.
[532] MA, Yifei, HAN, Jiemin, WANG, Mei, et al. Electrophoretic deposition of Graphene-based materials: A review of materials and their applications. Journal of Materiomics, vol. 4, no 2, p. 108-120, 2018.
[533] MAJKOWSKA-MARZEC, Beata, ROGALA-WIELGUS, Dorota, BARTMAŃSKI, Michał, et al. Comparison of Properties of the Hybrid and Bilayer MWCNTs—HAP Coatings on Ti Alloy. Coatings, vol. 9, no 10, p. 643, 2019.
[534] LEILEI, Zhang, HEJUN, Li, KEZHI, Li, et al. Multi-layer SiC/Mg and F co-substituted HAP/CS bioactive coating for carbon fibers. Materials Letters, vol. 164, p. 360-363, 2016.
[535] MOHAMMED, Eddya, BOUAZZA, Tbib, et KHALIL, El-Hami. A novel method for the elaboration of HAP with high purity by sol-gel using the albumin and comparison with the classical methods. In : AIP Conference Proceedings. AIP Publishing LLC, p. 030013, 2018.
[536] HARRIS, Peter JF. Nanotubes with horns: a clue to the growth mechanism?. Fullerenes, Nanotubes and Carbon Nanostructures, p. 1-4, 2020.
[537] HE, Bing, SHI, Yujie, LIANG, Yanqin, et al. Single-walled carbon-nanohorns improve biocompatibility over nanotubes by triggering less protein-initiated pyroptosis and apoptosis in macrophages. Nature communications, vol. 9, no 1, p. 1-21, 2018.
[538] ZHU, Shuyun et XU, Guobao. Single-walled carbon nanohorns and their applications. Nanoscale, vol. 2, no 12, p. 2538-2549, 2010.

[539] NGUYEN, Tuan Anh, THI THAM, Nguyen, NGUYEN THI HONG, Phuong, et al. Study on Industrial-Scale Fabrication of Graphene Nanoplatelets (GNPs) from Natural Graphite. In : Materials Science Forum. Trans Tech Publications, p. 101-105, 2018.
[540] JUN, Y. S., UM, J. G., JIANG, G., et al. A study on the effects of Graphene nano-platelets (GnPs) sheet sizes from a few to hundred microns on the thermal, mechanical, and electrical properties of polypropylene (PP)/GnPs composites. Express Polymer Letters, vol. 12, no 10, p. 885-897, 2018.
[541] SYAMA, S. et MOHANAN, P. V. Safety and biocompatibility of Graphene: A new generation nanomaterial for biomedical application. International journal of biological macromolecules, vol. 86, p. 546-555, 2016.
[542] GUO, Xiaoqing et MEI, Nan. Assessment of the toxic potential of Graphene family nanomaterials. Journal of food and drug analysis, vol. 22, no 1, p. 105-115, 2014.
[543] YANG, Kai, FENG, Liangzhu, SHI, Xiaoze, et al. Nano-Graphene in biomedicine: theranostic applications. Chemical Society Reviews, vol. 42, no 2, p. 530-547, 2013.
[544] BARI, Sarang Sharad et MISHRA, Satyendra. Recent Advances in Nanostructured Polymer Composites for Biomedical Applications. In : Nanostructured Polymer Composites for Biomedical Applications. Elsevier, p. 489-506, 2019.
[545] MUNIR, Khurram, WEN, Cuie, et LI, Yuncang. Graphene nanoplatelets-reinforced magnesium metal matrix nanocomposites with superior mechanical and corrosion performance for biomedical applications. Journal of Magnesium and Alloys, 2020.
[546] BROWN, Paul Wencil. Phase Relationships in the Ternary System CaO─ P_2O_5─ H_2O at 25° C. Journal of the American Ceramic Society, vol. 75, no 1, p. 17-22, 1992.
[547] PEREIRA, Kaio AB, CESTARI, Sibele P., NETO, Roberto P. Cucinelli, et al. Oxidized-sulfonated multi-walled carbon nanotube/HAP hybrid particles: Synthesis and characterization. Journal of Solid State Chemistry, vol. 279, p. 120924, 2019.
[548] GÓMEZ, Sofía, RENDTORFF, Nicolás M., AGLIETTI, Esteban F., et al. Surface modification of multiwall carbon nanotubes by sulfonitric treatment. Applied Surface Science, vol. 379, p. 264-269, 2016.
[549] SHACKLEY, M. Steven. An introduction to X-ray fluorescence (XRF) analysis in archaeology. In : X-ray fluorescence spectrometry (XRF) in geoarchaeology. Springer, New York, NY, 2011. p. 7-44.
[550] ROUSSEAU, Richard M. Detection limit and estimate of uncertainty of analytical XRF results. Rigaku J, vol. 18, no 2, p. 33-47, 2001.
[551] TOURBIN, M., BROUILLET, F., GALEY, B., et al. Agglomeration of stoichiometric HAP: Impact on particle size distribution and purity in the precipitation and maturation steps. Powder Technology, vol. 360, p. 977-988, 2020.
[552] TÜRK, S., ALTINSOY, I., ÇELEBIEFE, G., et al. Microwave–assisted biomimetic synthesis of HAP using different sources of calcium. Materials Science and Engineering: C, vol. 76, p. 528-535, 2017.
[553] BOUKHA, Zouhair, YESTE, María Pilar, CAUQUI, Miguel Ángel, et al. Influence of Ca/P ratio on the catalytic performance of Ni/HAP samples in dry reforming of methane. Applied Catalysis A: General, vol. 580, p. 34-45, 2019.
[554] JIANG, Yu, YUAN, Zhiyu, et HUANG, Jie. Substituted HAP: a recent development. Materials Technology, p. 1-12, 2019.
[555] KESSELI, Fioleda P., LAUER, Caroline S., BAKER, Ian, et al. Identification of a calcium phosphoserine coordination network in an adhesive organo-apatitic bone cement system. Acta Biomaterialia, 2020.
[556] CHOY, Man-Tik, YEUNG, Ka-Wai, CHEN, Ling, et al. In situ synthesis of osteoconductive biphasic ceramic coatings on Ti6Al4V substrate by laser-microwave hybridization. Surface and Coatings Technology, vol. 330, p. 92-101, 2017.
[557] KAROUSIS, Nikolaos, SUAREZ-MARTINEZ, Irene, EWELS, Christopher P., et al. Structure, properties, functionalization, and applications of carbon nanohorns. Chemical reviews, vol. 116, no 8, p. 4850-4883, 2016.

[558] FENG, Pei, PENG, Shuping, WU, Ping, et al. A nano-sandwich construct built with Graphene nanosheets and carbon nanotubes enhances mechanical properties of HAP–polyetheretherketone scaffolds. International journal of nanomedicine, vol. 11, p. 3487, 2016.
[559] BASIRUN, Wan Jeffrey, NASIRI-TABRIZI, Bahman, et BARADARAN, Saeid. Overview of HAP–Graphene nanoplatelets composite as bone graft substitute: Mechanical behavior and in-vitro biofunctionality. Critical Reviews in Solid State and Materials Sciences, vol. 43, no 3, p. 177-212, 2018.
[560] KOSTOPOULOS, Vassilis, KOTROTSOS, Athanasios, et FOURIKI, Kalliopi. Graphene Nanoplatelet- and HAP-Doped Supramolecular Electrospun Fibers as Potential Materials for Tissue Engineering and Cell Culture. International journal of molecular sciences, vol. 20, no 7, p. 1674, 2019.
[561] BASIRUN, Wan Jeffrey, NASIRI-TABRIZI, Bahman, et BARADARAN, Saeid. Overview of HAP–Graphene nanoplatelets composite as bone graft substitute: Mechanical behavior and in-vitro biofunctionality. Critical Reviews in Solid State and Materials Sciences, vol. 43, no 3, p. 177-212, 2018.
[562] DOS SANTOS, Z. M., CARONI, A. L. P. F., PEREIRA, M. R., et al. Determination of deacetylation degree of CS: a comparison between conductometric titration and CHN elemental analysis. Carbohydrate Research, vol. 344, no 18, p. 2591-2595, 2009.
[563] HAJJI, Sawssen, YOUNES, Islem, GHORBEL-BELLAAJ, Olfa, et al. Structural differences between chitin and CS extracted from three different marine sources. International journal of biological macromolecules, vol. 65, p. 298-306, 2014.
[564] BERTONI, Enrico, BIGI, Adriana, FALINI, Giuseppe, et al. HAP/polyacrylic acid nanocrystals. Journal of Materials Chemistry, vol. 9, no 3, p. 779-782, 1999.
[565] SZLACHTA, Monika, ORDON, Klaudia, NOWICKA, Katarzyna, et al. Thermal properties of polyurethane-based composites modified with CS for biomedical applications. Journal of Thermal Analysis and Calorimetry, p. 1-8, 2020.
[566] STEVANOVIĆ, Milena, DJOŠIĆ, Marija, JANKOVIĆ, Ana, et al. Antibacterial Graphene-Based HAP/CS Coating with Gentamicin for Potential Applications in Bone Tissue Engineering. Journal of Biomedical Materials Research Part A, 2020.
[567] PERMATASARI, Hestining Ajeng, WATI, Rosita, ANGGRAINI, Rista Mutia, et al. HAP Extracted from Fish Bone Wastes by Heat Treatment. In : Key Engineering Materials. Trans Tech Publications Ltd, p. 318-323, 2020.
[568] MATSUMOTO, Takuya, OKAZAKI, M., INOUE, M., et al. Crystallinity and solubility characteristics of HAP adsorbed amino acid. Biomaterials, vol. 23, no 10, p. 2241-2247, 2002.
[569] YILMAZ, Pelin, ÖZTÜRK ER, Elif, BAKIRDERE, Sezgin, et al. Application of supercritical gel drying method on fabrication of mechanically improved and biologically safe three-component scaffold composed of Graphene oxide/CS/HAP and characterization studies. Journal of Materials Research and Technology, vol. 8, no 6, p. 5201-5216, 2019.
[570] MOHAMMED, Eddya, BOUAZZA, Tbib, et KHALIL, El-Hami. Structural and Vibrational Study of HAP Bio-ceramic Pigments with Chromophore Ions (Co^{2+}, Ni^{2+}, Cu^{2+}, Mn^{2+}). In : International Conference on Advanced Intelligent Systems for Sustainable Development. Springer, Cham, p. 62-70, 2018.
[571] VAUTHIER, Christine. Issues related with the analysis of nanomaterials. In : Handbook of Nanomaterials in Analytical Chemistry. Elsevier, p. 473-490, 2020.
[572] PAHOMI, Alexandru, VLASE, Gabriela, TOMA, Alexandra, et al. Synthesis, thermal behavior and FTIR study of some HAP precursors doped with two metals. Journal of Thermal Analysis and Calorimetry, vol. 138, no 3, p. 2175-2183, 2019.
[573] EDDYA, Mohammed, TBIB, Bouazza, et KHALIL, EL-Hami. A comparison of CS properties after extraction from shrimp shells by diluted and concentrated acids. Heliyon, vol. 6, no 2, p. e03486, 2020.
[574] MOHRIG, Jerry R., HAMMOND, Christina Noring, et SCHATZ, Paul F. Techniques in organic chemistry. Macmillan, 2010.
[575] LIAO, Puhong. Synthesis, characterization and properties of phenalenyl-based neutral radical molecular conductors. University of California, Riverside, 2007.
[576] XU, Jianxun, TOMIMOTO, Hiroyuki, et NAKAYAMA, Tomonobu. What is inside carbon nanohorn aggregates?. Carbon, vol. 49, no 6, p. 2074-2078, 2011.

[577] BARTMANSKI, Michal, ZIELINSKI, Andrzej, JAZDZEWSKA, Magdalena, et al. Effects of electrophoretic deposition times and nanotubular oxide surfaces on properties of the nanoHAP/nanocopper coating on the Ti13Zr13Nb alloy. Ceramics International, vol. 45, no 16, p. 20002-20010, 2019.
[578] WOŹNIAK, Bartosz, SZAŁAJ, Urszula, CHODARA, Agnieszka, et al. Mechanism for sonocoating a polymer surface with nano-HAP. Materials Letters, vol. 249, p. 155-159, 2019.
[579] MOHAMMED, Eddya, BOUAZZA, Tbib, et KHALIL, El-Hami. Springer, Cham, p. 62-70, 2018.
[580] GIBSON, I. R., BEST, S. M., et BONFIELD, W. Chemical characterization of silicon-substituted hydroxyapatite. Journal of Biomedical Materials Research: An Official Journal of The Society for Biomaterials, The Japanese Society for Biomaterials, and The Australian Society for Biomaterials, vol. 44, no 4, p. 422-428, 1999.
[581] ŠENK, PRÁCE Bc VÍT et CIHLÁŘ, RNDr JAROSLAV. Keramické porézní materiály–příprava, struktura a vlastnosti. 2011.
[582] MIAO, Xigeng, TAN, Dawn Meifang, LI, Jian, et al. Mechanical and biological properties of hydroxyapatite/tricalcium phosphate scaffolds coated with poly (lactic-co-glycolic acid). Acta Biomaterialia, vol. 4, no 3, p. 638-645, 2008.
[583] SUCHANEK, Wojciech et YOSHIMURA, Masahiro. Processing and properties of hydroxyapatite-based biomaterials for use as hard tissue replacement implants. Journal of Materials Research, vol. 13, no 1, p. 94-117, 1998.
[584] ITO, Michio, HIDAKA, Yuichi, NAKAJIMA, Mituharu, et al. Journal of Biomedical Ma-terials Research Part A, vol. 45, no 3, p. 204-208, 1999.
[585] AKAO, Masaru, AOKI, Hideki, et KATO, Kazuo. Journal of Materials Science, vol. 16, no 3, p. 809-812, 1981.
[586] HEDIA, H. S. et MAHMOUD, Nemat-Alla. Bio-Medical Materials and Engineering, vol. 14, no 2, p. 133-143, 2004.
[587] LOF, R. W., VAN VEENENDAAL, M. A., KOOPMANS, B., et al.. Physical Review Letters, vol. 68, no 26, p. 3924, 1992.
[588] CALDERIN, L., STOTT, M. J., et RUBIO, A. Physical Review B, 2003, vol. 67, no 13, p. 134106.
[589] DE ARAUJO, Tatiana S., MACEDO, Zélia S., DE OLIVEIRA, Petrus ASC, et al. Journal of Materials Science, vol. 42, no 7, p. 2236-2243, 2007.
[590] BARD, Allen J. et FOX, Marye Anne. Accounts of Chemical Research, vol. 28, no 3, p. 141-145, 1995.
[591] ROBERTSON, John. Journal of Vacuum Science & Technology B: Microelectronics and Nanometer Structures Processing, Measurement, and Phenomena, vol. 18, no 3, p. 1785-1791, 2000.
[592] Thirunavukkarasu N (2005). Biology, nutritional evaluation and utilization of mud crab Scylla tranquebarica (Fabricius, 1768). Ph.D., Thesis, Annamalai University, India. p. 127, 2005.
[593] N. Almqvist, Fractal Analysis of Scanning Probe Microscopy images, Sur. Sci. 355 (1996) 221-228.
[594] N.R. Taskar, V. Natarajan, I.V. Bhat, S.K. Gandhi, J. Cryst. Growth 86. 288, 1980.
[595] N.F. Mott, E.A. Davis, Electronic Processes in Non-crystalline Materials, Clarendon Press, Oxford, 1979.
[596] David R. Lide, CRC Handbook of Chemistry and Physics, CRC Press, 2009, 90e éd., 2804 p., relié (ISBN 978-1-420-09084-0), 2009.
[597] BOUZIDI, A., YAHIA, I. S., et EL-SADEK, M. S. A. Dyes and Pigments, vol. 146, p. 66-72, 2017.
[598] LAGHZIZIL, A., ELHERCH, N., BOUHAOUSS, A., et al.. Materials research bulletin, vol. 36, no 5, p. 953-962, 2001.
[599] KRISHNA, S. Chenna, SUPRIYA, N., JHA, Abhay K., et al.Thermal. ISRN Metallurgy, vol. 2012, 2012.
[600]. TAYLOR, N. O. The Journal of the American Dental Association (1922), vol. 17, no 1, p. 112-124, 1930.
[601] MATYSIAK, M. Pratiques et Organisation des Soins, vol. 40, no 2, p. 133-144, 2009.
[602] ORLANDO, Francesca Romana, GUTIÉRREZ-CLAVERO, Francisca, PÉREZ-DOMÍNGUEZ, Servando, et al. Pétition Européenne" NON au mercure dentaire!.

[603] SAXE, Stanley R., WEKSTEIN, MERLE W., KRYSCIO, RICHARD J., et al. The Journal of the American Dental Association, vol. 130, no 2, p. 191-199, 1999.
[604] GROSMAN, M. et PICOT, A. Médecine & Longévité, vol. 1, no 1, p. 12-21, 2009.
[605] LHOTKA, Christian, SZEKERES, Thomas, STEFFAN, Ilse, et al. Journal of Orthopaedic Research, vol. 21, no 2, p. 189-195, 2003.
[606] DAHLSTRAND, Henrik, STARK, André, ANISSIAN, Lucas, et al.Elevated serum concentrations of cobalt. The Journal of arthroplasty, vol. 24, no 6, p. 837-845, 2009.
[607] CHRISTENSEN, Jytte Molin et POULSEN, Otto Melchior. Science of the total environment, vol. 150, no 1-3, p. 95-104, 1994.
[608] SCHULEIN, Thomas M. Significant. J Hist Dent, vol. 53, no 2, p. 63-72, 2005.
[609] SUN, Limin, BERNDT, Christopher C., GROSS, Karlis A., et al.Material. Journal of Biomedical Materials Research Part A, vol. 58, no 5, p. 570-592, 2001.
[610] THAMARAISELVI, T. et RAJESWARI, S. Carbon, vol. 24, no 31, p. 172, 2004.
[611] LEVITT, Stephen R., CRAYTON, Philip H., MONROE, Eugene A., et al. Journal of Biomedical Materials Research Part A, vol. 3, no 4, p. 683-684, 1969.
[612] MONROE, E. A., VOTAVA, Ward, BASS, D. B., et al.. Journal of dental research, vol. 50, no 4, p. 860-861, 1971.
[613] YIP, Kevin H.-K., SMALES, Roger J., et KAIDONIS, John A. International Journal of Prosthodontics, vol. 17, no 3, 2004.
[614] LINDH, Ulf, HUDECEK, Romuald, DANERSUND, Antero, et al. Neuroendocrinology Letters, vol. 23, no 5-6, p. 459, 2002.
[615] ROULET, J.-F. Clinical oral investigations, vol. 1, no 1, p. 40-46, 1997.
[616] WITTE, Frank, FEYERABEND, Frank, MAIER, Petra, et al. Biomaterials, vol. 28, no 13, p. 2163-2174, 2007.
[617] NEGROIU, Gabriela, PITICESCU, Roxana M., CHITANU, Gabrielle C., et al. Journal of Materials Science: Materials in Medicine, vol. 19, no 4, p. 1537-1544, 2008.
[618] MA, Guobin et LIU, Xiang Yang. Crystal Growth and Design, vol. 9, no 7, p. 2991-2994, 2009.
[619] BAHROLOLOOM, M. E., JAVIDI, M., JAVADPOUR, S., et al.. J. Ceram. Process. Res, vol. 10, no 2, p. 129-138, 2009.
[620] SOPYAN, Iis, MEL, M., RAMESH, S., et al. Science and Technology of Advanced Materials, vol. 8, no 1, p. 116-123, 2007.
[621] ZHOU, Hailong, WU, Tao, DONG, Xiuli, et al. Biochemical and biophysical research communications, vol. 361, no 1, p. 91-96.
[622] RUSU, Viorel Marin, NG, Chuen-How, WILKE, Max, et al. Biomaterials, vol. 26, no 26, p. 5414-5426, 2005.
[623] AREY, J. Samuel, SEAMAN, John C., et BERTSCH, Paul M. Environmental science & technology, vol. 33, no 2, p. 337-342, 1998.
[624] GUPTA, Umesh C. et GUPTA, Subhas C. Communications in Soil Science & Plant Analysis, vol. 29, no 11-14, p. 1491-1522, 1998.
[625] KUM, Kee-Yeon, ZHU, Qiang, SAFAVI, Kamran, et al. . Australian Endodontic Journal, vol. 39, no 3, p. 126-130, 2013.
[626] MESINKOVSKA, Natasha Atanaskova, TELLEZ, Alejandra, MOLINA, Luciana, et al. Archives of dermatology, vol. 148, no 6, p. 687-693, 2012.
[627] HALLAB, Nadim, MERRITT, Katharine, et JACOBS, Joshua J. JBJS, vol. 83, no 3, p. 428, 2001.
[628] BRUNE, D. Biomaterials, vol. 7, no 3, p. 163-175, 1986.
[629] LANSDOWN, A. B. G. Critical reviews in toxicology, vol. 37, no 3, p. 237-250, 2007.
[630] WATAHA, John C. The Journal of prosthetic dentistry, vol. 83, no 2, p. 223-234, 2000.
[631]. HENSTEN-PETTERSEN, Arne et JACOBSEN, Nils. The Journal of prosthetic dentistry, vol. 65, no 1, p. 138-144, 1991.
[632] KONTTINEN, Yrjö T. et PAJARINEN, Jukka. Nature reviews Rheumatology, vol. 9, no 1, p. 5-6, 2013.

[633] BARCELOUX, Donald G. et BARCELOUX, Donald. Cobalt. Journal of Toxicology: Clinical Toxicology, vol. 37, no 2, p. 201-216, 1999.
[634] KENNEDY, David O. Nutrients, vol. 8, no 2, p. 68, 2016.
[635] KAMACHIMUDALI, U., SRIDHAR, T. M., et RAJ, Baldev. Sadhana, vol. 28, no 3, p. 601-637, 2003.
[636] AL-IMAM, Hiba, BENETTI, Ana R., ÖZHAYAT, Esben B., et al. Contact dermatitis, vol. 75, no 6, p. 377-383, 2016.
[637] ELKABOUSS, Kaoutar, KACIMI, Mohamed, ZIYAD, Mahfoud, et al. Journal of Catalysis, vol. 226, no 1, p. 16-24, 2004.
[638] QAMAR, Zeeshan, RAHIM, Zubaidah Binti Haji Abdul, CHEW, Hooi Pin, et al. The Journal of the Pakistan Medical Association, vol. 67, no 1, p. 116-120, 2017.
[639] PRIYA, B. Anu, SENTHILGURU, K., AGARWAL, T., et al. RSC Advances, vol. 5, no 89, p. 72515-72528, 2015.